Universitat de les Illes Balears

DOCTORAL THESIS

EFFECT OF THE SURFACE THERMAL HETEROGENEITIES ON THE ATMOSPHERIC BOUNDARY LAYER

by

Gemma Simó Diego

2018

Universitat de les Illes Balears

DOCTORAL THESIS

Doctoral programme of physics

EFFECT OF THE SURFACE THERMAL HETEROGENEITIES ON THE ATMOSPHERIC BOUNDARY LAYER

by

Gemma Simó Diego

Supervisors:

Joan Cuxart, Vicente Caselles, Maria Antonia Jiménez

Doctor by the Universitat de les Illes Balears

June 2018

List of publications derived from this thesis

1. Gemma Simó, Maria A. Jiménez, Daniel Martínez-Villagrasa, Rodrigo Picos, Alvaro López-Grifol, Belen Martí, Jose A. Guijarro and Joan Cuxart. Observed atmospheric and surface variability on heterogeneous terrain at the hectometer scale. Submitted to JGR-Atmospheres

2. Vicente García-Santos,Joan Cuxart,Maria A. Jiménez,Daniel Martínez-Villagrasa, Gemma Simó, Rodrigo Picos and Vicente Caselles. Study of Temperature Heterogeneities at subkilometric scales and impact of surface-atmosphere energy interactions. Under review in Transactions on Geoscience and Remote Sensing

3. Gemma Simó, Daniel Martínez-Villagrasa, Maria A. Jiménez, Vicente Caselles and Joan Cuxart. Impact of the Surface-Atmosphere Variables on the relation between Air and Surface Temperatures. Accepted in Pure and Applied Geophysics (2018).

4. Veriozka Azeñas, Joan Cuxart, Rodrigo Picos, Medrano, H., Gemma Simó, Alvaro López-Grifol and Javier Gulías. Thermal regulation capacity of a green roof system in the Mediterranean region: The effects of vegetation and irrigation level. In Energy and Buildings (2018). Volume 164, 1 April 2018, Pages 226-238 DOI:10.1016/j.enbuild.2018.01.010
URL:https://www.sciencedirect.com/science/article/pii/S0378778817312252

5. Gemma Simó,Vicente García-Santos,Maria A. Jiménez,Daniel Martínez-Villagrasa, Rodrigo Picos, Vicente Caselles and Joan Cuxart. Landsat and Local Land Surface Temperatures in a Heterogeneous Terrain Compared to MODIS Values. In: Remote Sensing, (2016),8,849. DOI:10.3390/rs8100849. URL: http://www.mdpi.com/2072-4292/8/10/849

6. Maria A. Jiménez, Gemma Simó, Burkhard Wrenger, Maja Telisman-Prtenjak, Jose A. Guijarro and Joan Cuxart. Morning transition case between the land and the sea breeze regimes. In: Atmospheric Research (2015). Volumes 172-173, 15 May-1 June 2016, Pages 95-108. DOI:10.1016/j.atmosres.2015.12.019
URL:http://www.sciencedirect.com/science/article/pii/S0169809516000053

"Perquè hi haurà un dia que no podrem més i llavors ho podrem tot."

Vicent Andrés Estellés

Resum (en Català)

La Capa Límit Atmosfèrica és la capa de l'atmosfera que es troba més pròxima a la superfície terrestre. En aquesta capa, el gruix de la qual pot variar entre un centenar de metres i un parell de quilòmetres, hi ha un intercanvi constant d'energia i matèria. Aquests processos d'intercanvi d'energia que tenen lloc en la Capa Límit Atmosfèrica poden ser descrits per l'equació de balanç d'energia superficial, on la radiació neta total de la superfície s'assumeix igual a la suma dels fluxos de calor sensible, calor latent i calor de sòl que tenen lloc en ella. Però des dels anys 80, els científics s'han adonat que els termes d'aquesta equació de balanç d'energia no es cancel·len quan es fan mesures observacionals. Des d'aleshores, s'estan fent molts estudis per tal de veure a què és degut aquest problema: alguns ho atribueixen a errors de mesura, d'altres al fet que no s'identifiquen bé els fluxos de calor sensible i/o latent, o bé que hi ha més a tenir en compte a banda dels fluxos esmentats anteriorment.

En aquest treball hem estudiat quin és el paper que juguen les heterogeneïtats superficials en aquests processos. Per tal de dur-ho a terme, ens hem endinsat en els mons de la teledetecció i la meteorologia mitjançant estudis duts a terme en superfícies heterogènies tant a escala hectomètrica com quilomètrica.

Primerament, hem estudiat la variabilitat espacial de la temperatura superficial a escala hectomètrica en el Campus de la Universitat de les Illes Balears. Hem trobat diferències significatives en els valors de la temperatura superficial entre les diferents zones del Campus, tant en els mesos freds com en els càlids (sent superiors en aquests últims). A més, hem pogut comprovar que els satèl·lits amb resolució espacial menor que la mida de les heterogeneïtats no són capaços d'observar aquestes diferències.

En segon lloc, hem estudiat la variabilitat temporal de la relació entre la temperatura de l'aire i la temperatura superficial mesurades *in situ* en un punt d'aquesta superfície heterogènia, així com la seva dependència amb altres variables. Hem observat que durant el dia els valors estan ben correlacionats amb la intensitat del flux de flotabilitat, amb valors màxims en sòls molt càlids i secs. De nit en canvi, no hem trobat correlacions destacades amb cap magnitud. Aquest fet ens indica que el sistema atmosfera-sòl en conjunt respon a la demanda d'energia de la capa superficial i no permet l'establiment de forts gradients de temperatura en els primers 2 metres més pròxims a la superfície. Per tal de fer aquest estudi, hem fet una anàlisi prèvia sobre els diferents mètodes i instruments dels que disposàvem per tal d'obtenir la temperatura superficial.

En tercer lloc, hem analitzat la variabilitat espacial d'algunes variables importants com són la temperatura de l'aire i del sòl, la humitat de l'aire i la del sòl i el vent en

aquesta mateixa zona. Els principals resultats d'aquest estudi han estat que durant el dia la variabilitat horitzontal és pràcticament nul·la i predomina la variabilitat vertical i durant la nit predomina la variabilitat horitzontal, però també hi ha variabilitat vertical encara que molt més petita. Així mateix, mitjançant aquestes dades hem estimat els valors de l'advecció horitzontal i hem vist que en nits clares amb vents dèbils, aquestes poden ser majors que els fluxos de calor turbulents.

Pel que fa a l'estudi d'heterogeneïtats a escales quilomètriques hem analitzat un cas de transició matutina entre el terral i la brisa a Mallorca mitjançant dades mesurades *in situ* i resultats obtinguts amb el model Meso-NH. D'aquesta manera hem estudiat com es formen i es desenvolupen aquests vents generats degut a una diferència de temperatura entre el terra i la mar. Així mateix, hem comprovat que el model reprodueix realisticament l'organització dels fluxos en les capes baixes però té dificultats en capturar l'acumulació d'aire fred que es forma al centre de la conca. Aquest fet pot estar relacionat amb que els models no són capaços de representar correctament els processos que tenen lloc en la capa superficial, especialment de nit.

Per acabar, hem analitzat la relació entre la temperatura superficial i els components de l'equació de balanç d'energia, on hem obtingut que de dia aquesta temperatura és proporcional a la radiació neta, mentre que de nit, depèn de les condicions en les que es trobe el sòl. A més, hem observat que la temperatura superficial respon més bruscament en sòls secs que en humits. També hem vist quan ens trobem en temperatures pròximes a les temperatures on es produeixen els canvis de fase, la temperatura superficial té un comportament diferent ja que està rebent el calor produït per aquests canvis de fase.

Aquesta tesi ens ha permès comprovar que les heterogeneïtats superficials: (i) afecten directament a les principals variables atmosfèriques, superficials i de sòl; (ii) juguen un paper molt important en les circulacions que ocorren en aquestes zones, tant si són a petita o a gran escala; (iii) intervenen en els processos d'intercanvi d'energia que tenen lloc en la interfície atmosfera-sòl.

Els resultats més destacables han estat que les heterogeneïtats a petita escala són capaces de generar circulacions que poden afectar el sistema sòl-atmosfera. Per tal de caracteritzar una àrea d'estudi, es necessita mesurar en els diferents tipus de superfícies que hi ha, ja que podem trobar diferències en la temperatura superficial superiors als 10 °C en una mateixa zona, una variabilitat vertical en la temperatura de l'aire en els primers 2 m durant el dia que pot arribar a 5 °C i una variabilitat horitzontal en la temperatura de l'aire durant la nit major a 5 °C. A més, es necessiten instruments que enregistren a freqüències altes, de manera que puguin percebre els canvis que es produeixen en intervals temporals curts. Amb aquestes mesures, també hem pogut comprovar en diferents àrees d'estudi, que la temperatura superficial durant la nit no depén de la turbulència,

sinó dels termes de l'equació de balanç d'energia superficial, concretament de la radiació neta i del flux de calor del sòl.

Resumen (en Castellano)

La Capa Límite Atmosférica es la capa de la atmósfera más cercana a la superficie terrestre. En esta capa, la altura de la cual puede variar entre un centenar y un par de kilómetros, hay un intercambio constante de energía y de materia. Estos procesos de intercambio de energía que tienen lugar en la Capa Límite Atmosférica, pueden ser descritos por la ecuación de balance de energía superficial, donde la radiación neta total de la superficie se asume igual a la suma de los flujos de calor sensible, calor latente y calor de suelo que tienen lugar en la misma. Pero desde los años 80, los científicos se han percatado que los términos de esta ecuación de balance de energía superficial no se cancelan cuando se miden experimentalmente. Desde entonces, se están realizando muchos estudios para ver a que es debido este problema: algunos lo atribuyen a errores de medida, otros al hecho de que no se identifican bien los flujos de calor sensible y/o latente, o bien que hay más a tener en cuenta a parte de estos flujos.

En este trabajo hemos estudiado cual es el papel que juegan las heterogeneidades superficiales en estos procesos. Por tal de llevarlo a cabo, hemos utilizado y relacionado conceptos de teledetección y de meteorología, mediante estudios llevados a cabo en superficies heterogéneas a escala hectométrica.

Primero hemos obtenido la variabilidad espacial de la temperatura superficial a escala hectométrica en el Campus de la Universitat de les Illes Balears. Donde hemos encontrado diferencias significativas en los valores de la temperatura superficial entre las diferentes zonas del Campus, tanto en los meses fríos como en los cálidos (siendo superiores en estos últimos). Además, hemos podido comprobar que los satélites con resolución espacial menor que el del tamaño de las heterogeneidades, no son capaces de observar estas diferencias.

En segundo lugar, hemos estudiado la variabilidad temporal de la relación entre la temperatura del aire y la temperatura superficial medidas *in situ* en un punto de esta superficie heterogénea, así como su dependencia con otras variables. Además hemos observado que durante el día los valores están bien correlacionados con la intensidad del flujo de flotabilidad, siendo estas correlaciones mayores en suelos muy cálidos y secos. De noche en cambio, no hemos encontrado correlaciones destacables con ninguna magnitud. Este hecho nos indica que el sistema atmosféra-suelo responde en conjunto a la demanda de energía de la capa superficial y no permite el establecimiento de fuertes gradientes de temperatura en los primeros 2 metros de altura más cercanos a la superficie. Para llevar a cabo este estudio, hemos realizado un análisis previo sobre los diferentes métodos y instrumentos de los que disponíamos para obtener la temperatura superficial.

En tercer lugar, hemos analizado la variabilidad espacial de algunas variables importantes como son la temperatura del aire y la del suelo, la humedad del aire y la del suelo y el viento en esta misma zona de estudio (el Campus de la Universitat de les Illes Balears). Los resultados principales de este estudio han sido, que durante el día la variabilidad horizontal es prácticamente nula y predomina la variabilidad vertical, y durante la noche en cambio, la variabilidad horizontal predomina pero la vertical no es nula. Así mismo, mediante estos datos hemos podido estimar los valores de la advección horizontal, y hemos visto que en noches claras con vientos débiles, estas pueden ser mayores que los flujos turbulentos.

En cuanto al estudio de las heterogeneidades a escalas kilométricas, hemos analizado un caso de transición matutina entre la brisa de tierra y la de mar en Mallorca, mediante datos medidos *in situ* y con resultados obtenidos con el modelo Meson-NH. De esta forma, hemos estudiado como se forman y se desarrollan estos vientos generados debido a una diferencia de temperatura entre la tierra y el mar. Así mismo, se ha comprobado que el modelo reproduce realísticamente la organización de los flujos en las capas bajas, pero tiene dificultades para capturar la acumulación de aire frío que se forma en el centro de la cuenca. Este hecho puede estar relacionado con que los modelos no son capaces de representar correctamente los procesos que tienen lugar en la capa superficial, especialmente de noche.

Para terminar, hemos analizado la relación entre la temperatura superficial y las componentes de la ecuación de balance de energía superficial, donde hemos obtenido que durante el día esta temperatura es proporcional a la radiación neta, mientras que por la noche, depende de las condiciones en las que se encuentre el suelo. Además hemos observado que la temperatura superficial responde más bruscamente en suelos secos que en los húmedos. También hemos visto, que cuando nos encontramos a temperaturas que son cercanas a las temperaturas en las que se producen los cambios de fase, la temperatura superficial tiene un comportamiento diferente, ya que está recibiendo el calor producido por estos cambios de fase.

Esta tesis nos ha permitido comprobar que las heterogeneidades superficiales: (i) afectan directamente a las principales variables atmosféricas, superficiales y de suelo; (ii) juegan un papel muy importante en las circulaciones que ocurren en estas zonas, tanto si son a pequeña o a gran escala; (iii) intervienen en los procesos de intercambio de energía que tienen lugar en la interfaz atmosféra-suelo.

Los resultados más destacables han sido que las heterogeneidades a pequeña escala son capaces de generar circulaciones que pueden afectar el sistema suelo-atmósfera. Para caracterizar una área de estudio, se necesita medir en los diferentes tipos de superficies

que hay, puesto que podemos encontrar diferencias en la temperatura superficial superiores a los 10 °C en una misma zona, una variabilidad vertical en la temperatura del aire en los primeros 2 m durante el día que puede llegar a 5 °C y una variabilidad horizontal en la temperatura del aire durante la noche mayor que 5 °C. Además, se necesitan instrumentos que registren a frecuencias altas, de forma que puedan percibir los cambios que se producen en intervalos temporales cortos. Con estas medidas, también hemos podido comprobar en diferentes áreas de estudio, que la temperatura superficial durante la noche no depende de la turbulencia, sino de los términos de la ecuación de balance de energía superficial, concretamente de la radiación neta y del flujo de calor del suelo.

Summary (in English)

The Atmospheric BoundaryLayer is the layer of the atmosphere that is closest to the Earth's surface. In this layer, which height can vary between a hundred and a couple of kilometers, there is a constant exchange of energy and matter. These energy exchange processes can be described by the Surface Energy Balance Equation, where the total net radiation of the surface is the same to the sum of the fluxes of sensible heat, latent heat and heat of the ground. Since the 80s, different experimental studies have shown that the terms of the surface energy balance do not cancel out due to several reasons: some attribute it to measurement errors, others to the fact that sensible and/or latent heat fluxes are not well identified, others that there are more to take into account apart from these fluxes.

In this work, we have studied which is the role of the superficial heterogeneities in these processes. In order to carry it out, we have used and related concepts of remote sensing and meteorology, through studies carried out on heterogeneous surfaces at hectometric scale.

First we have obtained the spatial variability of the surface temperature at the hectometric scale in the Campus of the University of the Balearic Islands. We have found significant differences in the values of the surface temperature between the different areas of the Campus, in the cold months and in the warm ones (being higher in the latter). In addition, we have been able to verify that the satellites with lower spatial resolution than the size of the heterogeneities, are not able to observe these differences.

Secondly, we have studied the temporal variability of the relation between the air temperature and the Land Surface Temperature measured in situ at one point of this heterogeneous surface, as well as its dependence on other variables. We have observed that during the day the values are well correlated with the intensity of the buoyancy flow, with larger correlations in very hot and dry soils. At night, we have not found remarkable correlations with any magnitude. This fact indicates that the atmosphere-soil system responds together with the energy demand of the surface layer and does not allow the establishment of strong temperature gradients in the first 2 meters above ground level. To carry out this study, we have realised a preliminary analysis on the different methods and instruments that were available to obtain the Land Surface Temperature.

Thirdly, we have analysed the spatial variability of some important variables such as air temperature, soil temperature, air and soil humidity, and wind in this same area of study. The main results of this study have been that during the day the horizontal variability is practically null and the vertical variability predominates, and during the

night instead, the horizontal variability predominates but the vertical variability is not null. Likewise, by analysing these data we have been able to estimate the values of the horizontal advection, and we have seen that on clear nights with weak winds, these may be larger than the turbulent fluxes.

Regarding the study of the heterogeneities at the kilometric scales, we have analysed a case of Morning Transition between the Land and the Sea-Breeze in Mallorca, using in situ data together with results obtained with the Meson-NH model. In this way, we have studied how these generated winds are formed and developed due to a temperature difference between the land and the sea. Likewise, it has been verified that the model reproduces the organization of the flows in the lower layers but it has difficulties in capturing the accumulation of cold air that was formed in the center of the basin. This fact can be related to the fact that the models are not able to correctly represent the processes that take place in the Surface Layer, specially at night.

To finish, we have analysed the relation between the Land Surface Temperature and the components of the Surface Energy Balance Equation, where we have obtained that during the day this temperature is proportional to the net radiation, while at night, it depends on the conditions of the soil. In addition, we have observed that the Land Surface Temperature responds more sharply in dry soils than in wet soils. We have also seen that if the temperatures are close to the temperatures at which the phase changes occur, the Land Surface Temperature has a different behaviour, since it is receiving the heat produced by these phase changes.

This thesis has allowed us to verify that superficial heterogeneities: (i) directly affect the main atmospheric, surface and soil variables; (ii) play a very important role in the circulations that occur in these zones, whether they are small or large scale; (iii) intervene in the processes of energy exchange that take place in the atmosphere-soil exchanges.

The most remarkable results have been that small-scale heterogeneities are capable of generating circulations that can affect the soil-atmosphere system. To characterize a study area, it is necessary to make measurements in the different types of surfaces that there are, since we can find differences in land surface temperature higher than 10 °C in the same area, a vertical variability in the air temperature in the first 2 m during the day that can reach 5 °C and a horizontal variability in the air temperature during the night greater than 5 °C. In addition, instruments that record at high frequencies are needed, so that they can perceive the changes that occur in short time intervals. With these measurements, we have also been able to verify in different areas of study, that the Land Surface Temperature during the night does not depend on the turbulence, but depends on the terms of the surface energy balance equation, specifically of net radiation and the heat flux of the ground.

Acknowledgements

Encara recorde el dia que vaig decidir deixar els meus amics, la banda, la meua família, el meu poble... per vindre a Mallorca a fer el doctorat. Ha sigut una experiència inoblidable, tant personal com professional, que m'ha permès visitar molts llocs arreu d'Europa i conèixer a gent fantàstica. Però tota aquesta aventura no haguera estat possible sense els meus directors de tesi Joan Cuxart, Vicent Caselles i Maria Antonia Jiménez. Moltes gràcies per haver-me donat aquesta oportunitat, per la vostra paciència, dedicació i haver-me guiat durant aquest procés.

I want to express my most sincere gratitude to Dr. Tamás Weidinger for the invaluable lessons, hospitality and his attention when I visited ELTE University in Budapest and to all my colleagues in the field campaigns with whom we have shared many moments and experiences.

Així mateix, vull agrair als meus companys del grup de Meteorologia, companys del despatx i membres del departament de Física per la seva ajuda sempre que ho he necessitat. També vull agrair als tècnics de laboratori del segon pis, per la seua paciència i les hores de polseguera que feren possible la construcció dels pals.

A Maria del Mar, Aquilina, Maria Tous, Dani Salas, Alex, Diego, David, Jordi, Ruben i Joan Torrens per haver-me acollit des del principi com una més i fer-me sentir com en casa. Als meus companys i amics del dinar, Miguel Bezares, Carlos Palenzuela, Borja, Carles Bona i Dani Malagon, amb els que he compartit molt més que dinars. Als que heu arribat al final daquesta etapa Maria Cardell, Toni Grau, Aina Maimó i Dani Rodríguez, moltes gràcies pels moments de desconnexió.

A mi apoyo incondicional, Rocío por estar siempre a mi lado y contagiarme de tu alegría en todo momento. A Andrea Arreguín por formar parte de esta aventura y hacer que la distancia sea pequeña.

A Xisco per caminar al meu costat durant aquests anys, per fer que els moments dolents no ho foren tant, per creure en mi quan jo no ho feia, per convertir les llàgrimes en rialles i per tantes altres coses que han fet que valgués la pena.

A les meues amigues de sempre per fer-me sentir que res ha canviat i estar sempre al meu costat. Per acabar vull agrair a la meua família pel seu suport incondicional i fer de mi qui sóc, en especial als que ja no esteu peró sempre estareu.

Aquest treball ha estat possible grácies al finanament de la beca FPI-Grant BES-2013-065290 i al projecte de recerca CGL2015-65627-C3-1-R (MINECO/FEDER) del Ministeri dEconomia, Industria i Competitivat, amb el suport de European Regional Development Fund (FEDER).

Contents

List of Figures

List of Tables

Abbreviations

ABL	**A**tmospheric **B**oundary **L**ayer
AEMET	**A**gencia **E**statal de **MET**eorología
agl	**a**bove **g**round **l**evel
asl	**a**bove **s**ea **l**evel
ASL	**A**tmospheric **S**urface **L**ayer
ASTER	**A**dvanced **S**paceborne **T**hermal **E**mission and **R**eflection Radiometer
BLLAST	**B**oundary **L**ayer **L**ate **A**fternoon and **S**unset **T**urbulence
BOU	**B**alloon **O**stwestfalen-Lippe **U**niversity of the Balearic Islands
CBL	**C**onvective **B**oundary **L**ayer
CP	**C**old **P**ool
DN	**D**igital **N**umber
ECMWF	**E**uropean **C**entre for **M**edium-Range **W**eather **F**orecasts
ECUIB	**E**stació **C**ampus **U**niversitat **I**lles **B**alears
ETM+	**E**nhanced **T**ematic **M**apper plus
FOV	**F**ield **O**f **V**iew
GED	**G**lobal **E**missivity **D**atabase
GSW	**G**eneralized **S**plit- **W**indow
GIFOV	**G**round **I**nstantaneous **F**ield **O**f **V**iew
IFOV	**I**nstantaneous **F**ield **O**f **V**iew
IOP	**I**ntensive **O**perational **P**eriod
LB	**L**and-**B**reeze
LES	**L**arge **E**ddy **S**imulations
LLJ	**L**ow **L**evel **J**et
LST	**L**and **S**urface **T**emperature
LWS	**L**eaf **W**etness **S**ensor

MCT	**M**ercury **C**admium **T**elluride
MODIS	**MOD**erate Resolution **I**maging **S**pectroradiometer
MODTRAN	**MOD**erate Resolution Atmospheric **TRAN**smission
MOL	**M**eteorological **O**bservatory **L**indenberg
MSB13	**M**allorca **S**ea **B**reeze 20**13** Experiment
MT	**M**orning **T**ransition
NASA	**N**ational **A**eronautics and **S**pace **A**dministration
NBL	**N**eutral **B**oundary **L**ayer
NCEP	**N**ational **C**enters for **E**nvironmental **P**rediction
NIR	**N**ear **I**nfra**R**ed
OWL	**O**st**W**estfalen-**L**ippe
PDFs	**P**robability **D**ensity **F**unctions
PRT	**P**latinum **R**esistace **T**hermometer
PVC	**P**oly**V**inyl **C**hloride
RH	**R**elative **H**umidity
RMSE	**R**oot **M**ean **S**quare **E**rror
RTE	**R**adiative **T**ransfer **E**quation
SB	**S**ea-**B**reeze
SBL	**S**tably-Stratified **B**oundary **L**ayer
SL	**S**urface **L**ayer
ST	**S**oil **T**emperature
SWIR	**S**hort**W**ave **I**nfra**R**ed
TES	**T**emperature - **E**missivity **S**eparation
TIR	**T**hermal **I**nfra**R**ed
TKE	**T**urbulence **K**inetic **E**nergy
TOA	**T**op **O**f **A**tmosphere
UAV	**U**nmanned **A**erial **V**ehicle
UAV-OWL	**U**nmanned **A**erial **V**ehicle-**O**st**W**estfalen-**L**ippe
UAV-TIR	**U**nmanned **A**erial **V**ehicle-**T**hermal **I**nfra**R**ed
UIB	**U**niversity of the **B**alearic **I**slands
USGS	**U**nited **S**tates **G**eological **S**urvey
VWC	**V**olumetric **W**ater **C**ontent
WVS	**W**ater **V**apor **S**caling

WMO **W**orld **M**eteorological **O**rganization

Preface

Since ancient times, atmospheric phenomena have played a very important role for living beings, since rain and drought affect crops and animals, and therefore their way of life. In 334 BC appeared the first work that talks about meteorology, *The Meteorology of Aristotle*. The word *"meteoron"* means in Greek *between heaven and earth* and *"logos"* means *study*.

Until the XVII century when Galileo built the first thermometer in 1607, understanding was based on phenomenological observations. The thermometer was followed by the barometer in 1647 built by Torricelli. Twenty years later, Robert Hook built the first anemometer capable of measuring the wind speed, and a century later in 1780 Horace de Saussure built the first moisture hygrometer to measure humidity.

The study of meteorology has evolved until today when we can estimate the occurrence of these phenomena in advance through meteorological models.

There are many studies made from observations and theories developed over the years that have allowed us to know all current notions of meteorology. At first, it was studied observing the sky. This was followed by the use of balloons, airplanes and rockets that allowed a better observation of these phenomena. In 1959, the first meteorological satellite, the Vanguard 2, was launched, but due to the design of its axis of rotation it could not register many useful data. Two years later, in 1960 TIROS-1 was launched, considered as the first satellite successfully launched by NASA. The use of satellites to remotely observe atmospheric phenomena revolutionised meteorology, leading to very significant advances in its understanding.

In this thesis I intent to bring a little close these two worlds, meteorology and remote sensing.

Scientific objectives and structure of this thesis

This thesis is about how the circulations and the atmosphere-soil exchanges are affected by the heterogeneities of the terrain at different scales (small scales, from 1 m to 1 hm, in Chapters 3, 4 and 5 and large scales, from 1 hm to 1km, in Chapters 6 and 7). Another objective is to see how terrain heterogeneities affect the lower atmosphere and related processes such the surface energy budget. Finally, it is intended to explore the relationship between the Land Surface Temperature and the terms of energy balance. In order to characterise these processes occurring in the atmosphere-soil interface at different scales, in situ data, satellite products and models are used.

The thesis is organized as follows, Chapter 1 provides a quick review of the basic concepts related to atmospheric boundary layer and remote sensing in order to facilitate the understanding of the thesis. The chapter begins by introducing the atmospheric boundary layer, followed by the processes that take place in the atmosphere-soil interface. In this part, the surface energy balance equation, as well as its terms are introduced: solar radiation, sensible and latent heat fluxes, heat flux on the ground and any other energy fluxes. Next, a short introduction to remote sensing discuss this technique.

Chapter 2 is meant to be an overview of the material and methods used in the thesis, where it is explained how to measure the lower boundary layer, and the instrumentation, satellites and models that have been used.

In Chapter 3 the LST values measured in situ are compared with those observed with satellites of different resolution (Landsat-7 and MODIS), in a heterogeneous terrain at small-scale for a period of 2.5 years. The LST variability of the area is explored through the three sources of observations, and it is possible to have an estimation of the size of the heterogeneity. Besides, discrepancies made in the validation results when taking these three quantities as equivalent can be evaluated.

Chapter 4 is intended to check the radiation measurements made by different radiometers and the different methods of correcting these to obtain LST. The relationship between air temperature at 2 meters and LST over 2 years for the daytime and the nighttime has also been studied, as well as the correlation of this difference with other variables measured at the same point.

In Chapter 5, observations made with different Poles in a hegerogeneous area are used to study the spatial variability of the atmospheric and soil variables in a hectometric area. It has been studied and inspected if some quantities could be as estimators of this heterogeneity. Furthermore, a methodology is proposed to compute the thermal

advection over the SEB station and relate this magnitude with the energy imbalance and the net radiation at one point.

Chapter 6 deals with a Sea-Breeze campaign that took place in Mallorca. The morning transition between land and the sea breeze regimes is studied experimentally and with high resolution mesoscale simulations. In this campaign, heterogeneities are at larger scales, of the order of km and the resulting circulations are larger and more intense than for the previous chapters.

Chapter 7 shows the relation between LST and the surface energy balance for different campaigns at small scale and large scale that I have participated. We have focused on the behaviour of LST during the night and its dependence on the terms of the surface energy balance equation, obtaining different results depending on the conditions in which the soil and the atmosphere are.

Finally, in Chapter 8 the main results and conclusions obtained in this thesis are outlined.

Chapter 1

Introduction

The Atmospheric Boundary Layer (ABL) is the layer directly influenced by the surface in contact with the atmosphere. Therefore, its evolution is determined by the characteristics of the surface-atmosphere interface, including the heterogeneities of the terrain, which may induce spatial changes in the momentum and energy fluxes. These changes are related to the different mechanical and thermal properties of the different elements of the surface, which will in consequence have different values of the exchange fluxes for very close terrain patches. The essential features of the ABL circulations will be firstly described, including the diurnal and nocturnal typical regimes together with the transition periods between them. Then the values of the exchange fluxes of energy as they are used in the Surface Energy Budget are introduced, namely the Net Radiation, the sensible and latent turbulent heat fluxes, and the conduction flux in the soil. In this work, the heterogeneity will be assessed by means of the determination by remote sensing of the land-surface temperature (LST). There will be also introduced in this Chapter the main satellites, inboard instruments and products used here. Finally, a short review of the most important experimental efforts in homogeneous and heterogeneous terrain is given.

1.1 The Atmospheric Boundary Layer

The ABL is the layer of the atmosphere that interacts with the Earth's surface. It is directly influenced by the surface roughness, the energy balance and the lower boundary conditions. Over land, its vertical structure has a diurnal cycle (Figure 1.1). During the day the solar radiation heats the surface and the air in contact with it, favouring mixing and turbulence transport. This layer in contact with the surface is usually called the Convective Boundary Layer (CBL). At night, the radiative cooling of the surface

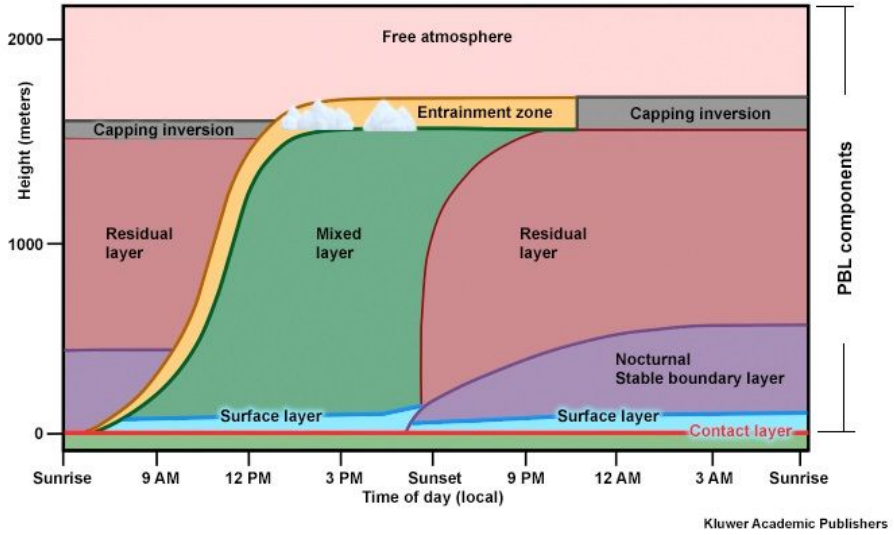

FIGURE 1.1: Diurnal cycle of the atmospheric boundary layer under high pressure conditions over land. It consists of three major parts: a very turbulent mixed layer; a less turbulent residual containing former mixed-layer air; and a nocturnal stable boundary layer of sporadic turbulence. Based on the Stull Diagram [Stull, 1988]. Source: Kluwer Academic Publishers.

produces stably stratified conditions at lower levels, known as the Stable Boundary Layer (SBL). Characterizing properly the ABL physics is very important because it is in this layer where the main exchanges of matter and energy between the surface and the atmosphere takes place, due to the high efficiency of the turbulent mixing processes. In this layer, wind velocity, temperature and humidity have large fluctuations and there is a significant vertical mixing [Stull, 1988]. The lower region of the ABL is called Surface Layer (SL). It is the layer near the Earths surface in which turbulent fluxes does not depend significantly on height [Paulson, 1970]; usually it is considered to occupy the lower 10% of the ABL.

1.1.1 Convective Boundary Layer

During the day, the solar irradiance reaches the ground and thermal convection develops. Hot air rises from the ground, creating a structure of instability (convective or thermal turbulence) in the lower layers of the atmosphere (CBL). CBL reaches its maximum depth at the end of the afternoon and disappears at sunset [Kaimal et al., 1976]. The

CBL has a height that may vary from hundreds to a few thousand meters. This active turbulence tends to diminish the gradients of heat, humidity and moment, creating a well-mixed layer.

Turbulence in the lower layers is characterized by its three-dimensionality and it is highly random and heterogeneous [Garratt, 1992]. Turbulent fluxes show a large variability in their spatio-temporal scales: the time scale of the turbulent motions varies from a few seconds for small eddies to approximately half an hour for larger eddies; the spatial scale covers values from the millimeters of the dissipative fluctuations up to a few hundred meters of the eddies of the boundary layer.

The turbulent processes that take place in the boundary layer have a diffusive and a dissipative character [McComb, 1990]. The diffusive character of the turbulence is one of the most important properties in this layer, since it is precisely this mechanism that facilitates the mixing of the different properties of the air.

One of the most evident manifestations of the turbulent nature of the atmosphere is the daily cycle of activation and dissipation of the turbulent energy associated with the diurnal cycle. A continuous supply of energy is needed [Stull, 1988]. The following stages are observed [Garratt, 1992]: destruction of the nocturnal radiative inversion in the early hours of the morning and beginning of a weak well-mixed layer while gradually destroying the stable nocturnal layer; formation of a thick well-mixed layer in central hours of the day, often delimited by the presence of a thermal inversion in height; decrease of instability as a consequence of the imbalance thermal that takes place at sunset; finally, formation of a new radiative thermal inversion that will deepen and intensify throughout the night.

In the top of the CBL there is a temperature inversion and mixing occurs intermittently between the ABL and free Atmosphere. This layer is called Entrainment zone (Figure 1.1).

1.1.2 Stable Boundary Layer

After sunset, the Earth's surface does not receive solar irradiance and instead, it emits long-wave irradiance (Stefan-Boltzmann's Law). Consequently, the soil and the air in contact with it, as well as the lower layers of the atmosphere, cool faster than the air at higher layers. In this way an increase of temperature with height occurs and, therefore, a stably stratified layer (SBL) is formed. Stably stratified conditions tend to suppress turbulence and to dump vertical motions. As the height increases, the inversion weakens or disappears, often giving way to the residual layer with neutral or indifferent

stratification resulting from the convection mixing of the previous day. Furthermore, the presence of stability allows the existence of phenomena that are not observed in other regimes, in particular gravity waves, Kelvin-Helmholtz instabilities, gravity currents, etc. The SBL over land has a height between ten and a few hundreds of meters, depending on the season of the year, the topographical configuration and the latitude of the site.

During the night, the wind speed in the surface layer is small due to friction with the surface, and increases logarithmically with the height, reaching the maximum close to the inversion layer. This velocity is greater than geostrophic and takes the form of a low-level jet (LLJ) that can be a source of turbulence due to shear. LLJs can be caused by three phenomena that can take place together or separately [Garratt, 1985]: (i) the inertial oscillation experienced by the wind at dusk, when it tries to reach its new equilibrium value (that of the geostrophic wind); (ii) the thermal wind in terrain with slope the ground cools down when falling the night and due to the inclination of the surface, in a level of constant height there will exist a gradient of temperature that will force a variation of the wind with the height according to the equations of the wind thermal; (iii) surface cooling on slopes generates gravity currents giving rise to lower wind maxima than in the previous cases.

In SBL there may be intermittent turbulence, defined in the Glossary of Meteorology (Glickman [2000], p. 410) as "the property of turbulence within one air mass that occurs at some times and some places and does not occur at intervening times or places." Some processes of this intermittency are wave instabilities [Blumen et al., 2001, Fritts et al., 2003, Newsom and Banta, 2003, Sun et al., 2004], density currents [Sun et al., 2002], and wind gusts [Acevedo and Fitzjarrald, 2003]. Large-Eddy Simulations (LES, Beare et al. [2006], Cuxart and Jiménez [2007], Jiménez and Cuxart [2005]), experimental campaigns [Cuxart et al., 2000, Poulos et al., 2002], mesoscale modelling studies [Cuxart and Jiménez, 2007] or parametrization evaluations [Cuxart et al., 2006] have been some works related to the SBL where members of the UIB Meteorology Group have been actively involved.

1.1.3 Neutral Boundary Layer

The neutral boundary layer (NBL) develops in situations with significant winds or cloudy skies in which the effect of wind transport and the absence of thermal processes due to the small heating of the ground are translated into atmospheres with little vertical mixing because the temperature gradient is small [Stull, 1988].

In near-neutral conditions, the temperature decreases with height and the shear production of Turbulent Kinetic Energy is much larger than buoyant production. This layer is

also known as Ekman Boundary Layer Stull [1988]. The wind behaves according to the Ekman spiral theory: near the Earth's surface the friction causes the wind to decrease in intensity below the geostrophic value. As a consequence, the Coriolis effect will also be reduced, establishing a new equilibrium between the baric force (caused by the pressure difference), the Coriolis force and the friction force. The final result is a slope of the wind with respect to the isobars towards the zone of low pressures, crossing the isobars obliquely [Holton and Hakim, 2012].

Under neutral conditions, it is possible not to consider the thermodynamic effects on turbulence and friction. The turbulent mixture is generated by mechanical conditions. In this way, the wind profile can be estimated analytically. These conditions are rarely observed, normally it is a mixture between neutral layer and stable or unstable layers.

1.1.4 Surface Layer

The surface layer is the lower layer in the ABL (typically about a tenth of the height of the ABL) where the flows of momentum, heat and humidity can be considered equal to their values at the surface level, since they barely change 10% of their magnitude with height. Therefore, it can be defined as a layer of constant flow. The characteristics of this layer depend on the nature of the surface, being little affected by the rotation. In this layer, the wind speed tends to increase as it rises and the Earth's surface exerts a friction or delay action on it.

The surface layer is influenced by surface heterogeneity, vegetation and topography. Since the turbulence is not homogeneous or isotropic, it can only be described using empirical equations. The laws of the processes in the surface layer have a general geophysical significance, since both (i) the dynamic interaction of the atmosphere and the substrate and (ii) the feeding of the atmosphere by moisture and heat are realized through the surface layer [Monin and Obukhov, 1954]. The study of how buoyancy modifies the relation between the flux-gradient and wind profile give the surface-layer similarity theory of Monin-Obukhov. When there is a gradient, there are flows that tend towards equilibrium. However, when the (system, layer) is not under neutral conditions, we must take into account the effect of hydrostatic thrust (buoyancy) as a consequence of the vertical density gradient, which will affect the flows and gradients.

The similarity theory of Monin-Obukhov describes the vertical behaviour of nondimensionalized mean flow and turbulence properties within the atmospheric surface layer as a function of the Monin-Obukhov key parameters (the height above the surface, the buoyancy parameter ratio of inertia and buoyancy forces, the kinematic surface stress, and the surface virtual temperature flux). This similarity hypothesis implies that: (i)

the moment and heat fluxes are constant (independent of height), (ii) the molecular exchanges are insignificant compared to the turbulent exchanges, (iii) the rotational effects can be ignored in the surface layer, (iv) the influence of the roughness surface can be ignored and (v) the height of the boundary layer are reflected by the friction velocity.

Since the independent variables in the Monin-Obukhov similarity hypothesis relate the three fundamental dimensions (length, time and temperature), according to Buckingham Π-theorem [Kantha and Clayson, 2000], it can be formulated only one dimensionless combination independent of the others. The combination traditionally chosen in the Monin-Obukhov similarity theory is the dimensionless parameter ζ=z/L where z is the height above the surface and L is the Monin-Obukhov length:

$$L = \frac{-u_*^3}{k\frac{g}{\theta_v}\left(\overline{w'\theta'_v}\right)_o} \tag{1.1}$$

where u_* is the friction velocity, k≈0.40 is the von Kármán constant, g the gravitational constant, θ_v the potential temperature and w' and θ_v' the perturbations of vertical velocity and virtual potential temperature.

This parameter can be used to know the static stability of the surface layer, so that when ζ is lower than 0 the surface layer is statically unstable and when ζ is larger than 0 the surface layer is statically stable. Under neutral conditions, ζ tends to zero.

Furthermore, any turbulent variable, if it is normalized by an appropriate combination of speed scales, temperature and humidity, must be a unique function of the dimensionless number ζ=z/L. In this way, the mean wind and temperature profiles satisfy the following equations: where $\varphi_M(\zeta)$ is the stability function of momentum, $\varphi_H(\zeta)$ is the stability function of heat and θ_*=-$\frac{\overline{w'\theta'_v}}{u_*}$ is the characteristic dynamical temperature:

$$\frac{\partial\overline{u}}{\partial z} = \frac{u_*}{kz}\varphi_M(\zeta) \tag{1.2}$$

$$\frac{\partial\overline{\theta}_v}{\partial z} = \frac{\theta_*}{kz}\varphi_H(\zeta) \tag{1.3}$$

These equations relate the fluxes of momentum and heat to the vertical gradients of wind and temperature.

1.1.5 Morning and Evening Transitions

The transitions between SBL-CBL and CBL-SBL, around sunrise and sunset, are less well characterized than the other times of the day because many processes take place in very short periods of time that are difficult to characterize experimentally. Furthermore, the similarity theories can not be applied because: (i) sometimes the heat fluxes and the wind are near zero, and there is not yet another accepted similarity theory [Foken, 2008b] describing the surface layer under these conditions [Lapworth, 2003, 2006] as in SBL; (ii) the definition and depth of the boundary layer [Lothon et al., 2014]; (iii) that turbulence may be discontinuous and not isotropic [Sun et al., 2012] as during the night; (iv) the temporal evolution of the surface flows and their dependence on the heterogeneity of the surface [Nadeau et al., 2011] and (v) the processes that take place in areas of complex terrain that complicate the dynamics of the morning transition [Lenschow et al., 1979]. Therefore, there are fewer studies on these transitions, although in recent years their interest has increased and more works have appeared [Nadeau et al., 2013, Nilsson et al., 2016, Sastre et al., 2015, Wildmann et al., 2015]. Morning and evening transitions remain difficult to observe and model, largely due its short and more and studies appear [Lothon et al., 2014].

Angevine et al. [2001] found that morning and evening transitions are different, since they have distinct dependencies in flows, variances and surface variables. This is the reason why they should be studied separately. During the evening transition (from CBL to SBL) a thermal surface inversion is established due to the radiative cooling of the surface. Whereas in the morning transition (SBL-CBL) this inversion disappears, due to the radiative warming of the surface and the initiation of vertical motions (mixing).

The evening transition was studied in detail in the Boundary Layer Late Afternoon and Sunset Turbulence (BLLAST) project, focusing on the turbulence decay during the afternoon over land [Lothon et al., 2014]. They found that the decay of turbulence within the surface layer behaves quite similarly to that in the CBL and residual layer above, although the decay of dissipation rate is often first observed in the upper part of the CBL

1.1.6 Local-scale circulations

Local winds represent a displacement of air, resulting from regional thermal differences (baroclinity) and determining the prevailing winds of a more or less wide area, in the absence of a well-defined pressure-gradient of a larger spatial scale. Its establishment is conditioned by orographic features or different surface properties that cause differential

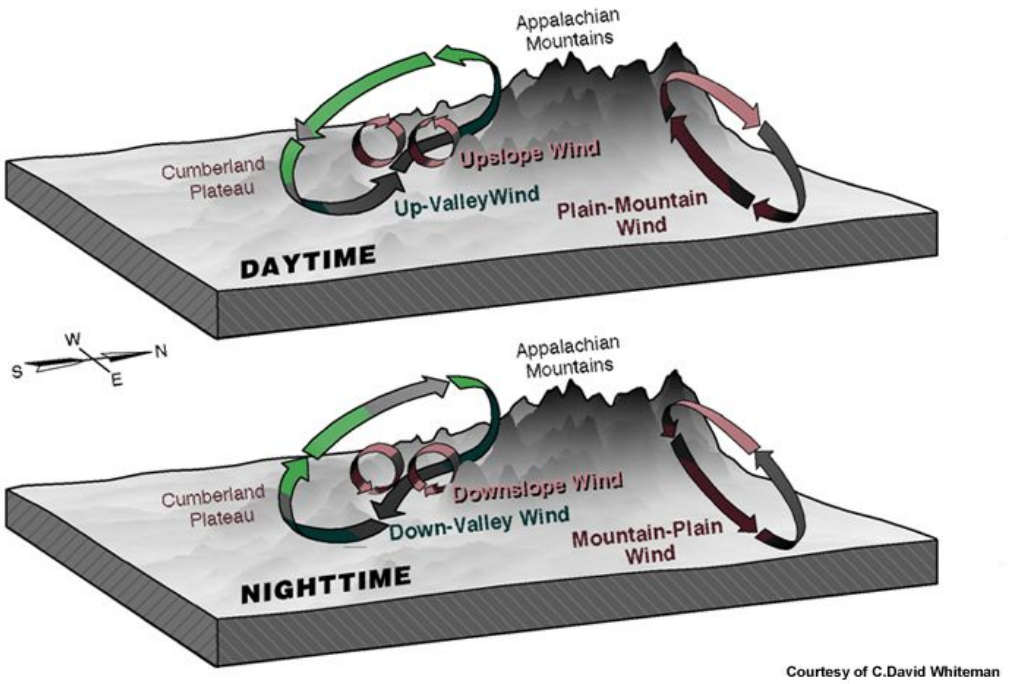

FIGURE 1.2: Mountain wind circulations diagram at daytime and night-time. Source: Whiteman [2000]

heating of the air masses [Simpson, 1994]. Among these types of winds stand out the sea and land breezes, as well as the thermally-driven topographic winds. These local winds can significantly affect weather conditions and climate on a local scale.

1.1.6.1 Slope winds

In mountain valleys at daytime, the air that is compressed laterally by the narrowing of the valley, tends to expand vertically and to flow following the upward direction of the valley axis. Simultaneously, anabatic (ascending) winds blow, which are formed as a result of the greater warming of the slopes illuminated by the Sun of the valley compared to its bottom. These sloping winds may rise above the summit of the mountains and feed a stream that would return along the valley line in a downward direction, which compensates for the valley wind (Figure 1.2). Often this return wind is not observed due to larger scale wind aloft.

Also during the night and with weak synoptic pressure gradients, the horizontal temperature differences favour the formation of thermal flows over complex terrain [Whiteman, 2000]. The cold and denser air near the upper elevations sinks into the depressions and valleys, producing what is known as katabatic wind. Similar to the daytime, a return current may flow, above the mountain wind, to close the circulation (Figure 1.2).

Downslope winds may be produced due to the negative buoyancy forces induced by the temperature difference between the air adjacent to the slope and the ambient air outside the slope [Jiménez and Cuxart, 2014]. In addition, these downslope winds may be related to the thermal gradient along the valley axis. In some valleys and basins, topographic depression filled with cold air were formed, called cold pool (CP) due to the cooling of the air near the surface for the atmospheric processes, as in the case of the Cerdanya Valley [Conangla et al., 2018]. CPs formed during the night often disappear after sunrise due to the growth of the CBL [Kondo et al., 1989, Whiteman et al., 2008], but there are cases where they persist, normally in winter when the daily cycle of heating and sensible convection are insufficient to destroy the stable layer on a daily basis [Whiteman et al., 2001], either due to cloudiness or seasonal reductions in sensible heat flux. These cases are more complex and arise due to numerous atmospheric processes. If they last a long time they can cause pollution problems because the air is not renewed [Malek et al., 2006, Silcox et al., 2012]. The size and the intensity of the CPs can also be studied using satellite scenes [Jiménez et al., 2015].

1.1.6.2 Land and Sea Breezes

In areas close to the coast, breezes may appear (Figure 1.3) due to the fact that during the day the land heats up faster than the sea, causing vertical expansion of the air column and a decrease in atmospheric pressure. The difference in atmospheric pressure between land and sea is responsible for the formation of Sea-Breezes that blow to the ground on the surface and are compensated in height by a wind in the opposite direction.

The Sea-Breeze (SB) is an onshore wind generated by a cross-shore pressure gradient produced by the land-sea differential heating [Atkinson, 1981]. Over the land, the interaction between the convective boundary layer and the SB enhances updraft motions that depending on the ambient conditions (moist air over the land) favours the formation of clouds and thunderstorms [Romero and Ramis, 1996].

In all the coastal zones, the physical mechanisms that generate SB can be produced, although the spatial and temporal characteristics of the SB depend on the characteristics of the area, such as (i) the shape of the coastline [Gilliam et al., 2004, McPherson, 1970] or the curvature [Miller et al., 2003], (ii) the direction of the synoptical (large-scale) wind [Atkins and Wakimoto, 1997, Zhong and Takle, 1993], (iii) the local topography [Darby et al., 2002, Miao et al., 2003], (iv) the interaction with other mesoscale processes, such a mistral event in the North-Western Mediterranean [Guenard et al., 2005] or (v) the surface heterogeneities (soil moisture as in Physick [1980], or the vegetation features as in Kala et al. [2010]).

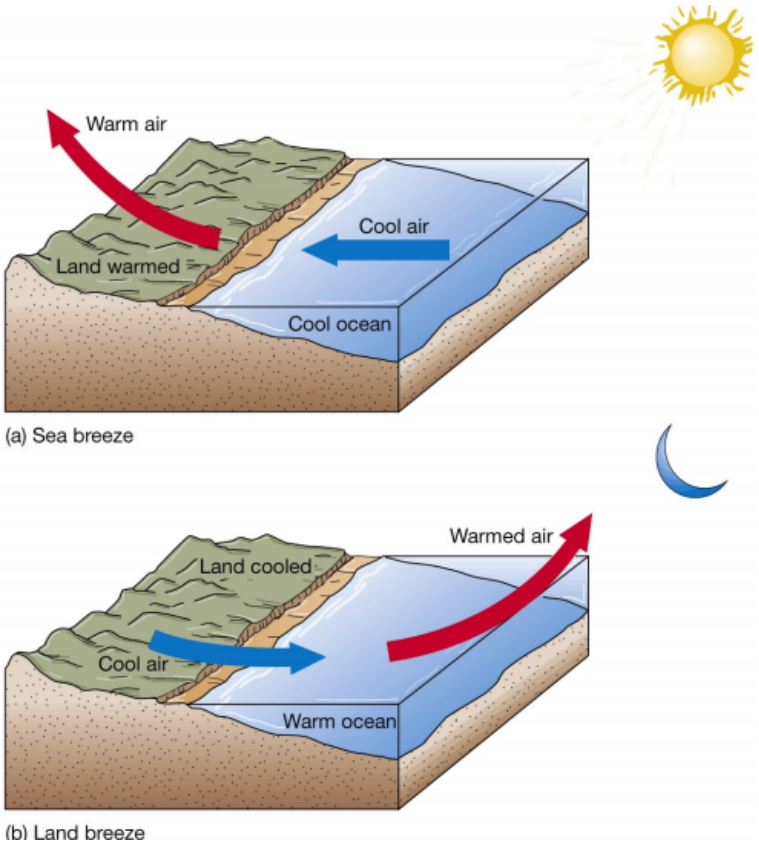

FIGURE 1.3: Sea-Breeze and Land-Breeze diagram. Source: Pearson Prentice Hall, Inc.

Different methodologies are currently used to study the SB. Most of the studies are based on numerical modelling (ideal cases, 2-dimensional or 3-D models). A complete list of the numerical studies can be found in the review article of (Crosman and Horel [2010], table 1) since the first numerical 2D simulation [Pearce, 1955]. Climatological studies are used to determine the spatial and temporal SB features through the analysis of surface observations.

Some breeze studies to highlight are Azorin-Molina et al. [2011] in the Eastern Iberian peninsula, Clarke [1989] in Australia, Furberg et al. [2002] in Sardinia and Orlić et al. [1988] in the Adriatic coast, among others that they typically cover from 1 to 6 years. In addition, satellite scenes can be used to study SB processes, such as the convection over land (for example the work of Wakimoto and Atkins [1994] for the coast of Florida in USA, or the work of Azorin-Molina and Chen [2009] for the Eastern Iberian Peninsula). In Mallorca several studies about SB have been done by members of our group: Cuxart et al. [2014], Jansà and Jaume [1946], Jiménez et al. [2016], Ramis and Alonso [1998], Ramis and Romero [1995], Romero and Ramis [1996].

During night-time, an opposite circulation is developed in coastal areas, the Land-Breeze (LB). The thermal gradient is inverted, T_{sea} is warmer than T_{land} because the land loses

its heat faster than the sea, due to differences in their heat capacity, and a flow from the land to the sea is formed. The LB ends after sunrise because the warming of the Earth. Cuxart et al. [2007] studied the nocturnal winds on the island of Mallorca, including LB.

1.2 The Atmosphere-Surface exchanges

The climate system can be divided in five subsystems: atmosphere, hydrosphere, cryosphere, lithosphere and biosphere. There are many processes that take place between the different subsystems and particularly the atmosphere, which is the closest part to the surface, and the surface of the Earth. These processes can last from minutes to centuries, and can be of biological, chemical or physical origin.

One of these processes is the energy flux, corresponding to the amount of energy that passes through a surface in a unit of time. The regime of the flow depends on three physical parameters that describe its conditions [Potter et al., 2016]: the first parameter is the scale of the field (L), such as the thickness of a boundary layer; the second parameter is a speed scale (v), for instance a spatial average of the velocity (if the speed is large enough, the flow could be turbulent); the third parameter is the kinematic viscosity (ν) (if the viscosity is small enough, the flow can be turbulent). The Reynolds number is a parameter that describes these features of the flow:

$$Re = \frac{vL}{\nu} \tag{1.4}$$

Thus, there is a threshold value, Re_{cri} ≈2300 that separates the flow in laminar or turbulent. If Re_{cri} is lower than Re_{cri} the flow is laminar, if Re is larger than Re_{cri} the flow is turbulent.

In general, during the day it is considered that in the ABL the flux is turbulent (Re is larger than Re_{cri}), so that at any point abrupt changes in the velocity, pressure, temperature or relative humidity are observed. This is due to the warming of the Earth's surface caused by the Sun, the air in contact with it induces turbulent vertical movements, producing a rapid mixing in the early hours of the morning. The effect of surface friction, surface heating and evaporation are transmitted quickly and efficiently to the whole ABL depth due to the turbulent mixing. From sunset to sunrise, SBL evolves giving rise to a stable layer on the surface up to few meters high (radiative cooling caused by soil) and a residual layer above it where potential temperature and

humidity are practically constant. This residual layer has its origin in the mixed layer of the diurnal hours of the previous day [Warner, 2009].

Heat fluxes between the land surface and the lower layers of the atmosphere are very important in the parametrization of the boundary layer for current models [Deardorff, 1972]. The diurnal variation of the thickness of this layer depends mainly on the amount of radiation received by the Earth's surface and the distribution of this energy [Imberger, 1985]. In simplified form, the transference of energy can be explained as follows: the solar radiation (R_n) heats the Earth's surface and thus increasing the soil heat, such that some heat excess is transmitted to the atmosphere as sensible heat, (H). If there is humidity in the soil or transpiration by plants, evaporation occurs, which allows heat removal from the soil as latent heat (LE). At the same time, part of the heat is also transmitted to deeper soil layers, (G). Traditionally, the surface energy balance equation can be written as:

$$R_n = LE + H + G \tag{1.5}$$

In textbooks as in Garratt [1992], it can be found a more detailed analysis of this equation. In order to understand the exchange of properties between the atmosphere and the surface, these terms are measured and studied in many works such as: Bastiaanssen et al. [1998], Foken [2008a], Leuning et al. [2012], Mauder et al. [2007], Moderow et al. [2009], Oncley et al. [2007], Sánchez et al. [2008], Viterbo and Beljaars [1995] where they found that there is an imbalance in this equation. It may be due to other terms that have not been taken into account (biological processes or advection among others) and they have been studied on various land uses: bare soil, mulched, urban areas [Coulter et al., 2006, Ramamurthy and Pardyjak, 2011, Wang et al., 2005] or natural surfaces such as in grasslands and mostly in forests [Adegoke and Pielke, 2007, Baldocchi et al., 2001, Barr et al., 2012, Fischer et al., 2012, Giambelluca et al., 2009, Jacobs et al., 2007, Kilinc et al., 2012, Moderow et al., 2011, Soegaard et al., 2003]. However, these terms do not normally take into account the phenology of vegetation. Cuxart et al. [2016a] developed the energy balance Equation (1.5) from the evolution equation of the temperature as follows:

$$R_n + H + LE + G = -TT - A + S + B + Ot = Imb \tag{1.6}$$

where TT is the temperature tendency, A the advection, S the storage, B the biological processes, Ot other terms and Imb the imbalance (Figure 1.4b). These terms will be described in more detail in the following sections. It is worth noting that the sign

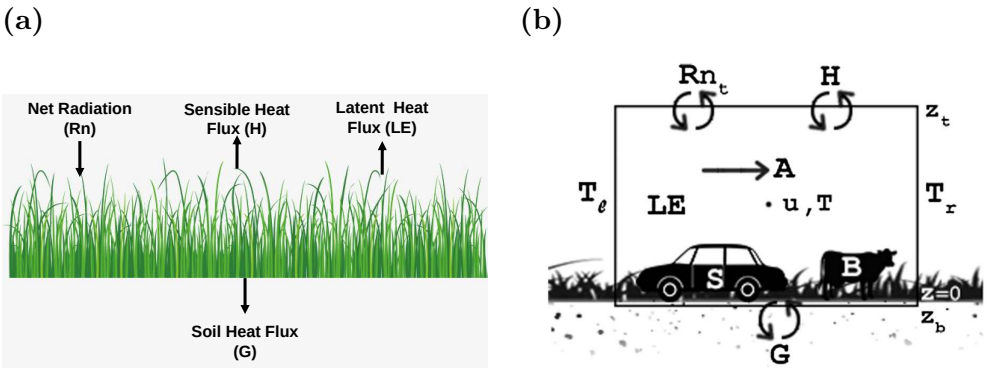

FIGURE 1.4: **(a)** Diagram of the traditionally surface energy balance and **(b)** Developed diagram of the surface energy balance, with a lower boundary condition into the soil and an upper boundary condition in the atmosphere. R_n stands for the net radiation, H for the turbulent sensible heat flux, LE for the heat related to phase changes, G for the ground heat flux, S for the storage, B for the biological processes, A for the advection across the box between temperature T_l and T_r. T and u stand for the temperature and the wind speed, and z_t and z_b for the height of the top and bottom of the box. Source of the figure **(b)**: Cuxart et al. [2016a]

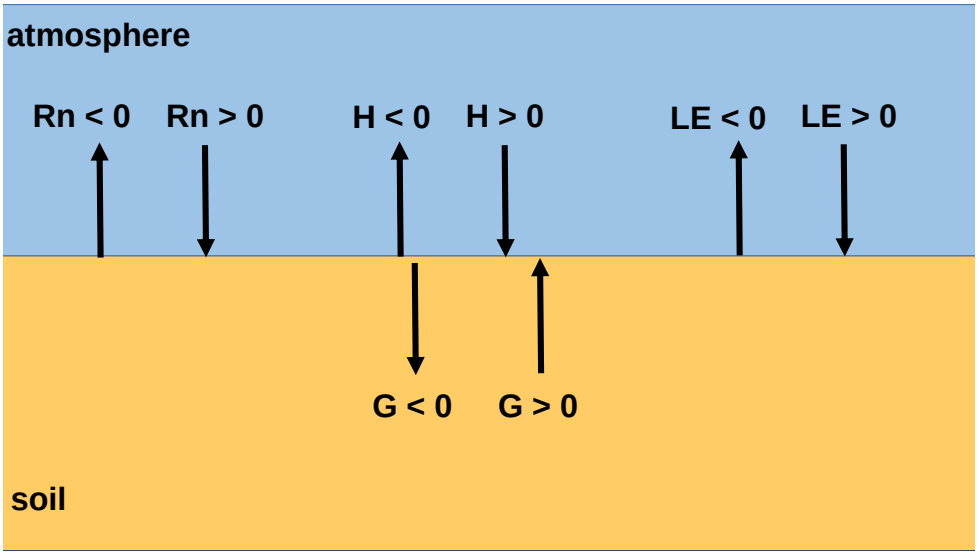

FIGURE 1.5: Scheme of the sign criterion used in the energy balance.

convention used in Equation (1.5) is not unique in the literature. The sign criterion that has been used in this thesis, is that energy arriving to the surface is positive, and energy leaving the surface is negative (Figure 1.5).

1.2.1 Net radiation (R_n)

Net radiation is the net flux of energy in the form of thermal radiation exchanged between the system and its environment. The components that determine R_n include downward ($S\downarrow$) and upward ($S\uparrow$) short wave radiation and downward ($L\downarrow$) and upward ($L\uparrow$)

long wave radiation. R_n provides the energy that heats the air, the plants and the soil or evaporates water.

- $S\downarrow$: is the radiation emitted by the Sun and transmitted through atmosphere that reaches the ground, it depends on solar altitude and transmissivity of the atmosphere above.
- $S\uparrow$: is the solar radiation reflected by the surface, it depends on $S\downarrow$ and the albedo (ratio of reflected to incoming shortwave radiation that depends on the surface), which is a properly of the ensemble of elements of the surface.
- $L\downarrow$: is the incoming longwave radiation from the atmosphere, it depends on the apparent sky temperature, sky emissivity and the concentration of absorbents, especially H_2O.
- $L\uparrow$: is the longwave radiation emitted by the surface, it depends on surface temperature and surface emissivity.

When there is more incoming radiation than outgoing radiation, net radiation is positive. This typically occurs during the daytime. At night, net radiation is usually a negative value as there is no incoming radiation from the Sun and the net longwave is dominated by the outgoing terrestrial longwave flow, yet the Earth's surface and atmosphere still emits outgoing radiation. Net radiation is practically zero when the incoming and outgoing components are compensated, which occurs close to sunrise and sunset and in cloudy nights.

If global net radiation from an annual cycle of whole Earth is analysed, it is observed that this is zero, pointing that the net positive radiation is compensated with the negative. Depending on the latitude, there may be a surplus or deficit of R_n [Allen et al., 1998]. Between about 40° N and 40° S there is a net radiant energy gain, incoming solar radiation exceeds outgoing longwave radiation throughout the year. Poleward of 40° N and 40° S instead, the net radiation is negative, outgoing longwave radiation exceeds incoming shortwave radiation [Pidwirny, 2006].

In Mallorca where most of the studies of this thesis took place, the net radiation in winter is about 400 W m^{-2} and in summer about 600 W m^{-2} during the day when it has Gaussian form, being larger in the central hours of the day. Instead, during the night it has very low values in cloudy nights and up to -70 W m^{-2} in clear nights, according to the data of the surface energy balance station located in the Campus of the University of the Illes Balears (UIB).

1.2.2 Sensible heat flux (H)

The sensible heat flux in the atmosphere is the amount of energy exchanged as heat by convection between the surface and the atmosphere, due to the temperature difference between these media.

When the sensible heat content of the air is high, the molecules have higher speeds and more collisions between them and their surroundings are produced, and therefore also more kinetic energy transfer [Snyder and Melo-Abreu, 2005]. As the sensible heat flux increases, so does the temperature and conversely.

The turbulent sensible heat flux is defined as:

$$H = \rho c_p \overline{w'T'} \tag{1.7}$$

where ρ is the air density (1.2 kg m^{-3}), c_p is the specific heat of air at constant pressure (1004.67 J K^{-1} Kg^{-1}), $< w'T' >$ are the turbulent fluctuations instantaneous of vertical velocity ($w = \overline{w} + w'$). The average of vertical velocity is represented by $\overline{w}$ and the fluctuation of vertical velocity by w'. Same for the temperature ($T = \overline{T} + T'$) where $\overline{T}$ is the average of temperature and T' is the fluctuation of the temperature. In order to measure these fluctuations, sensitive instruments that record values in small-time intervals are needed.

In clear sky conditions H is maximum in the central hours of the day, and during night-time it reaches negative values (air warmer than surface). During the evening and morning transitions its value is close to 0, according to the data of the surface energy balance station located in the Campus of the UIB.

1.2.3 Latent heat flux (LE)

The latent heat flux is the flux of energy as heat due to changes in the water phase, mainly to evaporation, condensation and water vapour transfer. When the water condenses, latent heat is converted into sensible heat, whereas when the water is vaporized, the sensible heat is converted into latent heat [Snyder and Melo-Abreu, 2005].

The turbulent latent heat flux is defined as:

$$LE = \rho L_v \overline{w'q'} \tag{1.8}$$

where L_v is the latent heat of vaporization, $\overline{w'q'}$ is the turbulent humidity flux.

LE is larger in the central hours of the day and smaller during the nighttime, according to the data of the surface energy balance station located in the Campus of the UIB. If LE=0 there are not changes in the water phase, and this may happen when the soil is very dry, without moisture.

1.2.4 Heat flux on the ground (G)

The heat flux on the ground is a heat transport mechanism in which the energy is transported between two layers at different temperature.

$$G = \lambda \frac{dT}{dz} \tag{1.9}$$

where G is the heat flux, λ is the thermal conductivity, T is the temperature and z the depth of the soil. The thermal conductivity of soil (λ) is the amount of heat transferred by molecular conductivity (heat is transferred from the parts of the soil with the highest temperature to the coldest parts). The thermal conductivity of soil particles is greater than that of water and much greater than that of air, consequently it will depend on the moisture content, porosity, granulometry and soil aggregation [Porta et al., 2003] and is related to microbial activity, mineralization and humification of organic matter [Montenegro et al., 1990]. When the thermal conductivity of a soil is high, the LST variations are lower. The thermal conductivity increases with the moisture content, affecting at the same time the changes in soil temperature; however, when there is pore saturation it does not increase in the expected proportions [Rojas et al., 2007]. In this way wet soils, in which there is a displacement of air induced by the underlying water, the heat conduction is more efficient than in drier ones thus also affecting more quickly the deeper layers. If the soil is dry, the heat flux on the ground may be very small, depending on its porosity and air content. Ultimately, G is higher in the central hours of the day, because the difference in temperature between the air, the surface and the ground is greater. During the night instead, it has an average positive value lower than 50 W m^{-2}, according to the data of the surface energy balance station located in the Campus of the UIB.

1.2.5 Other terms

As we have seen, although the simplified form of the Equation (1.5) is often used, it is only valid under ideal conditions, which in practice are usually not found. Therefore, besides these main terms, there are others that are not normally taken into consideration (Figure 1.4b): biological processes involving energy exchanges, storage in the elements

of the volume or unaccounted water phase changes [Cuxart et al., 2016a, Foken, 2008a, Leuning et al., 2012, Mauder et al., 2007, Moderow et al., 2009, Oncley et al., 2007]. In vegetated surfaces the size of the plant, its vertical structure, its spatial distribution and phenological stage also affects in the energy balance equation. Forests, grasslands and crops behave differently and vary depending on the time of year [OKE, 1978]. Furthermore in some cases, such as crops, there are different quantitative requirements of energy in winter and in the summer.

In general, following Cuxart et al. [2016a] it is possible to define these terms as: horizontal advection (A), net photosynthesis (Ph), increased internal energy of the system (ΔU) and the flow of carbon dioxide (CO_2). Advection is the horizontal transport of some properties such as temperature and relative humidity due to the wind, it is explained in more detail in Chapter 5. The net energy flow associated with photosynthesis is very small compared to other flows [Cuxart et al., 2016a]. It is also considered that the variation of internal energy, which is associated with the temperature variation of the system is small.

In Cuxart et al. [2016a] they also made a comparison between observed and modelled SEB data. This study was carried out in Raimat located in the Eastern Ebro Valley (Catalonia), in a typical Mediterranean climate, during 2009 and 2010. The imbalance during day in winter is on average above 60 W m^{-2} and in summer is above 150 W m^{-2}, and during the night in winter is on average above 10 W m^{-2} and in summer is above 15 W m^{-2}. Also, they found that the imbalance follows a similar pattern as the radiation, an annual cycle at noon peaking in summer and no cycle at midnight. During the daytime the values of the imbalance are approximately 34% R_n in fall and winter and 27% in spring and summer, whereas for the nighttime, spring and summer are close to 33% R_n and fall and winter approximately 24% R_n, therefore, the importance of having good R_n measurements.

1.3 Introduction to Remote Sensing

Remote sensing is the technique that allows us to obtain remote information of phenomena and bodies through radiation [Lillesand et al., 2014]. It is a measurement technique used for cases in which direct measurement is impossible, or remote panoramic observation is convenient and for cases in which it is a matter of studying objects or samples that are not to be destroyed or altered. It can be done from satellites, airplanes, drones, balloons or radiometers located on the surface, that is, any measure that occurs without coming into direct contact with the body to be studied.

1.3.1 Electromagnetic radiation

Remote sensing sensors measure electromagnetic radiation. Electromagnetic radiation is a perpendicular superposition of electric ($\vec{E}$) and magnetic ($\vec{B}$) fields that form the radiative field and propagate in a vacuum in the direction also perpendicular to $\vec{E}$ and $\vec{B}$ [Lillesand et al., 2014]. The electromagnetic waves transport energy between a transmitting source and a receiver (which can be a detector).

All surfaces are above 0 Kelvin and emit energy in the form of radiation. These electromagnetic waves are produced by the movement of electrical charges close to the surface of the emitter body. The monochromatic or spectral emittance pattern of a black body is a function of its temperature and wavelength and follows Planck's law (1900):

$$B_{\lambda,T} = \frac{2\pi hc^2}{\lambda^5} \cdot \frac{1}{exp(\frac{hc}{\lambda kT}) - 1} \tag{1.10}$$

where $B_{\lambda,T}$ is the spectral or monochromatic emittance of a black body at a certain wavelength, h is the Planck constant h=6,626·10^{-34} W s^2, k is the Boltzmann constant k=1,38·10^{-23} W s^2 K^{-1}, c is the speed of light c=3·10^8 m s^{-1} and T is the absolute temperature in Kelvin.

Through Planck's law it can be seen that the higher the temperature of a black body, the greater the amount of radiant energy emitted by it.

Taking the first derivative of Equation 1.6 in relation to the wavelength, another relation is obtained that provides the value of the wavelength of maximum spectral emittance of the blackbody at a given temperature. The relationship between the maximum emittance wavelength and the blackbody temperature is known as the Wien displacement law (1893):

$$\lambda_{max} T = 2898 \mu m K \tag{1.11}$$

Wien's law establishes an inversely proportional relationship between the wavelength of maximum emittance and blackbody temperature, that is, the higher the blackbody temperature, the lower the wavelength of maximum emittance.

Integrating the spectral emissivity of a black body for all wavelengths, a mathematical equation for calculating the total energy emitted per unit area by a black body at a given temperature is obtained. This is the law of Stefan-Boltzmann, that relates the radiation of a body to its temperature in the following way (1879):

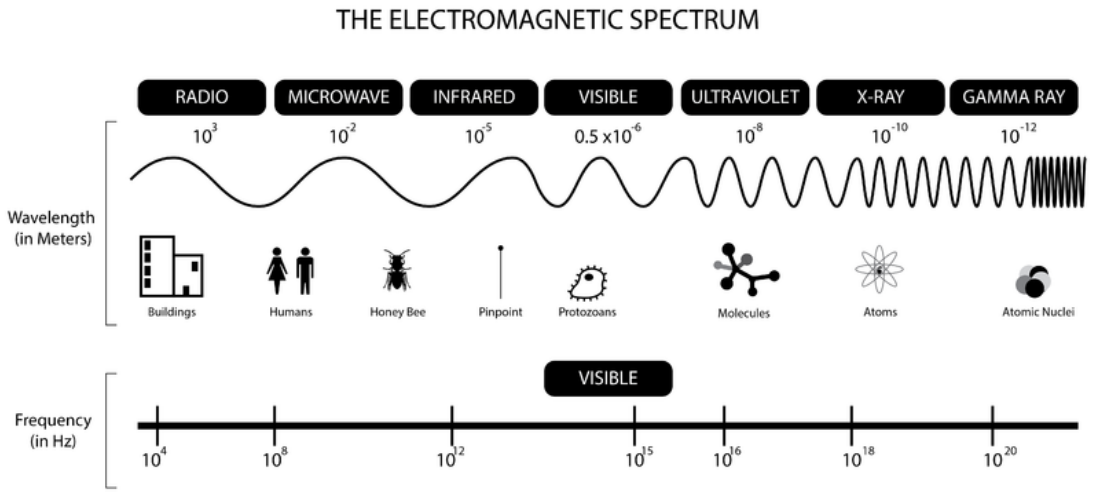

FIGURE 1.6: Infographic of the Electromagnetic Spectrum with the different regions (radio, microwave, infrared, visible, ultraviolet, X-Ray, Gamma-Ray), and wavelength and frequency of each region. Author: Jonathan S Urie

$$B_\lambda = \sigma \cdot T^4 \tag{1.12}$$

where σ is the Stefan-Boltzmann constant $\sigma = 5.669 \cdot 10^{-8}$ W m^{-2} K^{-4}.

The electromagnetic spectrum (Figure 1.6) is the set of different electromagnetic radiations grouped according to their spectral variable (frequency or wavelength) [Olsen, 2007]. The area of the spectrum corresponding to gamma rays is a zone that is not used in remote sensing since the atmosphere is opaque to this radiation. The ultraviolet range is a very useful band in the remote sensing of aerosols and pollutants since the atmospheric components absorb and disperse this radiation. The range corresponding to the infrared zone is very useful in the characterization of terrestrial surfaces, since in this range the terrestrial surface emits radiation. Microwave region is also used in the characterization of natural surfaces, cloudiness and precipitation. Finally, the region of radio waves is the region used by active sensors such as altimeters and scene radars.

The spectral radiation that reaches the sensor at a height h for a wavelength λ, R_λ(h), with an angle of observation θ, where z is the height relative to the Earth's surface it is given by:

$$R_\lambda(h) = R_\lambda(0) \cdot \tau_\lambda(0, h, \theta) + \int_0^h B_\lambda[T(z)] \cdot \frac{\partial \tau_\lambda(z, h, \theta)}{\partial z} \cdot dz \tag{1.13}$$

where $R_\lambda(0)$ is the spectral radiance at the surface level, B_λ[T(z)] is the Planck function of black body radiation (Equation 1.10) at temperature T(z) (temperature of the

atmosphere at height z) and τ_λ(z,h,θ) is the spectral transmissivity of the atmosphere between the heights z and h in the direction of the angle of observation (Equation 1.14):

$$\tau_\lambda(z,h,\theta) = exp\left[-\int_z^h \rho(z')\cdot\varepsilon_\lambda(z')\cdot\frac{dz'}{cos\theta}\right] \tag{1.14}$$

Thus, the radiance that reaches the satellite is the sum of the radiance at the level of the surface once it has crossed the atmosphere (first addend) and the radiance emitted upwards being the direction of observation of the satellite by the different layers of the atmosphere (second addend).

If the spectral radiance is analysed in more detail at the level of the surface $R_\lambda(0)$, it is normally considered that this radiance is given as the sum of the three different contributions: (i) the radiance emitted by the surface ($R^e_\lambda(\theta)$) that depends on the emissivity and the Land Surface Temperature, (ii) the radiance emitted by the atmosphere ($R^r_\lambda(\theta)$) towards the Earth that is reflected by the surface and (iii) the solar radiance reflected by the surface ($R^{sr}_\lambda(\theta)$).

$$R_\lambda(0) = R^e_\lambda(\theta,\varphi) + R^r_\lambda(\theta,\varphi) + R^{sr}_{\lambda,\varphi}(\theta) \tag{1.15}$$

where the radiance emitted by the surface is obtained as follows:

$$R^e_\lambda(\theta,\varphi) = \varepsilon(\theta,\varphi)\cdot B_\lambda[T(z)] \tag{1.16}$$

where $\varepsilon(\theta,\varphi)$ is the spectral emissivity of the surface for the angles of zenith observation θ and azimuthal φ.

Regarding the reflected component, it would be defined by the following expression:

$$R^r_\lambda(\theta,\varphi) = \int_0^{2\pi}\int_0^{\pi/2} \rho_{b\lambda}(\theta',\varphi',\theta,\varphi)\cdot R^\downarrow_\lambda(\theta')\cdot cos(\theta')\cdot sin(\theta')d\theta' d\varphi' \tag{1.17}$$

where $\rho_{b\lambda}(\theta',\varphi',\theta,\varphi)$ is the bi-directional reflectivity of the surface, which depends on the angle of incidence (θ',φ') and reflection (θ,φ) and $R^\downarrow_\lambda(\theta')$ is the radiation emitted by the downward atmosphere which is given by:

$$R^\downarrow_\lambda(\theta') = \int_h^0 B_\lambda[T(z)]\cdot\frac{\partial\tau'_\lambda(z,0,\theta)}{\partial z}dz \tag{1.18}$$

being τ'_λ(z,0,θ) the transmissivity of the atmosphere between the surface and height z.

These equations ideally describe the radiative transfer between the Earth surface crossing the atmosphere to the radiation measured by the satellites.

1.3.2 Meteorological satellites

Nowadays, meteorological satellites provide a very large quantity of data useful for initialising and validating forecast models. Concerning its movement in relation to the Earth rotation frequency it is possible to classify them in two types: geostationary or polar. The geostationary ones, describe orbits on the terrestrial equator with a distance to the Earth of 36000 km approximately and with the same angular speed of the planet, therefore they are always focusing on the same zone. An observer on Earth would see these satellites as if they were static. Satellites remain in orbit as a result of the balance between centrifugal and gravitational forces. On the other hand, the orbits for the polar satellites pass over the poles with a distance to the Earth of about 10000 km, they pass at the same time on the same place (heliosynchrons). Due to the differences of the distance to the Earth between geostationary and polar satellites, the former ones have larger temporal resolution whereas for the latter the spatial resolution is larger.

Satellites have onboard sensors to measure radiation, better known as radiometers. They scan the Earth's surface and register the radiation that reaches them from the terrestrial surface.

The resolutions of a sensor can be classified into temporal resolution, spatial resolution, spectral resolution and radiometric resolution [Mather and Koch, 2011]. Temporal resolution is the frequency of coverage, the time that the satellite takes to pass through the same place. The spatial resolution is the smallest distance measurement that the sensor can identify and it is represented by pixels. It is determined by: (i) the FOV (Field Of View) which refers to the angular extent of the image in the perpendicular direction to the sensor's advance, (ii) the $SWATH$ which is the projection of the FOV, that is, the width of the image in the perpendicular direction to the advance, (iii) the $IFOV$ (Instantaneous Field Of View) which is the angular extension of the area captured by an individual detector and (iv) the $GIFOV$ (Ground Instantaneous Field of View) which is the projection of the IFOV on the surface. Normally these two are linked, when a sensor has good spatial resolution takes longer to go through the same place, so it has lower temporal resolution, and conversely, the one that pass more frequently has lower spatial resolution. The spectral resolution refers to the number of bands and width that can discriminate. Finally, the radiometric resolution can be defined as the number of different grey levels recorded by the sensor. This resolution is expressed with the number of bits required for each image element (pixel) to be stored.

Satellite	Launch	Spatial Resolution	Temporal Resolution	Spectral Resolution	Radiometric Resolution
AQUA/MODIS	2002	1 km	every day	36 bands (0.4 μm to 14.4 μm)	12 bits
TERRA/MODIS	1999	1 km	every day	36 bands (0.4 μm to 14.4 μm)	12 bits
TERRA/ASTER	1999	90 m	16 days	14 bands (0.52 μm to 11.65 μm)	12 bits
Landsat-7	1999	60 m	16 days	8 bands (0.48 μm to 12.5 μm)	8 bits
Landsat-8	2013	30 m	16 days	11 bands (0.435 μm to 12.51 μm)	16 bits
NOAA-18/AVHRR	2005	1.1 km	2 passes per day	6 bands (0.58 μm to 12.5 μm)	16 bits
NOAA-19/AVHRR	2009	1.1 km	2 passes per day	6 bands (0.58 μm to 12.5 μm)	16 bits
MSG-2	2005	3 km	15 minutes	12 bands (0.4 μm to 13.4 μm)	10 bits
MSG-3	2012	3 km	15 minutes	12 bands (0.4 μm to 13.4 μm)	10 bits
Sentinel-3	2016	1 km	every day	11 bands (0.55 μm to 10.85 μm)	10 bits

TABLE 1.1: List of the main satellites that measure LST nowadays in South Western Europe, with the year of launch and spatial, temporal, spectral and radiometric resolutions. In this table are the resolutions corresponding to the TIR band from which we obtain the LST products.

Table 1.1 contains the most relevant satellites used to measure LST in the South West of Europe nowadays, that are available for research purposes.

1.3.3 Satellite-derived Land Surface Temperatures

LST is the radiative temperature of an element of the surface, sometimes also referred to as *the skin temperature of the surface* [Jin and Dickinson, 2010]. Since this layer is in contact with two media at the same time (atmosphere and soil/vegetation), it is very difficult to make a meaningful measurement of the temperature using a thermometer [Betts et al., 1996]. Instead, LST is determined by measuring the amount of energy radiated by the surface, using a radiometer, which can be located at a fixed point at few meters from the surface, as in the case of the infrared radiometer Apogee. They can also be placed in drones, helicopters or airplanes, or onboard meteorological satellites.

Sometimes the approximation that LST is equal to the air temperature is made, but this is often incorrect, because the Earth heats up and cools faster than the air. Therefore, they have to be measured separately or derive relations between them and use one through the other.

Users of remote sensing, can obtain rawdata scenes or final products that have undergone a correction and calculation process through a series of algorithms can be downloaded. This is the case, for instance of the LST products offered by MODIS.

1.4 Influence of Surface Heterogeneities

Surface heterogeneities have a non-negligible impact on the energy balance terms. As seen in Section 1.1.3, Monin–Obukhov similarity theory described the turbulent changes of energy, moment and moisture between the atmosphere-soil system over a homogeneous

surface. However, very often the land surface is heterogeneous: rugosities, changes of slope, areas with vegetation, areas without vegetation, different types of soils, etc. These surface characteristics interfere the turbulent flux over the surface and affects the processes that govern the exchange of momentum, heat, and mass between the complex surface and the ABL [Fesquet et al., 2009].

Therefore, superficial heterogeneities have a very important role in the surface energy balance, since they can modify the local turbulence flux. Foken et al. [2010] observed that if the small-scale heterogeneities are much smaller than the height of the boundary layer or the singularities of flow, they can be affected with the superficial energy flows. Vertical mixing in SBL is weak and it is characterized by small scales ($\sim$ 100 m). The superficial heterogeneities in flat areas with stable stratification are less likely to generate their own secondary circulations, because the pressure adjustments make vertical movement fields on a larger scale disappear [Smith and Mahrt, 1981], the role of surface heterogeneity is mainly to modify the local turbulence flux [Mahrt, 1999]. Besides, thermal heterogeneity may lead to local decoupling between the surface and higher levels as suggested by Beyrich and Kotroni [1993].

On the other hand, fields of vertical movement on a larger scale (1–10km) are normally inhibited by stratification and by pressure adjustments, therefore, mesoscale surface heterogeneity over plain surfaces with stable stratification is quite unlikely to generate its own secondary circulation [Smith and Mahrt, 1981].

The superficial heterogeneities affect up to a certain height of the atmosphere, the blending height, which depends on the type of heterogeneities that exist and the amount of these. In areas with surface heterogeneities on a small scale, this magnitude can not be calculated, since it is not well-defined [Foken, 2008b], such as the Campus of the University of the Balearic Islands.

Cuxart et al. [2016b] study the advection effects induced by surface heterogeneities with satellite and models data of 1 km of resolution and for smaller scales with direct measurements from remotely piloted aircraft and thermal cameras, finding that heterogeneities play a very important role in the determination of advection in one point. They also observed that for scales greater than a few kilometers, the advection term does not significantly affect the surface energy balance equation. On the other hand, very small scale heterogeneities, of the order of a few meters, seem to be taken in charge by the turbulence mixing. The motions that do seem to contribute significantly to the advection term, were those that were close to the hectometer scale.

Another important aspect are the temporal variations on the same surface. These are due to the soil changes during the year, such as changes in vegetation. The heat flux of

soil is linked to these changes, usually at night the soil heat flux plays a more important role than during the day, and this is influenced by the characteristics of the soil. If there is more vegetation in the soil, it will be drier because the vegetation absorbs most of the soil water content [Azeñas et al., 2018], if it is drier it will be warmer and directly affects the heat flux of the soil. Furthermore, when measuring the heat flux of the soil the heterogeneity of the soil can have a significant influence on the results [Liebethal et al., 2005].

Derbyshire [1995a,b] studied how small-scale heterogeneities affect the nocturnal boundary layer, because the mixed is smaller scale and weaker at night. He also found more intense turbulence in a heterogeneous zone than in a homogeneous one, which suggests that turbulence in models is underestimated in many areas at night.

There are many types of superficial heterogeneities, from which we can find on a small scale, of the order of one hundred meters (eg Raasch and Harbusch [2001]) or much larger scales (eg Kang et al. [2012]). It is important to determine the size of the heterogeneities to further understand the circulations that generate (spatial and temporal scales) and the physical mechanisms involved. Besides, the circulations induced by surface heterogeneities at different scales might interact, increasing the difficulty to characterize the processes involved.

1.4.1 The most important field campaigns in heterogeneous terrains

In order to study the processes that take place in the ABL, in addition to studies made with models, a lot of field campaigns have been carried out. Below we will see a summary of the most important internationally field campaigns, starting with the most important in homogeneous zones.

The first major campaigns that studied the atmospheric boundary layer in homogeneous terrain were KANSAS that was made in Kansas in 1968 (eg Gibson and Launder [1978], Kaimal and Finnigan [1994], Kaimal et al. [1976]) and WANGARA-1967 that was conducted in Hay, New South Wales in the summer of 1967 (eg Clarke et al. [1971], Yamada and Mellor [1975]).

CASES-99 that was carried out in southeast Kansas during October 1999 that studied some processes in the stable nocturnal boundary layer and the transition periods (eg Fritts et al. [2003], Newsom and Banta [2003], Poulos et al. [2002], Sun et al. [2012]).

In addition to these campaigns in homogeneous areas, many campaigns in heterogeneous areas such as the following, have also taken place in recent years.

LIFTASS-2003 was conducted close to the Meteorological Observatory Lindenberg (MOL) of the German Meteorological Service, a heterogeneous area of 20km^2 during May and June 2003. In this field campaign, apart from satellite data and models, data from micrometeorological stations located in different types of terrain (agricultural, grassland, forest and lake sites) were used, with the purpose of studying turbulent fluxes of momentum, sensible and latent heat among others (eg Beyrich and Mengelkamp [2006], Foken et al. [2010], Mauder et al. [2006], Meijninger et al. [2006]).

Another campaign was BLLAST-2011 that took place in Lannemezan at the south of France, near the Pyrenees during the summer 2011. This campaign focused in transitions between the unstable regime during the day to a stable regime at night. To this end, data from models and satellites, and stations located in the different types of soil in the area were used (eg Cuxart et al. [2016b], Lothon et al. [2014], Pietersen et al. [2015], Román-Cascón et al. [2015]).

Chapter 2

Material and Methods

This Chapter explains all the material and methods that have been used in this thesis to further understand the processes that take place in the atmosphere-soil interface at different spatial and temporal scales. Several in situ instruments are used depending on the scales of the heterogeneities in the surface layer. For instance, the vertical structure of the lower boundary layer is measured using a captive balloon and a remotely-piloted multicopter. The variability of the land-surface temperature fields is explored through satellite products. It is explained here which ones are the most adequate according to the objectives of the thesis and the main reasons to choose them. Meteorological models are also used in this thesis to complement and understand the observations and the main features of those used are explained in this chapter. Ground observations made are described at the end of this chapter, specially those used to compute the terms of the surface balance equation.

2.1 Measuring the lower Atmospheric Boundary Layer

To understand the processes occurring in the atmosphere-soil interface, measurements of atmospheric and soil variables are needed to properly characterise them.

Soundings are used to study the vertical structure of the atmosphere. Operational soundings are made twice a day, at 1200 and at 0000 UTC and they usually reach the stratosphere. The ascent is fast and therefore the vertical resolution of the measurements is relatively low.

If the studied region is far from a place were soundings are regularly launched, tethered balloons and multicopters can be used to measure the lower atmosphere (several hundreds of meters above the ground) with a higher vertical resolution and temporal

resolution (frequency) than the soundings. Therefore, the physical mechanisms studied in this thesis that take place in the lower atmosphere are better characterized. Besides, we can control, whenever the meteorological conditions allow us, when to proceed with the soundings, measuring as well their frequency and the maximum height. As a result, the vertical structure of the lower atmosphere is sampled more precisely.

2.1.1 Tethered balloons

A tethered balloon (Figure 2.1a) is a balloon filled with a gas lighter than the air that is linked to the surface through a thread. It is used to measure the vertical profile of various meteorological parameters such as relative humidity, atmospheric pressure, temperature, wind speed and direction. They carry radiosondes to measure these magnitudes and transmit the data to a receiver device located on the ground using radio frequency.

However, the price of commercial captive balloons and instruments are high and in some cases the availability of the equipment and its handling is difficult. Because of this, a home-made system was designed (Figure 2.1c) which we call BOU (**B**alloon-**O**stwestfalen-Lippe University-**U**niversity of the Balearic Islands), similarly to what other research groups have done [Gutiérrez et al., 2007]. A mechanical fishing reel attached to the ground with a large weight is used (Figure 2.1b). With this reel we can regulate the speed of release and collection of fishing line that is tied the balloon.

The measurement system and data acquisition is also home-made. The tethered balloon has sensors that are inside a protection box (Figure 2.1d) and hanging of the balloon by a thread. It is filled with helium. The ascent of the balloon is not vertical due to do the horizontal wind in the lower atmosphere. When large-scale wind is weak, the vertical velocity might also change the ascent rate. When the wind reaches high speeds, soundings can not be made, due to the intense turbulence and the risk of breaking the cable due to strength that the balloon exerts and in this way the instruments are in danger. With weak winds it can reach more than 300 meters height.

BOU uses a low-cost Arduino Mega board as the processor, and stores all the data in a SD card, sampling once per second. It carries sensors of temperature, humidity and air pressure. The system is powered by a Polymer battery of 1800 mA, allowing the system to run continuously for more than 6 hours. The temperature is measured using a HYT-271 calibrated sensor with an accuracy of $\pm$ 0.2°C. The humidity is obtained by the same calibrated HYT-271 sensor, which features an accuracy of $\pm$ 1.8%. We decided to use this sensor because it was economical as well as easy handling to work with it. In addition, it has been calibrated with standard sensors to check that measures correctly.

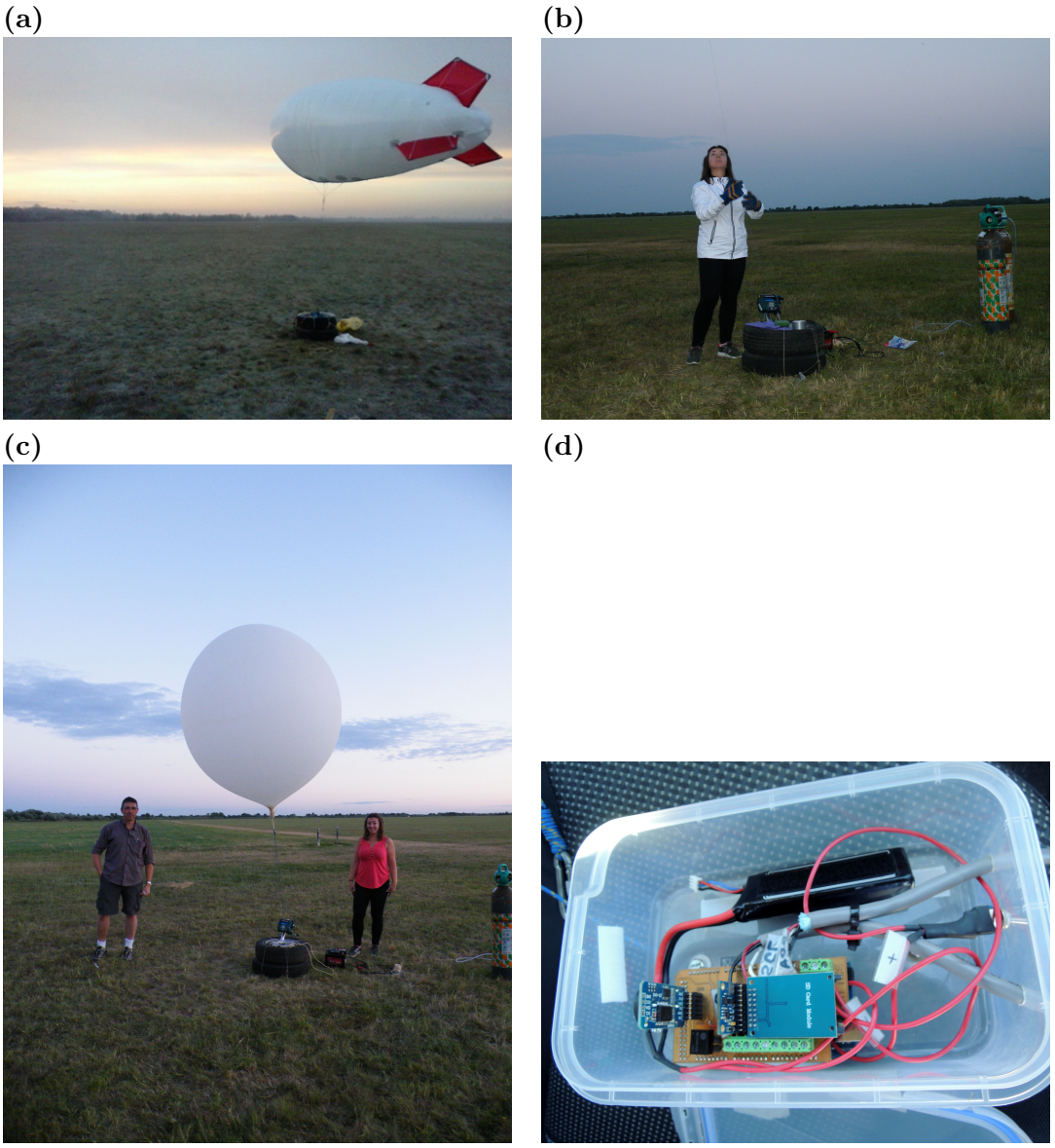

FIGURE 2.1: (**a**) Tethered balloon shaped like a zeppelin that we used in a field Campaign in Hungary in winter 2013. (**b**) The mechanical fishing reel with a large weight, the bottle of helium and how we handle the balloon. (**c**) The complete system with one of the balloons that we normally use. (**d**) The protection box where all the sensors and the data acquisition system are located.

Air pressure is measured using a BMP080 sensor. The height of the balloon (h) is obtained from the pressure (p) using the hydrostatic equation at each instant of time. From the maximum height obtained, the soundings are separated in ascents and descents and a quality control is applied to the observations. It consists in removing the erroneous values, which are the ones whose difference between the previous and the next is greater than 2σ. Afterwards, vertically-averages of the measured magnitudes are made to finally obtain vertical profiles at 1 m resolution.

With BOU we can reach heights of 300 meters on calm days and nights, however, in some cases, due to the presence of moderate winds and turbulence we can not reach those heights. If weather conditions are good, a sounding (ascent and descent) lasts from 30 to 40 minutes.

There are many studies that use tethered balloons for meteorological applications, for example Balsley [2008], Cuxart et al. [2012], Lothon et al. [2014], Whiteman et al. [2008]. In this thesis it has been used in the study of morning transition case between the Land and the Sea-Breeze (Chapter 6), in the campaigns of the Hungarian Pannonian (Chapter 7) and in the campaigns of the Cerdanya Valley (Chapter 7).

2.1.2 Remotely-Piloted multicopters

The use of remotely-piloted multicopters has increased significantly in the last years in remote sensing applications [Cummings et al., 2017] and in meteorology [Wrenger and Cuxart, 2017]. These applications include a variety of disciplines such as Agriculture, Forestry or Geology (an interesting list of published studies can be consulted in Table 1 of IJRS [2017]).

One of the advantage of using multicopters to measure the lower atmosphere is that they have more stability to the gusts of wind, since they are controlled remotely. Besides, horizontal cross-sections can be sampled from multicopters. The ascent of the multicopter is more controllable, performing almost vertical, compared to the balloon. However, they can not get as high as balloons and the flight is constraint to the duration of the battery.

In this thesis, two multicopters have been used for different purposes. The first one (UAV-OWL) has been used to sample the vertical structure of the lower atmosphere. Vertical soundings up to 100 m are sampled for the temperature, humidity and wind. The second one (UAV-TIR) has been used to make horizontal transects and estimate the Land Surface Temperature of a heterogeneous zone of 1 km^2. As a result, it is important to

decide which the type of sensor onboard a multicopter will be more adequate depending on the objectives of the work.

2.1.2.1 Vertical profiles

The remotely-piloted multicopter (Figure 6.5c) has on board a set of sensors to measure meteorological variables. It is also used to measure the lower atmosphere with a high vertical and temporal resolutions than the operational soundings. Thanks to the collaboration between the University of the Balearic Islands and Ostwestfalen-Lippe University [Wrenger and Cuxart, 2017], the multicopter used samples temperature using a fast thermocouple supplemented with a Pt1000 resistance thermometer. Relative humidity is measured using a capacitive sensor, and its relatively slow response time is corrected assuming a linear response of the sensor with time Cuxart et al. [2016a]. These sensors are located at the end of a pole at 1 m from the rotors to minimize the downwash effect of the measurements.

The multicopter measurements reach a maximum heights of 150 m agl but it cannot operate under strong wind conditions, as for the BOU. Instead, it reaches lower heights. The temporal interval between two consecutive soundings depends on the duration of the batteries and how long their charging takes.

Multicopter data are processed like the balloon data, and vertical profiles at 1 m resolution are obtained. When there are simultaneous profiles, we can compare the sensors of both systems. In this case, we can check if measurements taken from the two equipments are consistent.

In this thesis the multicopter has been used in the study of morning transition case between the Land and the Sea-Breeze (Chapter 6), in the campaigns of the Hungarian Pannonian (Chapter 7) and in the campaigns of the Cerdanya Valley (Chapter 7).

2.1.2.2 Land Surface Temperatures

The other UAV has assembled a TIR (Thermal InfraRed) camera (figure 5.4a) in order to reproduce a LST map of a heterogeneous area of 1 km x 1 km size (UIB Campus), at high spatial resolution (2 m x 2 m) when it flows at a height of 100 m above the ground. The TIR used is FLIR LEPTON Long Wave Infrared. Its FOV is 51° and 63.5° in the horizontal and diagonal views, which produces a TIR scene of 80 (horizontal) x 60 (vertical) active pixels in each camera shot, respectively. Figure 5.4b shows the spectral response of the FLIR LEPTON TIR camera between 6-15 μm.

After converting the digital numbers measured by the TIR camera into radiance (L_{FLIR}) accordingly to manufacturer indications, we obtain a LST map. The duration of the flicht is about 100 m to cover the UIB Campus. L_{FLIR} is a composition of different radiance terms, as we will see in Chapter 5. The atmospheric terms were obtained from introducing the NCEP (National Centers for Environmental Prediction) synthetic profile [Barsi et al., 2005], limited between geopotential heights of 0.08 km (altitude of UIB campus) and 0.28 km (height a.s.l. of UAV flight), into the MODTRAN code (MODerate resolution atmospheric TRANsmission). The broadband emissivity was considered as a unique constant value of 0.964 ± 0.015, for all pixels of the UIB Campus. The five different ε_i (i= ASTER channels 10-14) values of the ASTER GED, upscaled at 1 km^2 resolution [Hulley et al., 2015], were used to retrieve a constant value according to broadband emissivity expression proposed by Cheng et al. [2013]:

$$\varepsilon_{UAV} = 0.197 + 0.025\varepsilon_{10} + 0.057\varepsilon_{11} + 0.237\varepsilon_{12} + 0.333\varepsilon_{13} + 0.146\varepsilon_{14} \qquad (2.1)$$

We calibrated the TIR camera in the laboratory against reference LANDCAL P80P blackbody, and shows a RMSE (Root Mean Square Error) on retrieved TIR camera data of ±2 °C. This error together with the error associated to synthetic atmospheric profiles of ±2 °C in air temperature and ±2 % in relative humidity [Barsi et al., 2005], associated errors to synthetic atmospheric profiles are ±2 °C induced a corresponding average uncertainty in atmospheric parameters. These uncertainties with emissivity error of ± 0.015 and TIR camera temperature calibration uncertainty, established a total uncertainty on the LST retrieved from the UAV-TIR camera of ±3 °C.

The UAV-TIR multicopter, has been used in Chapter 5 to build a LST map of the UIB Campus. The multicopter emulates a satellite, with the advantage that with this we have a better spatial resolution (lower than 5 m) and we can make transects whenever we want, even in cloudy conditions.

2.2 Meteorological satellites

Meteorological satellites provide scenes (if clouds are not present) over a region or the entire Earth, depending on the type of sensors onboard and the height of the orbit. Each satellite has a different temporal and spatial resolution. Depending on the objective of the work we will use satellites with high spatial or temporal resolutions. These characteristics are inverse, if a satellite has a better temporal resolution, it will have a worse spatial resolution and vice versa. When the satellite passes faster over a region, it can not measure it in so much detail. Instead when it measures with high detail,

it takes longer to cover the region of interest. Depending on the spatial resolution of the satellites we use and the scale of the heterogeneities that exist at the study site, the satellites will be able to measure or distinguish them. Instead, satellite products will not capture the variability of the region, taking it as homogeneous and resulting in erroneous values of the satellite derived fields used.

In many studies scenes from MSG (Meteosat Second Generation) satellite are used. MSG has a geostationary orbit that allows us a good temporal resolution but a very low spatial resolution. Since the area of the studied regions is smaller than the size of the pixel of MSG, these scenes are not taking in this thesis. The satellites used are Landsat 7-ETM+, MODIS and ASTER, because they are: (i) easy to access, (ii) provide us with scenes for free and (iii) have appropriate spatial and temporal scans for our case studies. These satellites are used to obtain LST of the study area.

2.2.1 Landsat 7-ETM+

The satellite Landsat 7-ETM+ was launched into space on April 15, 1999, it forms part of Landsat satellites that began with the launching of Landsat 1 in 1972. This group of satellites has made it possible to have the longest serie of scenes from satellites of terrestrial observation, in which they have been able to follow the changes that happened in the surface of the Earth since then. The Landsat program is jointly run by NASA and the USGS in the United States.

It has a heliosynchronous polar orbit, which is completed in about 99 min, allowing the satellite to make fourteen rounds on Earth per day and they cover the entire planet in 16 days. However, there are locations where the temporal resolution varies between 7–9 days, because there are placed between the passage of two different orbits of Landsat 7-ETM+ (Figure 2.2a). This satellite has on board a ETM+ (Enhanced Thematic Mapper Plus), that measures the radiance in eight spectral bands (Table 2.1) ranging from the visible spectrum (blue, green and red) to TIR, passing by SWIR (Shortwave Infrared) range with a spatial resolution of 30 m (disaggregated from 60 m by the Landsat Team in the case of the TIR band). It also has a panchromatic band at 15 m spatial resolution. A failure in the Scan Line Corrector (SLC-off mode) occurred in 2003 and has affected, since that year, the scenes of the Landsat 7-ETM+, generating void-data bands of a width near 100 m every kilometre. Besides these and other short-term problems related with the scanning system, Ladsat 7-ETM+ has been used because of its gratuity and easy access. On the other hand, Landsat 8, which is the last in the Landat series, has not been used, because it has a problem in the TIR band and it was not solved at the time of using these fields to study the heterogeneities.

Band	Spectral Band	Wavelength (μm)	Resolution (m)
1	Blue	0.441–0.514	30
2	Green	0.519–0.601	30
3	Red	0.631–0.692	30
4	NIR	0.772–0.898	30
5	SWIR-1	1.547–1.749	30
6	TIR	10.31–12.36	60
7	SWIR-2	2.064–2.345	30
8	Panc	0.515–0.896	15

TABLE 2.1: Spectral bands of Landsat 7-ETM+. Blue, green and red refer to the visible light (VIS), NIR refers to Near InfraRed, SWIR-1 and SWIR-2 refer to Shortwave InfraRed, TIR refers to Thermal InfraRed and Panc refers to Panchromatic. The spatial resolution for each band is also included.

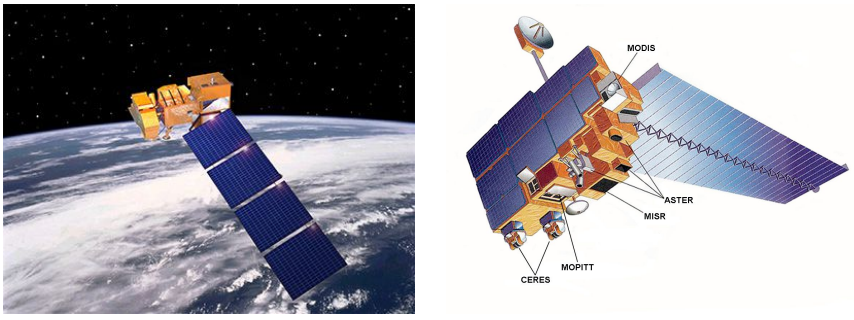

FIGURE 2.2: **(a)** Image of Landsat 7-ETM+, source: NASA. **(b)** Image of TERRA satellite with its sensors: MODIS, ASTER, MISR, MOPITT and CERES. Source: NASA.

Many studies have been done using the Landsat 7-ETM+ LST product (i.e. Coll et al. [2010], Li et al. [2004], Mallick et al. [2008], Walawender et al. [2014], Weng et al. [2004, 2014]), and we have used Land Surface Temperature scenes from Landsat 7-ETM+ in Chapter 3 (where it is explained how these scenes were obtained) and Chapter 5.

2.2.2 MODIS

The MODIS-Terra satellite was launched in 1999, and, since then, it has provided global coverage, offering twice-daily LST and emissivity products generated from three different algorithms.

MODIS (Moderate Resolution Imaging Spectroradiometer) has a polar orbit with a viewing swath width of 2330 km and views the entire surface of the Earth every one to two days. Its detectors measure 36 spectral bands between 0.405 and 14.385 μm, and it acquires data at three spatial resolutions – 250m, 500m and 1000m (Figure 2.2).

MODIS products are useful to study certain processes (i.e. Coll et al. [2005, 2016], Mildrexler et al. [2011], Niclos et al. [2014], Shamir and Georgakakos [2014], Vancutsem et al.

Band nr.	Bandwidth (nm)	Spectral domain	Spatial res. (m)
1	620 – 670	Shortwave / VIS	250
2	841 – 876	Shortwave / NIR	250
3	459 – 479	Shortwave / VIS	500
4	545 – 565	Shortwave / VIS	500
5	1230 - 1250	Shortwave / NIR	500
6	1628 - 1652	Shortwave infrared/ SWIR	500
7	2105 - 2155	Shortwave infrared/ SWIR	1000
8	405 - 420	Shortwave / VIS	1000
9	438 - 448	Shortwave / VIS	1000
10	483 - 493	Shortwave / VIS	1000
11	526 - 536	Shortwave / VIS	1000
12	546 - 556	Shortwave / VIS	1000
13	662 - 672	Shortwave / VIS	1000
14	673 - 683	Shortwave / VIS	1000
15	743 - 753	Shortwave / VIS	1000
16	862 - 877	Shortwave / NIR	1000
17	890 - 920	Shortwave / NIR	1000
18	931 - 941	Shortwave / NIR	1000
19	915 - 965	Shortwave / NIR	1000
20	3660 – 3840	Longwave thermal infrared/ TIR	1000
21	3929 – 3989	Longwave thermal infrared/ TIR	1000
22	3929 - 3989	Longwave thermal infrared/ TIR	1000
23	4020 – 4080	Longwave thermal infrared/ TIR	1000
24	4433 – 4498	Longwave thermal infrared/ TIR	1000
25	4482 – 4549	Longwave thermal infrared/ TIR	1000
26	1360 – 1390	Shortwave / NIR	1000
27	6535 - 6895	Longwave thermal infrared/ TIR	1000
28	7175 - 7475	Longwave thermal infrared/ TIR	1000
29	8400 - 8700	Longwave thermal infrared/ TIR	1000
30	9580 - 9880	Longwave thermal infrared/ TIR	1000
31	10780 - 11280	Longwave thermal infrared/ TIR	1000
32	11770 - 12270	Longwave thermal infrared/ TIR	1000
33	13185 - 13485	Longwave thermal infrared/ TIR	1000
34	13485 - 13785	Longwave thermal infrared/ TIR	1000
35	13785 - 14085	Longwave thermal infrared/ TIR	1000
36	14085 - 14385	Longwave thermal infrared/ TIR	1000

TABLE 2.2: Spectral Bands from MODIS. VIS refers to the visible light, SWIR refers to Shortwave InfraRed, NIR refers to Near InfraRed and TIR refers to Thermal InfraRed. Source: H. Eerens.

[2010], Wan et al. [2004], Williamson et al. [2014], Zhang et al. [2014]) and to validate model outputs (i.e. Benedetti and Janisková [2008], Conangla et al. [2018], Cuxart and Jiménez [2012], Cuxart et al. [2016b], Fréville et al. [2014], Jiménez and Cuxart [2014], Jiménez et al. [2008], Otkin and Greenwald [2008], Powers [2007]). Processed products can be downloaded directly from a web server (https://search.earthdata.nasa.gov/), and free of charge. We have used Land Surface Temperature products from MODIS. In Chapter 3 we explain how these scenes were obtained. LST products from MODIS that have been used are MOD11 and MOD21. MOD11 data are obtained using split-window algorithm (emissivities in bands 31 and 32 are estimated from land cover types, atmospheric column water vapour and lower boundary air surface temperature are separated into tractable sub-ranges for optimal retrieval) and at 6 km grids by the day/night algorithm (LST and surface emissivities are retrieved from pairs observations in seven TIR bands). Data from MOD21 are computed with a physics-based algorithm to dynamically retrieve the LST and emissivity simultaneously for the TIR bands. It is based in the TES method (Temperature Emissivity Separation) which is used for: (i) the atmospheric correction, (ii) the radiative transfer simulations and (iii) an emissivity model based on the variability in the surface radiance data to dynamically retrieve both LST and spectral emissivity.

2.2.3 ASTER

The Advanced Spaceborne Thermal Emission and Reflection Radiometer (ASTER) is an imaging instrument onboard Terra, the flagship satellite of NASA's Earth Observing System (EOS) launched in December 1999. ASTER is a cooperative effort between NASA, Japan's Ministry of Economy, Trade and Industry (METI) and Japan Space Systems (J-spacesystems). ASTER data are used to create detailed maps of Land Surface Temperature, reflectance and elevation. The coordinated system of EOS satellites, including Terra, is a major component of NASA's Science Mission Directorate and the Earth Science Division. The goal of NASA Earth Science is to develop a scientific understanding of the Earth as an integrated system, its response to change, and to better predict variability and trends in climate, weather, and natural hazards.

ASTER (Figure 2.2b) uses five TIR bands to measure the Earth emittance within the 8-13 μm range, offering a LST and Emissivity (ε) product at 90 m x 90 m spatial resolutions every 16 days, after applying the semi-empirical Temperature and Emissivity Separation (TES, Gillespie et al. [1998]) method. Uncertainties associated to LST and after the TES method are 1.5 °C for LST and 0.015 for emissivity. Retrieval of ASTER LST from TES shows inaccurate estimates over surfaces with low emissivity spectral contrast or under humid atmospheric conditions [Coll et al., 2007]. To minimize LST

errors associated to atmospheric correction [Tonooka, 2005] proposed a Water vapour Scaling (WVS) method which improves the accuracy of the water vapour atmospheric profiles on a band-by-band basis for each observation. Implementing both WVS and TES methods showed a significant improvement in the retrieved LST [Coll et al., 2016, Malakar and Hulley, 2016].

Furthermore, it is possible to extract the surface emissivity from the ASTER Global Emissivity Database (GED) (Hulley et al. [2015]). This database offers surface emissivity values at 100 m^2 spatial resolution for the five TIR channels of the ASTER sensor (Yamaguchi et al. [1998]) after applying the Temperature and Emissivity Separation method (Gillespie et al. [1998]) to the ASTER data from 2000 to 2008.

We have used the emissivity product from ASTER in Chapter 3 in order to know the emissivity map of the UIB Campus. Moreover, we have used its LST product in Chapter 5 that provides us Land Surface Temperature values on a smaller scale than MODIS.

2.3 Meteorological models. The Meso-NH model

Meteorological models are used in this thesis to complement the information reported from the observations and to further analyse the studied processes. The rapid increase in computational resources during the last decade has contributed significantly to the improvement and development of different types of meteorological and climate atmospheric models. For instance, spatial resolutions have increased as well as the physical processes included in the models.

Mesoscale models are often run at horizontal resolutions of the order of 1 km and vertical resolutions ranging from 1 m to 10 m. These models, use parametrizations in order to include processes that are smaller than the model resolution or that are too complex to be physically represented by the equations to solve, although there are settings that can not always be applied.

The Meso-NH model[1] [Lafore et al., 1998] is the non-hydrostatic mesoscale atmospheric model of the French research community. It has been jointly developed by the Laboratoire d'Aérologie and by Centre National de Recherches Mtorologiques (Meteo Frace). This model has been used in many studies [Cuxart and Jiménez, 2007, 2012, Cuxart et al., 2000, 2007, Jiménez and Cuxart, 2005, Jiménez et al., 2008, Martínez et al., 2010]. It incorporates a non-hydrostatic system of equations, for dealing with scales ranging from large (synoptic) to small (large eddy) scales. It also has a complete set of physical parametrizations (see Table 1 Cuxart et al. [2014]). It is coupled to the surface

[1]The information of this model has been obtained from http://mesonh.aero.obs-mip.fr

model SURFEX for the representation of surface atmosphere interactions by considering different surface types (vegetation, city, ocean, lake). Furthermore, Meso-NH allows a multi-scale approach through a grid-nesting technique. It is a versatile code, vectorized, parallelized, operating in 1D, 2D or 3D designed to handle real situations as well as ideal cases. The model has observation operators that compare model output directly with satellite observations, radar, lidar and GPS.

We use the Meso-NH model to know what is happening in areas where there are not meteorological stations and/or to know magnitudes that we do not measure. Their results are used to better understand the processes that take place in the atmosphere-soil interface. When there are available measurements, we use them to validate and verify that the model works well, since sometimes models depart significantly from the observations. Models are validated with in situ data comparing them point-to-point.

2.4 Instrumentation and sensors

In addition to data from satellites or models, in situ measurements are needed, to validate and verify the results from models and satellites. Surface stations are used in fixed sites or campaigns of a duration which may vary between several days or some months.

Automatic weather stations are usually far from where we want to measure. Very often observations made by meteorological services are wind, temperature, relative humidity at 10 meters or 2 meter every 10 minutes or 1 hour and covering a large temporal interval (several years with homogeneous records). In Spain data from the State Meteorological Agency (AEMET) are available. Therefore, the best way to study a phenomenon is to set up our own stations in the place of interest, as long as we want, with the instruments that are needed and even choosing freely the time sampling required to perform the study. For instance to sample the changes that take place at small-time scales (turbulence) high-frequency observations are needed (sampling rate of about 20 measures every 1 s, 20 Hz) to compute the fluxes. Instead, they cannot be computed from most of the meteorological services networks due to the coarser sampling rate (1 Hz or lower).

Usually, campaigns are carried out when there is a subject of study in a specific location. These are planned in advance, so to perform them in the moments that take place the phenomena that interest us. They can have a duration that varies between a couple of days and several months, to measure the physical processes of interest and to guarantee that the weather conditions will be optimal (for instance, no rain or no clouds). In the campaigns several meteorological measurement stations are installed, (Chapters 5, 6 and 7) that provide us with high-frequency measurements to measure the fluxes at several

levels and covering different regions. In addition, methods are available to measure vertical changes, such as the captive balloon, the multicopter and the drone.

2.4.1 Automatic surface station

An automatic station providing air temperature, relative humidity, wind speed and wind direction, was used in the campaigns. It consists on a 2D Sonic Anemometer (WindSonic) located at 2 meters, that is an ultrasonic anemometer for measuring wind speed and wind direction. Alongside this, there is a temperature and RH sensor (HC2S3). The probe uses a Rotronic's IN1 capacitive sensor to measure RH and a 100 ohm PRT (Platinum Resistance Thermometer) to measure the temperature. In some campaigns, several of these sensors were available at different heights. In the Sea-Breeze campaign (Chapter 6) only one at 2 m was available, in the energy balance station located in the ECUIB (Chapters 3 and 4) there are 2 levels (2 m and 0.20 m) and in the Poles used in the Subpixel Campaign (Chapter 5) there were 3 levels (2 m, 1 m and 0.20 m). There is also a thermistor 107 buried on the ground in order to know the soil temperature. This thermistor is encapsulated in an exposy-filled aluminium housing. Its operation is based on the variation of resistivity that a semiconductor shows with the temperature variation.

This is a portable station that has been installed in the areas of interest during the campaigns. With this system we have measurements every minute from air temperature, relative humidity, soil temperature, wind speed and wind direction. Data obtained from this station have higher frequency than those provided by the AEMET stations. Due to this higher frequency, it allows us to detect changes that occur with small durations and related to turbulence. Comparing these observations with other sources of data, it also allows us to estimate the averages and errors. In some campaigns, several of these sensors are located at different heights or depths.

One of the automatic surface station is permanently installed at the Campus of the University of the Balearic Islands (ECUIB). It was installed at the beginning of 2015, and which allows us to analyse longer time series than during the campaigns.

2.4.2 Surface energy balance station

Next to the automatic station that is located on the UIB Campus, there is a surface energy balance station that measures the fluxes. It is formed by an ultrasonic anemometer RMY 81000 for measuring wind speed in three dimensions (3D). It uses three pairs of

non-orthogonally oriented transducers to sense the horizontal wind. Each pair of transducers transmits and receives the ultrasonic signal. The time of flight is directly related to the wind speed along the sonic transducer axis. The speed of sound is directly related of the air density, like temperature and humidity. RMY 81000 can be used to measure average horizontal wind speed and direction or turbulent fluctuations of horizontal and vertical wind. From the turbulent wind fluctuations, momentum flux is calculated. The wind speeds are then transformed into the orthogonal wind components u_x, u_y, u_z and are referenced to the anemometer head; the reported speed of sound (c) or sonic virtual temperature (T_s), is the average between the three non-orthogonal sonic axes.

On the other hand, there is also has a gas analyser sensor (EC150) for fast measurements of CO_2 and H_2O. EC150 is an in situ, open-path, mid-infrared absorption gas analyser that measures the absolute densities of carbon dioxide and water vapour. The EC150 is a non-dispersive mid-infrared absorption analyser. Infrared radiation is generated in the upper arm of the analyser head before propagating along a 15.0 cm optical path. Chemical species located within the optical beam will absorb radiation at characteristic frequencies. A Mercury Cadmium Telluride (MCT) detector in the lower arm of the gas analyser measures the decrease in radiation intensity due to absorption, which can then be related to analyse concentration using the Beer-Lambert Law.

In this station there is also a Soil Heat Flux plate (HFP01) which measures the soil heat flux in the ground. This sensor uses a thermopile to measure temperature gradients across its plate. Operating in a completely passive way, it generates a small output voltage that is proportional to this differential temperature. Assuming that the heat flux is steady, that the thermal conductivity of the body is constant, and that the sensor has negligible influence on the thermal flux pattern, the signal of the instrument is directly proportional to the local heat flux.

The heat flux plate it is installed under the soil, and not directly at the soil surface for mainly two reasons according to the manufacturer of Hukseflux: (i) mounting at the surface would distort the flow of moisture, and the measured flux would no longer be representative for the flux in the surrounding soil; (ii) the absorption of solar radiation would not be representative and the sensor would be more vulnerable. Therefore, heat flux sensors in meteorological applications are typically buried at a depth of at least 0.05 m below the soil surface. The ground heat flux at the surface is usually estimated from the flux measured by the heat flux sensor plus the change of the energy stored in the layer above the sensor during the measuring interval t_1 to t_2. Applying the principle of conservation of energy it can be obtained:

$$\rho c \frac{\partial T}{\partial t} = -\nabla G \simeq \frac{\partial G}{\partial z} \tag{2.2}$$

where ρ and c represent the density and specific heat capacity per unit mass, respectively.

If Equation (2.2) is integrated between the ground (z=0) and the reference level z_r (where the heat flux plate is located), it can be obtained:

$$G_0 = G_r + \int_0^{z_r} \rho c \frac{\partial T}{\partial t} dz \tag{2.3}$$

where G_0 and G_r represent the soil heat flux at the surface and at level z_r, respectively. With these instruments, measurements are available to calculate the terms of the surface energy balance: net radiation, sensible heat flux, latent heat flux and soil heat flux.

2.4.3 Radiation measurements

The radiation components are sampled with the 4-component net radiometer sensor from Hukseflux (NR01). The radiometer of four components has separate measurements of solar (Short Wave or SW) and Far Infra-Red (Long Wave or LW) radiation using 2 sensors facing up to the sky and facing down to the ground. An optimal position is 1.5 m from the ground, keep in mind that does not affect any shade or object to its field of view. The solar radiation sensors are called pyranometers and the longwave sensors are called pyrgeometers. It provides the measurements of four main components besides the net radiation and the sky and LST.

Another sensor to measure the surface temperature is the IR120 radiometer from Campbell Scientific. This is an infra-red remote temperature sensor composed of a thermistor and a thermopile. The thermopile is a transducer formed by the union of two different metals that produces a very small potential difference that is a function of temperature. In this way, it gives us the average temperature of the surface to which it is focusing.

The main differences to measure LST between both sensors are that NR01 net radiometer measures in the spectral range 4.5- 50.0 μm and with a FOV of 150°, while IR120 has a smaller spectral range of 8-14 μm and a narrower FOV of 40°. Also NR01 is much more expensive than IR120, although it has the advantage that the provides the downwelling longwave radiation directly and in the case of IR120 we must estimate it.

Net radiation can be measured with the radiometer of four components that provides values of shortwave radiation reaching ($S\downarrow$) and reflected ($S\uparrow$) by the surface and long wave emitted by the surface ($L\uparrow$) and coming from sky ($L\downarrow$). Following the Equation (1.5), net radiation can be obtained.

In order to obtain LST, the measured upwelling longwave radiation $L\uparrow$ must be corrected from the reflected downwelling contribution $L\downarrow$, following the expression:

$$LST = \left[\frac{L\uparrow - (1-\varepsilon) L\downarrow)}{\varepsilon \cdot \sigma} \right]^{1/4}, \tag{2.4}$$

where ε is the surface broadband emissivity, $\sigma = 5.67 \times 10^{-8}$ W $\cdot$ m^{-2} $\cdot$ K^{-4} represents the Stefan–Boltzmann constant, L↑ and L↓ are in W·m^{-2} and LST in K.

2.4.4 Soil measurements

In addition to the T107 thermistor installed in the automatic station and the soil heat flux sensor installed in the surface energy balance station, other sensors are also available to measure other surface and ground characteristics. The dielectric leaf wetness sensor (LWS) that measures the dielectric constant of the upper surface of the sensor and is able to detect the presence of water or ice on its surface. It was located at 1 cm above the surface, to allow determining the presence and duration of the wetting on the surface of the leaves. In this way, we know if the water vapour has condensed near the surface.

There is a soil water content reflectometer CS650 measuring volumetric water content, temperature, electrical conductivity and dielectric permittivity. Volumetric water content information is derived from the sensitivity of the probes to the dielectric permittivity of the medium surrounding the probe stainless-steel rods. The CS650 is configured as a water content reflectometer, with the two parallel rods forming an open-ended transmission line. A differential oscillator circuit is connected to the rods, with an oscillator state change triggered by the return of a reflected signal from one of the rods. The two-way travel time of the electromagnetic waves that are induced by the oscillator on the rod varies with changing dielectric permittivity. Water is the main contributor to the bulk dielectric permittivity of the soil or porous media, so the travel time of the reflected wave increases with increasing water content and decreases with decreasing water content, hence the name water content reflectometer. Electrical conductivity is determined by exciting the rods with a known non polarizing waveform and measuring the signal attenuation.

All these sensors, (T107, Soil heat flux sensor, LWS sensor and CS650) allow us to characterize the soil, knowing the temperature at different levels, the heat flux, the permittivity and humidity of the soil.

2.5 Measuring the Surface Layer

These instruments and sensors have been used in several field campaigns in which I participated: (i) MSB13 and MSB14 conducted in the south of Mallorca to study the Sea-Breeze in a heterogeneous area on a kilometric scale [Jiménez et al., 2016]; (ii) PABLS13 and PABLS15 that took place in Szeged, in southern Hungary, a practically homogeneous area in which the characteristics in the diurnal cycle of ABL and its interaction with the underlying surface was studied; (iii) CCP15 and CCP16 that took place in the Cerdanya valley, eastern Pyrenees, an area with topographical heterogeneities in which the formation of Cold-Pools among others was studied [Conangla et al., 2018]; (iv) Subpixel Campaign in the summer 2016 that took place in the Campus of the University of the Balearic Islands in order to study the effects of the surface heterogeneities at hectometer scale [Simó et al., 2016]. These campaigns will be explained in more detail throughout the thesis.

In addition to these stations, during the Subpixel Campaign (Chapter 5) 9 autonomous Poles were designed and locally assembled: including the structure of the Poles, the choice of sensors and the data acquisition system. This network of Poles was intended to measure the following relevant variables: temperature and RH at three levels, wind, volumetric water content and soil temperature in the different types of soil at the Campus of the University of the Balearic Islands, as an example of locally heterogeneous area.

The structure of the Pole (Figure 2.3) is made of three PVC (PolyVinyl Chloride) cylinders making a tripod, on the top of which a two-dimensional Gill windsonic is installed at 2 m above ground level (agl). A PVC arm is mounted at 2 m agl in which an HyT temperature and humidity sensor is inside a shelter consisting in a double PVC cylinder covered in aluminium paper and with holes in the bottom. This shelter has been successfully tested comparing it with the traditional one made of double surface small dishes in the ECUIB station (Figure 2.4). Temperature and relative humidity recorded by Pole 0 have been compared to the ones measured by HC2S3 sensor 2 m distant and the correlation coefficient and the RMSE for temperature are 0.9974 and 0.3 °C, respectively, while for humidity values differences lower than 5% are obtained according to statistics. In Figure 2.4 both temperatures can be seen for a cloudy and for a sunny day, and the small temperature difference between both sensors. Two more levels of air temperature and humidity are set at 1 m and 0.2 m agl, in order to study the vertical temperature profile. The upper soil water content and temperature is monitored using a Campbell CS655 water content reflectometer at 5 cm below the surface. The data acquisition system has been developed locally using Arduino micro-controllers and self-programmed boards, and the data were stored in a SD card. The system is powered by solar plates.

(a) **(b)**

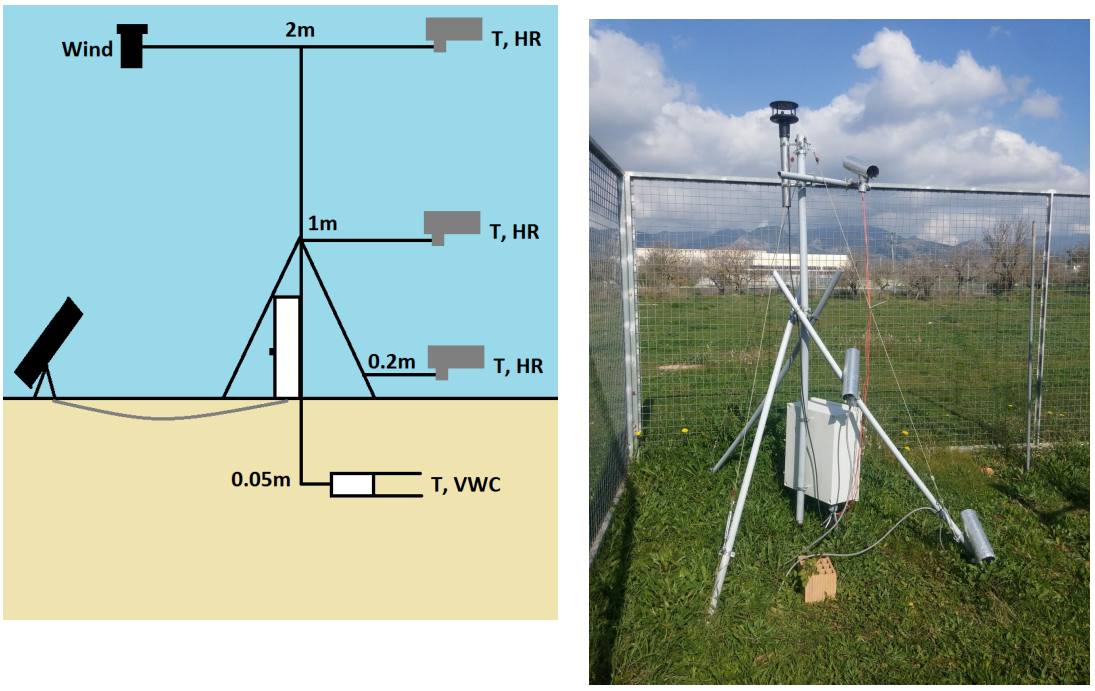

FIGURE 2.3: **(a)** Design of the Pole indicating the heights where the different sensors are located. **(a)** Photo of the Pole 0 located at the research station in the Campus of the University of the Balearic Islands (ECUIB).

To optimize the energy use and data storage, sensors were interrogated every 5 minutes but every minute in the case of the windsonic (from where 5 minutes averages are computed).

This network of Poles has been designed, in order to study the variability in all the different areas of the Campus which is a heterogeneous zone on a hectometric scale. In this way, we can see how the temperature, humidity, speed and direction of the wind, soil water content and soil temperature change in the horizontal and vertical, within an extension of 1 km x 1 km size.

2.6 Statistical analysis

Some statistical analysis are made along this thesis. Together with standard estimations, the mean value $\overline{x}$, the standard deviation σ, the Bias or RMSE, other quantities have been compared including the variances and covariances of the turbulence measurements.

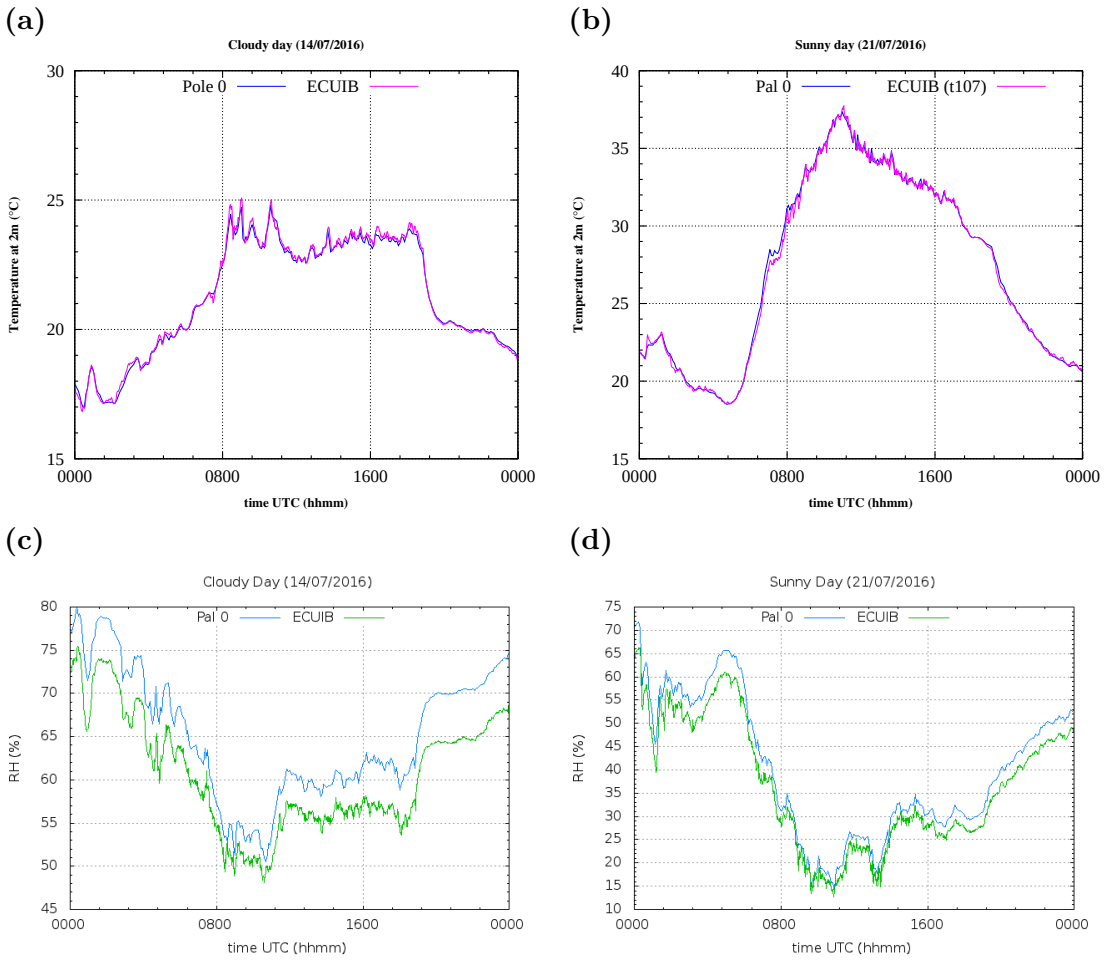

FIGURE 2.4: Comparison between air temperature of Pole 0 and ECUIB during a **(a)** cloudy day (14-15/07/2016) and **(b)** sunny day (21-22/07/2016).

On the other hand, probability density functions (PDF) have also been used. PDFs are calculated as follows:

$$\int_{-\infty}^{\infty} P(x)dx = 1. \tag{2.5}$$

where $P(x)dx$ is the probability of the variable x taking a value between x and $x + dx$.

In addition, as was done in [Jiménez and Cuxart, 2005], other statistical values can be obtained from the PDFs [Tennekes and Lumley, 1972]. Such as the mean (2.6), the standard deviation (2.7), the skweness (2.8) and the kurtosis (2.9).

The first moment $< x >$ is the mean:

$$\overline{x} = \int_{-\infty}^{\infty} xP(x)dx. \tag{2.6}$$

The second moment is the variance σ^2 from which the standard deviation can be obtained by making the square root:

$$\sigma_x^2 = \overline{x}^2 = \int_{-\infty}^{\infty} (x - \overline{x})^2 P(x) dx. \tag{2.7}$$

The third moment divided by σ^3 is the skewness. With the skewness could be know the asymmetry of the PDF, it can be positive, negative or zero. In a Gaussian distribution, the skewness is zero. It is obtained as follows:

$$S_x = \frac{\overline{x}^3}{\sigma_x^3} = \frac{1}{\sigma_x^3} \int_{-\infty}^{\infty} (x - \overline{x})^3 P(x) dx. \tag{2.8}$$

The fourth moment divided by σ^4 is the kurtosis. With the kurtosis we can analyse the degree of concentration of the values obtained through a given variable around the central area of the distributio, without generating the graph. In a Gaussian distribution, kurtosis has a value of 3. It is obtained as follows:

$$K_x = \frac{\overline{x}^4}{\sigma_x^4} = \frac{1}{\sigma_x^4} \int_{-\infty}^{\infty} (x - \overline{x})^4 P(x) dx. \tag{2.9}$$

Analysing the shape of the PDFs and the computed parameters it is possible to determine the spatial or temporal variability of LST. It is used in many studies as in those of Cuxart and Jiménez [2007], Jiménez and Cuxart [2006] for wind speed and potential temperature, Vich et al. [2007] for temperature and wind speed, Chernyshov et al. [2009] for velocity and magnetic field components or Cava et al. [2012] for the inter-pulse durations.

The turbulent parameters used in our study are estimated with the measurements taken with a sonic anemometer after applying the Eddy Correlation technique [Aubinet et al., 2012]. This sensor provides high-frequency time series of the three-dimensional wind (u, v, w) and the sonic temperature T_s. Since these measurements are based on the speed of sound, which depends on the air temperature and (to a lesser degree) humidity, the sonic temperature is very similar to the virtual temperature T_v [Foken, 2008b]. Therefore, the covariance of this variable with the vertical wind ($< w'T_s' >$) is equivalent to the kinematic flux of virtual temperature or buoyancy flux, which depends on the sensible and latent heat fluxes through the form [Schotanus et al., 1983]:

$$< w'T_s' > = < w'T' > + 0.51 < T >< w'q' > \tag{2.10}$$

where q and T represent the mixing ratio of water vapour and the actual air temperature, respectively. The calculation of variances and covariances for the wind components leads to the estimation of the Turbulent Kinetic Energy (TKE) and friction velocity ($u*$):

$$TKE =< u'^2 > + < v'^2 > + < w'^2 > \tag{2.11}$$

$$u* = (< u'w' >^2 + < v'w' >^2)^{1/4} \tag{2.12}$$

The turbulent parameters used in some Chapters of this thesis are obtained from these Equations.

The following summarizes which instruments are used in each chapter and for what purpose:

Chapter 3: in this chapter, we use the meteorological satellites Landsat 7-ETM+ and MODIS for LST measurements, ASTER for the emissivity measurements and the radiation measurements of LST from Hukseflux RN01. With these data, we have studied the variability of LST in a heterogeneous area with different spatial resolutions.

Chapter 4: in this chapter, we use the automatic surface station to obtain the variables T2, RH, WS, WD, the energy balance station to obtain TKE, <w'T_s'>, Rn, G, the radiation measurements to obtain LST_{NR01}, LST_{IR120}, and the soil measurements for ST, VWC. With these data, we have studied the variability of the temperature gradient in the surface layer and its relations with other magnitudes.

Chapter 5: in this chapter, we use a remotely piloted multicopter UAV-TIR to obtain the LST of the Campus, the meteorological satellites Landsat 7-ETM+, MODIS and ASTER to obtain LST at different resolutions, the automatic station and Poles to obtain the variables T2, RH, WS, WD, the surface energy balance station for the imbalance, the radiation measurements to obtain the LST_{NR01} and the soil measurements to obtain ST and VWC. With these data, we have studied the atmospheric and surface variability on heterogeneous terrain.

Chapter 6: in this chapter, we use a tethered balloon and a remotely piloted multicopter UAV-OWL to obtain the vertical profiles of temperature and humidity of the first hundreds of kilometres in the atmosphere, the meteorological model Meso-NH to obtain the atmospheric and surface variables anywhere in the mesh, and automatic station to obtain T2, RH, WS, WD and data from AEMET stations to study the thermal heterogeneities at kilometre scale.

Chapter 7: in this chapter, we use an automatic surface station to obtain T2, RH, WS, WD, the surface energy balance station to obtain the energy balance equation terms R_n, G, H, LE, the radiation measurements to obtain the LST and the soil measurements of ST in order to study the relation between LST and the energy balance equation terms.

These are all the instruments and methods used throughout this thesis with the purpose of studying how heterogeneities affect the circulations and the processes that occur in the atmosphere-soil interface at different scales. In the next Chapters, some of them are explained in more detail, adjusting to the needs and characteristics of the study area and the instruments available in each study.

Chapter 3

Study of LST variability in a heterogeneous terrain through satellite observations

In this Chapter[1] the variability of Land Surface Temperature in a heterogeneous terrain is analysed using satellite scenes. The aim of this work is to quantify the LST heterogeneities over a period of 2 years, in order to evaluate their annual cycle.

LST as provided by remote sensing onboard satellites is a key parameter for a number of applications in Earth System studies, such as numerical modelling or regional estimation of surface energy and water fluxes. In the case of MODIS onboard Terra or Aqua, pixels have resolutions near 1 km^2, where the LST values are actually an average of the real LST subpixel variability, which can be significant for heterogeneous terrains. MODIS products have been used even though they have lower spatial resolutions than other satellites, because most models use them, since they are accessible and validated. Furthermore, Landsat 7-ETM+ LST decametre-scale fields is used to evaluate the temporal and spatial variability at the kilometre scale and compare the resulting average values to those provided by MODIS for the same observation time, at the very heterogeneous Campus of the University of the Balearic Islands (Mallorca, Western Mediterranean), with an area of about 1 km^2 and for a period between 2014 and 2016. Variations of LST between 10 and 20 °C are often found at the sub-kilometre scale. In addition, MODIS values are compared to the ground truth for one point in the Campus, as obtained from a four-component net radiometer, and a BIAS of 3 °C and a RMSE of 4 °C were found.

[1]This Chapter is based on Simó et al. 2016: Landsat and Local Land Surface Temperatures in a Heterogeneous Terrain Compared to MODIS Values. *Remote Sensing* 2016, 8(10), 849; doi:10.3390/rs8100849

An indication of a more elaborated local measurement strategy in the Campus is given, using an array of radiometers distributed in the area.

3.1 Introduction

Land Surface Temperature is the radiative temperature of the most superficial part of the soil and vegetation of an element of the surface, sometimes also referred to as *the skin temperature of the surface* [Jin and Dickinson, 2010]. Temperature varies upwards significantly with height, being this effect more pronounced in the lowest layers of the atmosphere [Jin et al., 1997]. The same happens as the progressively deeper layers in the soil are explored [Popiel et al., 2001], with variations of contrary signs, with usually LST being the highest (lowest) value of the temperature profile in the daytime (nighttime). In applications, LST is usually taken as a boundary condition either for the atmosphere or for the soil, where the estimated surface fluxes are taken as the main drivers of the physical processes involved in the surface energy and water balances [Anderson et al., 2012, Kalma et al., 2008, Li et al., 2013, Sellers et al., 1997, Tierney et al., 2008]. An adequate spatial and temporal characterization of LST is needed to properly understand the contributions of the different terms in these surface budgets [Cuxart et al., 2016a].

Since this layer is in contact with two media at the same time (atmosphere and soil/vegetation), it is very difficult to make a meaningful measurement of the temperature using a thermometer [Betts et al., 1996]. Instead, LST is determined by measuring the amount of energy radiated by the surface, determined by a radiometer. Land and vegetation emit radiation in longwave form, and, therefore, LST is estimated by means of TIR sensors, using the Stefan–Boltzmann relation for a black body—modified with the emissivity of the surface—and substracting the downward longwave radiation reflected upwards. LST is currently determined from satellite or *in situ* radiometric measurements.

If LST is obtained from SL, which is a layer of air with a thickness of a few meters above the surface, there are a number of well identified issues that may influence LST measurements: (i) the very small scale heterogeneities [Cuxart et al., 2016b], implying that the radiometer receives radiation from elements of the surface radiating differently; (ii) the determination of the emissivity of the emitting surface, which strongly depends on the amount of water in the upper centimetres of the soil and the state of the vegetation, and, nonetheless; (iii) the possible high-concentration of atmospheric emitters between the radiometer and the surface, such as CO_2 and water vapour, especially on stable nights. The usual strategies are to sample homogeneous surfaces, to determine the emissivity of the sampled area and to measure the radiation emitted through a window partially transparent to CO_2 and to water vapour.

When a radiometer is onboard a satellite, the same limitations as if the sensor was in the SL exist, but their effect is severely amplified. Depending on the sensor and the height of the orbit, the resolution may vary between some decametres (as for Landsat 7-ETM+) and one to few kilometres (the case of MODIS onboard Aqua and Terra or SEVIRI onboard Meteosat Second Generation). It is clear that the surface heterogeneities at these scales will be very important depending on the type of surface, and the average value of the pixel may be significantly different from a point measurement on the ground.

A disadvantage for satellite-derived LST is that normally high spatial resolution (60 m for Landsat 7-ETM+ against 1000 m for Terra MODIS) involves low temporal frequency (several days for ETM+ against two per day for MODIS), so in situ measurements are needed to fulfill the spatial and temporal gaps of current orbiting TIR sensors. Most studies comparing satellite measurements and direct LST measurements occur in homogeneous areas (Coll et al. [2010, 2016], Ermida et al. [2014], Krishnan et al. [2015], Li et al. [2004], Niclòs et al. [2015], Zhou et al. [2014]; etc.). There are a few studies for heterogeneous areas, like the downscaling ones of Mukherjee et al. [2015], Wu et al. [2015] between MODIS and ETM+ sensors, or LST validation campaign of Krishnan et al. [2015], Weng et al. [2014], Yu and Ma [2015] where LST satellite data was compared with in situ measurements. It is usually concluded that errors are higher in heterogeneous areas than in homogeneous ones (a summary is shown in Table 3.1). All these validation works have demonstrated good operational performance of the three MODIS LST algorithms at different surface types with discrepancies respect to reference data of around 1 °C. However, the coarser spatial resolution of the MODIS TIR bands is not probably the most suitable for other research goals, which demand LST data at sub-kilometer resolution.

Emissivity may also vary largely along the pixel, especially depending on the distribution of water in the ground, the soil materials and the vegetation cover. Finally, since practically the whole atmosphere is between the emitting surface and the receiver, the correction of the longwave emission by the atmospheric compounds is compulsory.

To use LST values given by a sensor onboard a satellite, these must have gone through processes of validation and calibration that provide an estimation of the uncertainty of the value. This information is obtained primarily with ground-based data used for comparison, usually for ground homogeneous conditions. However, validation studies for heterogeneous terrains are more difficult [Jiménez et al., 2008] and they are more rarely found in the literature. Furthermore, the suitability of a point measurement for verification is in question in these conditions. It may well happen that the pixel-averaged value or the local measurement point are in fact not representative of the actual conditions governing the surface atmosphere exchanges over each of the subpixel tiles. This could

Sensor	Surface Type	Radiometer	RMSE (K)	BIAS (K)	Referenece
MODIS	Bare soil	**8–14 µm broadband (×1, handheld)**	1.1	–	Zhou et al. [2014]
	Shrubland	8–14 µm broadband (×1)	2.7	0.8	Niclòs et al. [2015]
	Rice crop		1.8	0.1	
	Oak woodlan	**8–14 µm broadband (×3)**	2.4 (3.2)	1.5 (2.7)	Ermida et al. [2014]
	Seed corn, roads and buildings	**8–14 µm broadband (×7)**	–	(15%) [53%] < 1 K (42%) > 3 K	Yu and Ma [2015]
		5–50 µm 4 component (×1)	–	(33%) [57%] < 1 K (15%) > 3 K	
	Rice crop	**multispectral (×4) 8–14 µm broadband (×2)**	0.6 *	0.1 *	Coll et al. [2016]
	Grassland and hardwood deciduous forest	**8–14 µm broadband (×3)**	2.8 (3.1)	0.6 (1.8)	Krishnan et al. [2015]
	Grassland, crops, asphalt, wet regions	5–50 µm 4 component (×1)	(4.2)	(3.2)	Simó et al. [2016]
ETM+	Rice crop	**multispectral (×3)**	(1.1)	0	Coll et al. [2010]
	Soybean and corn crops	**8–14 µm broadband (×12)**	(1.2)	–	Li et al. [2004]
	Grassland, crops, asphalt, wet regions	5–50 µm 4 component (×1)	(1.7)	(−0.5)	Simó et al. [2016]

TABLE 3.1: Root Mean Square Error (RMSE) and BIAS of the differences between the in situ measurements minus the satellite-derived LST (MOD11 from MODIS and ETM+ from Landsat 7-ETM+). The last rows for MODIS and ETM+ show results from this study. For each comparison, a brief description of the surface site and the radiometer type is given: bold in the *surface type* column refers to heterogeneous sites; ground measurements computed as an average from different point measurements are indicated in bold in the *radiometer* column and, in brackets, the number of devices used. Statistics are computed from both day and nighttime cases together. In brackets, the results are obtained only considering the daytime cases. (*) indicates that the statistics refer to the robust RMSE and Median, providing very similar results to the corresponding RMSE and BIAS according to Coll et al. [2016]. The study from Yu and Ma [2015] shows the percentage of cases that fall into different absolute BIAS ranges, distinguishing nighttime results in square brackets.

be important since it would provide inadequate values of surface temperature or sensible and latent energy fluxes for numerical models or agricultural applications Jiménez et al. [2015].

In this Chapter, the average values for the MODIS pixel centered on the Campus of the University of the Balearic Islands, very heterogeneous, will be compared to the averaged values computed from available Landsat 7-ETM+ scenes (one every seven to nine days), at 30 m resolution (disaggregated from 60 m by the Landsat Team) for a period of 2.5 years. The representativity of the MODIS average value will be assessed, and an estimation of the subpixel variability provided. Furthermore, the radiometric data obtained at one spot of the Campus will be compared to the MODIS value and to the corresponding Landsat 7-ETM+ pixel, allowing assess to the possible discrepancies made in the validation results when taking these three quantities as equivalent.

3.2 Description of the site and tools

The study site is placed in Mallorca (Figure 3.1a), the largest of the Balearic Islands, located in the Western Mediterranean Sea, 200 km East of the Iberian Peninsula. The Campus of the University of the Balearic Islands (UIB, indicated in Figure 3.1b) has been taken in this study as an example of heterogeneous area. It is located in the west of the island, in the Palma basin, at the foothills of the Northern mountain range (Serra de Tramuntana). The UIB Campus has an approximate area of 1 km^2 with heterogeneous terrain composed of many different types of surfaces such as buildings, asphalted roads, terrain slopes, farmed areas with green vegetables or orange and almond trees, wet grass, drier extensions, etc. (Figure 3.1c). Previous studies [Cuxart et al., 2007, 2014] showed that during high-pressure gradient and clear sky conditions, locally generated winds are present in Mallorca and especially in the three main basins. This is the case for the diurnal Sea-Breeze (especially from April to October) or the nocturnal Land-Breeze which is often coupled with downslope winds.

A complete surface energy budget station (yellow dot in Figure 3.1c), operating at the UIB Campus since January 2015, is used in this study as a ground reference value of LST measurement for satellite validation purposes. In addition, a total of nine different points were selected inside the UIB Campus as representative of the different type of surfaces mentioned above (see red dots in Figure 3.1c). Designated points 1, 3, 4, and 9 are in the midst of almond trees, orange trees, carob trees and fields of different crops, respectively. These reference points are representative of the fields that are also surrounding the Campus. Points 2 and 5 are over a gully usually with wet soil, the latter next to a pond. Points 6 and 8 are surrounded by buildings and point 7 is in a parking lot.

LST fields used in this study are taken from two types of sensors: (i) MODIS (Moderate Resolution Imaging Spectroradiometer) onboard the Terra and Aqua platforms and (ii) ETM+ (Enhanced Tematic Mapper plus) onboard the Landsat 7 platform. These satellites have been chosen because of the availability of the scenes (free and easy to access) and especially because both cover our study site at two different spatial and temporal resolutions. Images for clear sky days from 1 January 2014 to 1 June 2016 over the Campus area are taken in the analysis.

3.2.1 Landsat 7-ETM+ Land-Surface Temperatures

Landsat 7-ETM+ has a heliosynchronous polar orbit, which is completed in about 99 min, allowing the satellite to make fourteen rounds on Earth per day and cover the

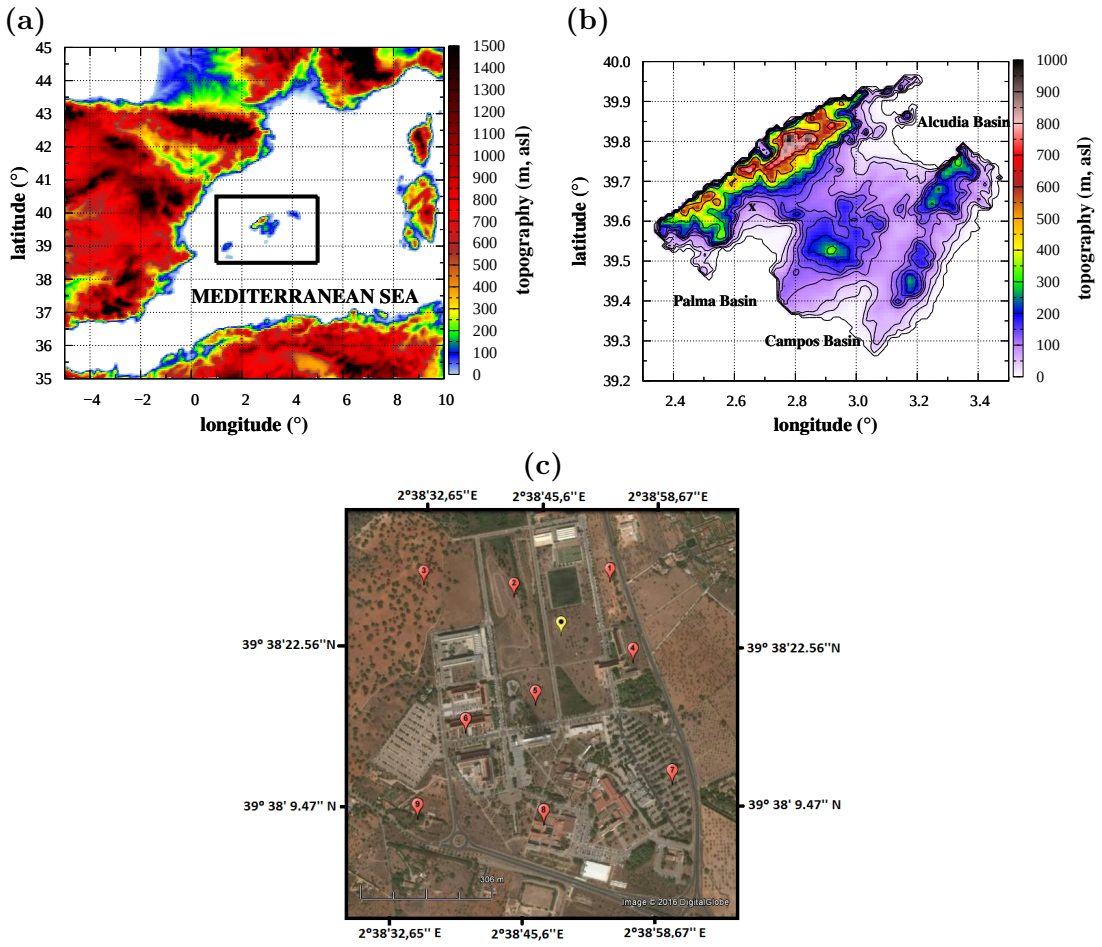

FIGURE 3.1: (**a**) location and (**b**) topography of the island of Mallorca (Balearic Islands, Western Mediterranean Sea) with the location of the Campus of the UIB and in (**c**) a zoom over it. The **yellow** dot indicates the location of the complete surface energy balance station and the **red** dots other locations that are further explored in this Chapter.

entire planet in 16 days. Due to the location of the island of Mallorca, Landsat 7-ETM+ passes over it every 7–9 days at approximately at 1030 UTC because the island is placed between the passage of two different orbits of Landsat 7-ETM+. Therefore, we get a higher temporal resolution in the study area than in other regions. ETM+ measures the radiance in eight spectral bands ranging from the visible spectrum to TIR range with a spatial resolution of 30 m (disaggregated from 60 m by the Landsat Team in the case of the TIR band). It also has a panchromatic band at 15 m spatial resolution. A failure in the Scan Line Corrector (SLC-off mode) occurred in 2003 and has affected, since that year, the scenes of the Landsat 7-ETM+, generating void-data bands of a width near 100 m every kilometre.

Retrieval of LST from Landsat 7-ETM+ is based on the single-channel method [Hook et al., 1992], which corrects the Top of Atmosphere (TOA) spectral radiance measurements performed by the ETM+ at band 6 (10–12 μm), from atmospheric attenuation

and surface emission. LST variable is cleared from the Radiative Transfer Equation (RTE) in Equation (3.1)

$$L_{TOA,i} = [\varepsilon_i B_i(LST) - (1-\varepsilon_i)L^{\downarrow}_{hem,i}]\tau_i + L^{\uparrow}_{atm,i}, \tag{3.1}$$

where $L_{TOA,i}$ (in W·sr^{-1}·m^{-2}·μm^{-1}) is the TOA radiance measured by the ETM+ sensor, ε_i is the surface emissivity, $B_i(LST)$ is the Planck function of a blackbody emitting at the surface temperature (LST) and $L^{\downarrow}_{hem,i}$, τ_i and $L^{\uparrow}_{atm,i}$ are the atmospheric parameters corresponding to hemispherical downwelling radiance, atmosphere transmissivity and upwelling radiance, respectively. Subscript *i* refers to the channel-effective quantity of each parameter in the RTE (e.g., band 6 (10–12 μm) of the ETM+ in this case).

$L_{TOA,i}$ in Equation 3.1 is calculated with the conversion of the Digital Number (DN) measured from band 6 of the ETM+ to radiance, following (Landsat 7-ETM+ Science Data Users Handbook, use [1998])

$$L_{TOA,i} = 0.037DN + 3.1628. \tag{3.2}$$

The surface emissivity used in Equation 3.1 was extracted from the ASTER Global Emissivity Database [Hulley et al., 2015]. This database offers surface emissivity values at 100 m^2 spatial resolution for the five TIR channels of the ASTER sensor [Yamaguchi et al., 1998] after applying the Temperature and Emissivity Separation method [Gillespie et al., 1998] to the ASTER data from 2000 to 2008. In this study, the emissivity used to correct the surface emission at the disaggregated TIR scene of the ETM+ sensor at 30 m× 30 m pixel, was calculated from the mean value of the ASTER GED emissivities in channels 13 (10.25–10.95 μm) and 14 (10.95–11.65 μm), since both channels cover the spectral resolution of the band 6 in ETM+ Landsat 7 sensor. We obtained a range of emissivities of 0.960–0.982 for the area of study, with an average of 0.972 and 0.004 deviation (this is shown in Figure 3.2b as an example for 8 November 2015). With this procedure, the associated uncertainty is about 0.015 and therefore LST values might also have an uncertainty of about 1.5 °C [Gillespie et al., 1998]. In situ observations of the surface emissivity at the UIB Campus are needed to have more realistic emissivity values to reduce the uncertainty in the derivation of LST products.

Atmospheric variables in RTE were calculated with the MODTRAN radiative transfer code (v. 5.2.1, Berk et al. [2006]) using as input the atmospheric profile modeled with the web-tool calculator implemented by Barsi et al. [2005]. This simulated profile is interpolated spatially and temporally to the selected site and it is representative of the atmosphere in a 1° × 1° spatial resolution. This atmospheric profile was demonstrated

to be the best option to correct the atmospheric effect compared with other profiles like that offered by the MOD07 product [Pérez-Planells et al., 2015].

Once the variable $B_i(LST)$ in the RTE is cleared, LST is obtained with the expression proposed in the Landsat 7 Science Data Users Handbook [use, 1998] to convert radiance to temperature (in K) at band 6 as:

$$LST = \frac{1282.71}{ln(\frac{666.09}{B_i(LST)} + 1)}. \tag{3.3}$$

For the studied area (1 km^2 centered in the UIB Campus, Figure 3.1b) and period (January 2014–May 2016), a total of 63 ETM+ scenes are used corresponding to clear-sky conditions, providing LST fields at around 1030 UTC.

3.2.2 The MODIS-Terra Land-Surface Temperatures

The MODIS-Terra satellite was launched in 1999, and, since then, it has provided global coverage, offering twice-daily LST and emissivity products generated from three different algorithms: the MOD11 L2 (and Level 3 MOD11A1) using the generalized split-window (GSW) algorithm [Wan and Dozier, 1996], the MOD11B1 with the physically based day/night (D/N) algorithm [Wan and Li, 1997] and the new MOD21 LST and emissivity (MODTES) product [Hulley et al., 2012] adapted from the temperature-emissivity separation (TES) method [Gillespie et al., 1998] and the water vapor scaling (WVS) method [Tonooka, 2005] for refined atmospheric correction. First validation works of the MODIS LST product have been published since very soon after its launch for the first proposed GSW method [Coll et al., 2009, Hook et al., 2007, Wan et al., 2002]. The D/N method has also been validated [Hulley and Hook, 2009], and, more recently, the MODTES LST product has been validated in several studies [Coll et al., 2016, Ermida et al., 2014].

MODIS has a polar orbit covering the whole Earth every one or two days. Terra-MODIS passes over, in its ascending orbit, the Balearic Islands (39°N, 3°E) every day between 1000 and 1100 UTC acquiring data in its 36 spectral bands, at approximately the same instant as ETM+, with LST fields at a spatial resolution of 1 km × 1 km. The collection 5 and Level 3 of MOD11A1 daily LST product [Wan, 2008] is selected, which provides LST values at 1 km spatial resolution gridded in the Sinusoidal projection. The LST product is generated by the generalized split-window LST algorithm [Wan and Dozier, 1996].

A total of 469 Terra-MODIS scenes are used in this study covering the period of (January 2014–May 2016) with clear-skies in the UIB Campus (Figure 3.1b) at approximately

the same instant as those obtained from ETM+. Therefore, a direct comparison of the corresponding LST fields is possible.

3.2.3 In situ Land Surface Temperatures

The ground-measured LST is calculated with a Hukseflux RN01 net radiometer (Delft, The Netherlands) installed at the reference measuring point. This sensor provides the four terms of the radiation budget at the Earth's surface. It consists of a pair of pyranometers facing upward and downward to measure the surface down and upwelling shortwave radiation terms, respectively, while two pyrgeometers are similarly located to measure the far-infrared longwave radiation contribution, within a spectral range of 4.5–50.0 μm. The FOV for both pyrgeometers is 150° (180° for the pyranometers). Therefore, considering that the RN01 radiometer is located at 1 m height, the measured upwelling longwave radiation corresponds to a surface area with a diameter of 7.5 m. The terrain in this part of the area of study is homogeneous for an extension of several tens of meters.

In order to obtain the in situ LST, the measured upwelling longwave radiation $L\uparrow$ must be corrected from the reflected downwelling contribution $L\downarrow$, following the expression:

$$LST = \left[\frac{L\uparrow -(1-\varepsilon)L\downarrow)}{\varepsilon \cdot \sigma}\right]^{1/4}, \tag{3.4}$$

where $\varepsilon = 0.97$ is the surface broadband emissivity, a value taken from Snyder et al. [1998] corresponding to senescent sparse shrubs, a common soil type of the UIB Campus. $\sigma = 5.67 \times 10^{-8}$ W $\cdot$ m^{-2} $\cdot$ K^{-4} represents the Stefan–Boltzmann constant, L↑ and L↓ are in W·m^{-2} and LST in K.

The data used for the ground-based observations correspond to the 1 min average measured every day at 1030 UTC from 1 January 2015 to 1 June 2016. The time of the day is selected according to the pass time of the satellites involved in this study to minimize the temporal mismatch between the three observational sources. The radiation instrument was calibrated by the manufacturer in June 2013, and it was mounted for the first time in January 2015. Data quality control has been performed since then by cleaning the sensor domes periodically and critically reviewing the measured data.

3.2.4 Previous validations of satellite-derived Land Surface Temperatures

Table 3.1 shows the results from recent studies where the satellite LST is validated using ground-based measurements over different surface types. The selected works report products from MODIS and Landsat 7-ETM+ and retrieve LST using a variety of algorithms and methods to deal with atmospheric and emissivity effects. When possible, the biases and RMSEs included in Table 3.1 correspond specifically to the same satellite products used in the current study. For MODIS, most of the results included correspond to cases where the gridded (Level 3) product MOD11A1 in its collection 5 was used [Ermida et al., 2014, Niclòs et al., 2015, Yu and Ma, 2015, Zhou et al., 2014], although Coll et al. [2016], Krishnan et al. [2015], Niclòs et al. [2015] for the rice crop area, the swath product MOD11_L2 was used, which was prior to the gridded one. For the ETM+ studies Li et al. [2004], local-radiosonde profiles were used to retrieve the atmospheric parameters in RTE instead of the synthetic ones generated by the web-tool calculator described in Section 3.2.1, while Coll et al. [2010] compared both methodologies over a homogeneous surface, obtaining better results for the interpolated profiles.

Regarding the ground truth calculation, different instruments and methods were applied depending on the study. Generally, averages from several ground measurements taken over different parts of the area of interest were preferred [Coll et al., 2010, 2016, Krishnan et al., 2015, Li et al., 2004, Yu and Ma, 2015, Zhou et al., 2014], although Yu and Ma [2015] obtained better results with a single measurement from a four-component net radiometer located at 6 m height over a strong heterogeneous site. Niclòs et al. [2015] uses a single thermal-infrared radiometer that measured at different observation angles, while Ermida et al. [2014] built the ground truth LST after identifying the fractions of the main surface elements seen by the on-board sensor.

All the studies in Table 3.1 show that MODIS products underestimate LST compared to ground-based measurements (despite of the method used to calculate the in situ LST) and the bias is larger over more heterogeneous surfaces. Similarly, bias and associated RMSE increase during the day, when spatial thermal differences are larger. ETM+ products do not seem to improve the MODIS results over homogeneous surfaces (see, for instance, bias and errors from Coll et al. [2010, 2016] in Table 3.1, both studies performed at the same site in summer time). In the following section, we will evaluate what the results are over a heterogeneous surface.

3.3 Land Surface Temperature variability

3.3.1 Spatial Variability of the Land Surface Temperatures

An example of LST difference between ETM+ and MODIS products is shown in Figure 3.2, for a scene from 8 November 2015 at 1030 UTC. Let us remind readers here about the no-data bands as introduced above. Figure 3.2a is a true color composite of a Landsat 7-ETM+ scene centered on the UIB Campus and surroundings: R (Band 3, 0.63–0.69 μm), G (Band 2, 0.52–0.60 μm) and B (Band 1, 0.45–0.52 μm). Figure 3.2b shows the average emissivity of ASTER TIR bands 13 and 14. The UIB Campus is defined with a white square that consists of 33 × 33 Landsat 7-ETM+ pixels (a total of 1089 pixels) at 30 m spatial resolution (Figure 3.2c, corresponding to the disaggregated TIR scene from the original 60 m spatial resolution). Therefore, the averaged Landsat 7-ETM+ LST at the UIB Campus is computed from the values of Landsat 7-ETM+ included in the 1 km^2 of the Campus without considering the data inside the black bands. On the other hand, four pixels of MOD11A1 are partially included in the UIB square (M1, M2, M3 and M4 in Figure 3.2d), and the averaged MOD11A1 LST is the weighted average of these four pixels (44% for M1 and M2 and 6% for M3 and M4).

Figure 3.2c shows, for the same Landsat 7-ETM+ scene of Figure 3.2a, the LST map calculated with the single-channel method explained in Section 3.2.1. Differences as large as 15 °C can be seen in the full scene and up to 12 °C just in the area corresponding to the UIB Campus, marked with a white square. The warmer area corresponds to a soccer field covered by artificial grass, while the coldest areas are located close to buildings in the Campus.

The corresponding MOD11A1 LST (6 pixels at 1 km^2) is seen in Figure 3.2d for the same day and time of the Landsat 7-ETM+ scene in Figure 3.2c, and painted with the same color palette. In this case, there is a difference of 1.4 °C in the whole picture and 1.2 °C in the UIB pixel. Therefore, in this single scene, it is checked that with lower spatial resolution (1 km^2), significant temperature gradients at the hectometre scale are not detectable, pointing to the need of higher horizontal resolution fields to monitor their evolution, something currently out of reach with the satellites at disposal for the scientific community that have these scenes just once every several days and for a single instant. However, heterogeneities of this size may contribute significantly to measured surface energy and water budgets over land, according to other previous studies [Cuxart et al., 2016b].

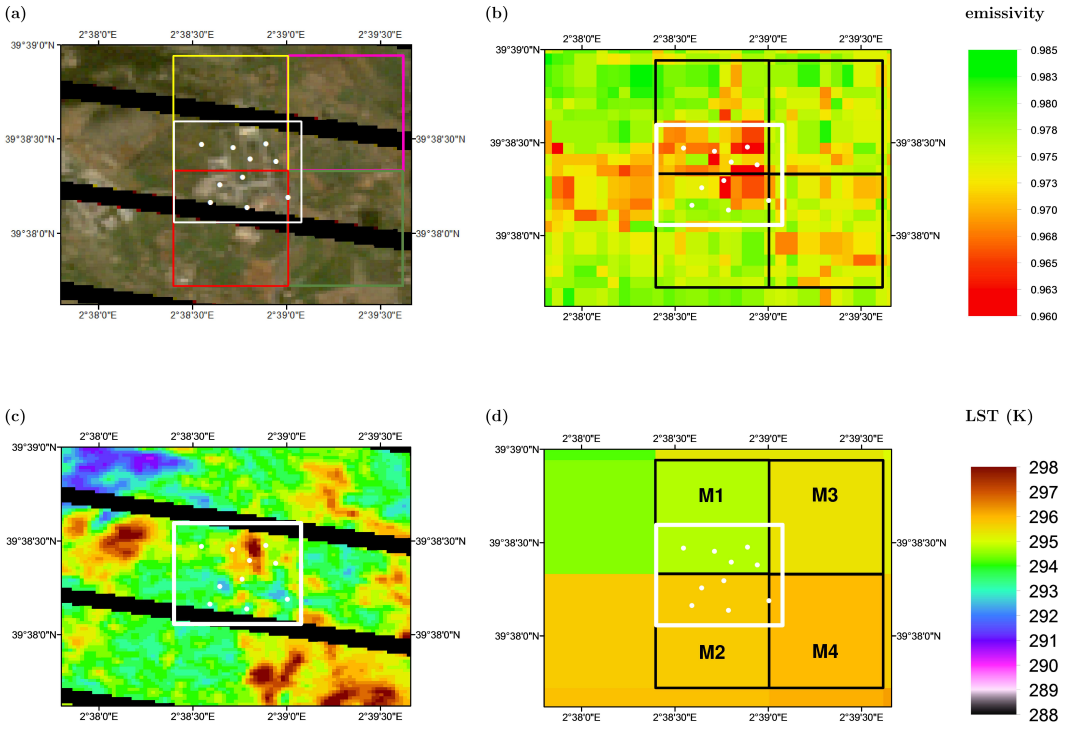

FIGURE 3.2: (**a**) RGB scene obtained on 8 November 2015 at 1030 UTC for the study area and its surroundings from Landsat 7-ETM+. **Yellow**, **purple**, **red** and **green** squares correspond to the pixels of MODIS. The corresponding ASTER emissivity (bands 13 and 14) and LST for Landsat 7-ETM+ and MODIS are shown in (**b**–**d**), respectively. The **white** square is the 1 km^2 studied area at the UIB Campus (Figure 3.1b) and **white** dots indicate the location of the selected points further analysed. M1, M2, M3 and M4 indicate the location of the MODIS pixels that fall within the study area.

3.3.2 Annual evolution of the Land Surface Temperatures

After exploring the heterogeneities for one single scene, the evolution of LST is shown in Figure 3.3a for the period January 2014–May 2016. It represents the annual evolution of LST for Landsat 7-ETM+ (averaged value of the 1089 pixels included in the 1 km^2 in Figure 3.2c, see Section 3.2.1), Terra-MODIS (four pixels' weighted average as indicated in Section 3.3.1) and the ground-based measurements (derived from the longwave radiation components as seen in Section 3.2.3) taken at the reference station (starting on 1 January 2015). At the scale displayed in the graph, there is good agreement between the three data sources; however, discrepancies on the order of 5 K are common, and they can rise up to 10 K in summer.

To have a first quantification of the discrepancies, Figure 3.3b shows the comparison between pairs of LST temperatures. A total of 24 days are used in Figure 3.3b when MODIS, ETM+ and in situ measurements are available at about 1030 UTC (only covering the period January 2015–May 2016, limited by the temporal interval when in situ measurements were taken).

The first noteworthy issue is that the Landsat 7-ETM+ 30 m size pixel LST value closest to the measurement site compares very well to the observed LST in situ value for the whole range of observed temperatures ($r^2 = 0.98$, BIAS $= -0.5$ K and RMSE $= 1.7$ K). This indicates that LST variability at scales under 30 m is not very large in this region of the UIB Campus. Discrepancy between the observed in situ value and the closest MODIS pixel is relatively small below 305 K (on the order of 1–3 K) and increases to 5 K or more for higher temperatures ($r^2 = 0.95$, BIAS $= 3.2$ K and RMSE $= 4.2$ K for the whole temperature range). In hot weather, LST variability seems to be very large and the point measurement may be a poor surrogate of the pixel-average value. Similar results are found when Landsat 7-ETM+ and MODIS LST values averaged over the UIB Campus are compared ($r^2 = 0.98$, BIAS $= 2.5$ K and RMSE $= 3.1$ K). It is worth noting that the effect of surface emissivity accounts for a significant part of the discrepancies on LST found between MODIS and an appropriate average of Landsat 7-ETM+ LST over the site. It is known that the MOD11A1 LST product in its collection 5 presents too emissivity values that are too high [Wan et al., 2002]. Thus, this could be an important cause of such discrepancies between the two sensors, particularly in summer, when LST values are higher and emissivity is lower due to surface drying.

The preliminary conclusions are that (i) Landsat 7-ETM+ is an adequate tool to compute the variability of LST at the sub-kilometre scale, since it compares very well with local data; (ii) the uncertainty in the computation of LST product is smaller than the variability of these fields over the UIB Campus and (iii) for LST below 300 K the three estimations seem to be of similar quality, with MODIS diverging significantly for higher temperatures.

Uncertainties and biases obtained in the present study are consistent with those obtained in previous studies (see Table 3.1) for both satellite products analysed here. In our case, these discrepancies are slightly larger, most likely because of the heterogeneities of the terrain [Yu and Ma, 2015] and also because the ground truth is built with a single-point measurement with a reduced FOV of 7.5 m. Land surface heterogeneities lead to strong LST differences during daytime, as seen in Ermida et al. [2014], Krishnan et al. [2015], Yu and Ma [2015]. This effect is also evident during the year, where discrepancies between satellite and single-point ground measurements increase in summer. It is important to take into account the source of the differences shown in Figure 3.3b such as: (i) the different algorithms (and assumptions considered) to derive LST for MODIS, ETM+ and the radiometer; (ii) the area representative of the pixel (for MODIS and ETM+) and the representativeness of the single-point measurement, especially in such an heterogeneous place; (iii) differences in emissivity may induce temperature differences of about 1.5 K [Gillespie et al., 1998] (or higher due to emissivity overestimation in the algorithm of the MOD11A1 LST product commented on previously), but, in any case, this difference

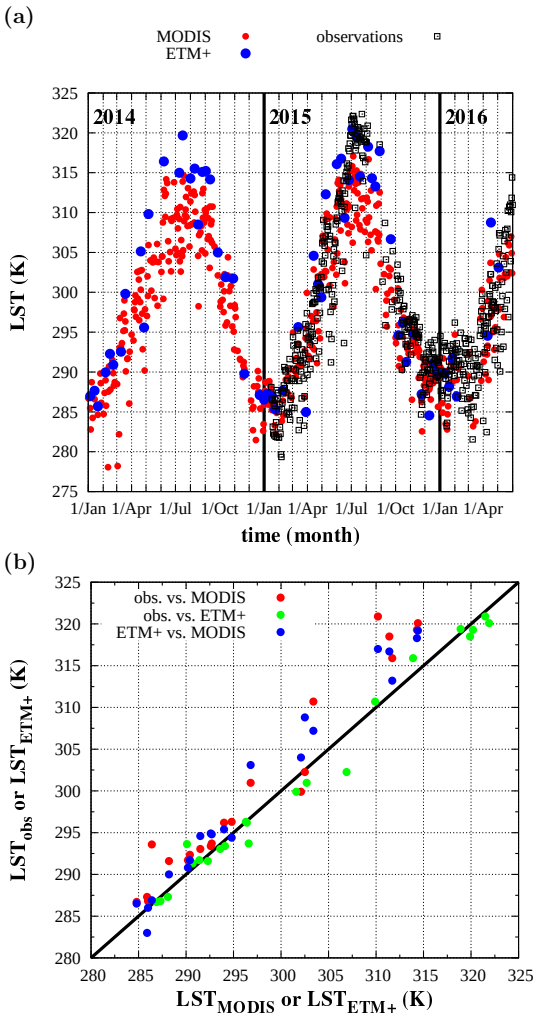

FIGURE 3.3: (**a**) time series of averaged LST over the 1 km ^{2} studied area in the UIB Campus for Terra-MODIS (weighted average) in **red** and Landsat 7-ETM+ in **blue**. Data from the meteorological station (see location in Figure 3.1b, **yellow** dot) are also included in **black** empty squares; and (**b**) the correlation of LST obtained from the three different sources. Here, the Landsat 7-ETM+ LST corresponds to the closest value when compared to the ground station, and it is the 1 km^2 spatial average when it is compared to MODIS.

is lower than the temperature variability typically reported in the Campus area (see, for instance, Figure 3.2c) during the studied period; and (iv) the 30 min temporal mismatch between MODIS and Landsat 7-ETM+ overpass could be a significant factor in the LST difference between both sensors that could reach a value up to 1.5 K in hot weather conditions [Vlassova et al., 2014].

To inspect the spatial variability within the UIB Campus and assess how representative a single station would be, the values of the 10 points with different surface characteristics and representative of the UIB Campus variability are taken (Figure 3.1b, one of them is placed in the measurement site). Figure 3.2c shows that they are located in points with very different LSTs. Figure 3.4 shows the temporal evolution of the maximum

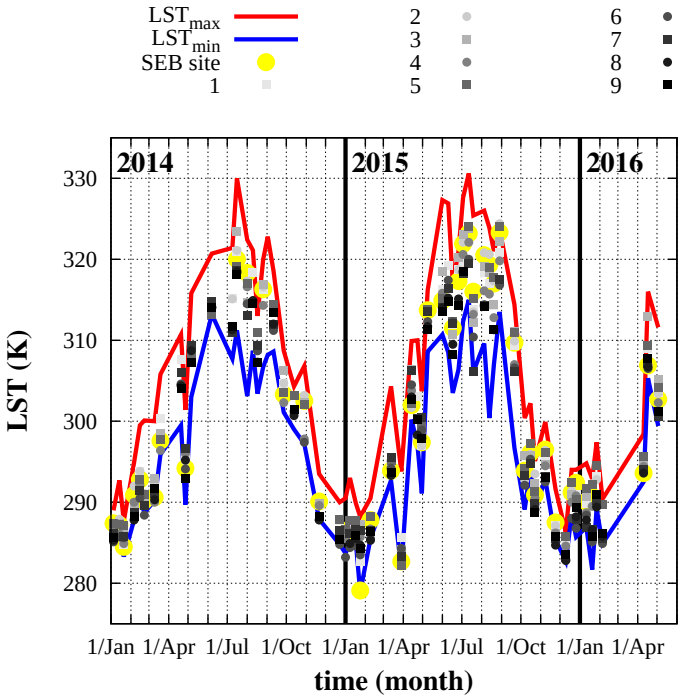

FIGURE 3.4: Time series of the maximum (in **red**) and minimum (in **blue**) LST obtained from Landsat 7-ETM+ for the 1 km^2 studied area at the Campus. LST evolution for the closest Landsat 7-ETM+ pixel is also included from the nine selected points and the energy balance measurement site (see locations in Figure 3.1b).

Landsat 7-ETM+ LST (red line) and minimum (blue line) values for the entire study area (Campus UIB, Figure 3.1b). Individual LSTs for each of these ten points are also included. Along the 2.5 years represented, the maximal LST range for the UIB pixel is found in the summer, when it is between 15 and 20 K, while it is reduced to 5–10 K in the cold seasons. The spread of points between the lines indicates that the selected locations cover well the thermal variability within the 1 km^2 studied area of the Campus. These selected points may be considered for taking in situ measurements and building a more accurate ground truth LST to compare against satellite products in a future research action.

3.3.3 Seasonal distribution of the Land Surface Temperatures heterogeneities

To further explore the heterogeneity of the Landsat 7-ETM+ LST fields during the studied period at the UIB Campus, the corresponding Probability Density Functions are computed as it was done in Jiménez and Cuxart [2006]. Figure 3.5a shows the PDFs for some selected days that are taken to be representative of the cold seasons (5 January 2014 and 8 November 2015 corresponding to the field in Figure 3.2c) and the warm ones (1 June 2014, 12 July 2014 and 26 August 2015). The x-axis is normalized by the mean

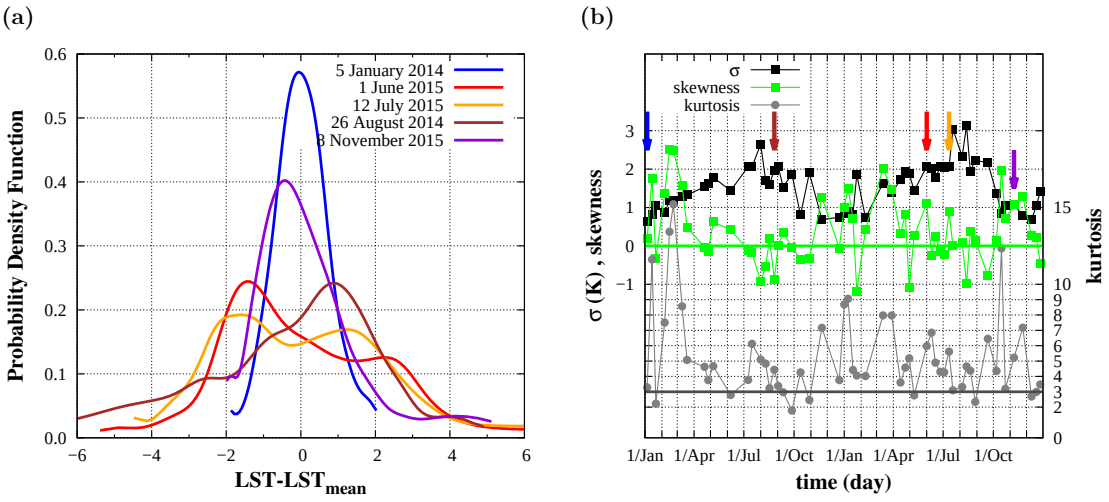

FIGURE 3.5: (**a**) normalized probability density functions (PDFs) computed from the Landsat 7-ETM+ LST fields over the UIB Campus for different days within the cold and hot seasons (see Figure legend). (**b**) time series of the standard deviation (σ), skewness and kurtosis of the PDFs computed from the Landsat 7-ETM+ LST fields from 1 January 2014 to 1 January 2016. The arrows indicate the statistical parameters of the PDFs shown in (**a**).

value to make all of these PDFs comparable. In addition, the temporal evolution of the statistical parameters extracted from the PDFs (standard deviation σ, skewness S, and kurtosis K) are shown in Figure 3.5b for all the available scenes.

Figure 3.2c (8 November 2015) shows the variability of the LST field, with the warmest and coldest areas constrained to some specific locations on the Campus. This variability is illustrated by the PDF in Figure 3.5a that indicates that temperatures lower than average occupy a larger area than the more intense warmer ones. In addition, in agreement with Figure 3.4, it is seen for this case that the spread of LST for the UIB Campus is smaller than in the warm seasons. The statistics of this distribution ($\text{LST}_{mean} = 294.8$ K, $\sigma = 1.1$ K, $S = 1.1$ and $K = 5.2$) show that it is far from the normal distribution ($S = 0$, $K = 3$).

It is clear that the use of PDF illustrates in a compact manner the characteristics of the LST field for the area under study (Figure 3.5b). For cold season days, such as 5 January 2014, there is a small spread and a distribution very close to the normal one. During the warm season, the distribution shows indication of bi-modality, the maximum evolving during the summer from the cold to the warm side, therefore departing largely from normality. This shift may be related to the progressive drying of the surface during summer, which reduces the areas on the Campus able to be refreshed by evapotranspiration.

The seasonal PDFs (Figures 3.6a and 3.6b) have also been calculated, in spring and autumn. It is found that they occupy a greater range of LST and do not have a Gaussian

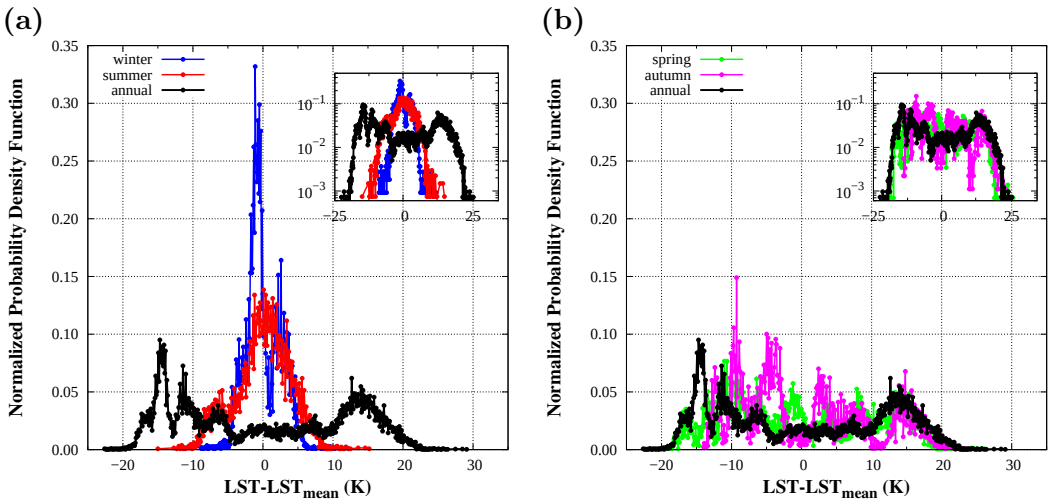

FIGURE 3.6: (**a**) normalized probability density functions (PDFs) computed from the Landsat 7-ETM+ LST fields over the UIB Campus for winter and summer and (**b**) for spring and autumn compared with annuals.

form as in the cases of summer and winter. The annual PDF is more similar to those of autumn and spring, and has a bimodal behavior centered on the -15 and 15 K, which refers to the cold and warm cases respectively.

3.4 Concluding remarks

A satellite-derived LST field provides one value of temperature for each pixel. In this study, the MODIS LST values at a resolution of 1 km—for the area corresponding to the UIB Campus—have been compared to the average values as computed from the available Landsat 7-ETM+ data which are at an approximate resolution of 60 m. The comparative analysis shows that, for the very heterogeneous UIB Campus, the variability at scales under 1 km is very large, the range of LST being on the order of 5–10 K in the winter time and as high as 20 K in the summertime, with standard deviations of about 2 K.

Heterogeneity has an impact on the choice of a position for a station providing ground information. Locating the station arbitrarily in a heterogeneous area may result in a large bias compared to the pixel average if the values at that location are far from the average, compromising even the concept of ground truth validation. The computations made in this study show that the RMSE between in situ LST measurements and MODIS values for the pixel are significantly larger than for homogeneous surfaces, in good correspondence with previous studies. For the Landsat 7-ETM+ higher resolution pixels, the comparison between in situ and satellite-derived LST compares well for the rather

homogeneous area surrounding the station, as for previous studies over homogeneous surfaces.

The analysis of the PDFs of LST from Landsat 7 ETM+ allow inspection of the distribution depending on the time of year for the mid-morning scenes. The winter time has a more compact distribution as it shows a small spread and a shape closer to normal, whereas the summertime indicates a tendency to bi-modality, the mode moving from cold to warm as summer advances. These distributions may be linked to the contents of water in the soil-vegetation system, since evapotranspiration reduces surface heating wherever it takes place, and, if there is water availability in the whole pixel, heterogeneities may reduce substantially. This effect may reduce its importance as the summer progresses and the land becomes dry.

Results from this Chapter point that there is LST variability in the annual cycle for a heterogeneous terrain. To study this variability, satellite-derived LST products can be used, but only those with spatial resolutions of about 100 m to properly capture the heterogeneities of the study site.

Chapter 4

Inspection of the variability of the temperature gradient in the surface layer (T2-LST)

In the previous Chapter, variations of LST between 10 and 20 K at the sub-kilometre scale have been obtained for an heterogeneous area of 1 km size. The main features of the air in contact with this soil, and special the atmospheric surface layer, will strongly depend on this thermal heterogeneity. In this Chapter[1], the relation between the screen temperature of the air at 2 m (T2) and LST has been studied, since it is a key parameter in the determination of the energy, momentum and mass exchanges between the soil and the atmosphere that take place in the surface layer.

An analysis of the difference T2-LST is made with data from the complete surface energy balance station (yellow dot in Figure 3.1c). While most studies in the literature are often built for relatively short temporal intervals (from several days to a few months), this study analyses two-year long series with a 30-min temporal resolution, in particular the diurnal and seasonal variability. After an initial estimation of the uncertainties of the LST data, the dependence of the temperature difference on other parameters in the surface-atmosphere interface is evaluated. In the center of the day, the differences are typically between -3 and -10 °C, arriving to about -18 °C for dry summer days. At night the values are usually under 3 °C, with very small values under 1 °C in the summer nights. The parameters that show higher correlation with the temperature difference are the soil moisture and temperature, together with the sensible heat flux, especially in the daytime. The lack of strongly stratified cases near the ground, even in clear and

[1]This Chapter is based on G.Simó et al. 2018: Impact of the Surface-Atmosphere Variables on the relation between Air and Surface Temperatures. Accepted in *Pure and Applied Geophysics*

calm nights show the important role of the soil to supplement heat as the surface cools radiatively.

4.1 Introduction

The experimental determination of LST (relative to the ground surface temperature) close to the surface is of great importance for a number of applications. These include the validation of estimations of the LST values from satellite [Li et al., 2013, Peres and DaCamara, 2004, Wan et al., 2004] and its use in many numerical modelling tools [Sellers et al., 1997, Tierney et al., 2008]. It is one of the key parameters in the surface-atmosphere interactions, especially in the determination of the exchange fluxes of heat [Anderson et al., 2012, Kalma et al., 2008, Kustas and Norman, 1996, Kustas et al., 2011]. LST is determined by measuring the long-wave radiation emitted by the surface, since a thermometer cannot be used at the soil-atmosphere interface because it does not reach thermodynamical equilibrium with any of the two components [Betts et al., 1996].

Obtaining the LST value in a certain location requires a determination of the long-wave radiation components, which are the irradiance emitted by the surface (L_{up}) and the downwelling radiation (L_{dn}) [Jin and Dickinson, 2010, Mannstein, 1987, Schmugge and Becker, 1991, Sellers et al., 1988]. Furthermore, since the surface behaves as a grey body the value of its emissivity (ε) must be estimated [Li and Becker, 1993]. The L_{up} measurement should be close enough to the ground to be able to assume a negligible absorption by the atmosphere [Liou, 2002].

The uncertainties in the estimation of LST values derive from different sources: i) those relative to the measurement of the upward long-wave radiation (L_{ms}) and to the measurement or estimation of L_{dn} [Zhang et al., 1995], ii) those ones related to the prescription of the surface emissivity [Plokhenko and Menzel, 2000] and, iii) those related to the local heterogeneities of the target surface which is in fact assumed to be homogeneous. The latter point has been studied recently by Simó et al. [2016], who found that surface heterogeneities at spatial scales of decametres may imply uncertainties of a few degrees in temperature. This contribution to the uncertainty of LST will not be treated in this Chapter.

Being able to relate T2 and LST may help to provide one of the fields knowing the other one, such as estimating screen temperature from satellite-determined LST, as in Jiménez et al. [2015] for agrometeorological applications, or in regions where the network of surface weather observations is not very dense [Prihodko and Goward, 1997]. In the other sense, LST derived from T2 values may be very useful to estimate the exchange

fluxes between the atmosphere and the surface [Mintz and Walker, 1993], or to generate first-guesses of LST in numerical modelling [Noilhan and Planton, 1989].

Previous studies have already studied the relation between air temperature and surface temperature. They can be divided in three groups: those that use the LST from satellite [Chen et al., 1983, Davis and Tarpley, 1983, Green and Hay, 2002, Jiménez et al., 2015, Recondo and Pérez-Morandeira, 2002, Shamir and Georgakakos, 2014, Urban et al., 2013, Vogt et al., 1997, Williamson et al., 2014, Zhou et al., 2014] which obtain a linear correlation of r^2= 0.7-0.9 with an error between 1.6-4.9 °C; studies that use LST from satellite as well as other variables such as the temperature/vegetation index (TVX, [Czajkowski et al., 2000, Niclos et al., 2014, Prihodko and Goward, 1997, Saravanapavan and Dye, 1995, Sun et al., 2005]) or geographical variables [Cristóbal et al., 2008] where the errors are usually below 4 °C and r^2= 0.24-0.92; and those that use in situ data as input to obtain the T2 from different models and methods [Niclòs et al., 2010, Pape and Löffler, 2004], where r^2= 0.1-0.9 and an error of 0.18-2.04 °C. In this study, in situ data will be used to estimate T2 from LST as in the last group noting that, in comparison to Niclòs et al. [2010] many more surface-atmosphere variables have been studied with a larger temporal range, over a period of two years.

The aim of this Chapter is twofold. On the one hand, a detailed analysis of the importance of instrumentation and emissivity is made. On the other hand, it has been analysed how LST is related to T2, measured in a meteorological shelter at 2 m, taking advantage of a simultaneous determination of two years for both magnitudes. This is done inspecting the difference T2-LST, both for the daytime and the nighttime, exploring patterns during the year and assessing on the value of this difference. Furthermore, the relation of the difference T2-LST with other variables measured at the same point is explored. Together with the solar radiation and wind speed [Niclòs et al., 2010], we have also focused our analysis on the state of the soil or the intensity of turbulence, as significant correlations with these factors are sought.

4.2 Location and instrumentation

The research station at the Campus of the University of the Balearic Islands (ECUIB) (Figure 4.1) is in a semi-rural area outside the city of Palma, in the island of Mallorca in the Western Mediterranean Sea (Figure 3.1), as we explained in the previous Chapter.

The surface is made of recent soil, due to fillings from terrains of construction work sites in the surrounding areas in the 1980's. The ground is covered with short vegetation consisting in wild grass between October and May that dies in the summertime, when

FIGURE 4.1: Complete research station located in the Campus of the University of the Balearic Islands.

the surface becomes mostly a mixture of bare soil and dead vegetation. The root depth of these plants is typically less than 10 cm and the amount of organic material in the upper horizon is relatively small. The soil is essentially not modified under 10 cm and it consists of a mixture of clay, silt and stones of some centimetres of diameter.

The instrumentation (Table 4.1) allows to determine some turbulent parameters of the surface layer such as the buoyancy flux ($< w'Ts' >$), TKE and friction velocity (u*); in addition to the net radiation, computed through the observed upward and downward components of the solar and long-wave radiation, and the ground heat flux. Furthermore, wind vector and air temperature and humidity at 2 m height together with the soil temperature and moisture are also measured. Data from this station were already used for the study of the previous Chapter.

The ground-measured LST is calculated with two different sensors: a four-component net radiometer and a thermal infrared radiometer. The Hukseflux NR01 net radiometer (Delft, the Netherlands) consists of a pair of pyranometers and pyrgeometers facing upward and downward that measure separately the four terms of the radiation budget at the Earth's surface. The far-infrared long-wave radiation contribution is measured within a spectral range of 4.5 – 50.0 μm and with a FOV of 150°, while the relative expanded uncertainty provided by the manufacturer calibration is within 6%. The thermal infrared radiometer is a Campbell Scientific IR120 (Logan, USA) that detects the thermal long-wave radiation from a targeted surface within a smaller spectral range (between 8 and 14 μm) and a narrower FOV of 40°. This sensor was calibrated in May

Instrumentation	Model	H/D (cm)	Variable	Period
Sonic anemometer	RMY 81000	300	TKE & $< w'Ts' >$ & u*	27/01/2016 - end
2D Sonic anemometer	WindSonic	215	WS	16/01/2015 - end
T and RH sensor	HC2S3	201	T2 & RH	16/01/2015 - end
Net radiometer	NR01	103	LST & L_{dn} & R_n	16/01/2015 - end
Infra-red radiometer	IR120	103	LST_{IR120}	16/03/2016 - 17/03/2017
Infra-red radiometer	SI-121	200	$L_{dn}(53°)$	09/04/-09/10/2016
Soil water content reflectometer	CS616	-4.5	VWC	30/01/2015 - end
Temperature probe	CS107	-1	ST	31/03/2015 - end
Soil heat flux plate	HFP01	-8	G	30/01/2015 - end

TABLE 4.1: List of instruments used during this study, with their heights (positive values) or depths (negative values) where they are installed. The observed magnitudes are: Turbulent Kinetic Energy (TKE), buoyancy flux ($< w'Ts' >$), friction velocity (u*), wind speed (WS), air temperature at 2 meters (T2), relative humidity (RH), surface temperature (LST), downwelling radiation L_{dn}, net radiation (R_n), surface temperature (LST_{IR120}), downwelling radiation at 53° ($L_{dn}(53°)$), volumetric water content (VWC), soil temperature (ST) at 1 centimeter depth, soil heat flux (G). The period of data that has been used is also indicated and the end is 15/01/2017.

2015 with a Blackbody Source LANDCAL P80P in the range of -3 to 60 °C, giving an uncertainty of ±1.7 °C.

Both sensors are installed at approximately 1 m height and separated by a distance of 5 m. Considering their respective FOVs, the net radiometer's targeted surface is much larger than the thermal radiometers (44.0 versus 0.4 m^{-2}, respectively), although both surfaces share the same type of soil and vegetation. Both types of models are broadly used as ground truth for validating the estimated LST from satellite platforms [Coll et al., 2016, Ermida et al., 2014, Krishnan et al., 2015, Li et al., 2004, Niclòs et al., 2015, Simó et al., 2016, Yu and Ma, 2015, Zhou et al., 2014]. Their measurements have been compared for a one-year period to assess about the uncertainty of LST related to the type of instrument, but only NR01 data have been used in all computations for a two-year period. A second IR radiometer pointing to the sky at an angle of 53° from the zenith was used during some months to test the Kondratyev [1969] estimation of the downwards long-wave radiation.

4.3 Experimental uncertainties in the determination of Land Surface Temperatures

4.3.1 Type of sensor

NR01 and IR120 are compared for one year (16/03/2016 – 15/03/2017), both located at the ECUIB station (Figure 4.1). Figure 4.2 depicts the measured difference between the two sensors as a function of the uncorrected value of LST, namely the values obtained from the NR01 sensor without correction for the reflected part of L_{dn}. For uncorrected

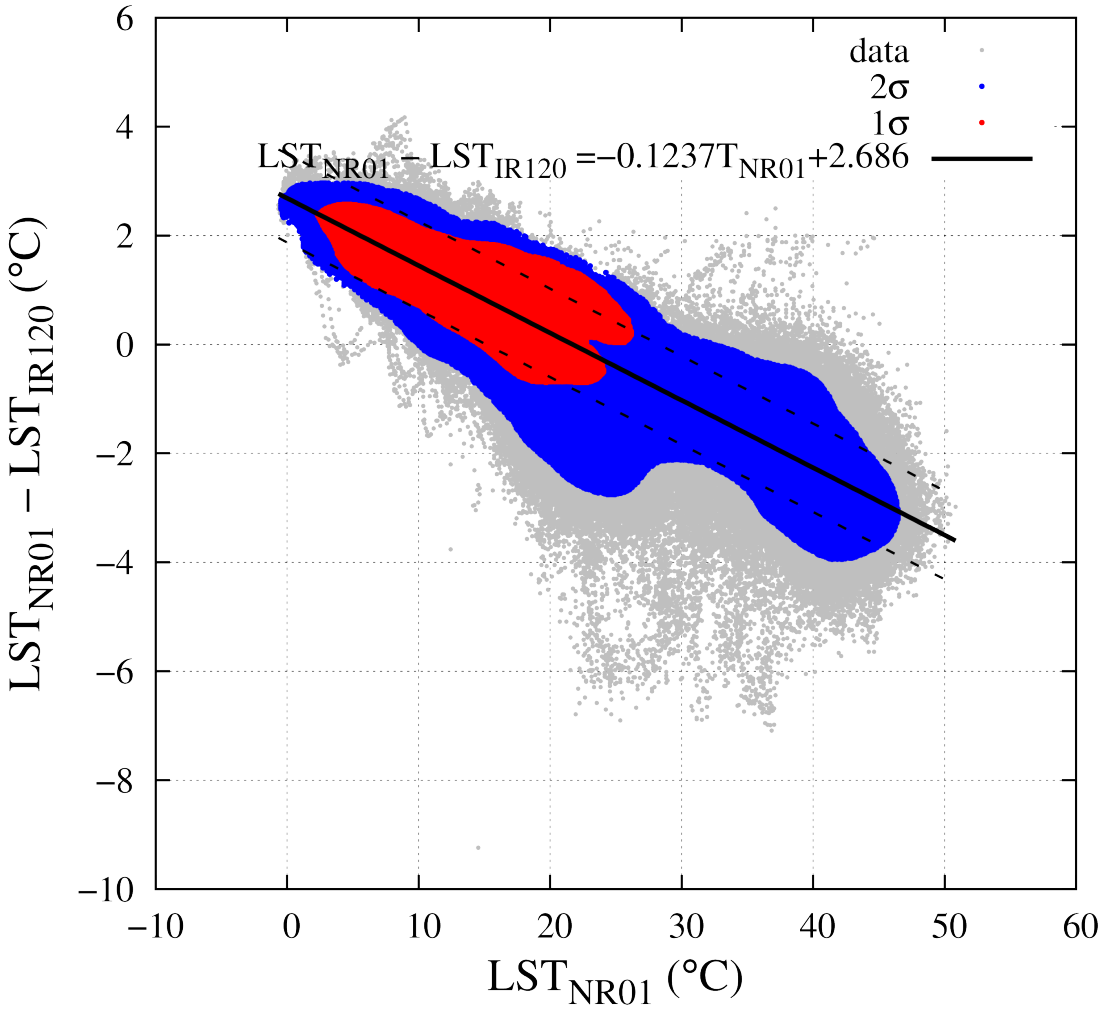

FIGURE 4.2: Comparison between temperature from NR01 Four-Component Net Radiation Sensor and temperature from IR120 Infra-red Remote Temperature Sensor, 1-minute averages data between 16 March 2016 to 15 March 2017. In red and blue it is shown the area with the highest probability density (1σ and 2σ, respectively). The solid line represents the line obtained with the least squares fit and the dashed line is the error of this fit ≈0.9 °C.

LST of about 20 °C, both sensors provide similar values, with a standard deviation close to 1 °C. For colder LSTs, NR01 provides higher values than IR120, whereas the situation is inverted for warmer LSTs. The former situation is normally found at night and in cold weather, the latter essentially in summer daytime, the largest differences taking place at very high LSTs. This result is comparable to the ones found by Blonquist et al. [2009]. It must be stressed that both sensors are not measuring over the same wavelength interval neither the same amount of surface and even point to different surface spots separated a few meters (see section 4.2). In any case it is clear that uncertainties of 1 to 3 °C exist related to the sensor type and the local surface variability, and we may assume a combined error related to these two factors of 0.9 °C, which has been obtained with the error of the least squares fit of Figure 4.2.

4.3.2 Land Surface Temperature uncertainty formula

The irradiance measured (L_{ms}) by a long-wave sensor looking downwards to the surface is the sum of L_{up} emitted by the surface plus the one resulting of the reflection of the downward radiation L_{dn} coming from the sky. The expression, for a surface with long-wave emissivity ε, assuming that the surface is opaque (r=1-ε), reads

$$L_{ms} = L_{up} + (1 - \varepsilon)L_{dn} \tag{4.1}$$

writing $L_{up} = \varepsilon\sigma LST^4$, we may express

$$LST^4 = \frac{L_{ms} - (1 - \varepsilon)L_{dn}}{\varepsilon\sigma} \tag{4.2}$$

where σ is the Stefan-Boltzmann constant ($\sigma = 5.67\text{x}10^{-8}$ W m^{-2} K^{-4}). The uncertainty of LST is estimated using the general formula of error propagation:

$$\delta LST = \frac{1}{4\varepsilon\sigma LST^3}\left[\delta L_{ms} + \left|\frac{L_{ms} - L_{dn}}{\varepsilon}\right|\delta\varepsilon + |(\varepsilon - 1)|\,\delta L_{dn}\right] \tag{4.3}$$

The Equation 4.3 indicates that uncertainity in LST depends on the indeterminations of: the irradiance measured, the emissivity and the downward radiation coming from the sky.

4.3.3 Estimation of the uncertainty values of Land Surface Temperature

The emissivity ε is usually prescribed as a function of the type of soil and the state of the vegetated surface. Following Snyder et al. [1998], we take ε=0.97 that corresponds to senescent sparse shrubs (ECUIB surface) for the ensemble of data and assume an error $\delta\varepsilon$=0.01 for this region. The same value was obtained in Simó et al. [2016] analysing the ASTER data emissivity of the studied region over 2.5 years.

Regarding the measurement of the long-wave radiation, a sensitivity of 6% is indicated by the NR01 manufacturer (see section 4.2) which, for values around 300 W m^{-2} of L_{ms} and L_{dn}, would typically result in uncertainties of 18 W m^{-2}.

As a preliminary estimation, considering in Equation 4.3 approximate values for $L_{ms} - L_{dn}$= 50 W m^{-2}, $\delta L_{up} = \delta L_{dn}$= 15 W m^{-2}, ε= 0.97, $\delta\varepsilon$=0.01, the first term inside the brackets would be one order of magnitude larger at least than the other two, indicating

that the main source of uncertainty of LST is the one coming from the measurement of the radiometer or the estimation of this value. Furthermore, Coll et al. [2005] indicate that an uncertainty of 0.2 to 0.4 °C can be expected for an uncertainty of 0.01 in emissivity. For surface temperatures of 25°C, δLST is about 2.5 °C just for the first term.

The experimental uncertainty of the radiation may come from the sensor itself, as indicated by the sensitivity provided by the manufacturer, or from the variability from one sensor to another as indicated above, in both cases being around 2 to 3 °C.

4.3.4 Estimation of L_{dn} and related uncertainty

There is a different source of uncertainty if L_{dn} is estimated instead of directly measured. Following Kondratyev [1969], a point measurement looking at the sky with an angle of 53° from the zenith represents approximately well the hemispherically integrated L_{dn} value from the sky [Göttsche et al., 2013],

$$L_{dn} \approx L_{dn}(53°) \tag{4.4}$$

If no direct measurement of L_{dn} is available, the classical parameteritzation of Brutsaert Brutsaert [1975] allows to estimate L_{dn} using the values of the air temperature (T_a) and water vapour pressure (e_a) at screen level (usually 2m above the ground).

$$L_{dn} = \varepsilon_{ac} \sigma T_a^4 \tag{4.5}$$

where $\varepsilon_{ac} = a \left(\frac{e_a}{T_a}\right)^b$ is the emissivity of the air, with a=1.24 and $b = 1/7$.

In this case we assess the uncertainty of the estimation of L_{dn} by comparison of each of these two methods with the values obtained using measured long-wave components. Two examples are given in Figure 4.3 for a hot summer day and a cloudy day respectively, in which the results are consistent with the findings from Figure 4.2. For LSTs lower than 20 °C NR01 provides higher values than IR120, the behaviour being the opposite for warmer temperatures. These L_{dn} estimations generate added uncertainties of several degrees around noon, but they are smaller than the differences between sensors. In general the corresponding corrections are below 1 °C, as indicated in Table 4.2, listing the differences between uncorrected measurements of different sensors, and the corrected values of each sensor with different correction methods for the whole year, winter and summer time.

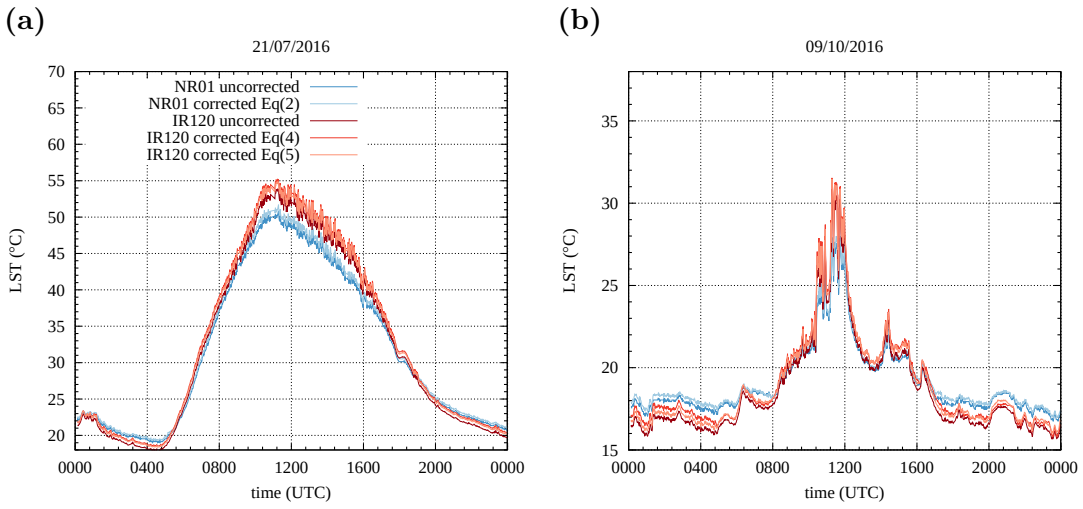

FIGURE 4.3: Comparison between different sensors and methods to correct the surface temperature: NR01 uncorrected, NR01 corrected with Equation 4.2 using L_{dn} measured by NR01, IR120 uncorrected, IR120 corrected with Brutsaert method (Equation 4.5) and with Tsky method (Equation 4.4), for a hot summer day **(a)** and a cloudy day **(b)**.

	All year	**Winter**	**Summer**
$LST(NR01_{uncorrected})$ - $LST(IR120_{uncorrected})$	0.4 ± 1.4	0.86 ± 1.10	-0.1 ± 1.5
$LST(NR01_{uncorrected})$ - $LST(NR01_{corrected})$	-0.32 ± 0.19	-0.26 ± 0.17	-0.38 ± 0.19
$LST(IR120_{uncorrected})$ - $LST(IR120_{correctedBrutsaert})$	-0.48 ± 0.14	-0.45 ± 0.09	-0.51 ± 0.17
$LST(IR120_{uncorrected})$ - $LST(IR120_{correctedTsky})$	-	-	-0.7 ± 0.3

TABLE 4.2: Mean values and standard deviation of the land surface temperatures (LST) difference between each sensor, four component sensor Hukseflux NR01 net radiometer (NR01) and infrared radiometer IR120 (IR120), and its corrections for different temporal periods: all year (2016/03/16 – 2017/03/15) cold period (2016/03/16 – 2016/04/08 & 2016/10/10 – 2017/03/15) and warm period (2016/04/09 – 2016/10/09).

The previous analysis of LST leads us to assume a general uncertainty in the determination of LST of about 2 to 3 °C, essentially linked to the uncertainty of the value of the long-wave radiation, as long as the emissivity does not vary significantly in the measuring area.

4.4 Temperature difference between the air (T2) and Land Surface Temperature (LST)

In this section we have used as values of LST those derived from the irradiances L_{ms} and L_{dn} measured with the sensor NR01, as indicated by Equation 4.2. We inspect the relation between LST and T2 at the ECUIB site, for a complete 2-year series (16/01/2015 to 15/01/2017). In comparison to previous studies [Niclòs et al., 2010] where T2 is estimated from LST, here we are looking for relations between these two variables and other relevant quantities in the surface-atmosphere interphase, such as the soil state

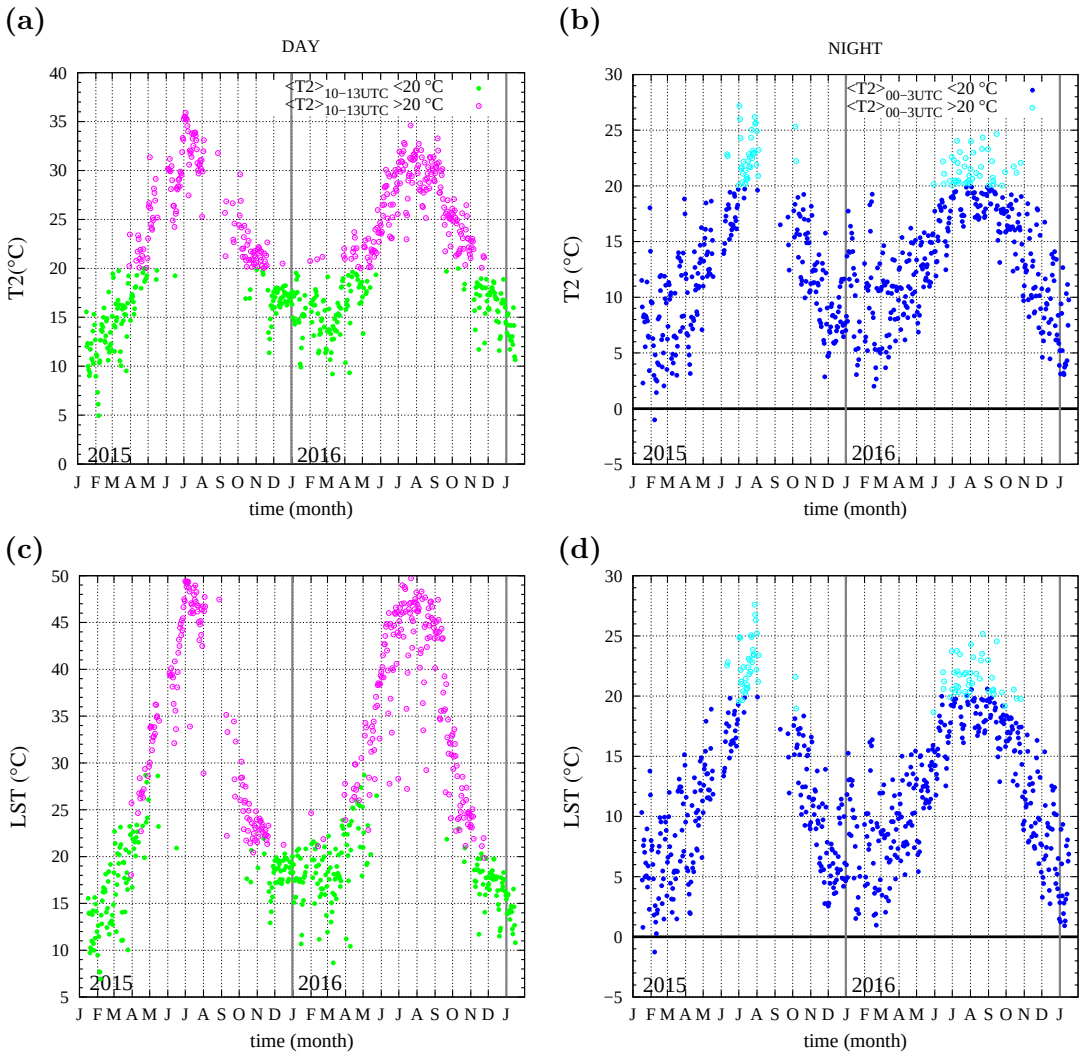

FIGURE 4.4: **(a)** and **(b)** show the daily mean values of air temperature at 2 m (T2), **(c)** and **(d)** for land surface temperature (LST) during the two years of study. These averages are made between 1000 and 1300 UTC for diurnal values and between 0000 and 0300 UTC for nocturnal.

or the intensity of the turbulence. The focus will be essentially put on the difference T2-LST.

Figures 4.4a and 4.4c describe a well-defined annual cycle for diurnal values of T2 and LST respectively. At all times LST is greater than T2, being the biggest difference in summer that can reach 15 °C. The same is shown in Figures 4.4b and 4.4d but for nighttime. The average value for each day between 1000 and 1300 UTC is taken as representative of the central hours of the day and between 0000 and 0300 UTC of the central part of the night. In this case, for the warm periods of the year the values of T2 and LST are very similar, but in winter they can reach 5 °C. The time series of other variables explored in this study is shown in Appendix A.

4.4.1 Yearly evolution of T2-LST

In Figure 4.5 is shown one value per day in the daytime (Figure 4.5a) and at night (Figure 4.5b) without performing any filtering related to the particular weather conditions on each day (a test filtering cloudy cases did not provide any significant difference in the results -Appendix B).

Figure 4.5a describes a well-defined annual cycle of T2-LST in the central hours of the day, with an increase from nearly 0 °C in winter to values of -15 °C in summer, a result consistent with the study by Shamir and Georgakakos [2014] that obtained differences between 0-20 °C being the highest in summer, whereas the values in spring and autumn are typically between -3 and -10 °C. The days with T2 higher than 20 °C indicate the warm seasons of the year (from mid spring to mid autumn). It is seen that, as in Mildrexler et al. [2011] for an ensemble of official meteorological stations, there is a clear increase of the value of T2-LST for T2 above 20 °C. Averages and standard deviations for T2-LST are (-2.2 ± 2.0) °C for mild and cold days and (-9.3 ± 5.7) °C for warm days.

A similar analysis is made for the nocturnal averages, where the nights with T2 above 20 °C are considered tropical nights [Data, 2009] and are just found for very hot summer periods. In Figure 4.5b, the amplitude of the annual cycle, compared to the diurnal values, is much smaller and in opposite phase. In the summer, a very hot surface during day generates large superadiabatic temperature gradients, whereas at night the surface stays warm and does not produce significatively stably stratified gradients. The opposite happens in winter, when the surface cools intensively at night allowing stably stratified stratification, whereas the mild insolation at day is not able to generate strongly unstable stratification. The main differences (between 2 and 5 °C) are found in winter, whereas in summer the gradient takes values close to zero with some occurrences of negative values, that we do not discuss in detail due to uncertainty of the LST values. Again in spring or autumn, intermediate values close to 2 °C are found. Tropical nights, marked light blue, show very small values, indicating very weak thermal stratification near the surface. In this case, averages and standard deviations for T2-LST for ordinary nights are (1.0 ± 1.1) °C, while for warm nights the values are (0.1 ± 0.9) °C. These values are small and of low confidence due to the uncertainties of LST, but at least they show that it is unlikely to have large temperature gradients (strong stable stratification) between 2 m and the surface for this location.

Figures 4.5c and 4.5d show the correlations between the average T2 and LST during the daytime (1000-1300 UTC) and during the nighttime (0000-0300 UTC) for the two years of the study, obtaining determination coefficients for T2 higher than 20 °C of

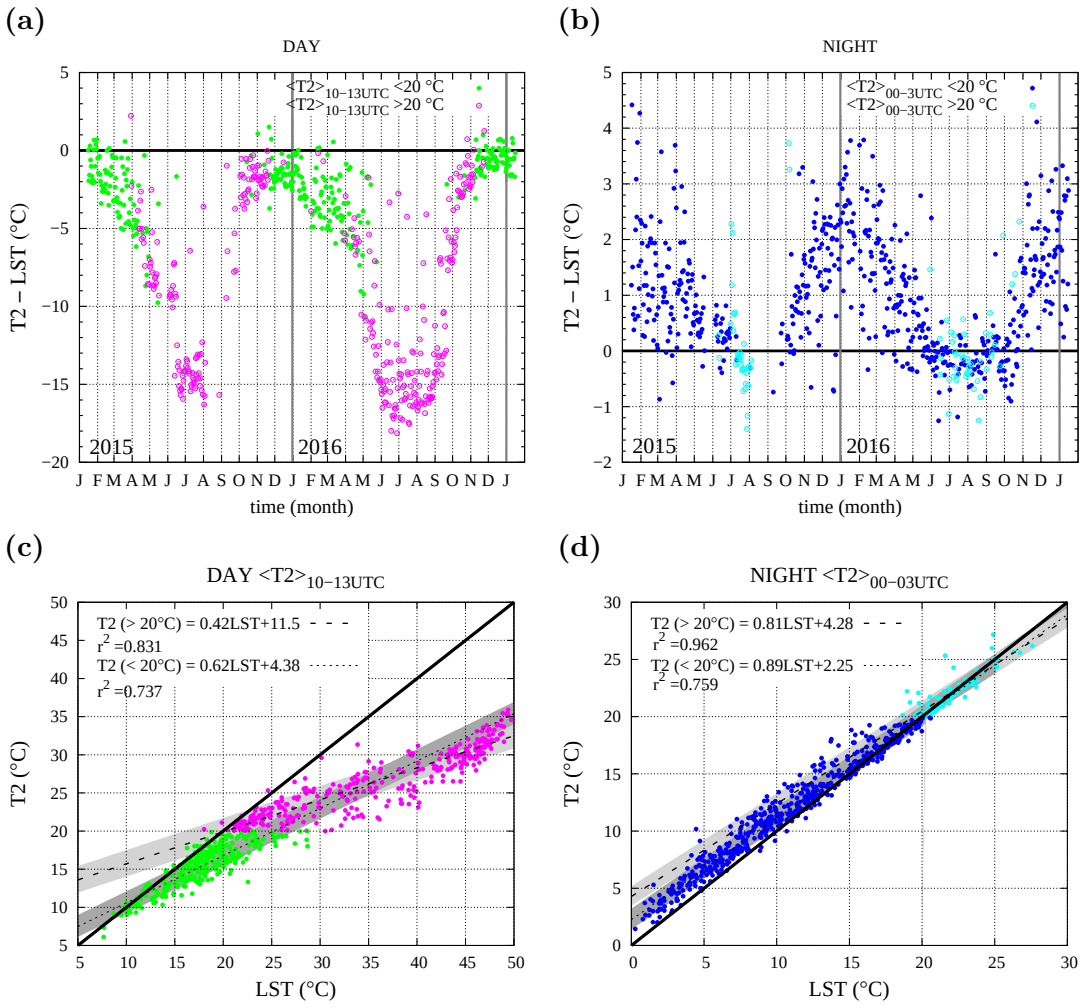

FIGURE 4.5: **(a)** and **(b)** show the daily mean values of temperature difference during the two years of study. These averages are made between 1000 and 1300 UTC for diurnal values and between 0000 and 0300 UTC for nocturnal values respectively. **(c)** and **(d)** show the correlations between air temperature at 2 meters above the surface (T2) and the surface temperature (LST) measured by four component sensor Hukseflux NR01 net radiometer, with the least squares fit equations, correlations, the 1-1 line in solid line and the error in grey for T2>20 °C and T2<20 °C during the daytime and nighttime respectively.

0.831 and for lower than 20 °C of 0.737 during the day and 0.759 and 0.962 respectively during the night. Although the methodology is valid anywhere, the linear fit for T2 and LST and the obtained equation are strictly only valid for climate and soil like those in the study region. If we compare these results with those of studies in areas with the same climate, similar results found in Andalusia with correlations for 24 hours period of 0.792 although they used NOAA LST [Vogt et al., 1997], in Mallorca using MSG LST obtained a correlation of 0.75 [Jiménez et al., 2015] and in Valencia with in situ data with a correlation of 0.73 [Niclòs et al., 2010].

Figure 4.6 provides further detail on the temporal evolution of this gradient, as hourly

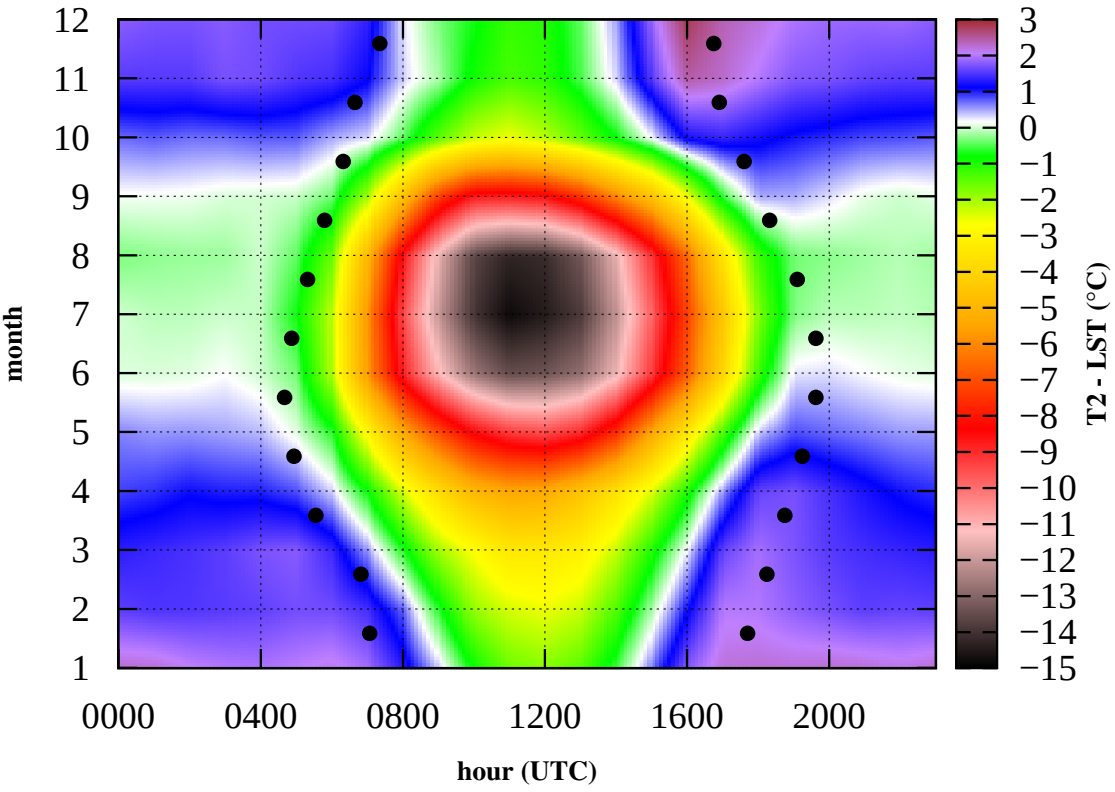

FIGURE 4.6: Hourly average values of T2-LST for every month of the year, where full circles represent sunrise and sunset at the central day of each month.

averages per month are plotted. This refinement in the averaged time evolution of T2-LST shows that the central hours of the day are clearly unstable, centered around noon and July. At night the differences have absolute values larger than 2 °C especially for the first part of the night during all the cool months. The values are very small during all year morning and evening transitions, summer nights and winter days and we consider them of low confidence.

4.4.2 Correlation of surface-atmosphere variables with T2-LST

As mentioned above, the sensible heat flux at the surface is normally parameterised as a function of T2-LST. This flux is also the result of the surface energy budget at the ground atmosphere interface. The available database allows to inspect indirectly through an statistical analysis if there is a clear correlation between T2-LST and the different heat fluxes. Furthermore, some important parameters of the physics of the land surface-atmosphere interface will also be correlated, as Niclòs et al. [2010] did for the solar radiation and the wind speed, focusing here more on the state of the soil and of the atmospheric surface layer.

R^2	**T2**	**LST**	$\mathbf{R_n}$	**RH**	**WS**	**VWC**	**ST**	**G**	$\mathbf{w'T'}$	**TKE**
$\mathbf{T2_{day}}$**<20°C**	0.061	0.503	**0.700**	0.109	0.007	0.081	0.375	0.502	**0.870**	0.025
$\mathbf{T2_{night}}$**<20°C**	0.123	0.283	0.038	0.137	0	0.057	0.485	0.069	0.317	0.096
$\mathbf{T2_{day}}$**>20°C**	0.551	**0.907**	0.402	0.375	0.008	0.472	**0.825**	0.445	**0.812**	0.194
$\mathbf{T2_{night}}$**>20°C**	0.013	0.150	0.003	0.390	0.002	0.285	0.349	0.018	0.365	0.047

TABLE 4.3: Correlations R^2 between the temperature difference of the air at 2 meters (T2) and the surface temperature (LST) with the variables described in Table 4.1 for the day (1000 - 1300 UTC) and night (0000-0300 UTC) and for the cold and warm (temperatures lower and larger than 20 °C) intervals. Values in bold show correlations higher than 0.7.

Correlation coefficients R^2 have been computed between them and T2-LST for day and night conditions (Figures 4.7 and 4.8 and Table 4.3).

Table 4.3 lists R^2, that indicates the proportion of the variance of T2-LST that may be due to the variable with which is correlated. The first two rows inform about the values for day and night excluding warm cases, which are displayed in the last two rows.

In the daytime the higher values are, in descending order, the buoyancy heat flux ($< w'T'_s >$), the net radiation (R_n) and LST, while for the warm days the dominant parameters are LST, upper soil temperature at -1 cm (ST) and also the buoyancy flux ($< w'T'_s >$). This points out that the main mechanism in the daytime is the net radiation warming of the upper soil. This generates $< w'T'_s >$, that in the case of warm days is controlled by the heat available in the upper soil.

The nocturnal correlations do not show clearly dominant values. Contrarily to the daytime, here R_n is not the principal term. ST, $< w'T'_s >$ and LST are still the parameters with more importance, R_n being completely uncorrelated with T2-LST. The warm nights also have a significant correlation with the soil volumetric water content (VWC) and the air relative humidity (RH).

If we focus on the importance of the soil state and processes in the daytime, we observe that VWC is only significantly correlated with T2-LST in the warm days. Figure 4.7c shows that the largest values of T2-LST occur when the soil is very dry. This is probably linked to the fact that there is enough water in the soil during the year to make the soil thermal conductivity relatively insensitive to VWC, except in the hot summer months, when the soil thermal conductivity diminishes significantly with decreasing VWC. Coherently, ST and LST become dominant in the summer, since the surface strongly heated by the solar radiation is not able to efficiently transmit this heat downward, becoming very hot and creating a large T2-LST difference (Figure 4.7a). The soil heat flux (G), measured well below that layer, shows less correlation in warm days than in the rest of the year (Table 4.3).

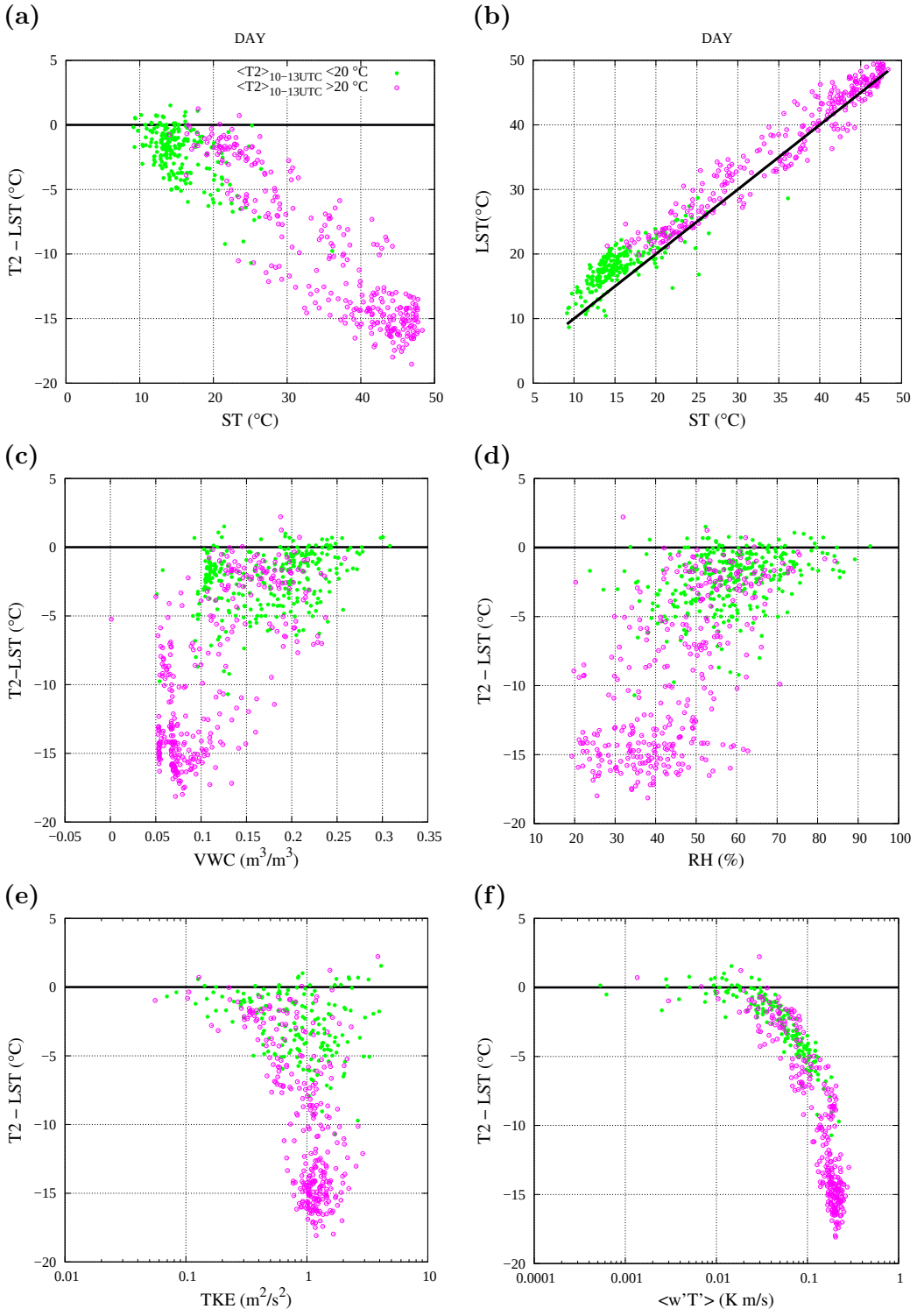

FIGURE 4.7: Relation of the diurnal (1000 – 1300 UTC) temperature difference between surface (LST) and air at 2 m height (T2) respect to the **(a)** soil temperature at 1 cm depth (ST), **(c)** soil volumetric water content (VWC), **(d)** relative humidity of the air (RH) at 2 m height, **(e)** Turbulence Kinetic Energy (TKE) and **(f)** buoyancy flux ($< w'Ts' >$). In panel (b) it is shown the relation between daily averages of LST and ST.

At night, the soil parameter with the largest correlation is ST, indicating that processes taking place in the surface layer affect the state of the upper levels of the soil. Figure 4.8a shows a decrease of T2-LST with increasing ST, and Figure 4.8b indicates that in the warm months ST is substantially warmer than LST at night. The low correlations with G and VWC may indicate that, under these conditions, soil thermal conductivity is large enough to provide heat flux upwards as needed independently of the actual value of T2-LST. For the warm summer nights, when VWC may be small, its correlation with T2-LST increases accordingly.

The atmospheric surface layer values indicate that the wind speed (WS), momentum flux (u_*) and turbulence intensity (TKE) are poorly correlated with T2-LST either at day or night (Figures 4.7e, 4.7f, 4.8e and 4.8f). More interesting is the correlation with T2 that is very low except for the warm days. It indicates that the value of T2-LST is determined essentially by LST and that T2 adapts to it in consequence. In the warm days, both the upper soil and the lower atmosphere are warm and well coupled and the correlation increases. RH is only significantly correlated for warm days and nights, when the contents of water vapour in the air is high. However the highest T2-LST values are found for summer dry cases (Figure 4.7d).

4.5 Concluding remarks

This chapter has addressed two issues related to LST. Firstly, the uncertainties related to the determination of its values using different sensors and approximations over locally homogeneous terrain have been inspected. The sensitivity of the long-wave radiation sensor is the main factor contributing to the uncertainties, with a minor extra correction related to the uncertainty of the value of emissivity. The associated uncertainties are in the range of 2 to 3 °C. This uncertainty range has to be taken into account when performing validation studies for LST estimated from satellite measurements or model simulations. In the latter cases, uncertainty related to terrain heterogeneity has also to be included, as indicated in Simó et al. [2016].

The second subject of analysis has been the statistical analysis of a two-year series of data of LST at the ECUIB station in Mallorca, derived from the measurements of a 4-component radiometer over a locally homogeneous surface. In particular the difference T2-LST has been characterized showing that the diurnal values are about -3 °C in winter and -10 °C in summer, increasing to -15 °C or more for hot and dry soil conditions. The difference is much smaller at night, typically between 0-1 °C in summer and 1-2 °C in winter. These differences are small and poorly significant compared to the uncertainty

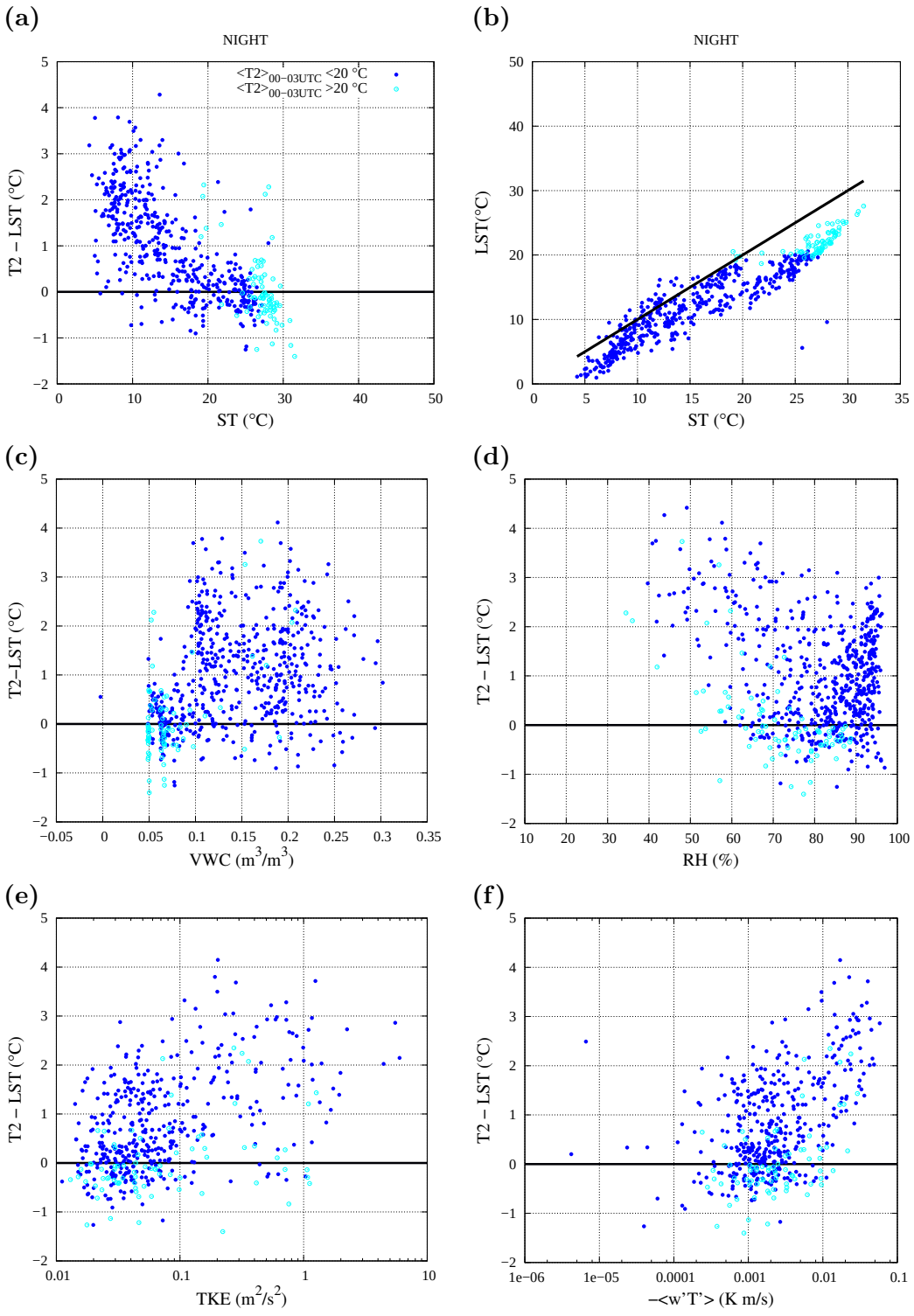

FIGURE 4.8: The same as in Figure 4.7 but for nocturnal values (0000 – 0300 UTC).

of LST, nevertheless indicating that very strong stable stratification is rare for this measurement location.

It is shown statistically that in the daytime T2-LST is mostly dominated by the solar heating of the surface transmitted upwards by the turbulent mixing. The maximum values in summer are due to the fact that the heat in the upper soil is poorly transmitted downward in a dry soil. At night all the terms of the energy budget are playing a role. However the major correlations of T2-LST are with the upper soil and surface temperatures and $< w'T_s' >$, while R_n and G seem to be responding in all conditions (therefore showing no correlation) to keep T2-LST typically below 3 °C. In hot summer nights the very weak values of T2-LST are related to the large amount of heat stored in the upper soil during the day, that does not allow the surface to become significantly colder than the surface layer air.

The sound estimations of the uncertainty of in-situ LST measurements and the characterisation of the annual cycle of T2-LST can be used as guidelines for future studies. To progress further, a systematic inspection of the evolution of the temperature profile between 2 m and the surface would be needed, including the canopy and the first centimetres below the surface, in the line of the work by Martí et al. [2016]. This would allow to increase the understanding on the processes behind the results found in this work, from which we have inferred some likely mechanisms that may be taking place.

Results from Chapters 3 and 4 have shown that thermal heterogeneities exists in the UIB Campus, and other magnitudes in the Atmospheric Surface Layer and in the soil are affected by them. The next step is to measure the heterogeneity of the atmospheric and soil magnitudes in the Campus of UIB, as it will be described in the next Chapter.

Chapter 5

Observed atmospheric and surface variability on heterogeneous terrain at the hectometer scale

In the two previous Chapters, the features of the spatial and temporal thermal heterogeneities are explored. Results have shown that the evolution of the magnitudes in the surface layer strongly depends on these heterogeneities. In this Chapter[1], the objective is to study the vertical and horizontal spatial variability of other magnitudes such as air temperature, relative humidity, wind speed and direction, water content in the soil and soil temperature. Observations are taken from an experimental field campaign in the Campus where different Poles where installed over the area at different locations to capture the variability of the soil properties. Meteorological measurements should be made in a location representative of the surrounding area, specially when they are used to validating model results or for climate studies. Over land, local surface heterogeneity is common, and it is often unclear which is the optimal location for a meteorological station.

To evaluate how the measurements in a precise location would differ compared to the ones made in nearby locations, nine stations are deployed during several weeks of summer 2016 in the Campus of the University of the Balearic Islands (a semi-rural heterogeneous area of 1 km side). The distance between stations is typically 150 m, and they are over different types of terrain. The variability of the atmospheric variables is large when the synoptic forcing is weak, especially in the nighttime, when 2m-temperatures may differ

[1]This Chapter is based on G.Simó et al. 2018: Observed atmospheric and surface variability on heterogeneous terrain at the hectometer scale. Submitted in *JGR-Atmospheres* and V.García-Santos et al. 2018: Study of Temperature Heterogeneities at subkilometric scales and impact of surface-atmosphere energy interactions. Under review in *Transactions on Geoscience and Remote Sensing*

more than 5 °C and there may be simultaneously very different wind directions in the Campus. In the daytime, turbulence manages to reduce the differences in temperature and humidity significantly, close to the resolution of the instrumentation. The variability of soil temperature and water content has also been inspected, showing sustained differences between the stations that are maintained along the diurnal cycle, although each point reacts differently to the atmospheric forcing. The effects of this variability in the values of the surface fluxes and in the Surface Energy Budget are explored, assessing the importance of the advection term over heterogeneous terrain.

In addition, during the study period, 5 IOPs (Intensive Operational Period) took place, in which LST measurements from a TIR camera onboard an unmanned aerial vehicle and scenes from the Landsat-7, ASTER and MODIS satellites were available. LST products were validated with in situ field data and corroborated that variations in LST up to 18 °C were appreciated with the UAV-TIR camera, and significant differences were also present in the LST products obtained from simultaneous overpasses of high-resolution satellite TIR sensors.

5.1 Introduction

The representativeness of an observation is the degree to which it accurately describes the value of the variable needed for a specific purpose [WMO, 2014]. For synoptic uses, the data should be representative of an area of about 100 km surrounding the station, for mesoscale this area reduces to a few kilometers, whereas for a specific site, such as an agricultural field, it should be just representative of that particular field. The quality of the data depends on the instrumentation used and the adequate exposure of the station. An inadequate location may generate values that can significantly depart of what would be an average value for the area of interest [Ehinger, 1993].

Specifically, WMO (World Meteorological Organization) recommends that stations are located on a level piece of ground, covered by short grass or a surface representative of the locality, surrounded by terrain with slope angles less than 19°, away from obstructions. In what concerns temperature, the main discrepancies between locations are caused by the type of surface and the eventual shading on the sensor. It is considered that a station is adequate when it is located in flat ground and at a distance of 30 m or more to obstacles or significant heterogeneities, provided that the surface over which it is located is representative of the area (WMO classes 1 and 2). Closer obstacles or heterogeneities imply adding uncertainty to the temperature data (1 °C for distances between 10 and 30 m, 2 °C between 1 and 3 m).

Data may enter the Integrated Global Observing System (WIGOS, WMO 2017) and be used for all kinds of weather and climate scientific and operational purposes, including reanalisis and verification. This work looks at the variability of the atmospheric and surface data in a moderately inhomogeneous flat terrain, where the homogeneous parcels have a hectometre scale, therefore each of them fulfilling WMO requirements. If significant variability was found, reflection on the current criteria for locating a station would be necessary.

Furthermore, in a number of applications, it is necessary to determine energy and water fluxes at the surface-atmosphere interaction [Bastiaanssen et al., 1998, Finnigan and Belcher, 2004, González-Dugo et al., 2017, Sánchez et al., 2008, Viterbo and Beljaars, 1995]. These may be obtained by direct measurement or estimated from the basic atmospheric variables [Bolle et al., 1993, Braud et al., 1993, Panin et al., 1998, Twine et al., 2000]. These fluxes are used, for instance, to develop and validate parameterizations to be used in numerical models, or to validate and adjust the models themselves. For heterogeneous terrain, which is the most frequent situation over land, the values of these fluxes will vary depending on which surface the measurements are made, for instance having different Bowen ratios (latent over sensible heat fluxes), net radiation or ground fluxes, [Geiger et al., 2009, Kang et al., 2007, LeMone et al., 2003a,b, 2007a,b, Mahrt, 2000, Panin et al., 1998, Patton et al., 2005, Strunin and Hiyama, 2005] depending on the state of the surface (degree of vegetation or soil moisture, among others). It is important to consider the heterogeneity of the region when, for instance, model outputs are validated with observations because the differences might be related to the representativeness of the meteorological station [Jiménez et al., 2008].

The terms of the energy budget will vary over the different elements of an heterogeneous landscape, the corresponding temperature of the air as well, and compensating thermal advective motions will setup between them. For instance, the spatial variability of soil roughness or soil temperatures might be responsible of local-scale circulations that have to be taken into account when considering all the contributions of the surface energy balance equation [Eder et al., 2013, Foken, 2008a, Foken et al., 2012, Mahrt, 2010]. These advective contributions may partially explain the observed imbalance of the energy budget [Cuxart et al., 2016a, Foken, 2008a] as well as significant differences in the values of the evapotranspiration [Kroon and De Bruin, 1995]. The study of Cuxart et al. [2016a] points out that heterogeneities at the hectometre scale may be the ones more relevant for this process, and Wrenger and Cuxart [2017] estimated that thermal advections close to well-defined heterogeneities (such as river and land) may have a thermal effect as large as turbulence at night. The study of Simó et al. [2016] for the Campus of the UIB using LST from Landsat-7 ETM+ indicated that variability in the Campus was very large and provided indications on where to deploy the stations. In the

same region, García-Santos et al. [2018] showed that the advection contribution in the surface energy balance depends on the scale of the heterogeneities of LST.

In this study, we deploy 9 instrumented Poles in a heterogeneous area of roughly 1 km side, that also contains a complete Surface Energy Budget (SEB) station with the purpose of inspecting the observed heterogeneity of the Surface Layer (SL) and upper soil variables. With the available information it is intended to quantify the corresponding variabilities and to inspect if some quantities could be used as estimators of this heterogeneity, such as the standard deviation, and to provide conclusions on the representativeness of each Pole for this area. Furthermore, the variability of the vertical gradients of temperature and moisture in the Surface Layer is also analysed to see how these first-order surrogates of the sensible and latent heat fluxes may vary. In addition, a study of the surface temperatures at sub-kilometric scales through a combined inspection of satellite-derived LST products and obervations from an UAV have done. Besides, these fields are used to explore the contribution of such heterogeneities in the imbalance of the SEB. An estimation of the thermal advection has also been obtained using the network of stations, and it is compared with the energy imbalance and the net radiation, indicating how significant the advection of energy can be over heterogeneous terrain.

This Chapter is organized as follows. Section 5.2 describes the experimental site and the available data and in Section 5.3 the variability at the hectometer scale is analysed, specifically for air temperature, humidity and wind and their vertical gradients, together with LST, soil temperature and humidity. Section 5.4 compares an estimation of the advection of temperature with the imbalance and the net radiation at a Surface Energy Budget station in the Campus. In the last two sections, the analysis shows a very distinct behaviour between day and night. Finally some conclusions are provided in Section 5.5.

5.2 Site and data

This study has been made in the Campus of the UIB, at Majorca, an island of 3640 km^2 in the Western Mediterranean basin, 200 km distant to the coast of the Iberian Peninsula. The Campus is located in a flat rural area at 7.5 km north of the center of the city of Palma and at about 3.5 km distance to the limit of the urban continuum, its height above sea level (asl) is 80 m. To the East of the Campus, cultures of carob, olive and fig trees dominate, whereas to the South and Southwest the same cultures are combined with sparse urbanization. To the North and the Northwest the terrain becomes hilly and covered by a combination of the same tree cultures and natural woods of pines and oaks,

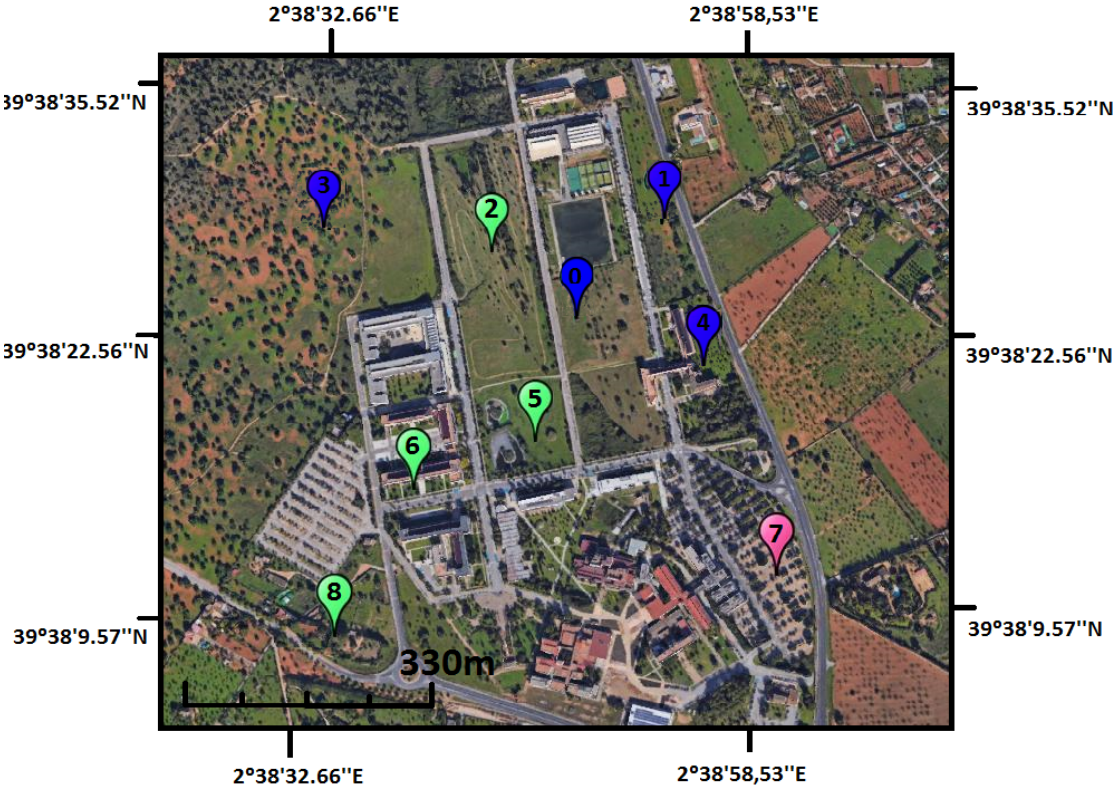

FIGURE 5.1: Position of the Poles in the Campus. The colour of the dots indicate the different soil uses within the Campus: short vegetation that dyes in summer (blue), vegetated areas such as sparse trees (green) and a paved region (pink). Source: Google Earth.

the Tramuntana range being just a few kilometres away in the same direction (Figure 3.1).

The UIB Campus is an approximately squared area of 1 km side. The faculty buildings are located mostly on a strip at the South and Southwestern parts and there are a few more buildings distributed over the rest of the area. The remaining terrain is covered by sports installations, green areas, tree cultures, vegetable gardens and inner roads. The situation between the coast and the Tramuntana range makes the coupled sea-mountain breeze systems are dominant at night [Cuxart and Jiménez, 2007] and during day [Cuxart et al., 2014, Jiménez et al., 2016] when the area is influenced by high pressure systems. Otherwise westerlies prevail.

To analyse the sub-kilometre variability, a number of identical instrumented Poles were set over different representative areas of the various types of terrain in the Campus, trying to keep a distance between Poles of the order of hundreds of meters (Figure 5.1). Nine Poles were at the ground level and another one was at the roof of one of the buildings at the South of the Campus (midway between Poles 7 and 8) and has not been used here. Their location was based on Figure 3.4, which shows that these sites are

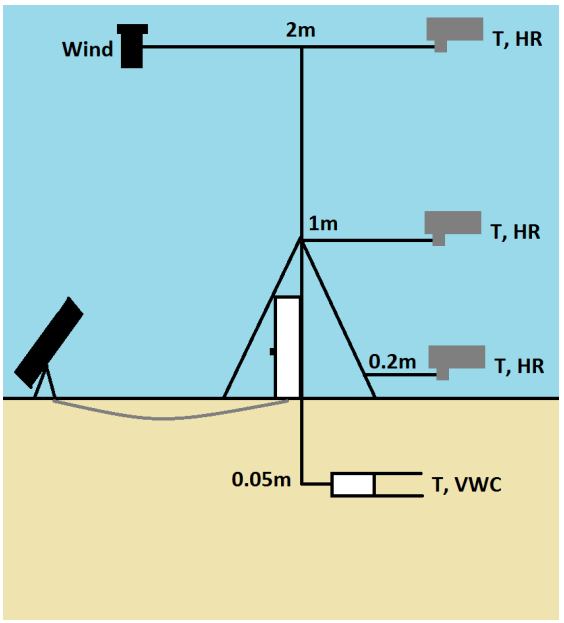

FIGURE 5.2: **(a)** Sketch of a Pole indicating where the different sensors are located and the magnitudes that they are measuring.

representative of the LST variability observed by Landsat 7-ETM+. Pole 0 was set aside a complete Surface Energy Budget (SEB) station to be able to check the goodness of the Pole data. The SEB comprises a Campbell NR01 4-component radiometer, a 81000 Young sonic anemometer, a Campbell EC150 open-path gas analyser and a Hukseflux HFP01SC ground heat flux plate, allowing to estimate the 4 main terms of the Surface Energy Budget and to compute the resulting imbalance.

The Poles have been setup by the authors. The structure (Figure 5.2) is made of three PVC cylinders making a tripod, on the top of which a two-dimensional Gill windsonic is installed at 2 m above ground level (agl). A PVC arm is mounted at 2 m agl in which an HyT temperature and humidity sensor is inside a shelter consisting in a double PVC cylinder covered in aluminium paper and with holes in the bottom. This shelter has been successfully tested comparing it with the traditional one made of double surface small dishes in the SEB station.

Temperature recorded by Pole 0 has been compared to the one measured by HC2S3 sensor 2 m distant and the correlation coefficient and the RMSE are 0.9974 and 0.3 °C, respectively. Two more levels of air temperature and humidity are set at 1 m and 0.2 m agl. The upper soil water content and temperature is monitored using a Campbell CS655 water content reflectometer at 5 cm below the surface. The data acquisition system has

been developed locally using Arduino micro-controllers and self-programmed boards, and the data were stored in a SD card. The system is powered by solar plates.

The data analysed here were taken in 2016, between March 21st and July 26th. The Poles were progressively installed and they were all functioning by June 30th. The installation day and the available data for each Pole are indicated in Table 4.3, in which the type of surface over which they are set are also noted (see also Figure 5.3). Poles 0, 1, 3 and 4 are over short vegetation that dies as we approach summer (in blue in Figure 5.1), Poles 2, 5, 6 and 8 are over vegetated areas (irrigated for Pole 6) including sparse trees (green dots in Figure 5.1) and Pole 7 is over a partially paved area (a parking area made of stripes of macadam and land with trees, in pink in Figure 5.1). For the latter no soil measurements were installed and for Pole 2 the temperature and humidity sensors at 1 and 0.2 m agl malfunctioned.

To optimize the energy use and data storage, sensors were interrogated every 5 minutes but every minute in the case of the windsonic (from where 5 minutes averages are computed). There is a temporal variability in the amount of data, related to the number of working Poles and also to the occurrence of periods with no data for a particular Pole due to technical problems. Therefore, depending on the variable being analysed, a different amount of data will be used and this will be described in the text as needed.

The period with more simultaneous data was the one between June 30th and July 26th, for which most of the aspects of horizontal variability have been explored, a period with high air temperatures and low soil water content. For integrated diagnostics, such as standard deviation, averaged horizontal gradients or advection estimates, the available information has been used since the beginning of the Pole installation at the end of March, using 3h-averages at noon (1000 to 1300 UTC) and midnight (0000 to 0300 UTC) to isolate the persistent heterogeneities. The same temporal intervals where used in previous Chapter to obtian values representative of the daytime and nighttime. The variability of the vertical gradients is computed from June 16th on, since that date was when most of the 0.2 m sensors were installed, and also 3h-averages at noon and midnight are used. For comparison to the energy imbalance at the SEB station for a particular period, 30-minute averages of the advection estimates are used whereas 10-minute averages are used to deploy advection against wind and temperature. As an example, the period 14th-15th July is taken as a cloudy day and 21st-22nd July as a clear sky day.

The satellite LST data that have been used in this study are those of MODIS, Landsat-7 and ASTER, these are explained in Chapters 2 and 3. In addition, the UAV-TIR (Figure 5.4, further details in Chapter 2) has been used to make transects and obtain the surface

(a)

(b)

(c)

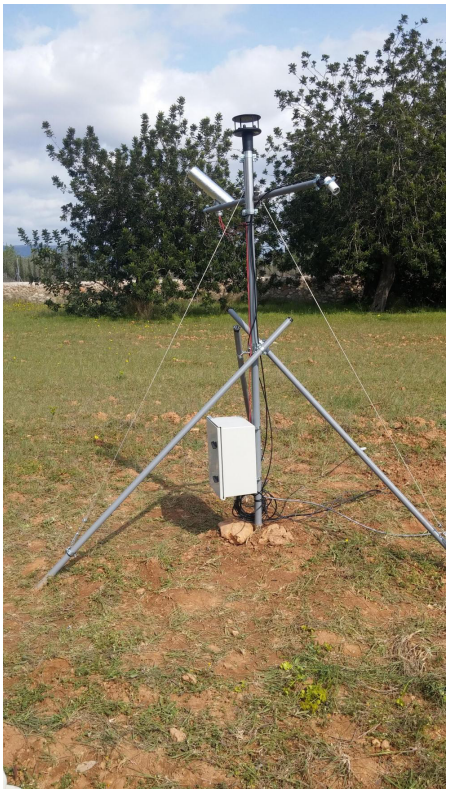

(d)

FIGURE 5.3: Pictures of the different poles: **(a)** Pole 0, located at ECUIB; **(b)** Pole 6; **(c)** Pole 1 and **(d)** Pole 4 before its installation was completed.

	Pole 0	Pole 1	Pole 2	Pole 3	Pole 4	Pole 5	Pole 6	Pole 7	Pole 8
Air temperature at 0.2m	X	X	X	X	X		X	X	X
Air temperature at 1m	X	X	X	X	X		X	X	X
Air temperature at 2m	X	X	X	X	X	X	X	X	X
RH at 0.2m	X	X	X	X	X		X	X	X
RH at 1m	X	X	X	X	X		X	X	X
RH at m	X	X	X	X	X	X	X	X	X
Wind Speed at 1m	X	X	X	X	X	X	X	X	X
Wind Direction at 2m	X	X	X	X	X	X	X	X	X
Soil temperature at -0.05m	X	X	X	X	X	X	X		X
Volumetric water content	X	X	X	X	X	X	X		X
Soil type	1	1	2	1	1	2	2	3	2
installation date	03/21	03/21	03/21	04/09	03/21	03/21	06/10	06/30	06/06

TABLE 5.1: Variables measured by each Pole and type of soil over which they are located. Soil type 1 is short/dead vegetation, soil type 2 is with grass and sparse trees and soil type 3 is partialy paved area (coloured in blue, green and pink, respectively, in Figure 5.1). The data of installation of each Pole is indicated in the lowest line (month/day

FIGURE 5.4: UAV-TIR camera ensemble prior to start the flight.

temperature of the entire Campus during 5 IOPs (19-20/06/2016, 28-29/06/2016, 05-06/07/2016, 14-15/07/2016, 21-22/07/2016), which allows complementing the measures of the Poles. In this study, we have defined as IOPs the days with available Landsat-7 and ASTER scenes over the region, in addition to the flights with the UAV-TIR.

5.3 Spatial variability of air and soil variables

The availability of simultaneous information at 9 different locations within the Campus allows inspecting several aspects concerning the small scale heterogeneity of the measured atmospheric and soil variables and some derived quantities, such as some terms of the Surface Energy Budget.

5.3.1 Observed variability within the UIB Campus

Figure 5.5 displays Hovmöller plots for the five selected variables using the mean hourly value for the period between June 30th to July 26th 2016, when the weather was mostly with clear skies, but comprising a few cloudy days and a rainy event at June 29th. The averages computed from observations of the 9 Poles are used here to explore the horizontal variability of these fields within the Campus.

The diurnal cycle of the wind speed for all the Poles is very close (Figure 5.5a). For all the Poles it is maxima during the central hours of the day (between 1.5 and 3 m s^{-1}) with a clear predominance of winds from the northern sector (not shown). On the contrary, winds are weaker during the nighttime (about 0.5 m s^{-1}) and mainly from the southern sector. These winds correspond to Sea-Breeze and Land-Breeze circulations present during day and night, respectively [Cuxart et al., 2007, 2014, Jiménez et al., 2016]. Sea-Breeze is very common in the warm season of the year and in the Campus it is reinforced by the upslope winds due to the presence of the mountains at its north [Cuxart et al., 2007]. The Sea-Breeze is stronger at the Poles 0 and 2, where the wind has overcome the obstacles at the southern part of the Campus. For the rest of the Poles the diurnal cycle of the wind is weaker because some of them are in the shade of the breeze. During nighttime the largest winds are reported in Pole 2 because it is placed in a creek and channeling of the downslope winds occurs during nighttime.

The air temperature (Figure 5.5b) shows a relatively small horizontal variability (about 2 °C) in the central daytime hours. The morning warming and the early evening cooling take place very similarly at all Poles. These temperature patterns are related to the presence of Sea-Breeze and slope winds in the Campus. Under such conditions, the atmospheric boundary layer is well mixed by turbulent motions and therefore no significant differences are reported between the Poles. Pole 8 is warmer than the others at the central hours of the day. This might be related to the fact that Pole 8 is located in densely vegetated area with small size plants and the soil volumetric water content is the smallest of the Campus (Figure 5.5e) because plants use the water from the soil. As a result, the most vegetated areas are the driest and the hottest (largest soil temperatures, Figure 5.5c) and therefore the air temperature is also warmer than for the rest of the Poles, as it was found in according to Azeñas et al. [2018]. Nighttime displays a more clear variability increasing along the night (up to 5 °C), with Poles 2, 3 and 5 taking the lowest values, all located in open areas away from buildings, Pole 5 sitting in a very shallow terrain depression.

The soil temperature (Figure 5.5c) displays a well-defined diurnal cycle at every Pole. For Pole 8 (green vegetation) has more than 20 °C of amplitude, while for Pole 0 (bare

ground and dead vegetation) is of about 10 °C. Spatial variability for an instant either at day or at night is in the range of 10 to 15 °C, and the largest variations correspond to vegetated terrain. This variability is comparable with the one found by Simó et al. [2016] when inspecting the land surface temperature estimated with Landsat-7 over the same area at a resolution of 30 m. Another interesting features is that for all the Poles the morning warming and the early evening cooling take place in an interval of 2 hours (between 0800-1000 UTC and 1700-1900 UTC, respectively), depending on the soil features. However, these transitions are more simultaneous when inspecting the 2 m-temperature (Figure 5.5b).

The amount of specific humidity (Figure 5.5d) has a less clear diurnal cycle, displaying the highest values after 1000 UTC, probably related with the arrival of the Sea-Breeze according to Jiménez et al. [2016] that usually lasts until sunset. Pole 5 has a problem with the sensor. Nocturnal values are usually smaller, which may indicate either condensation at the surface or advection of drier air. Minimal values take place after sunrise and before the breeze starts. Pole 2 increases humidity at night, it is in a relatively vegetated area of the Campus, also somewhat more sheltered than the other Poles.

The soil water content (VWC, Figure 5.5e) takes low values with large differences between Poles that show very little diurnal variation, with the noteworthy result that the areas with higher VWC correspond to the Poles over surfaces essentially bare or with dead vegetation (Poles 1, 2 and 3). The ones with lower VWC are those in areas with green vegetation (Poles 2, 6 and 8), indicating that the vegetation is drying the ground faster through transpiration than the simple evaporation process from the soil that rules in Poles 1, 2 and 3. It is also noticeable that Pole 3 is the only one with a clear diurnal cycle with maximum values close to noon. This is the most porous soil and during the night it is able to store moisture whereas during daytime it is easily evaporated. Note that Pole 7 has no underground data and that the threshold value of the CS650 sensor is about 0.05 m^3 m^{-3} and averaged values close to it might be no reliable.

Summarizing, observations from the Poles show that the horizontal variability in the Campos is related to the differences in the soil features. Besides, the radiative warming and cooling during day and night, respectively, and the wind speed also contribute to enhance or diminish this variability, as it was also found in LeMone et al. [2003b] or in Acevedo and Fitzjarrald [2001].

The air temperature at 2 meters depending on the wind direction, at North (downslope winds) and at south (Sea-Breeze) is shown in Figure 5.6. During the night the wind in most of the Poles is from North (corresponding to downslope and Land-Breeze direction), except in the Pole 6, placed in a street (East-Weast oriented) with a building 5 meters away in the North. Therefore the wind in Pole 6 is biased and strongly channeled in

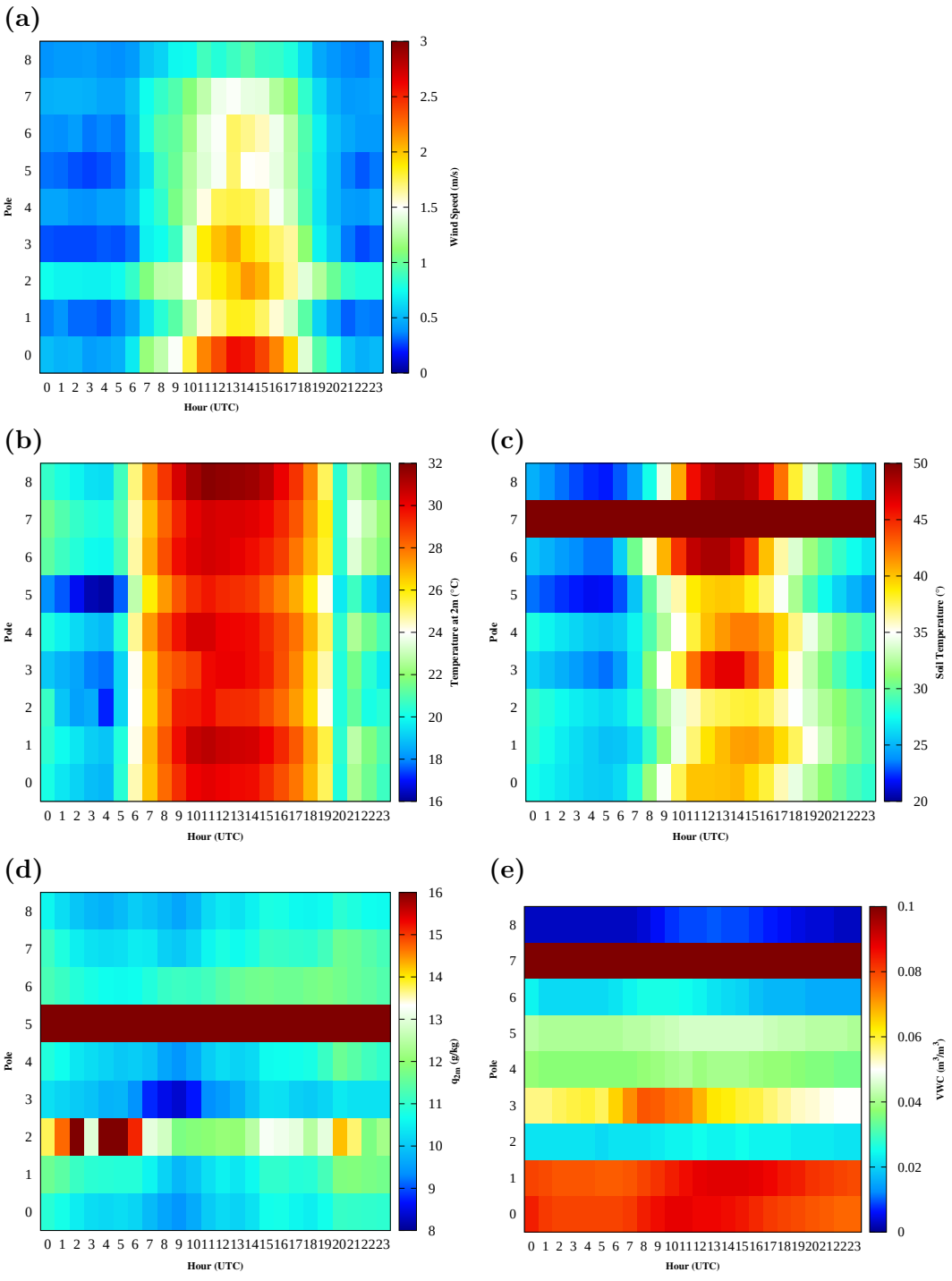

FIGURE 5.5: Hourly means for each Pole during the whole period analysed (table 1) to explored the diurnal cycle of the horizontal variability within the Campus of several magnitudes: **(a)** wind speed at 2 meters, **(b)** temperature at 2 meters, **(c)** soil temperature, **(d)** specific humidity at 2 meters and **(e)** volumetric water content.

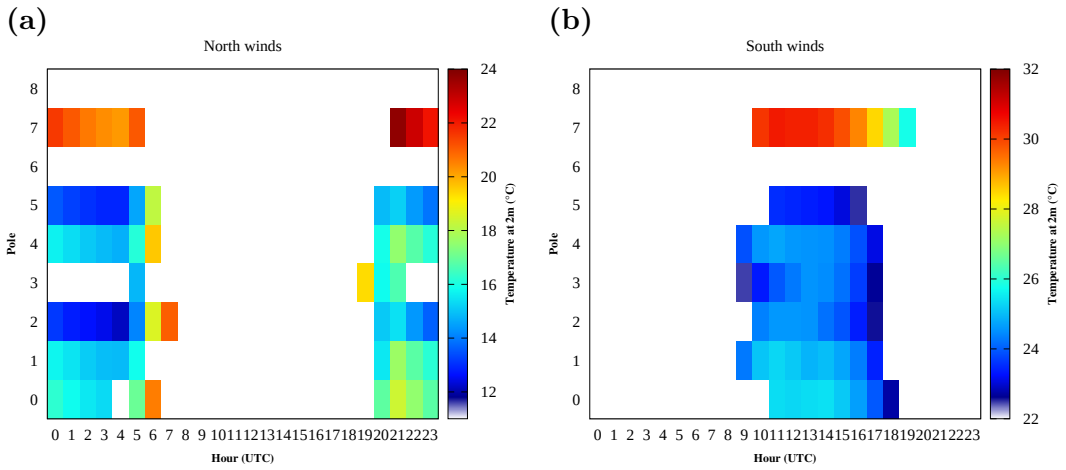

FIGURE 5.6: Temperature at two meters hourly means for the whole period analysed (Table 5.1) depending on wind directions for the different Poles located through the Campus: (a) North winds and (b) South winds. White values indicate that there are no observations following this criteria.

that direction. During day, the wind blows in the direction of Sea-Breeze (South) as expected except in Pole 6 which is biased as explained before and Pole 8 that generally records very weak winds due to the nearby obstacles (trees, houses and wall). Pole 7 is the warmest, for northerly and southerly directions. This might be related to the surface conditions. The ground heats a lot during day and does not cool down during night as the ohter Poles.

5.3.2 Integrated estimators of the horizontal variability.

In order to provide a more synthetic value to evaluate the degree of inhomogeneity of these values we compute two quantities, the average of the differences between the measurement points[2] (Δx) conceptually similar to a mean gradient over a grid mesh, and the standard deviation of the observed values[3] (σ_x, where x is any magnitude measured by the Poles) and see how these two quantities compare in value and in temporal behavior. In fact the substitution of ΔT by σ_T was made in Cuxart et al. [2016a] to estimate the value of the thermal advection for a heterogeneous terrain, there taken as a strong hypothesis that here we aim to see how far it was from observations. Figures 5.7a, 5.7c and 5.7d show Δx and σ_x for x=(T, ST, VWC) computed every 5 minutes and averaged for the nearly stationary periods 1000 to 1300 UTC in the daytime and 0000 to 0300 UTC in the nighttime, providing series of diurnal and nocturnal data along the experiment between March 21st and July 26th.

[2] $\Delta x=[(x_0-x_1)+(x_0-x_2)+...+(x_{n-1}-x_n)]/n$

[3] $\sigma=\sqrt{\left(\sum_{i=1}^{n}(x_i-\overline{x})^2\right)/(n-1)}$

In the daytime ΔT and σ_T take values about 0.3 °C (Figure 5.7a top), both evolutions being very similar and in general σ_T being slightly larger. The nocturnal values are 1 °C above the diurnal ones, indicating that the spatial variability is larger at night (as in LeMone et al. [2003a]) in absence of convective mixing. If we focus in one particular period, a very warm day with clear skies (Figure 5.7b), now using 5-minute values, we observe that σ_T nearly doubles the value of ΔT for the whole period, but the qualitative evolution of the two quantities is almost identical, being larger at nighttime than at daytime. The heterogeneity seems to reach a minimum value just before the sunset, during the evening transition, when the convective mixing ceases and before the nocturnal radiative cooling enhances the thermal contrasts between the different areas within the Campus. We conclude that these two quantities can be taken as reasonable indexes to characterize thermal heterogeneity.

The thermal heterogeneity of the upper soil (Figure 5.7c) is larger than the one of the air temperature, with the diurnal values of the heterogeneity indexes ranging typically between 2 and 6 °C and the nocturnal ones between 1 and 2 °C. This significant surface heterogeneity in the daytime is therefore diminished in the SL, most likely due to convective turbulent mixing as anticipated before. In the nighttime, the surface and the SL have very similar values and time evolution, as already shown in Simó et al. [2018], indicating that both quantities are very well linked for this period, with the surface heterogeneity presumably driving the SL one, because its value is larger.

The variability of the soil moisture (Figure 5.7d) shows a slow evolution, with no obvious difference between the diurnal and nocturnal averaged values. The large increases seem to correspond to periods immediately after a rain event (such as after June 29th), when each type of surface manages differently the new water. The values are in general very small, similar in magnitude to the measured water content, which is very low for this period.

5.3.3 Horizontal variability of the vertical air temperature and humidity gradients.

It is also of interest to inspect how the vertical gradients of temperature and specific humidity change between Poles, since they can be considered a first-order surrogate of the variability of the turbulent sensible and latent heat flux respectively [Stull, 1988]. The differences between the Pole measurements at 2 m and 0.2 m are taken, using the 3-h averaged values in day (1000 – 1300 UTC) and night (0000 – 0300 UTC), which are relatively stationary periods. Figures 5.8 and 5.9 show the evolution of these gradients for the temperature and humidity, respectively, between June 16th and July 26th. The

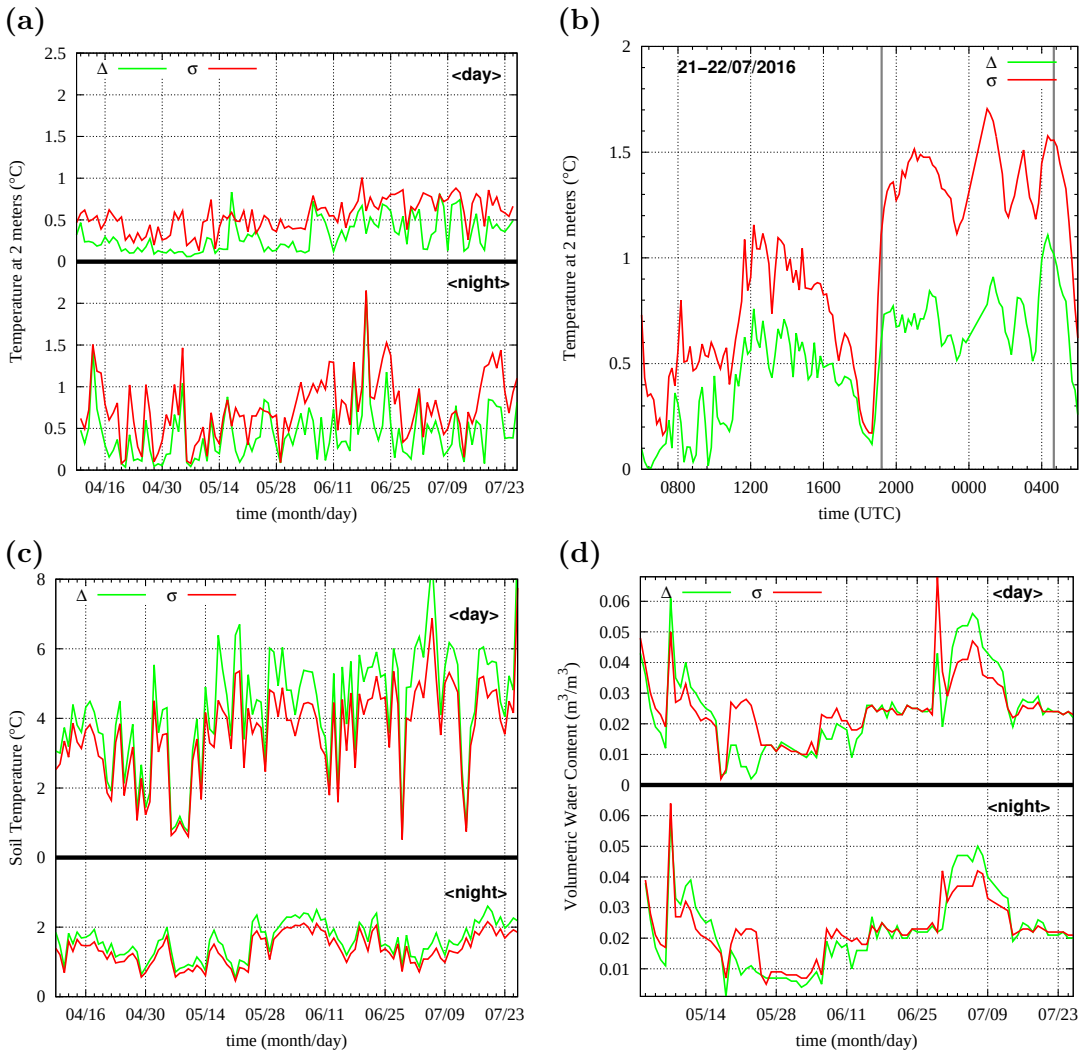

FIGURE 5.7: Diurnal daily averages (1000 – 1300 UTC) on the top and nocturnal daily averages (0000 – 0300 UTC) on the bottom of each Figure between Δ and σ calculated using data for the different Poles (from March 21st and July 26th) located through the Campus: **(a)** temperature at two meters, **(c)** soil temperature and **(d)** volumetric water content (from May 1st to July 26th). In **(b)** Δ and σ for the temperature at two meters during the IOP5 (June, 21-22) that was clear sky day where gray bars indicate the sunset and sunrise.

PDFs computed from the observed gradients within these intervals are also included in the figures to compare the variability of the vertical gradient for the different Poles. The horizontal variability of the vertical gradients of the temperature and humidity is clearly seen by the combined inspection of the time series and the PDFs. Other heights have also been explored (Appendix D), as well as the dependence between air temperature at 2 m and air temperature at 0.2 m with other variables (Appendix E) as it was found in the previous Chapter for T2-LST.

Figure 5.8 clearly shows that the variability of the temperature gradient during day is larger than during night. During the day, all Poles are in unstable conditions (maximum

of the PDF in the negative values) and the variability is very close (the width of the PDFs is similar, although the temperature range is different). The ones over bare surface have larger thermal instability (Pole 0,1,3,4), whereas the less unstable one is Pole 6, placed over an irrigated grass field. Pole 2 has a bimodal behavior, this is due to the wind direction (not shown), if it comes from the North direction which is a colder and more humid zone, the difference between the temperature at 2 meters and at 0.2 is larger. Pole 8 is centered around -3 °C, although in some days these differences are lower, becoming positive in some cases. The nighttime temperature gradients vary from neutrality to very stable (the maximum of probability in the PDFs is in the positive values), except for the Pole 7, located in a paved area. This is because this soil heats up much more during the day and takes longer to cool at night, and on many nights its temperature remains higher than the air temperature.. The largest vertical gradients (2.5 °C in 1.8 m) are reported in Pole 8, placed over green vegetation and in an area with low wind speeds, so there is not much air renewal.

The vertical gradients of specific humidity (Figure 5.9) in the daytime show that the value decreases with height in almost all the cases (except for some days in Pole 2 due to instrumental problems) and the maximum of probability in the PDFs is centered in the negative values. The largest gradient corresponds to Pole 6, placed over an irrigated grass. The other Poles have very small vertical specific humidity gradients in accordance to the very low soil water availability below them. More interesting is the situation at night, when some Poles have negative gradients and other positive ones (maximum probability centered in positive and negative values). The former would correspond to evaporation as in the daytime, while the latter would indicate loss of humidity to the ground, therefore condensation at the surface. This implies that within the Campus there are simultaneous occurrences of positive and negative latent heat flux at night with a consequently large spatial variability of the SEB terms.

5.4 Land Surface Temperature heterogeneities at sub-kilometric scale

Vegetated surface targeted by IR-120 radiometer is representative of the surface surrounding the SEB station, and it is even representative of the 42% of the surface of the UIB Campus. Therefore, we consider that this LST could be used as reference to validate the LST product calculated by ASTER-Terra, Landsat 7-ETM+ and UAV-TIR Camera sensors.

Figure 5.10 shows the validation results for LST product of ASTER, ETM+ and TIR Camera compared with the IR-120 radiometer from data from the pixel located at the

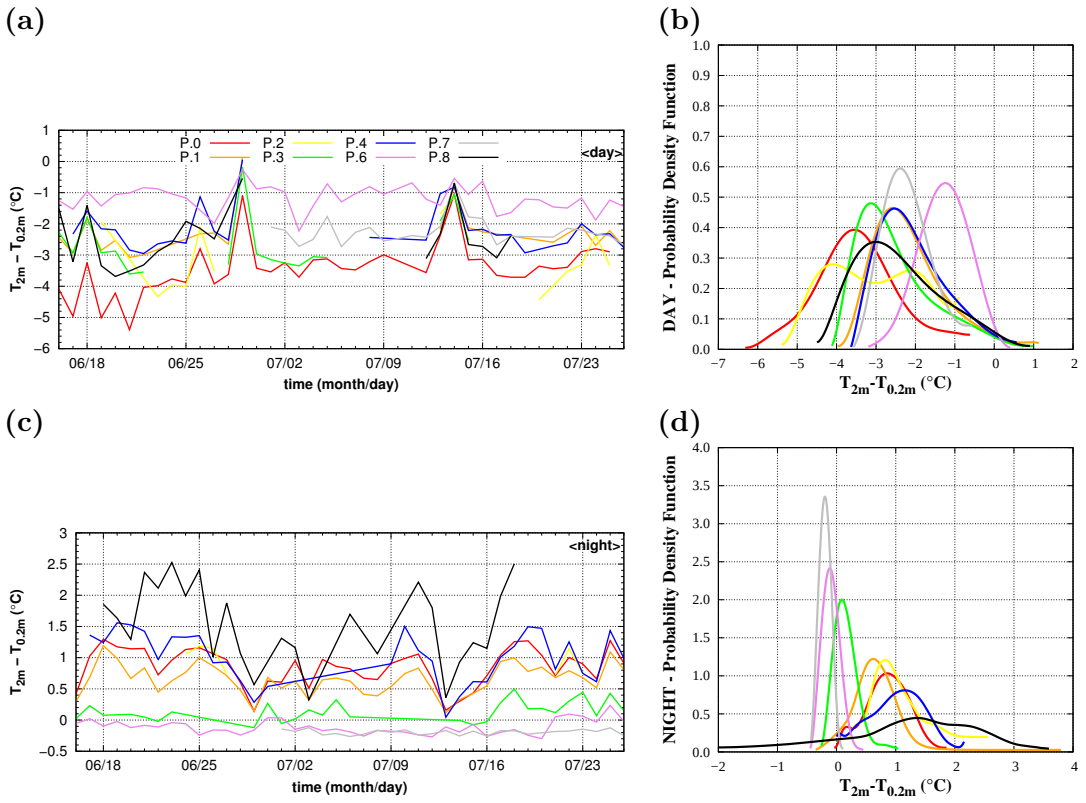

FIGURE 5.8: **(a)** and **(c)** Time series of the diurnal daily averages (1000 – 1300 UTC) and nocturnal daily averages (0000 – 0300 UTC) of the temperature gradient (temperature differences between 2 meters and 0.2 meters) for each Pole. The corresponding Probability Density Functions are shown in **(b)** and **(d)**.

ECUIB for the times that the corresponding sensors pass. Comparison between MODIS LST product and that measured by the ground radiometer was not considered because spotted surface measured with the IR-120 is not comparable with kilometric LST value derived by MODIS, especially in a heterogeneous terrain (Chapter 3). ASTER, ETM+ and TIR Camera LST product show a RMSE respect to radiometer temperature of ± 1.3°C, ± 1.8°C and ± 3.1°C and a bias of -0.5°C , -0.5°C and -0.6°C, respectively. In the case of the ASTER sensor a RMSE of ± 1.4°C for both morning and night overpasses was observed. For the ETM+ LST product a RMSE of ± 1.6°C and ± 2.3°C was observed for the different orbits.

Validation results of this study are confident with previous validation works. So for the ASTER sensor LST uncertainties of $\pm(1-2)$°C were observed [Coll et al., 2005, Hook et al., 2007, Tonooka, 2005]. In the case of the Landsat 7-ETM+, the validation results of this study are also in good agreement with a previous UIB Campus study (Chapter 3) and with other past published works [Coll et al., 2010, Li et al., 2004] where a RMSE of $\pm(1-2)$°C was found in the LST product derived from the band 6 of the ETM+ sensor.

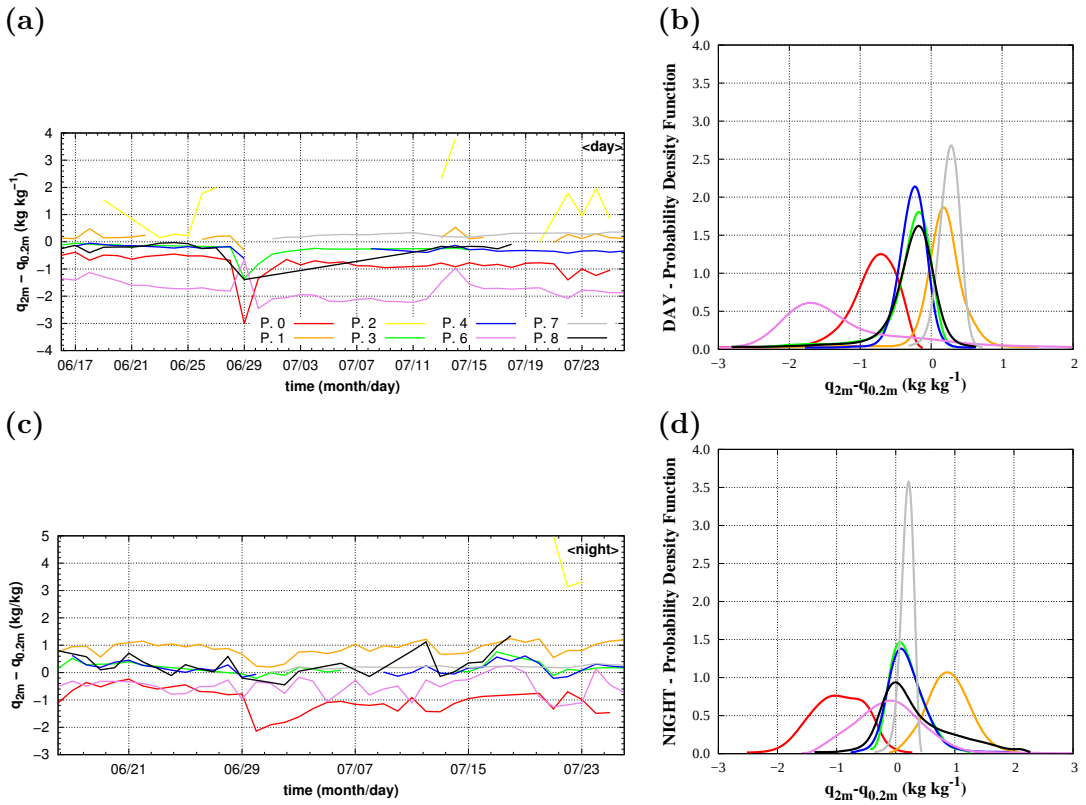

FIGURE 5.9: The same as Figure 5.8 but for the vertical gradient of humidity.

Once the retrieval method of the LST product for the 4 different sensors considered (MODIS, ASTER, ETM+ and TIR Camera) have been described and the corresponding uncertainties of such products stipulated, it is time to analsze the possible LST heterogeneity of the UIB Campus.

Figure 5.11 shows the LST maps of the UIB Campus for four of the nine UAV-TIR Camera flights (0400, 1000, 1200 and 2200 UTC) during an IOP (21/07/2016). LST variability shown in maps of Figure 5.11 is representative of the four IOPs carried out in cloudless condition. These IOPs showed significant LST differences within the campus from the first flight. The maximal LST variations observed in each IOP ranged within (3–18) °C along the day. They ranged (6–10) °C during the first flight before the sunrise (0400 UTC), (3–4) °C during the second flight after the sunrise (0600 UTC) and increased significantly to (11–18) °C during the central hours of the day (0800–1600 UTC). The hottest point is located at the artificial grass of the soccer field and the coolest point is usually located in one of the roof of the multiple buildings of the UIB Campus or in humid creek area, situated to the North of the campus. The last two flights before the sunset (1600–1800 UTC) showed a slightly decreased LST variability (6–12) °C that increased later in the early night flight at 2200 UTC to (8–13) °C (Figure 5.115d) where the asphalted areas are the warmest ones and increase the nocturnal LST variability.

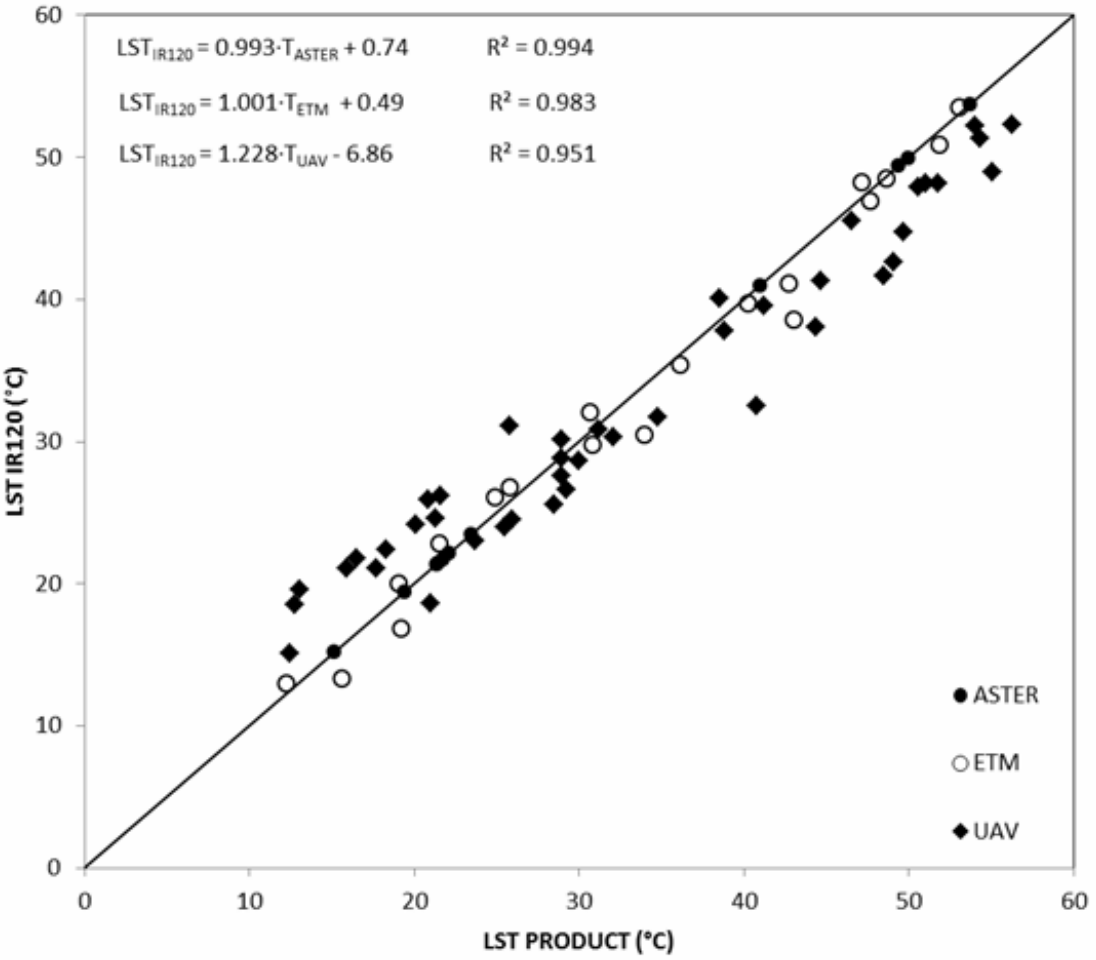

FIGURE 5.10: Comparison of the LST measurements of the IR120 field radiometer with LST products retreived from ASTER and ETM+ orbiting sensors and aerotransported TIR Camera. Linear Trendline for the three sensors and R^2 are included.

Figure 5.12 shows the LST product of the four sensors at their different spatial resolution for the IOP under cloudlees conditions. The high LST heterogeneity observed by the UAV-TIR Camera product at a resolution of 2 m x 2 m (Figure 5.12d) is considerably reduced as seen by the spatial resolution of 30 m x 30 m of the LST product calculated for the Landsat 7-ETM+ TIR data (Figure 5.12c), where almost all the cold pixels of the UAV LST map are effectively converted to temperate LST values as a consequence of the spatial degradation. The loss of information of the LST heterogeneities is more evident with the LST product offered by the ASTER sensor (Figure 5.12b) at 90 m x 90 m and this heterogeneity is imperceptible with the MOD11 LST product (Figure 5.12a) at 1 km x 1 km.

Despite the loss of LST information, with the high resolution LST product of ETM+ and ASTER sensors with regard to that offered by the UAV-TIR Camera, both sensors still show significant LST variability. So, for instance the maximum LST difference observed between the soccer field and the wet creek in the North of the UIB Campus is 16°C for

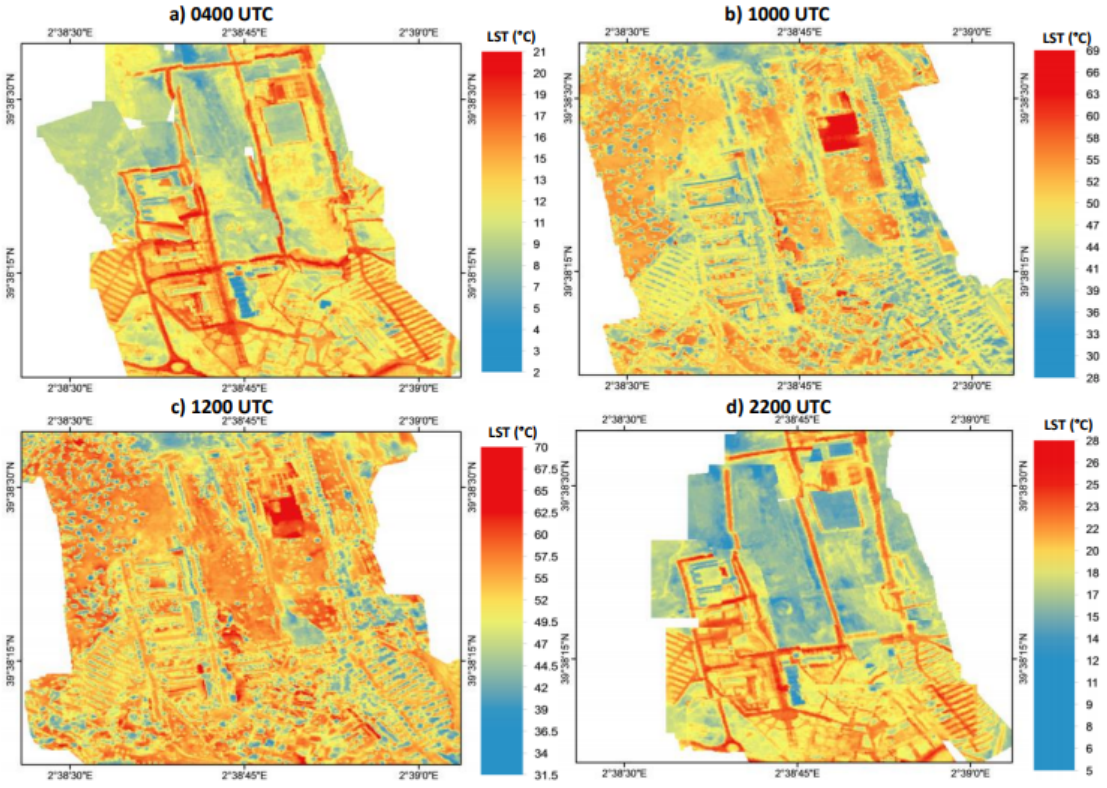

FIGURE 5.11: Comparison of the LST measurements of the IR120 field radiometer with LST products retreived from ASTER and ETM+ orbiting sensors and aerotransported TIR Camera.

the UAV-TIR Camera product, but despite this difference was reduced to 11°C with the ETM+ and to 9°C with the ASTER LST products, both differences are still very significant.

The same fields during night overpass of the sensors ASTER and MODIS, onboard the Terra platform, compared with the LST product calculated from the simultaneous UAV-TIR Camera flight over the UIB Campus are shown in Figure 5.13. Under those stably stratified thermal conditions at night, significant LST differences are seen, like the 14°C between the artificial grass of the soccer field (cold point) and the road in the South-Western part of the UIB Campus (warm point). This difference is reduced to 7°C with the LST product offered by the ASTER sensor, which is still very significant. MODIS showed LST differences of 2°C for the four pixels covering partially the UIB campus.

Figures 5.12 and 5.13 are a clear example that high spatial resolution on LST products is of key importance to study heterogeneities in zones composed of different surface types. In both cases it was observed that the pixels composed by dense vegetation, like the wet creek, showed the coldest zones and other pixels composed by tarmac roads, bare soil or the soccer field, made with artificial grass, showed the hottest points of the LST map at midday. At midnight the presence of grass (even the artificial one of the soccer

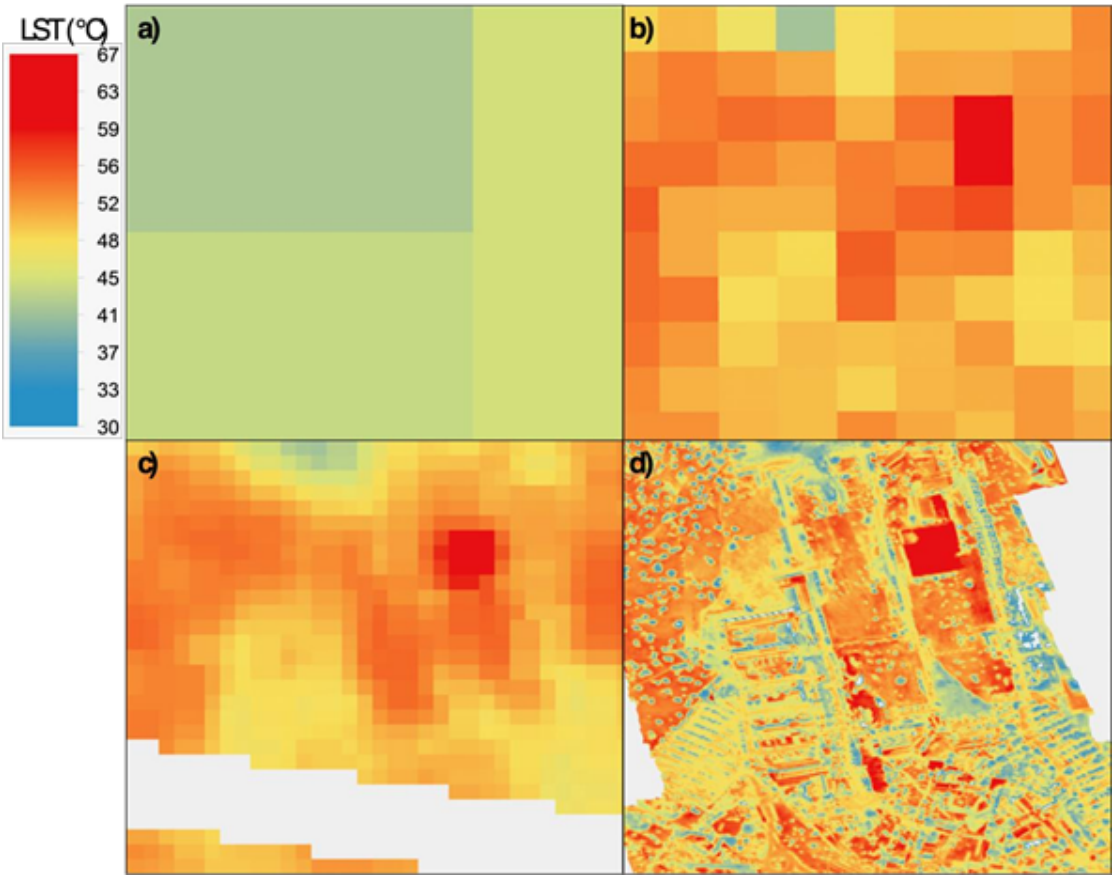

FIGURE 5.12: LST product of the simultaneous overpassing sensors on 21/07/2016 between 1033-1049 UTC for: **(a)** MODIS, **(b)**) ASTER, **(c)** ETM+, and **(d)** UAV-TIR Camera Flight.

field) and the asbestos roof of some buildings are the coldest points and the influence of tarmac roads produce the hottest pixels of the map. These temperature differences in both cases remain in the LST product of ETM+ and ASTER sensors, but MODIS does not show them, since they correspond to sub-kilometric spatial resolutions.

5.5 Impact of the variability in the Surface Energy Budget at one point

As mentioned above, the variability of the surface and SL temperature and moisture may explain significant variations of the different terms of the SEB depending on the specific location where they are measured. The SEB can be derived from the equation of the evolution of the temperature for a volume comprising the air-ground interface [Cuxart et al., 2016a] as

$$R_n + H + LE + +G = Imb \tag{5.1}$$

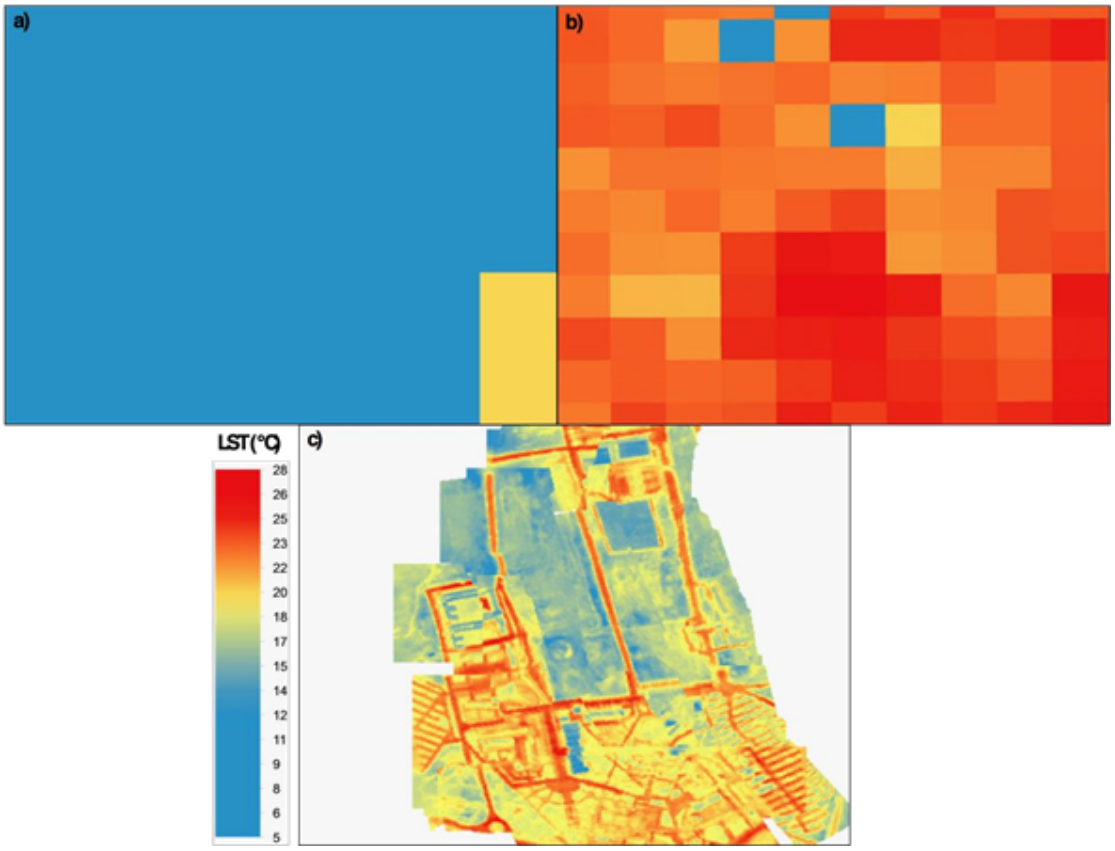

FIGURE 5.13: LST product of the simultaneous overpassing sensors on 21/07/2016 at 2153 UTC for: **(a)** MODIS, **(b)** ASTER, **(c)**) UAV-TIR Camera Flight.

where R_n is the Net Radiation term, G the ground heat flux and H and LE are respectively the sensible and latent turbulent heat fluxes. Imb is the sum of advective processes (A), temperature tendencies, the ensemble of natural and anthropic heat sinks and sources and any other process, including instrumental issues and uncertainties. Therefore Imb will approach zero in nearly-homogeneous landscapes, with slow time tendencies and very well set instrumental displays.

It has been already indicated that upper soil temperature and moisture vary largely in the domain of study, which directly affects R_n and G, and it also influences the values of H and LE as indicate the significant spatial variability in the SL vertical gradients of temperature and moisture. Warm spots will experience upward air motion over them and colder air will flow from the neighboring areas. The related thermal effects should essentially be described by the advection term A, which should include the horizontal and the vertical motions corresponding to these circulations. A could be computed along the direction x of the wind and vertically as

$$A = A_x + A_z = -u\frac{T_f - T_i}{\Delta x} - w\frac{T_u - T_l}{\Delta z} \tag{5.2}$$

where T_f and T_i are respectively the temperatures of the point of destination of the flow and of its origin, whereas T_u and T_l represent the temperatures of two points in the vertical of the location of interest. The minus sign comes from considering these terms in the r.h.s. of the equation of evolution of the temperature, where a positive term implies a heating (warm advection) and vice versa. To obtain the advection in W m^{-2} Equation 5.2 is multiplied by a factor ρc_p taken as ρ= 1.225 kg m^{-3} and c_p= 1.006 kJ kg^{-1} K^{-1} which are the density of the air and the specific heat respectively.

Cuxart et al. [2016a] estimated the order of magnitude of A_x based on a number of observed and numerical estimations of the surface variability for scales between tens of kilometers and a few meters for an area in Southwesterly France. They concluded that thermal gradients at large scales contributed very little to changes in SEB, whereas hectometer-scale heterogeneity provided estimated values of A_x in the range of the observed imbalance, especially at night. Smaller scale heterogeneity is essentially managed by turbulent mixing. This conclusion has been further stressed by a recent study by García-Santos et al. [2018] that showed how, for our current area of study, the estimated order of magnitude of the advection term from satellite scenes fits best at hectometer scales with the observed imbalance for the SEB at the UIB Campus.

Those previous works did not consider the effect of the sign in the advection term and provided upper values for the estimated horizontal thermal advection. With the instrumental display available in this study, where wind and temperature are measured at nine different locations distant each other a few hectometers, we may estimate positive and negative horizontal thermal advections for the location of the SEB at the Campus, which is nearby Pole 0, and provide more realistic estimations of the values of horizontal advection in the SL.

5.5.1 Computation of the advection term using data from the Poles

To proceed the direction of the wind at Pole 0 is taken and the horizontal advection is computed considering the thermal differences between Pole 0 and the Poles located in the two quadrants that the wind blows above, as displayed in Figure 5.14 for two examples. The warm and cold contributions are computed separately, each one being the average of the number of pairs, and finally the total horizontal advection is given as the difference between both quantities. For instance in Figure 5.14a, with NE wind only differences of Poles 1, 5, 6 and 8 with Pole 0 are computed, the differences that are positive are added and divided by the number of positive contributions and the same is done with the negative differences. This way, the larger the number of contributions of one sign, the better its estimation.

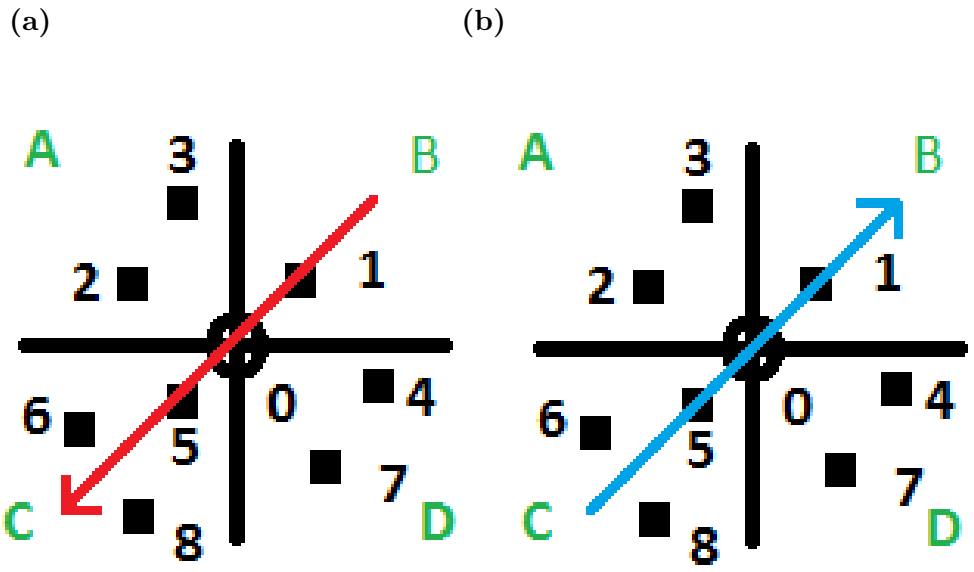

FIGURE 5.14: Graphical diagrams to show how the advection has been calculated. The red arrow indicates warm advection and the blue one cold advection. The location of the Poles is indicated with a square and the number of the Pole aside. Pole 0 is centered in this diagram.

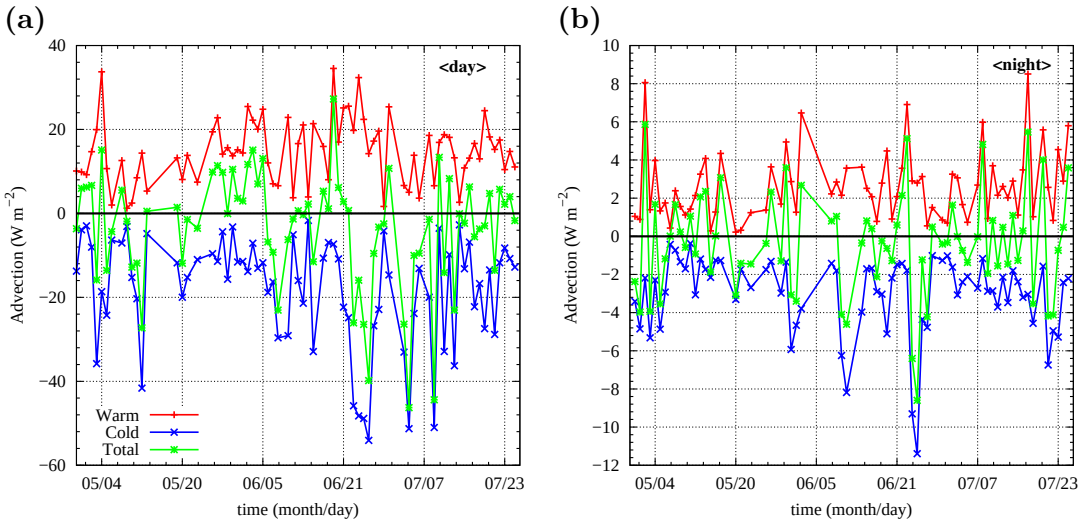

FIGURE 5.15: Time series of the advection computed in Pole 0 at the middle of the Campus averaged over two periods: **(a)** diurnal daily averages (1000 - 1300 UTC) and **(b)** nocturnal daily averages (0000 - 0300 UTC). Cold , warm and total advections are indicated in blue, red and green colours whereas the zero value is shown in black.

Figure 5.15 displays the evolution of the values of the diurnal and nocturnal estimations of the cold and warm horizontal advections over the SEB position using the average values between 1000 and 1300 UTC in the day and 0000 and 0300 UTC in the night. In the daytime each contribution is of the order of a few tens of W m^{-2} that added result in an average value typically between 20 W m^{-2} and -20 W m^{-2}, whereas at night the values are one order of magnitude smaller, amounting only a few W m^{-2}. However at night, this value is of the same order as other terms in the SEB, especially H and LE when the turbulence is weak. Instead, the values in the daytime are much smaller than other main terms of the SEB, including the Imbalance.

5.5.2 Contribution of the advection from the measured imbalance

SEB is usually computed for shorter time periods (some tens of minutes) in most applications. In Figure 5.16a and 5.16b are displayed the 30-minute values for the SEB imbalance (computed as a residual of the observed RN, G, H and LE) and A_x for two days, a cloudy one (July, 14-15 2016) and one with clear skies (July, 21-22 2016). The cloudy day has smaller imbalance than the clear day and very small A_x. The day with clear skies shows clearly that A_x is much smaller than the imbalance in the daytime, and tending to cool that spot, which is warmer in average than its surroundings [Simó et al., 2016]. In the nighttime with clear skies, A_x and imbalance are of similar magnitude and both are negative. This indicates that in the SL A_x is cold, probably a circulation flowing to a nearby warm spot, and that in this case very likely it would be the vertical advection (A_z) by subsidence that could compensate this cooling. An estimation of vertical advection of 1°C/2 m by a speed of -0.01 m s^{-1} at night for Pole 0 would provide a heating of about 10 W m^{-2}, similar to the horizontal advection cooling, sustaining the idea of a three-dimensional advective process.

5.5.3 Correlations between the estimated advection and measured magnitudes

The 10-minute values of the estimated advection are displayed against air temperature at 2 m, relative humidity, soil temperature, VWC and the wind speed and direction in Figure 5.17, together with the same plots where the advection is divided by the net radiation. In the daytime, the values of the advection grow with increasing air and soil temperature and wind speed, and decreasing with RH, but the ratio with net radiation remains almost constant, below 30%. During the nighttime, the values are smaller but the ratio with net radiation is larger than in the daytime, especially for weak winds.

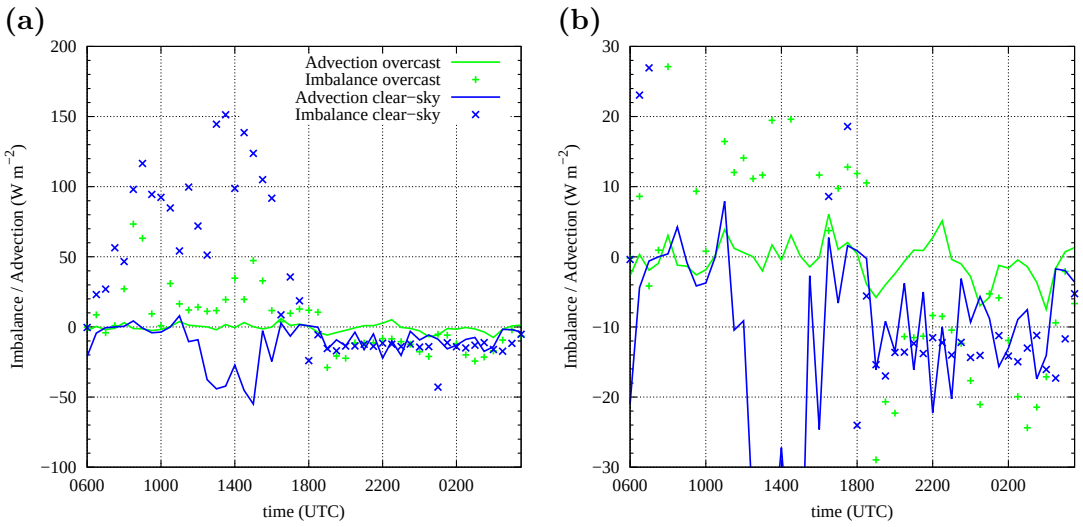

FIGURE 5.16: **(a)** Comparison between the diurnal cycle of the estimated imbalance (derived from the residual of the SEB observations) with the estimated advection computed from the Poles for a overcast (14-15 July) and a clear-sky (21-22 July) days. A zoom to better show the nocturnal values in **(b)**.

Zooming for wind speeds below 1 m s^{-1} at two meters, we see that most of the nocturnal weak winds blow from the northern sector (Figure 5.18), when the local circulations prevail, with very significant values for A_x, in many cases comparable to the typical values of the imbalance at night (near 30%). Figure 5.17 makes clear that the largest nocturnal advection values are for wind speeds at 2 m between 0.3 and 0.7 m s^{-1} when they can amount for several tens of W m^{-2}, very likely much larger than H and LE.

In Figure 5.19, it can be observe the dependence of the difference between imbalance and advections compared to other variables. In general it is observed that during the day (in red) the biggest differences are found, especially for the sunny day (Figures 5.12, 5.13 and 5.16), but instead, this night is when the smallest differences between imbalance and advection were found. It can be concluded that on clear nights with weak winds, with the presence of downslope winds, advection is the main cause of the imbalance.

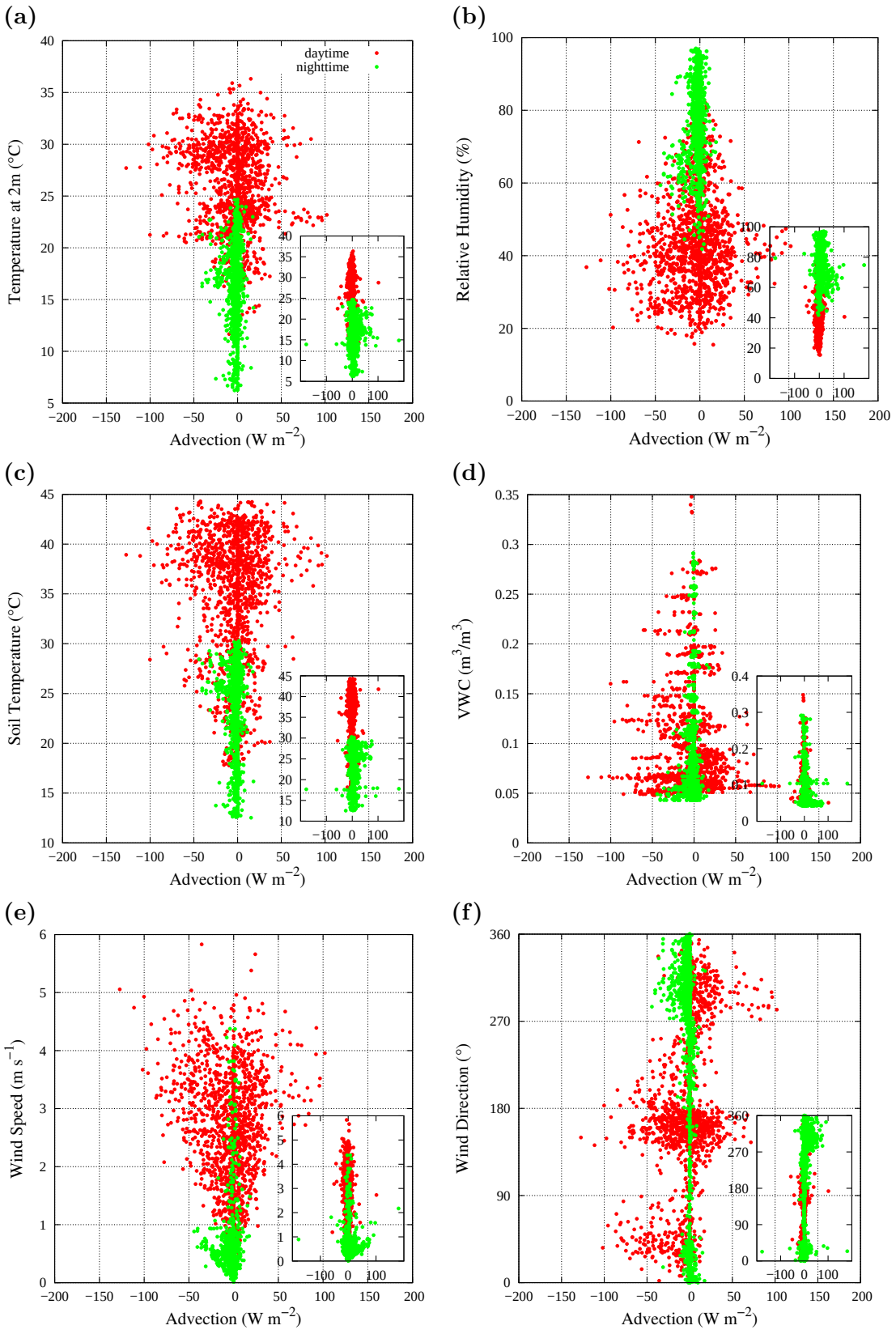

FIGURE 5.17: Correlations between the estimated advection and the different variables measured at Pole 0 during the period April 29th to July 26th 016 for: **(a)** temperature at two meters, **(b)** relative humidity at two meters, **(c)** soil temperature, **(d)** volumetric water content, **(e)** wind speed at two meters and **(f)** wind directino at two meters. 10min data are taken and the colours indicate the diurnal (1000–1300 UTC) and nocturnal (0000–0300 UTC) values. There is the same plot inside each figure at the corner but for the percentage of advection of the net radiation.

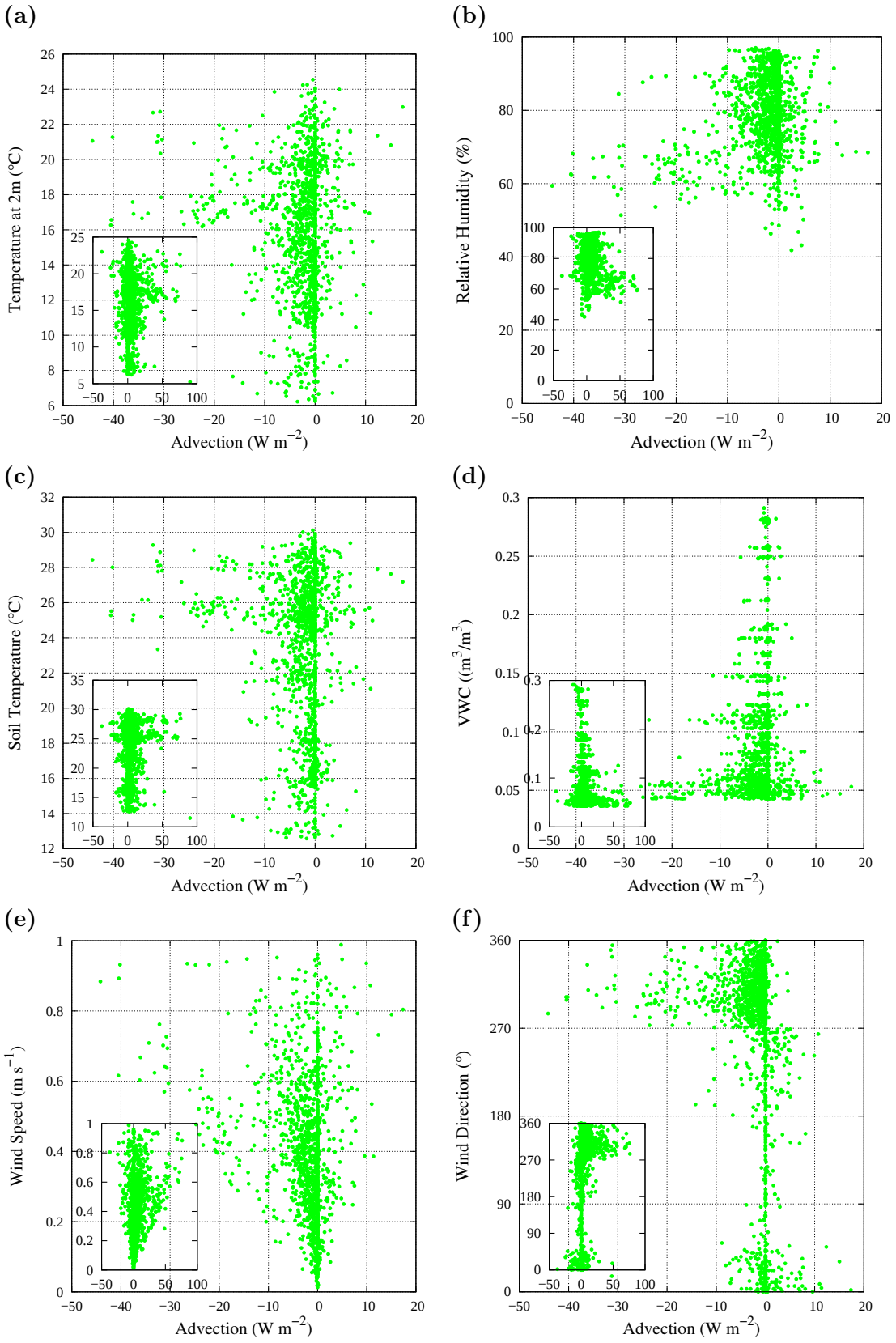

FIGURE 5.18: Same than Figure 5.17 but for nights with wind speeds lower than 1 m s^{-1}.

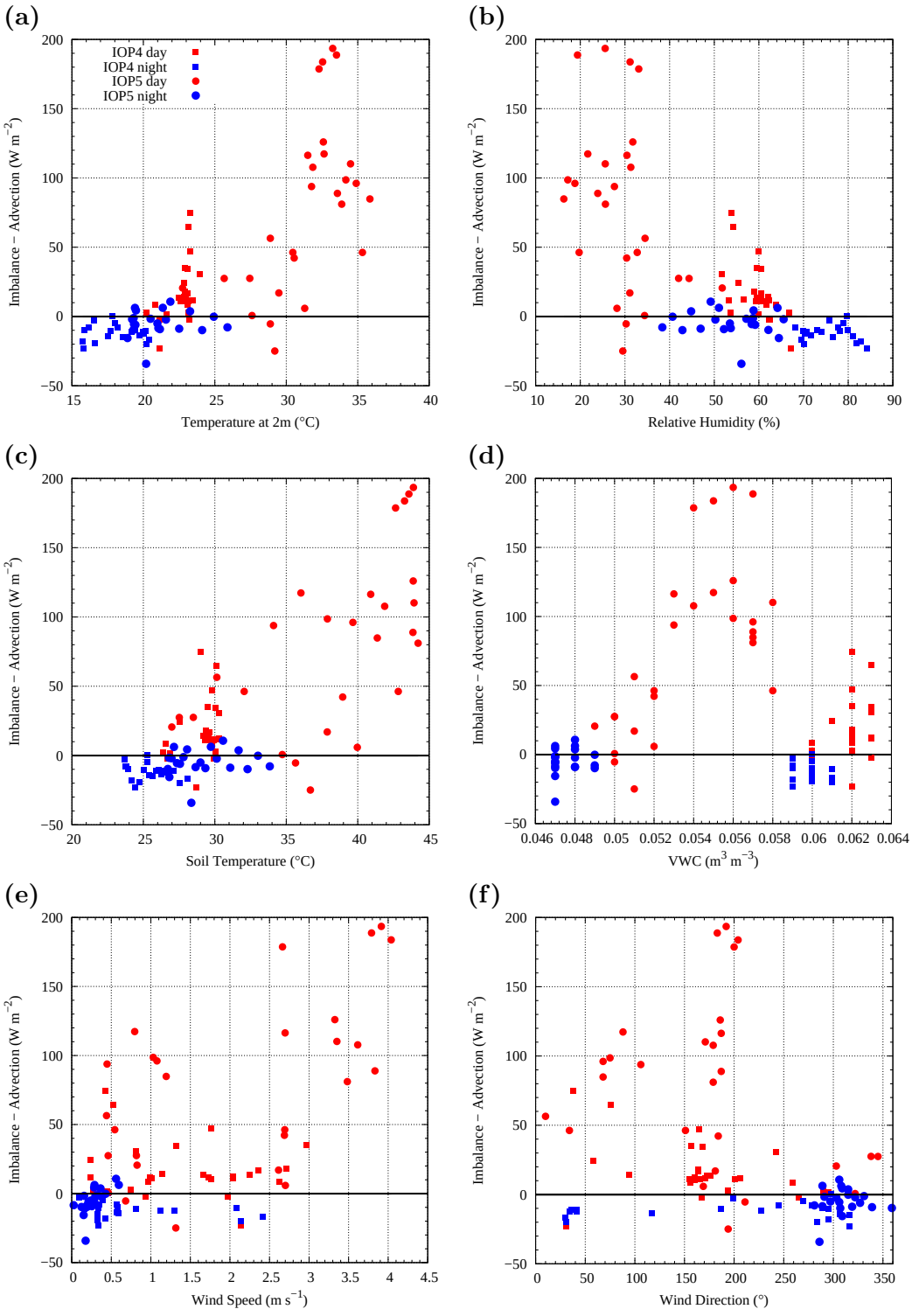

FIGURE 5.19: Difference between the imbalance and the advection with some variables for clear-sky (triangles) or overcasts (squares) conditions during daytime (red) and nighttime (blue): **(a)** temperature at two meters, **(b)** relative humidity at two meters, **(c)** soil temperature, **(d)** volumetric water content, **(e)** wind speed and **(f)** wind direction. Data are averaged over 30 minutes.

5.6 Concluding remarks

The use of nine instrumented Poles in the UIB Campus has allowed to inspect the spatial variability at the hectometer scales of the temperature, humidity and wind in the SL and of the upper soil temperature and moisture. Simultaneous plotting allows to see direct differences between Poles, but the computation of mean differences or the standard deviation of the inspected variables provides good estimators of the heterogeneity using a single quantity.

For one single instant in the daytime of a day with clear skies, the variability in the SL is small, of a couple of degrees in temperature and 2 g kg^{-1} in the specific moisture or 1 m s^{-1} in the wind speed, which is not departing much of what are the requirements of a measuring site according to WMO. This relative homogeneity of the air variables, forced by turbulence mixing, is not seen in the upper soil variables, that have a significant spatial heterogeneity during daytime.

At night, the upper soil variability behaves as in daytime, but the SL displays larger variability, that may reach differences between Poles up to 5°C in the 2 m air temperature, essentially depending on the state of the surface below it, due to the very low mixing efficiency of turbulence in clear and calm nights. It is clear that the choice of a representative location should follow a previous study to determine what specific site would behave more closely to the average value of the area that must be represented by the measurement, especially for the nocturnal hours.

On the other hand, the availability of several measuring levels of air temperature and humidity has allowed to study the variability of their vertical gradients in the SL. It is found that temperature and specific humidity gradients are all negative in the daytime indicating that for all Poles there are positive values of sensible and latent heat fluxes of different values along the Campus. Instead at night, the temperature gradient may vary from very weak positive values to significant negative gradients, showing that depending on the Pole there will be unstable or stable stratification. The same occurs with the specific humidity gradient, showing likely evaporation or condensation depending on the Pole.

Results show that such LST products, after validation, are capable of detecting significant temperature gradients in a heterogeneous area, which can reach differences in the case of the UAV-TIR camera system of up to 18°C during the morning and 14°C at night. These differences remain significant with the high resolution satellite TIR sensors, but were not seen with the medium resolution LST product of the MODIS sensor.

This spatial variability of the estimated turbulent heat fluxes, together with the one of the upper soil temperature and moisture that affects the ground heat flux and net radiation, indicates that the terms of the SEB will vary significantly between spots, and also its imbalance. Only one SEB station was available on site and the imbalance of its energy budget is compared to an estimation of the horizontal advection. It is seen that the average values of A_x are relatively small, specially in the daytime, but that they become significant in nights with clear skies and very weak winds, when they may be larger than the turbulent heat fluxes.

For 10-minute values and winds below 1 $\mathrm{m\,s^{-1}}$, A_x may amount in some cases about 30% of the net radiation, being of the same order of magnitude as the imbalance of energy. However, the imbalance is usually negative at night, meaning that the terms compensating the radiative cooling of the surface do not manage to compensate, the imbalance being much larger than the one corresponding to the actual cooling of the SL. Instead, A_x can take either positive or negative signs, the negative ones dominating and contributing to the increase of the imbalance. It is a pending issue to explore if subsidence warming in the SL, a part of A_z probably well linked to A_x, could reduce the imbalance, as some rough estimations given in this work seem to indicate.

To conclude, results from this Chapter show a methodology to identify the heterogeneities of an area and to estimate the corresponding local circulations. A combined inspection of satellite-derived LST at hectometric scale with in situ observations can give a clear picture of their spatial and temporal variability. The UIB Campus heterogeneity is influenced by the hectometric and kilometric surface heterogeneities that produce circulations that are predominant depending on the hour of the day or the season. To continue, in the next Chapters we will expand the spatial range of heterogeneities to better study the thermal circulations.

Chapter 6

Thermal heterogeneities at the kilometer scale: a case of Sea-Breeze

In the previous chapters, heterogeneities have been studied at the hectometric scale, with the purpose of understanding how they affect the circulations and atmosphere-soil exchanges. In this Chapter[1] heterogeneities are studied on a larger scale and a case of an observed Sea-Breeze is taken. An experimental field campaign took place in September 2013 near the coastline in the South-Eastern Campos basin on the island of Mallorca, to measure the lower atmosphere during the transition between the Land and Sea-Breezes. Favourable weather conditions were only found for one episode that comprised a well-formed nocturnal Land-Breeze, followed by the morning transition to Sea-Breeze until noon the next day, when incoming clouds switched off the breeze regime.

This case was further analysed together with a high-resolution mesoscale simulation. The official network of stations is used, supplemented by a portable station close to the shore and soundings of temperature (taken by a captive balloon and remotely controlled multicopter). These data are taken to check the goodness of the corresponding simulation at a horizontal resolution of 1 km. Model and observations see similarly the transition, showing some differences in the timing and the details in the surface layer. This transient event is analysed in terms of phases, going consecutively: through Land-Breeze; previous phase (land heating starts but it is still colder than the sea); preparatory phase (land becomes warmer than the sea) and development phase (breeze front progresses inland).

[1]This chapter is based on Jiménez et al., 2015: Morning transition case between the land and the sea breeze regimes. *Atmospheric Research* 172-173,pp. 95-108.

6.1 Introduction

The Atmospheric Boundary Layer, which is the layer of air directly affected by the presence of the underlying surface, can have different regimes, depending on the large-scale forcings. When the general winds are weak and the cloudiness is low enough to allow the surface net radiation to have a diurnal cycle, the ABL shows a characteristic evolution, with a Convective Boundary Layer in the daytime and a Stably stratified Boundary Layer at night, with the two corresponding morning and evening transition events in between [Garratt, 1992].

Whereas the CBL is essentially a turbulence driven regime by surface heating, the SBL over homogeneous terrain is mainly controlled by the surface radiative cooling, that can be transported upwards if there is turbulence generated by the wind shear. The transitions are governed by the establishment of a thermal surface inversion in the evening and by the destruction of the inversion in the morning. These transitions are currently a subject of study of deep interest due to their incomplete characterization so far for several reasons: (1) the difficulties to measure the surface energy budget and the relative importance of the terms [Cuxart et al., 2016a], (2) the similarity theories that may not be of application since the heat fluxes and the wind are nearly zero, and there is still not a widely accepted similarity theory to describe the surface layer in these conditions [Lapworth, 2003, 2006], (3) the definition and quantification of the boundary-layer depth [Lothon et al., 2014], (4) the fact that turbulence may be intermittent and anisotropic [Sun et al., 2012], (5) the temporal evolution of the surface fluxes and their dependence on the heterogeneity of the surface [Nadeau et al., 2011], (6) the processes in complex terrain regions that make a more complicated picture of the dynamics of the morning transition [Lenschow et al., 1979]. In heterogeneous terrain, the slope winds generated by horizontal thermal differences interact with other flows and modify the ABL state. Typical cases are the slope and the valley flows that increase the wind shear at lower levels and enhance mixing close to the surface [Whiteman, 2000], or the sea and Land-Breezes, that may even change the turbulence regime, for instance making it thermally unstable at night over the sea by the coast [Cuxart et al., 2007].

The Land-Breeze (LB) and the Sea-Breeze (SB) have already been studied numerically by some authors of this study (Cuxart et al. [2007, 2014], from now on CJTG14) for the island of Mallorca, using data from the operational network for validation of the model results. The regimes are strongly modulated by the presence of moderate terrain slopes that contribute to the establishment of LB and SB and the topographical features of the three main basins of the island (Figure 6.1). At night downslope flows converge to the center of the basins and are expelled towards the sea enhanced by the LB, whereas in the daytime, SBs from the different basins tend to converge at the center of the island

[Ramis and Romero, 1995]. In CJTG14 a deeper analysis was performed for the SB in the Campos basin, at the SE of the island. The budgets of momentum, temperature and turbulence extracted from the model were used and a proposition of phases of the evolution of the SB was stated.

In this Chapter, the focus is put on the morning transition (MT), whereas the previous efforts were devoted to the LB and SB separately. At this time the thermal circulations due to temperature difference between land and sea are initiated. Here the coastal area is the zone of study, instead for those studies the analysis was performed for the central part of the Campos basin, exploring the interaction of the breeze and the slope flows. As before, we dispose of numerical simulations and the operational network of AEMET (Spanish Agency of Meteorology), but an additional experimental display is set, operating a supplemental weather station close to the coastline, and a tethered balloon and a multicopter drone to provide profiles for the lowest hectometers of the atmosphere. This configuration has allowed to characterize a MT case between a LB and a SB regimes, both experimentally and numerically, progressing towards a more complete picture of the daily cycle of this regime.

6.2 The studied case and the model setup

6.2.1 Description of these regimes and their occurrence in Mallorca

The diurnal variation of the land-sea differential heating produces a cross-shore pressure gradient and an onshore/offshore wind is generated during the day/night (SB/LB) [Atkinson, 1981]. The general knowledge about the main features of the SB show that a maximum wind speed is formed below 800 m (above ground level, agl) of about 5 m s^{-1} [Bechtold et al., 1991] just after the maximum insolation (between 1500-1700 UTC for the island of Mallorca, CJTG14). Most of the studies related to the SB are mainly focused on the mature phase, being worth mentioning the study of the establishment of the SB/LB, their return currents at higher levels of Johnson and O'Brien [1973] in the central Oregon coast (USA), the impact on the modelled surface features to properly capture the onset of SB by Miao et al. [2003] or their interactions with the larger-scale wind (Bora, Telisman-Prtenjak et al. [2010]).

The climatological analysis of Azorin-Molina and Chen [2009] of the surface observations in the easterly Iberian Peninsula shows that the initiation of the SB depends on the strength of the LB and also on the direction and intensity of the synoptical wind. Panchal [1993] indicates that the initiation of the SB also depends on the features of the previous SB, besides the thermal difference between land and sea.

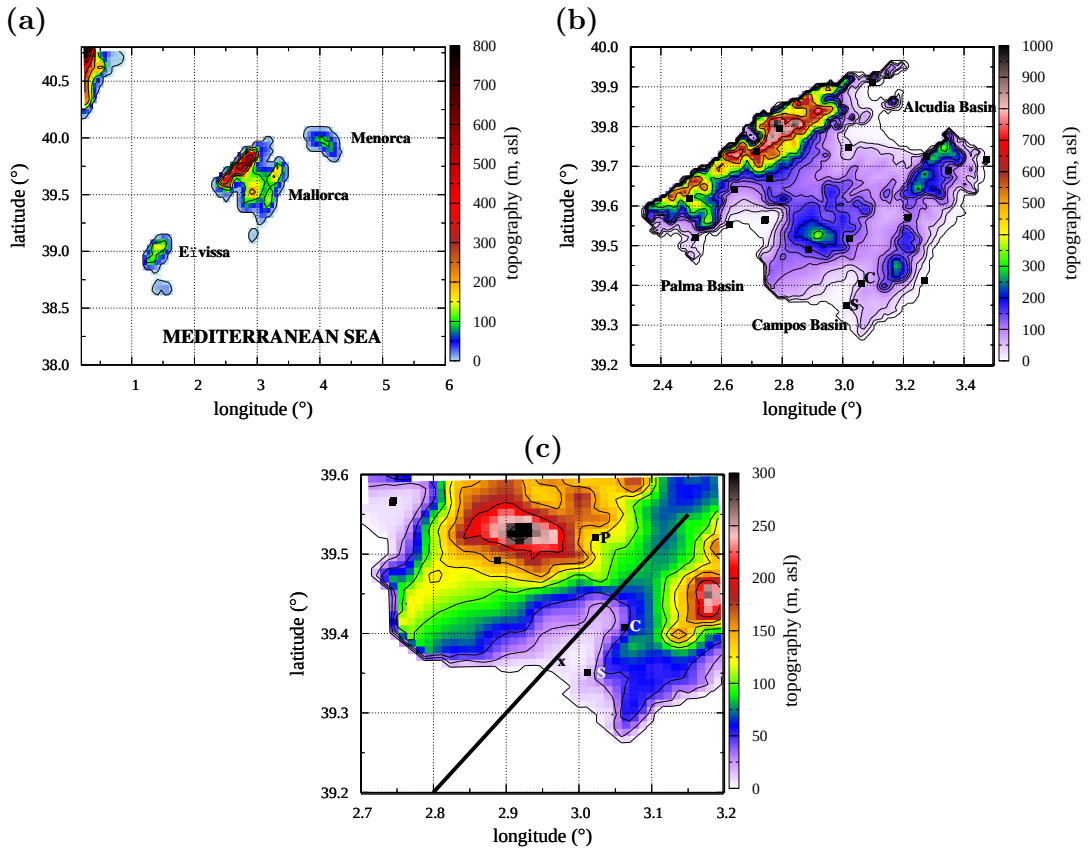

FIGURE 6.1: **(a)** Location of the Balearic Islands in the Western Mediterranean Sea. The image indicates the limits of the outer domain of the simulation. The topography of Mallorca (inner domain of the simulation) is shown in **(b)** and in **(c)** a zoom in the Campos basin. The locations of the surface weather stations from the Spanish Agency of Meteorology (AEMET) are indicated with a black square and those placed in the Campos basin are labelled as: (C) Campos; (S) Ses Salines and (P) Porreres. The central parts of the three main basins are coloured in purple, and their names are indicated in **(b)** over the sea, in front of the coastline. The cross in **(c)** indicates the place where the MSB13 experimental field campaign took place (tethered balloon, multicopter and surface observations). The black line indicates the vertical cross-section showed in Figures 6.9 and 6.13.

Mallorca, an island located in the Western Mediterranean Sea, 200 km to the East of the Iberian Peninsula, has two mountain ranges at the North and East together with an elevated area in the central part and in between there are three well-defined basins with different topographical characteristics (see Figure 6.1). The SBs formed in these basins converge at the center of the island, where an updraft area is found [Ramis and Alonso, 1998], prone to storm developments if unstable conditions are found at higher levels and there is enough moisture between 850 hPa and 700 hPa to support further development (as it is reported in South-Eastern Italy in Nelci et al. [2015] or in Istria, Croatia, in Poljak et al. [2014]). The SB regime in Mallorca was first studied by Jansà and Jaume [1946] and later Ramis and Romero [1995] made an idealized numerical study that showed the importance of the surface conditions, specially soil moisture, in

the development of the SB.

The recent numerical study of CJTG14 has suggested to define different consecutive phases for the SB (previous, preparatory, development, mature and decaying) with respect to the different ABL regimes over land and over sea and with a detailed description of the mature phase of the SB. On the other hand, previous studies [Cuxart et al., 2007, Jiménez and Cuxart, 2006] were devoted to studying the LB regime. In this Chapter, the processes that take place during the transition between LB and SB regimes are further studied, now aided by specific observational evidence, gathered during an experimental campaign in 2013.

Figure 6.2 shows the main patterns of the Sea-Breeze in Mallorca from the studies of Cuxart et al. [2014], Jansà and Jaume [1946], Ramis and Romero [1995]. In general, throughout the island the marine air can enter inland, aided by the effect of upslope flows [Ramis and Romero, 1995], but in the North-Western part of the island where the Sierra de Tramuntana is located, does not pass this marine air. In the Figure 6.3 from CJTG14 for 5 June 2010 (where the sunrise was at 0430 UTC), a summary of the Sea-Breeze phases for the day of their study can be found. It is important to mention that depending on the day of the year, the hours of these phases will change.

6.2.2 The Mallorca Sea-Breeze 2013 (MSB13) experimental field campaign

In September 2013 a 5-day measurement campaign took place at the site of Ses Covetes (indicated with a cross in Figure 6.1) centrally located in the Campos basin, 500 m inland. The SB intensity at that time of the year allows to operate safely tethered balloons or drones, compared to the stronger and very turbulent wind conditions found in July or early August. During the campaign, Mallorca was under the influence of a high-pressure system on the Atlantic Ocean, centered to the west of the Iberian Peninsula (Figures 6.4). Synoptic forcing and cold air at upper levels generated clouds and storms and prevented the SB regime to develop until September 20, when weak winds allowed the establishment of a well defined LB at night and a good MT afterwards, leading to a SB development that was later interrupted by clouds and rain following a convective development (as in Azorin-Molina et al. [2014]). However the interval between 0400 and 1100 UTC was an optimal case of MT between LB and SB.

The Campos basin has a number of automated weather stations belonging to AEMET. In this work we use those from Ses Salines, Campos and Porreres, located respectively at 3 km, 10 km and 25 km inland from Ses Covetes. A supplementary station of the UIB was installed at Ses Covetes (Figure 6.5a) which sampled at a rate of 1 Hz wind, temperature

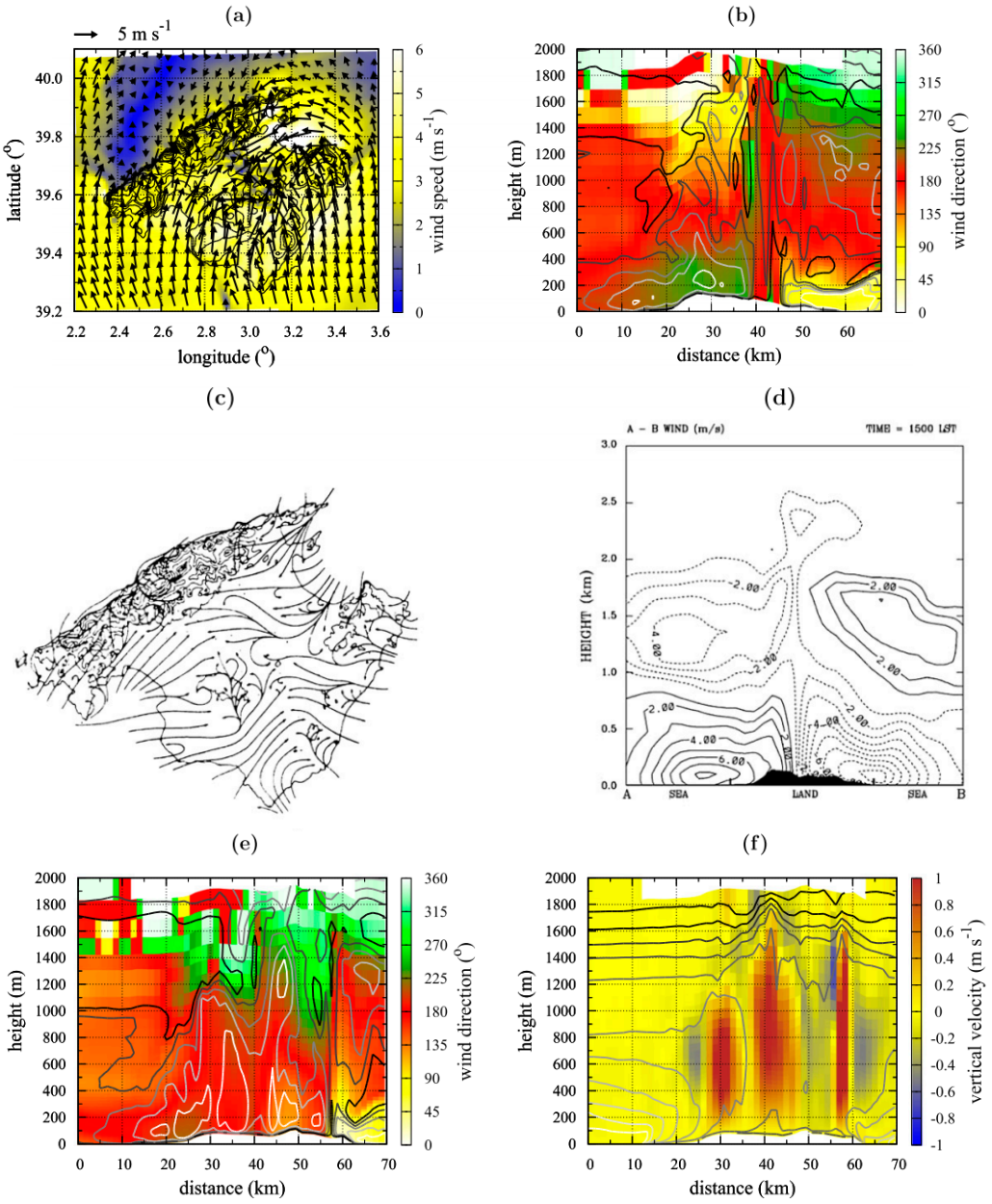

FIGURE 6.2: **(a)** Horizontal cross section of the 10-m wind vectors together with the wind speed and the topography (black lines) from the model at 1200 UTC from Cuxart et al. [2014]; **(b)** vertical cross section of the wind direction (color scale) and the wind speed [lines every 1 m s^{-1}, from 2 (black) to 6 (white) m s m s^{-1}] over the Palma and Alcúdia basins at 1200 UTC from Cuxart et al. [2014]; **(c)** near-surface wind, as determined experimentally by Jansà and Jaume [1946]; and **(d)** vertical cross section of the wind speed over the center of the island for the idealized case (no synoptic wind) of Ramis and Romero [1995]. **(e)** As in **(b)**, but for a line over the Campos and Alcúdia basins from Cuxart et al. [2014]. **(f)** As in **(e)**, but for the vertical velocity (color scale) and the potential temperature [lines every 1 K, from 294 (white) to 304 (black) K] from Cuxart et al. [2014]. Source: Cuxart et al. [2014]

Phase	Interval (UTC)	Patterns	Budgets and processes in surface layer over land		
			T	TKE	V
Previous	0430–0730	Cold offshore wind; initial warming of land; LST < SST	Warming over land uncompensated	Thermal production	Negative pressure gradient (toward sea)
Preparatory	0730–0900	Offshore wind stops; LST > SST; CBL building over land; wind inland just over the coastline	Initial inland cooling close to the coast	Thermal production	Pressure gradient changes sign
Development	0900–1200	Wind inland; front speed $\approx 3\,\mathrm{m\,s^{-1}}$; max turbulence; LST $\gg$ SST	Cooling by marine advection equilibrates radiation/turbulence warming	Shear production starts and becomes larger than thermal production at the end	Acceleration inland; main terms: pressure and turbulence
Mature	1200–1500	Wind, TKE, and LST–SST constant; T slowly decreasing	Marine advection compensates turbulence/radiation	Shear production larger than thermal production	All terms decrease with time
Decay	1500–1900	Wind decreases, turning near the coast; T and TKE decrease; LST–SST weakens and changes sign	All terms decay until nighttime values	Shear and thermal production terms similar, decreasing until they nullify at sunset	Pressure term weakens but stays positive (flow inland); turbulence not compensating

FIGURE 6.3: Main features of the different phases of Sea-Breeze case in Mallorca (5 June 2010). Source: CJTG2014.

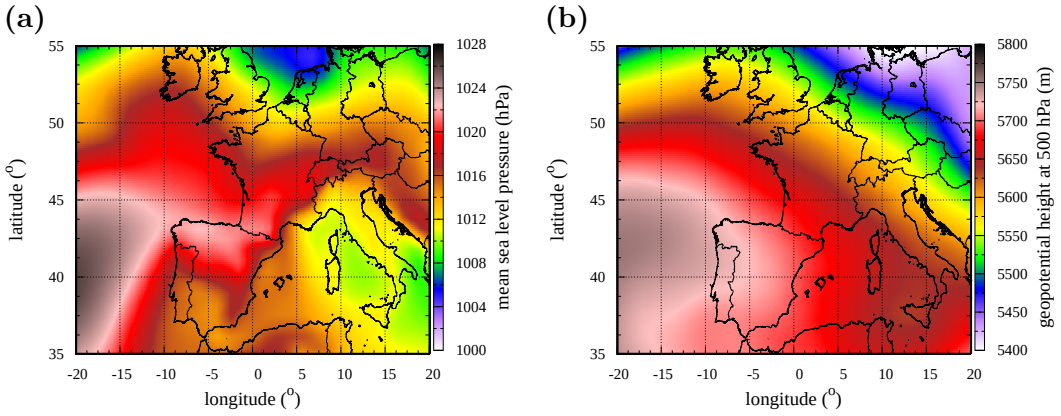

FIGURE 6.4: Meteorological situation of 20/09/2013 extracted from ECMWF. **(a)** mean sea level pressure (hPa) and **(b)** geopotential height at 500 hPa in Eastern Europe.

and relative humidity at 2 m agl. A tethered balloon (Figure 6.5b) developed by UIB and the Ostwestfalen-Lippe (OWL) Hochschule was operated when possible and provided profiles of temperature at a rate of 1 Hz, that were later post-processed to give profiles with a vertical resolution of 1 m. A similar equipment was aboard a remotely controlled OWL multicopter (Figure 6.5c). The balloon and multicopter sensors were calibrated with the UIB station and corrections have been made to remove the effects of solar radiation during daytime operation in profiling.

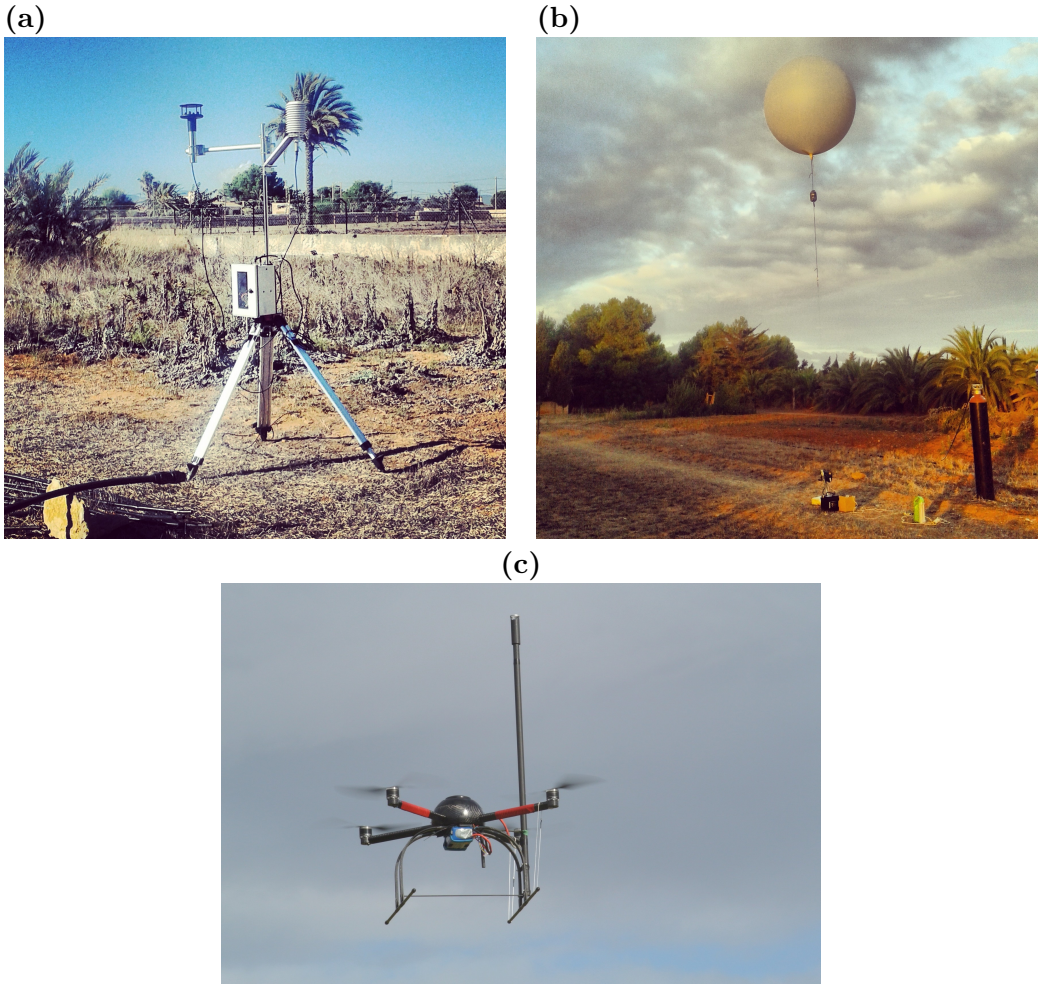

FIGURE 6.5: **(a)** Station in Ses Covetes, **(b)** tethered balloon and **(c)** remotely controlled OWL multicopter, that were used in the field Campaign in Ses Covetes.

6.2.3 Surface layer observations in the Morning Transition

As mentioned above, the MT between LB and SB of September 20, 2013 is taken for analysis. The surface observations in the Campos basin are shown in Figure 6.6 (in dots) for the AEMET surface stations (Campos, Ses Salines and Porreres) together with the ones measured in Ses Covetes (see locations in Figure 6.1c).

During the night-time and until two hours after sunrise, the wind is weak (about 1 m s^{-1}) in all the surface stations of the Campos basin. Mechanical anemometers of the AEMET network have threshold values of around 1 m s^{-1} and under these conditions the wind direction remains fix. Therefore, their measurements are to be taken with caution during that period. On the contrary, since the UIB wind sensor at Ses Covetes is a 2D sonic anemometer, it does not have a low threshold value and it is able to measure the changes in the wind direction for weak wind speeds. The observed wind in Ses Covetes is close to zero most of the night-time and therefore the wind direction is fluctuating.

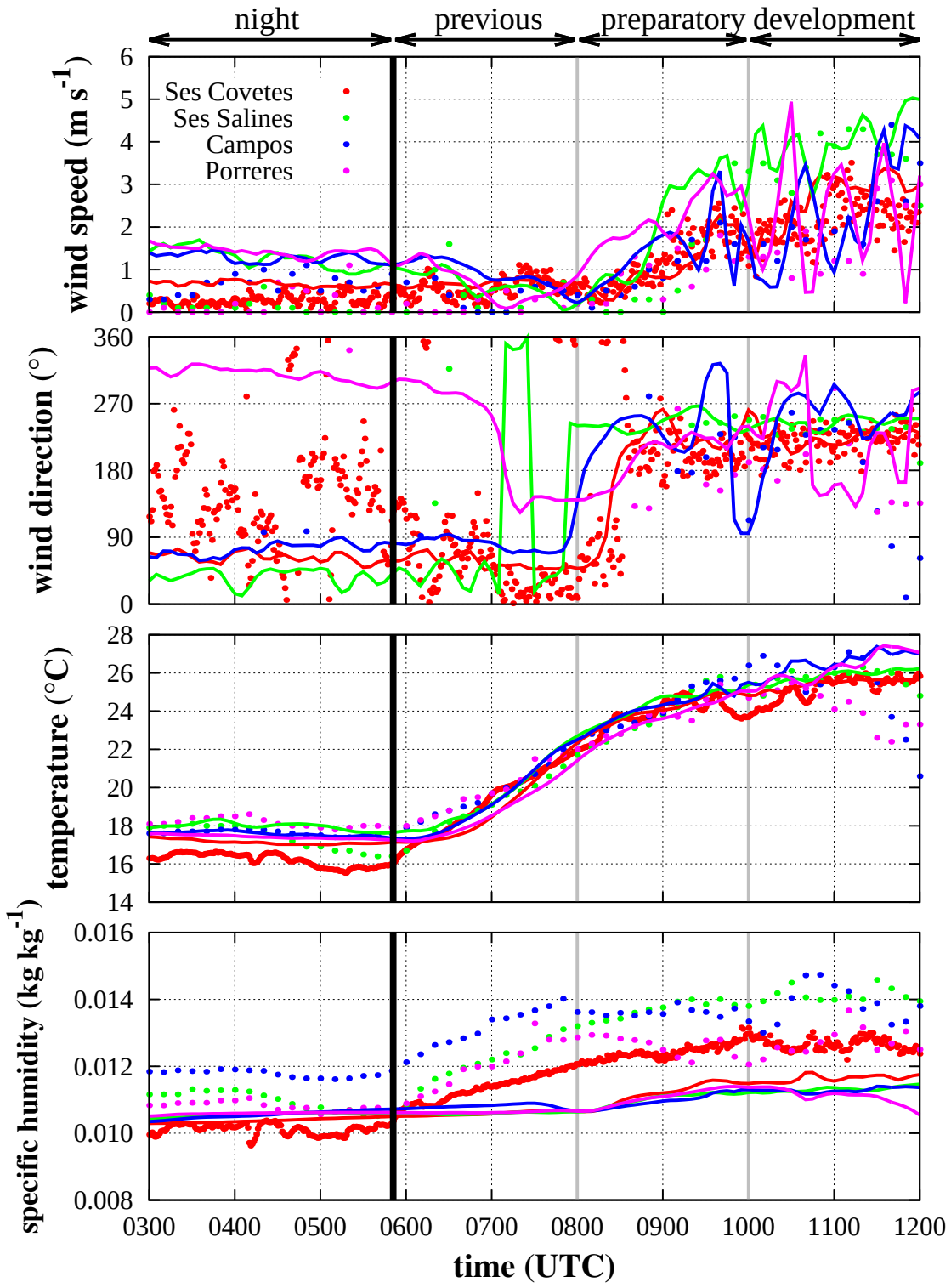

FIGURE 6.6: Observed (dots) and modelled (lines) time series during the different phases of the morning transition of the SB (names indicated in the top of the plot) reported on 20 September 2013 during the MSB13 experimental field campaign for: **(a)** wind speed (in m s^{-1}), **(b)** wind direction (in °, North is 0°), **(c)** temperature (in °C) and **(d)** specific humidity (in kg kg^{-1}). The wind is measured at 10 m agl and the temperature and humidity at 2 m agl in the AEMET surface weather stations and in the MSB13 site (Ses Covetes) all magnitudes are at 2 m agl. The black vertical line indicates the sunrise time and the grey ones the different phases during the morning transition.

It is important to mention that for the AEMET network the wind is observed at 10 m agl whereas observations in Ses Covetes are taken at 2 m agl, closer to the surface and within the surface layer inversion that, under these conditions, is decoupled from the layer aloft [Cuxart and Jiménez, 2007] Therefore, the observed wind in Ses Covetes is strongly influenced by the local effects, such as local slopes or surface heterogeneities [Martínez et al., 2010]. During night, observations in Ses Covetes indicate predominance of weak winds from E and NE, the usual direction of LB in this part of the basin. About two hours after sunrise, the wind speed progressively increases while it turns towards the S-SW direction in all the surface stations, corresponding to the SB in this region.

Observations along the Campos basin show that the temperatures are similar for all the stations in the LB phase (before sunrise, at about 0600 UTC) although the coldest temperatures are found near the coastline (in Ses Covetes) and decrease towards the inland direction. This might be related to the fact that measurements in Ses Covetes are taken in the lower part of the Campos basin, where cold air accumulates as it is found in the Duero basin [Martínez et al., 2010]. After sunrise, the temperature becomes homogeneous for all stations in the basin, increasing until the SB starts blowing, near 1000 UTC that day. Afterwards, warming stops and the temperature stays approximately homogeneous and constant in all the stations in the basin except for the most inland surface weather stations (Campos and Porreres) because they are influenced by the presence of clouds.

The specific humidity is nearly constant during night-time, with the wettest locations in the center of the basin. This pattern is kept over the MT and it might be related to the differences in the amount of soil moisture and soil cover between the coastal (mainly devoted to cereal crops) and inland areas of the basin (fruit trees and vegetable crops). After sunrise, the specific humidity increases (about 0.002 kg kg^{-1}) in all locations in the Campos basin but specially in those close to the coastline where this increase is slightly larger. This might be related to the moist evaporation from the soil. Finally, once the SB is established, the specific humidity remains nearly constant everywhere in the basin. There seems to be an equilibrium between the moisture evaporation due to the solar surface heating and the advection of the sea moisture by the SB.

The temperature profiles obtained by the tethered balloon and the multicopter are discussed together with the model outputs in the next section.

6.2.4 Model setup

To supplement the observations made during the studied MT case, a numerical simulation is performed using the Meso-NH model [Lafore et al., 1998]. The Meso-NH model

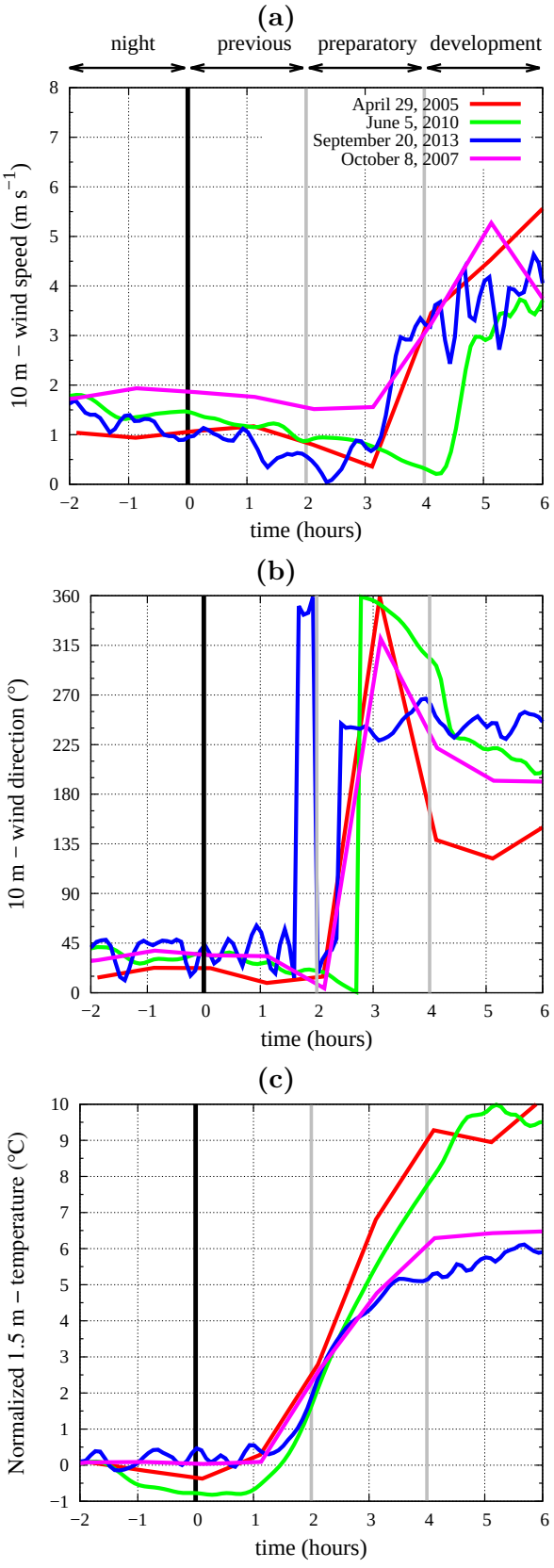

FIGURE 6.7: Time series obtained in Ses Salines (see location in Fig. 6.1) for different simulated cases with a similar setup and under Sea-Breeze conditions for: **(a)** 10m-wind speed (in m s^{-1}), **(b)** 10m-wind direction (in °) and **(c)** normalized 1.5 m - temperature parameter (in °C) computed as T(t)-T_{ini} being T(t) the temperature at any instant t and T_{ini} the one 2 hours before sunrise for each of the run. The x-axis is normalized by the sunrise time (negative values correspond to hours before sunrise and the positive ones are hours after sunrise). The black vertical line indicates sunrise and those dotted the phases during the morning transition of the SB.

successfully simulates the SB cycle, as also shown by Talbot et al. [2007] and it has been used by the authors to study the flow at lower levels in the island of Mallorca and in other basins such as the Duero [Martínez et al., 2010], the Ebro [Cuxart and Jiménez, 2012] or the Pyrenees [Jiménez and Cuxart, 2014].

The model setup is identical to the one used in CJTG14. Two nested domains are taken. The outer one (at 5 km $\times$ 5 km horizontal resolution, Figure 6.1a) covers the Balearic Archipelago whereas the inner one (at 1 km $\times$ 1 km horizontal resolution, Figure 6.1b) covers Mallorca. A vertical resolution of 3 m is taken close to the surface and is slowly stretched upwards.

The simulation is run for 24 h starting at 1200 UTC of September 19, 2013. Initial and lateral boundary conditions are taken from the ECMWF analyses, refreshed every 6 hours. As in CJTG14, the computation of the temperature, Turbulence Kinetic Energy (TKE) and momentum budgets are activated to allow a substantiated study of the physical processes taking place during the MT.

In order to see how representative the present case is, the evolution of the 1.5 m-temperature and 10 m-wind is compared to the ones of other simulations made for the same area that included a MT in Figure 6.7. All evolutions -plotted in reference to the sunrise time- are very similar. About 2-3 hours after sunrise the wind veers from N-NE towards S-SW, corresponding to the LB to SB conditions in the Campos basin, meanwhile the temperature warms up. The temperature has been normalized by T_{ini}, corresponding to the temperature 2 hours before sunrise. The amplitude of the diurnal cycle depends on the time of the year (the amount of solar radiation) and the case in June is the one with the largest temperature amplitude. Observations for each of these runs (not shown) agree with these patterns. Figure 6.7 allows us to consider the present case as representative of a MT between LB and SB. Besides, it strengths that the classification of the SB stages in CJTG14, and specially those during the MT, can be based on sunrise time since all the simulated cases shown in Figure 6.7 have the same patterns (i.e. time and duration of the warming and wind veering).

6.3 The modelled flow

6.3.1 Modelled patterns at lower levels

The modelled patterns during the morning transition between the LB and SB in the Campos basin are shown in Figure 6.8 where the 10 m-wind and 1.5 m-temperature are plotted for times corresponding to the relevant periods of the LB (0500 UTC), the

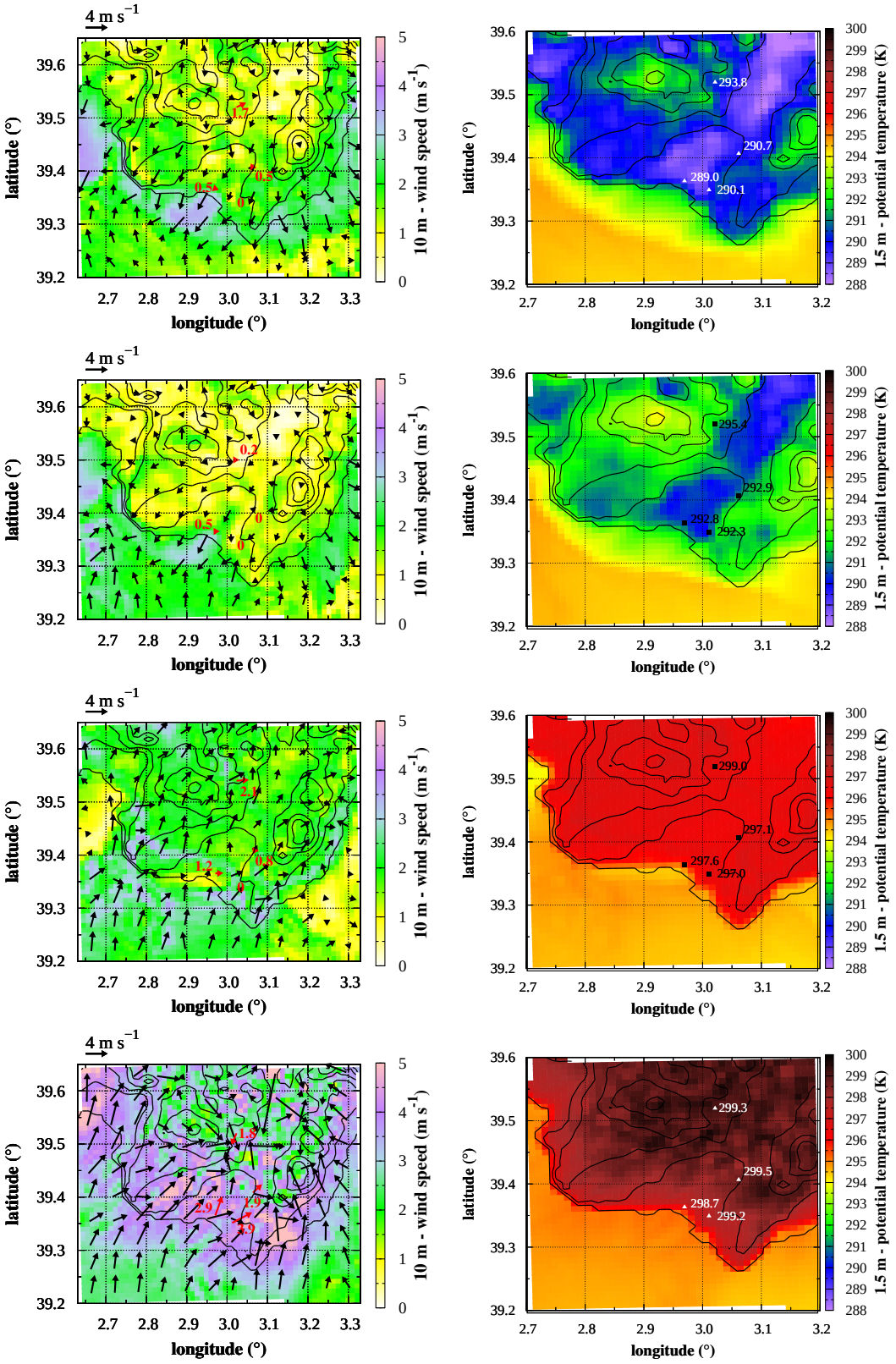

FIGURE 6.8: Modelled horizontal cross-sections for the Campos basin on September 20, 2013 for **(a)** 10m-wind direction (black arrows) and speed (in colours) together with the topography (black lines) at 0500 UTC. The numbers and arrows in red indicate the surface observations at this instant. The same in **(b)** but for the 1.5m-temperature (in colours) with the observed values in black and white. The same in **(c)** and **(d)** at 0700 UTC, in **(e)** and **(f)** at 0900 UTC and in **(g)** and **(h)** at 1100 UTC.

MT (0700 UTC, corresponding to the phase previous to the SB, and 0900 UTC, the preparatory phase) and the SB development (at 1100 UTC). This classification is based on the organization of the flow at a basin scale and the precise times of the different SB phases depends on the sunrise time, as proposed by JCTG14.

The SB is present in the island from late spring to early autumn, and some examples of previous studies are given and Figure 6.7. The LB may take place along all year. Therefore the MT that is analysed here can be considered an example of a transition case in the warm period of the year. Figure 6.7 also illustrates that the defined phases can be seen consecutively in changes in the temperature (for the previous phase), the wind direction (in the preparatory phase) and in the wind speed (in the development phase). The focus is put here on a deeper analysis of the phases during the MT.

The *LB* plots (0500 UTC) indicate the presence of downslope flows over the topography surrounding the flat inner area of the Campos basin, where the flow is directed outland with cold air flowing over the sea near the coast. The coldest air is over the lowlands and the area in the sea affected by the cold outflow has lower air temperature values (about 2 °C) than the immediate sea areas not reached by the LB. The model is able to capture this spatial temperature gradient although it is smaller than the observed one because it is not reproducing the accumulation of cold air in Ses Covetes due to an excess of mixing. Furthermore, the model is not reproducing the observed spatial variability of the 1.5 m specific humidity reported at different locations in the Campos basin. This might be related to the fact that the spatial heterogeneity of the soil moisture and vegetation cover are poorly represented in the model (at 1 km $\times$ 1 km resolution) similar to what is described in Cuxart et al. [2016a]. The simulated organization of the flow agrees with data (Figure 6.6 and Figures 6.8a and 6.8b). In Ses Covetes, the model tends to slightly overestimate the wind speed and to provide less variability in direction in comparison with observations, nevertheless it captures the main characteristics of the nocturnal regime, also for temperature and humidity (Figure 6.6).

During the *previous phase* (0600 - 0800 UTC) wind speed in the Campos basin is still weak and with the LB or downslope directions meanwhile the solar heating warms the land and the specific humidity increases (Figure 6.6) due to the evaporation from the surface. The strength of the downslope winds decreases (Figure 6.8c) as the temperature difference between the slope and the center of the basin tends to zero (the ground temperature of the slope and the one at about 400 m agl over the center of the basin are about 294 K, not shown). Although the land surface temperature is warmer than in the previous phase (Figures 6.8b and 6.8d), in the center of the basin it is still colder than the one over the sea (Figure 6.8d). Thus, LB winds are still present in the coastal region (Figure 6.8c) but less intense than in the previous phase because the thermal difference

between land-sea is reduced as well as the strength of the downslope winds during this stage. The model results indicate that downslope winds decrease faster than LB winds, in agreement with the ground observations (Figures 6.8c and 6.8d).

The radiative heating of the land continues during the *preparatory phase* (0800 - 1000 UTC) as it is seen from Figure 6.6 meanwhile the surface temperature over the land becomes warmer than the one over the sea (about 1 K at 0900 UTC, Figure 6.8f). Therefore the SB is initiated in the coastal region (Figures 6.6 and 6.8e) and its strength increases as time (radiative heating) advances. The air in contact with the slopes warms faster than the one in the center of the basin (thermal difference of about 1 K at 0900 UTC, not shown) favouring the formation of upslope winds. The upslope winds in the mountains at the East side of the Campos basin are strong enough to blow uphill, surpassing the ridges and imposing downslope direction in the East coast. Similarly, there is a combined effect of upslope winds and SB at the South side of the mountain range at the west of the Campos basin and they blow uphill the mountain generating downslope winds in the North side of the mountain range (Figure 6.8e).

Finally, during the *developing phase* (1000 - 1200 UTC) the wind speed and direction, the temperature and the humidity (Figure 6.6) remain constant. The land surface temperature is warmer than the sea and this thermal difference is the responsible of the progressing of the SB inland through the lowlands, enhanced by the upslope winds (Figure 6.8g). The location of the SB front is clearly indicated in pink in Figure 6.8g at about 15 km from the coast to the inland direction at 1100 UTC (the progress of the SB front is about 15 km in 2 hours, corresponding to an approximate speed of the breeze front of 2 m s^{-1}). In complex terrain regions, as the Campos basin, upslope winds interact with SB, as it is described in Papanastasiou et al. [2010] for the East coast of Greece. Regarding the temperature, during the developing phase the 1.5m-temperature levels off (Figure 6.6) because the SB favours the advection of cold air from the sea over the land. As a result, the ground temperature in the coastal region over the land is colder than further inland (Figure 6.8h) where it is nearly homogeneous. Observations agree with the model results, as it is indicated in Figures 6.6, 6.8g and 6.8h.

6.3.2 Vertical structure of the simulated flow

Vertical cross-sections along a line through the central part of the Campos basin and perpendicular to the coastline (Figure 6.1c) are shown in Figure 6.9 for the wind and potential temperature for the different phases during the MT. In the LB period, the wind flows outland (corresponding to the NE direction, in blue in Figure 6.9a) for a distance near 12 km, with a depth slightly above 100 m, speeds between 3 and 4 m s^{-1} with

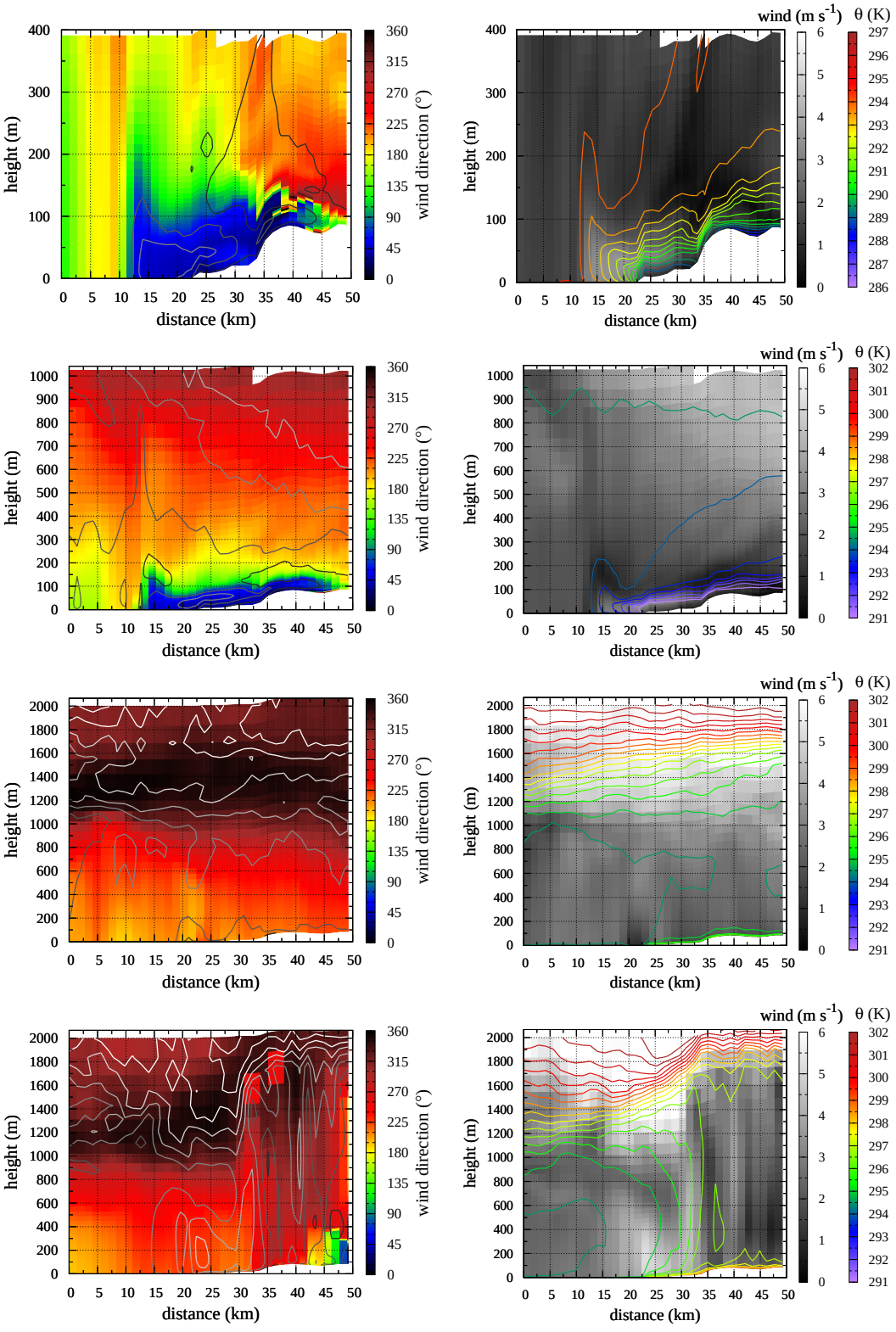

FIGURE 6.9: Modeled vertical cross-sections along the black line in Figure 6.1 for different instants on September 20, 2013. **(a)** Wind direction (in colours) and speed (in black and white lines every 1 m s^{-1}) and **(b)** wind speed (in black and white) and potential temperature (in coloured lines every 0.5 K) at 0500 UTC (LB phase). The same in **(c)** and **(d)**, **(e)** and **(f)** and **(g)** and **(h)** at 0700 UTC (previous phase), 0900 UTC (preparatory phase) and 1100 UTC (development phase), respectively. For **(a)-(b)** the vertical profiles are shown up to 400 m (asl), for **(c)-(d)** up to 1000 m (asl) and for **(e)-(h)** up to 2000 m (asl) to include the whole boundary layer extend. The colour scale of the temperature changes for the different phases to better show the boundary layer extend.

maximal values near 50 m agl. Unstably stratified conditions are found in the surface layer over the sea (Figure 6.9b) due to the cold advection present under LB conditions. Over land, downslope winds are found at the slopes with wind maxima weaker (about 2-3 m s^{-1}) and lower (about 30 m agl) than the ones related to the LB. Besides, downslope winds flow over the surface thermal inversion enhancing the transport of cold air over the sea.

In the previous phase (0600 - 0800 UTC), already under the sunlight, the structures keep the same shapes as the ones on the LB, but progressively weakening. The horizontal extent of the LB over the sea diminishes and the outflow vertically shrinks, while the regime is still unstable over the sea and stable over the land (Figures 6.9c and 6.9d).

The preparatory phase (Figures 6.9e and 6.9f) indicates that the outland wind has vanished -although there is still an area of minimal wind speed offshore where the end of the LB flow was- and there is the establishment of a local wind maximum over the shore, still not progressing inland. A well mixed convective boundary layer is found and neutral stratification prevails over land and sea with an homogeneous temperature of about 295 K up to 1000 m above sea level (asl). Over the land, the surface layer becomes unstable due to the radiative heating of the terrain.

This heating causes that during the development phase (Figures 6.9g and 6.9h) an horizontal thermal gradient between the air over land and sea is found at 1100 UTC (2.5 K in 20 km). The cold air flows over a heated land (unstably stratified conditions in the surface layer) along this horizontal temperature gradient and a maximum of wind related to the SB direction (SW) is found (wind speed reaches values of 6 m s^{-1} over a depth of 400 m). Further inland (distances 35-50 km in Figure 6.9g) the convective boundary layer grows due to the radiative heating of the ground without any horizontal advection of cold air due to the SB resulting in a height of 1600 m agl (Figure 6.9h) larger than the one in the coastal region. Besides, winds are weaker than those related to the SB and from NW (Figure 6.8g), indicating that the SB front has still not reached this region.

6.3.3 Thermal structure during the Morning Transition

The surface weather stations in the basin, as well as the surface observations in Ses Covetes, are used to validate the model results (see Figures 6.6 and 6.8). Furthermore, the observed vertical profiles of temperature in the lower atmosphere taken during MSB13 allow us to verify the modelled thermal profiles in the lower atmosphere in Ses Covetes.

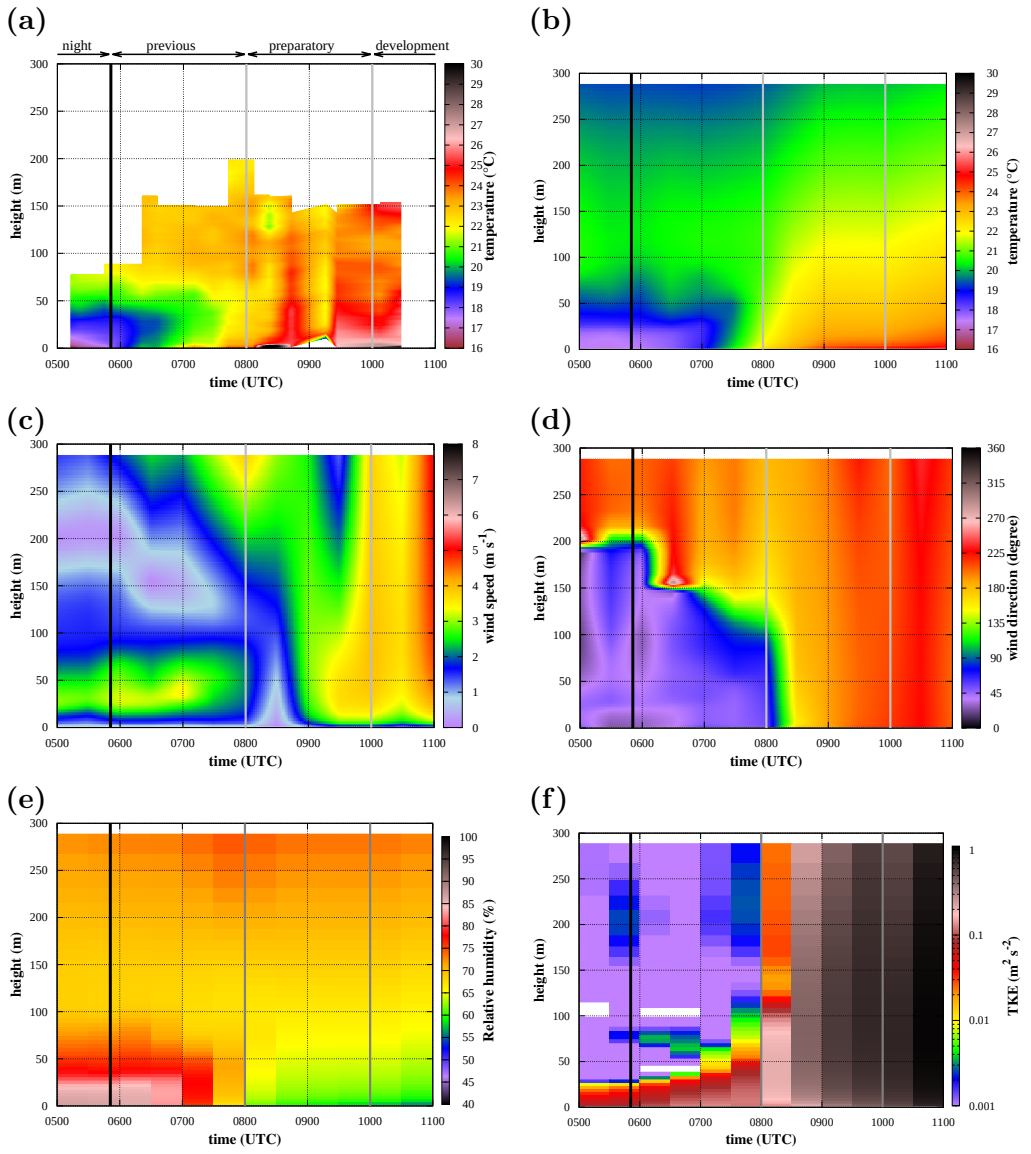

FIGURE 6.10: Time evolution of the vertical profiles in Ses Covetes during the morning transition on September 20, 2013 for **(a)** temperature observed by the multicopter and the model results for **(b)** temperature, **(c)** wind speed, **(d)** wind direction, **(e)** relative humidity and **(f)** TKE. The black vertical line indicates the sunrise time and the gray ones the different phases during the morning transition (names in **(a)**).

During this period, 16 soundings have been made with the tethered balloon. The temperature profiles show the thermal inversion during the early soundings (Figure 6.12a) that progressively disappears meanwhile the Sun heats the ground. The relative humidity (Figure 6.12b) decreases after sunrise at the same rate as the temperature increases.

The time evolution of the temperature profile in Ses Covetes as observed by the multicopter is plotted in Figure 6.10a and compared to the corresponding field extracted from the model (Figure 6.10b). The modelled wind speed and direction, relative humidity and TKE are also included in the plot (Figures 6.10c, 6.10d, 6.10e and 6.10f) although these

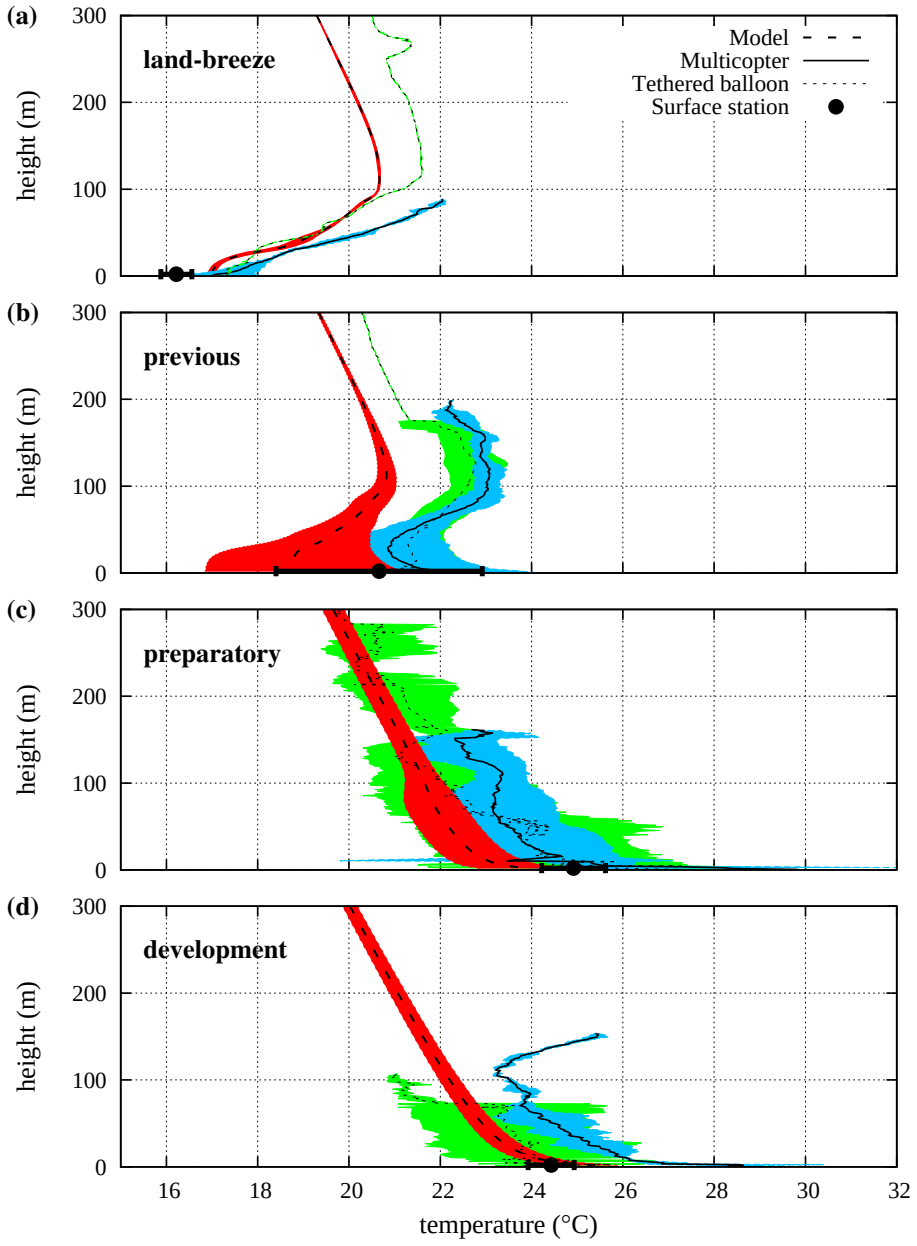

FIGURE 6.11: Vertical profiles in Ses Covetes measured by the multicopter (solid line) and tethered balloon (dotted line) together with those obtained from the Meso-NH model (dashed line). The corresponding value measured by the surface station at 2 m agl is also included (mean value with a dot and the standard deviation with error bars). The profiles are averaged over the different phases during the morning transition of September 20, 2013: **(a)** night-time (0500 - 0600 UTC), **(b)** previous (0600 - 0800 UTC), **(c)** preparatory (0800 - 1000 UTC) and **(d)** development (1000 - 1200 UTC). The mean values are indicated with a line and the colours indicate the standard deviation.

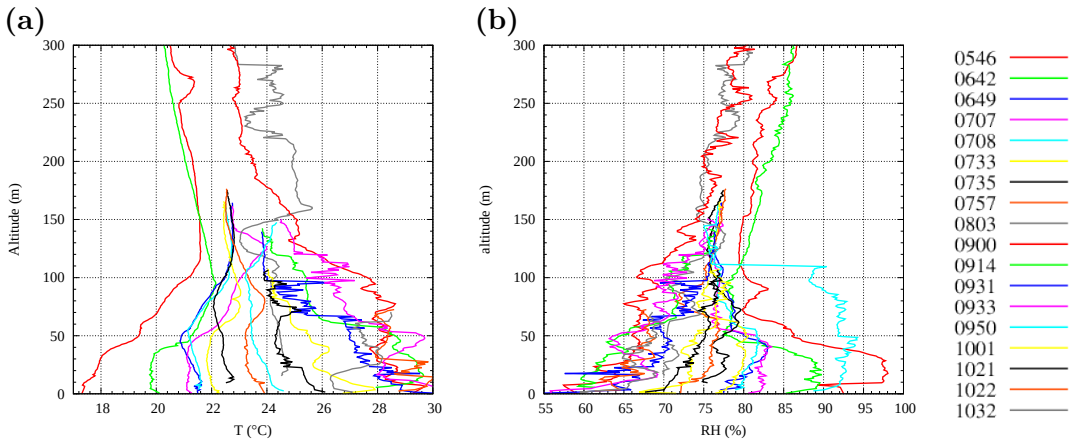

FIGURE 6.12: Vertical profiles measured by the tethered balloon balloon (BOU): **(a)** temperature and **(b)** relative humidity. Each line corresponds to a different sounding, labelled with the launching time (in UTC).

magnitudes are not measured along the lower atmosphere. Furthermore, Figure 6.11 compares time-averaged values for the different phases from the model, the multicopter, the tethered balloon and the surface observations at the site.

During the *LB phase* in Ses Covetes, a surface thermal inversion up to about 50-70 m agl is found for the model and observations (Figures 6.10a and 6.10b) although the observed surface layer is more stably stratified than the one simulated (see Figure 6.11a). From the model results it is found that in the first 200 m agl, there is a layer of NE winds (Figure 6.10d, corresponding to LB direction) with maximum speeds of 2-3 m s^{-1} at about 40 m agl (Figure 6.10c). The averaged observed and modelled thermal profiles during this phase (from 0500 to 0600 UTC, Figure 6.11a) are very similar, indicating a thermal inversion up to 100 m. In the surface layer, the model mixes in excess compared to observations, a fact known from long as a default particular for this model and some similar ones [Bravo et al., 2008].

Concerning Relative Humidity (Figure 6.10e), around the sunrise arrive until 85% in the first 50 meters, while in higher levels there are a constant value of 70%. Two hours after sunrise, it drops to 60% in the first 50 meters and in higher layers it remains constant. It is possible to see how the turbulence starts at 0830UTC (Figure 6.10f).

After sunrise, the solar radiative warming of the ground is responsible for the increase of the 1.5m-temperature. The modeled and observed 1.5m-temperatures are similar at the end of the *previous phase* although at the beginning, the observed one was colder than the modelled one (Ses Covetes, Figure 6.6). The progressive warming explains the large value of standard deviation of the averaged modelled and observed temperatures during this phase (Figure 6.11b). Nevertheless, at the end of the previous phase (0800 UTC) both temperatures are similar although their temporal evolution along this phase

somewhat differ (Figure 6.10a and 6.10b) being the averaged modelled temperatures colder than those observed (Figure 6.11b). Observations (Figure 6.10a) show that the solar radiative warming starts close to the surface (at about 10 m agl) and the heat is transported upwards. This is not captured by the model (Figure 6.10b) where the whole boundary layer depth warms up just after the LB weakens (Figures 6.10c and 6.10d). Transitions are the most difficult part of the diurnal cycle for the models to reproduce adequately [Lothon et al., 2014].

During the *preparatory phase* the warming of the surface layer continues but at a lower rate (Figure 6.6). The temperature in the lower atmosphere continues increasing and a cooling event is reported between 0900-0930 UTC (Figure 6.10a). The model is not able to capture this event although at this time the temperature in the lower atmosphere levels off (Figure 6.10b), the wind speed increases (Figure 6.10c) and the wind direction corresponds to the SB (Figure 6.10d). As in the previous phase, probably the strong mixing in the model is the responsible of not capturing the cooling event related to the arrival of the SB front in Ses Covetes. The observed and modelled averaged vertical profiles (Figure 6.11c) are similar although the standard deviation in the observed ones is larger than on the simulated ones where the cooling related to the arrival of the SB is not captured.

Finally, the averaged thermal structure in the model during the *development phase* is similar to the one measured by tethered balloon (Figure 6.11d). The differences of the temperature values in this phase between the multicopter and tethered balloon may be in the different response of each device to the effect of the solar radiation. Nevertheless, model and observations are producing a well-mixed boundary layer meanwhile the wind increases intensity (Figure 6.10c) and remains from the SB direction (Figure 6.10d). A temperature inversion is reported by the multicopter at about 120 m agl (Figure 6.11d), but this may be related to its sampling of a turbulent eddy, a feature not captured by the model

Figure 6.11 shows that the model is able to capture the observed temperature profile during the different phases of the MT, except for the temporal evolution during the previous phase, when LB is still present but the solar radiative warming starts. These differences might be related to a poor representation in the model of the physical processes that take place there, specially those related to the interaction between the land and atmosphere. Besides, if the surface parameters (such as the soil moisture) are far from the real ones, the modelled surface fluxes can depart very much from the observed ones, as it is shown in Cuxart et al. [2016a].

6.4 Temperature, momentum and Turbulent Kinetic Energy budgets

Similarly to the analysis made in CJTG14, the budgets of temperature, TKE and V-budget are discussed for this case. The budget study is the name given to an evolutions of the contributions of each term in prognostic equations [Stull, 1988]. Figure 6.13 displays the spatial distribution of these budgets along the line normal to the coast (Figure 6.1) for the different phases during the MT, averaged for one hour.

The temperature budget clearly indicates that in all phases except in the preparatory phase (land warming but the SB already not blowing) the main process is the advection by the LB or the SB respectively, and the main response is the turbulence mixing, that redistributes vertically the heat as necessary (Figure 6.13a). A key mechanism keeping the system going is the radiation heating of the lower layers of the air over the sea at night and over the land in the daytime, especially in the preparatory and developing phases over land, periods during which there is a clear warming tendency over the latter.

The TKE budget terms are very weak in the LB and the previous phase but they are stronger for the preparatory and development phases (Figure 6.13). In the preparatory phase (Figure 6.13c), the surface heating over land results in the predominance of the thermal production of turbulence and the resulting vertical transport of it, with local circulations associated that produce dynamically some extra turbulence. In the development phase (Figure 6.13d), the inflow produces, through shear production, as much TKE as the surface heating, and this excess of turbulence is transported upwards by the turbulence transport.

The momentum budget (Figure 6.13) indicates that the main driving factor is the pressure gradient term, that results from having different densities at both sides of the coastline. The response is an advection of momentum, delayed by the turbulent mixing, mechanisms that are active in all phases, except in the preparatory one.

The vertical structure of the budgets during the LB, previous, preparatory, development and mature phases are further inspected in Figures 6.14, 6.15 and 6.16, respectively, averaged over 1 hour for one point over the sea (left column) and over the land (right column). The budgets during the LB phase (Figure 6.14) show more activity over the sea where, according to the temperature budget, the radiative warming by the sea surface of the lowest layers of air is transported upwards up to 120 m agl by the turbulence. The TKE budget shows that thermal production of turbulence dominates near the surface and that the dynamic production prevails above, where the speed gradients are largest. Over land radiation cools near the surface and turbulence diffuses this cooling upwards

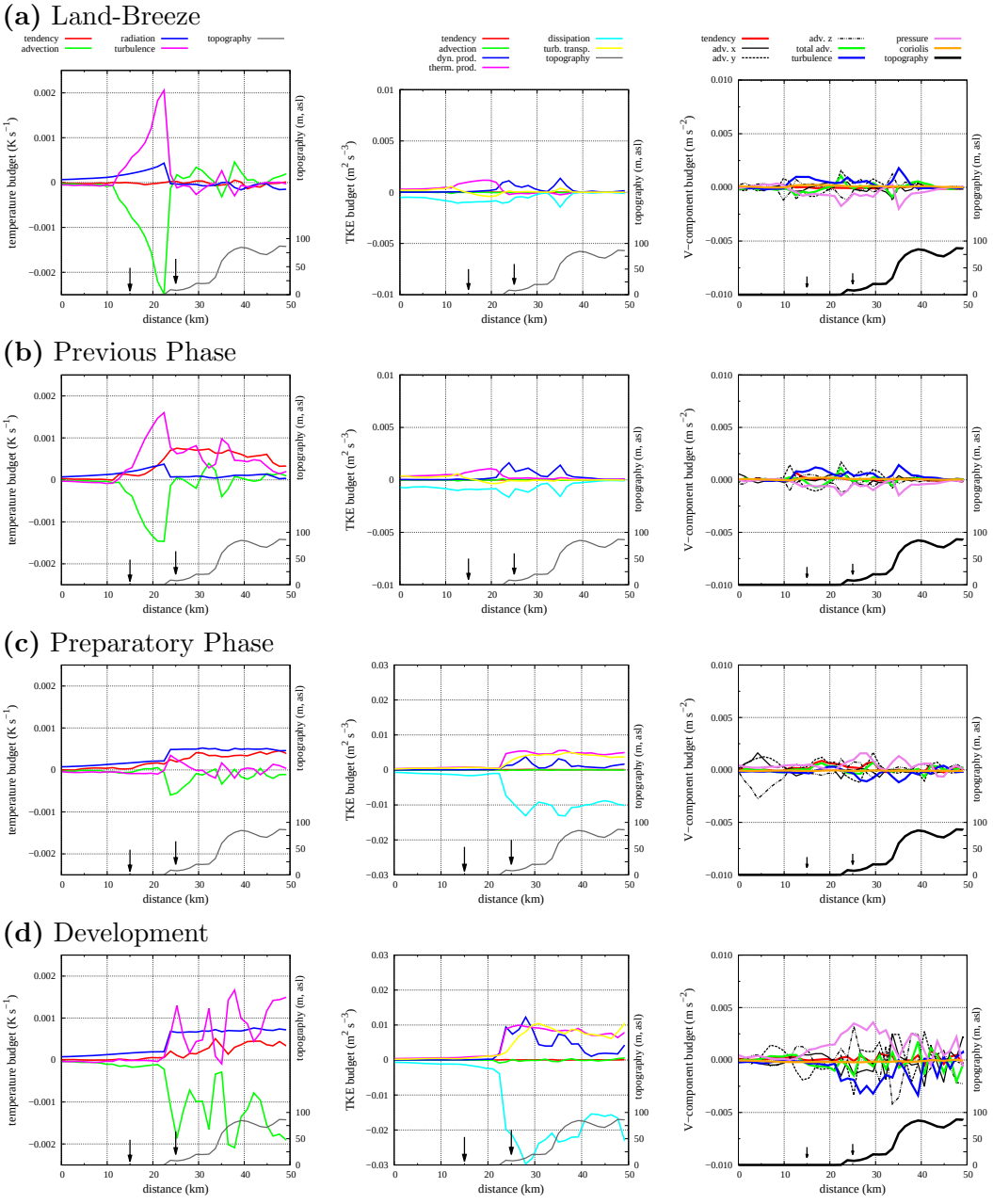

FIGURE 6.13: Temperature and TKE budgets at 10 m agl along a line normal to the coast (see location in Figure 6.1) averaged over 1 hour and at different instants: **(a)** night-time (0430-0530 UTC); **(b)** previous (0630-0730 UTC); **(c)** preparatory (0830-0930 UTC) and **(d)** development (1000-1100 UTC). The arrows indicate the location of the vertical profile budgets shown in Figures 6.14, 6.15 and 6.16. For the TKE budgets the y-axis is changed in **(f)** and **(h)** to clearly see the patterns during the different SB phases.

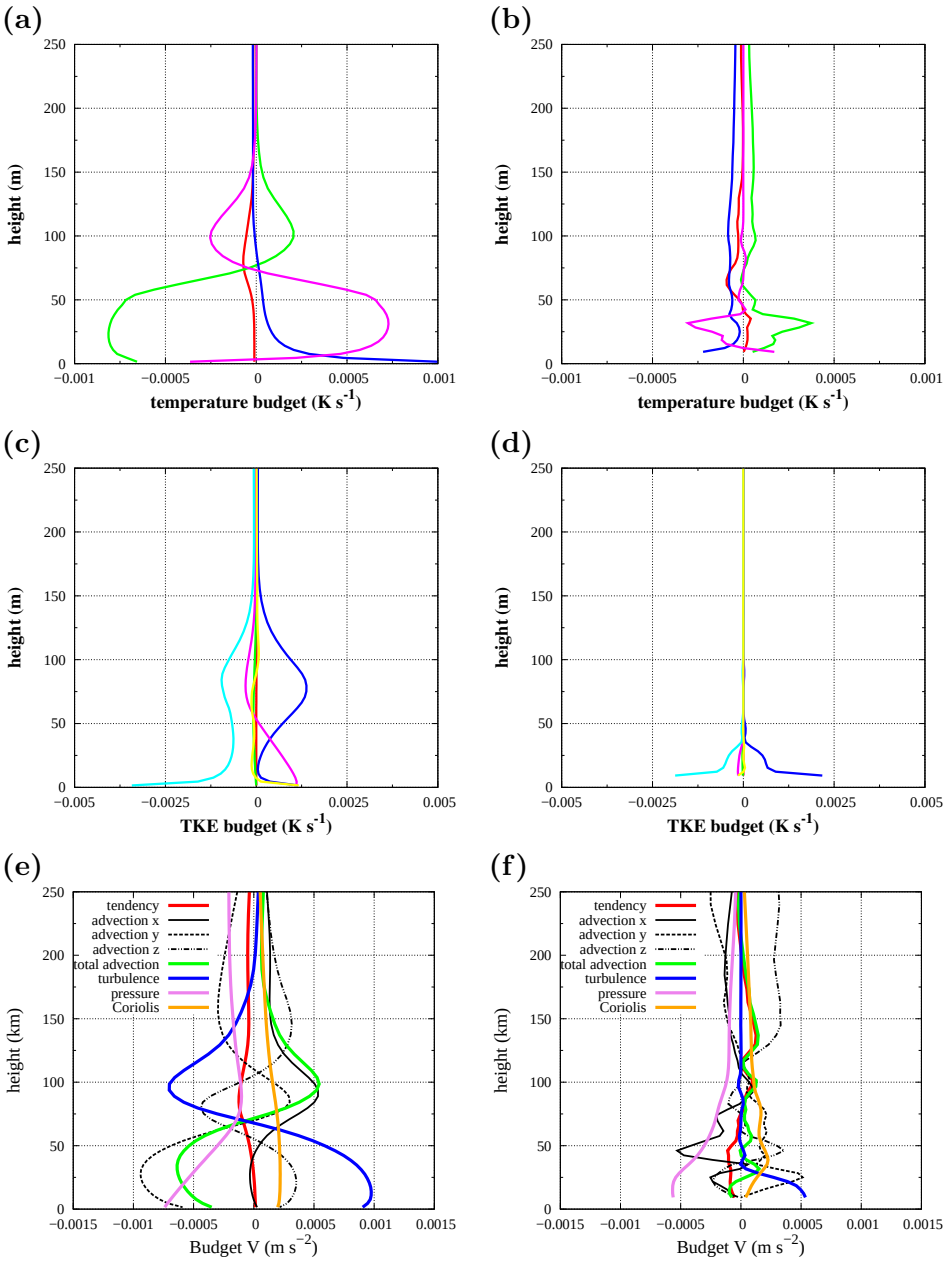

FIGURE 6.14: Temperature budget averaged between 0430 - 0530 UTC for a point **(a)** 6.5 km offshore and **(b)** 3.5 km inland, respectively. The same in **(c)** and **(d)** for the TKE budget. And in **(e)** and **(f)** for the V-budget. The location of these points and the colours of the lines are explained in Figure 6.13.

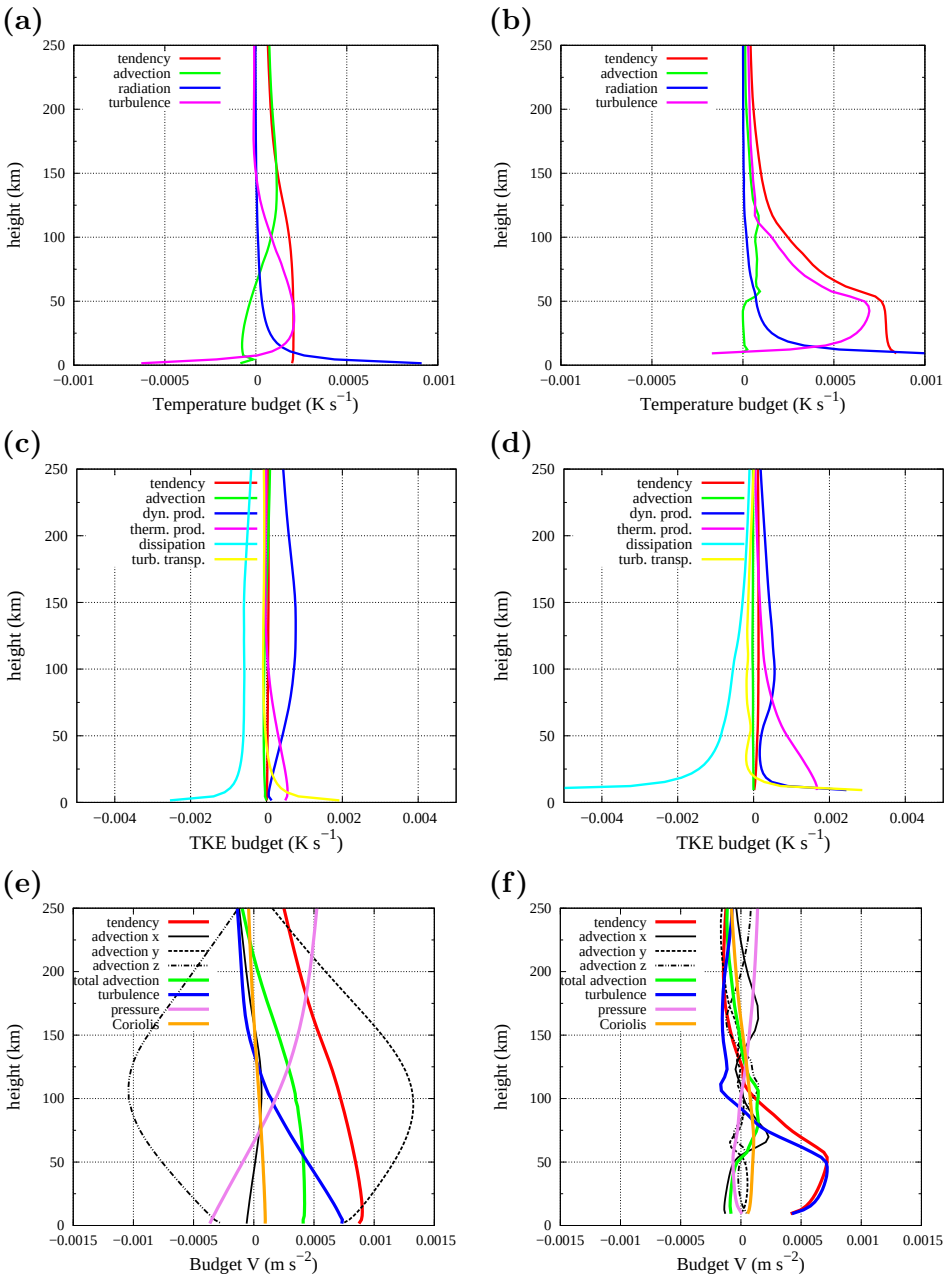

FIGURE 6.15: The same as Figure 6.14 but for the period 0730-0830 UTC.

compensated by a slight warming advection of the katabatic flow warmed by adiabatic compression, but all these processes are much smaller in magnitude than over the sea, and extend only up to 50 m agl at most. The production of turbulence is only through the wind shear close to the surface, significant but very shallow as well.

Figure 6.15 shows that during the previous and preparatory phases the terms over the sea decrease meanwhile those over land increases. At some point, the terms over the sea and land are very close, probably related to the calm wind conditions during the MT and the initiation of the reverse of the flow (from LB to SB).

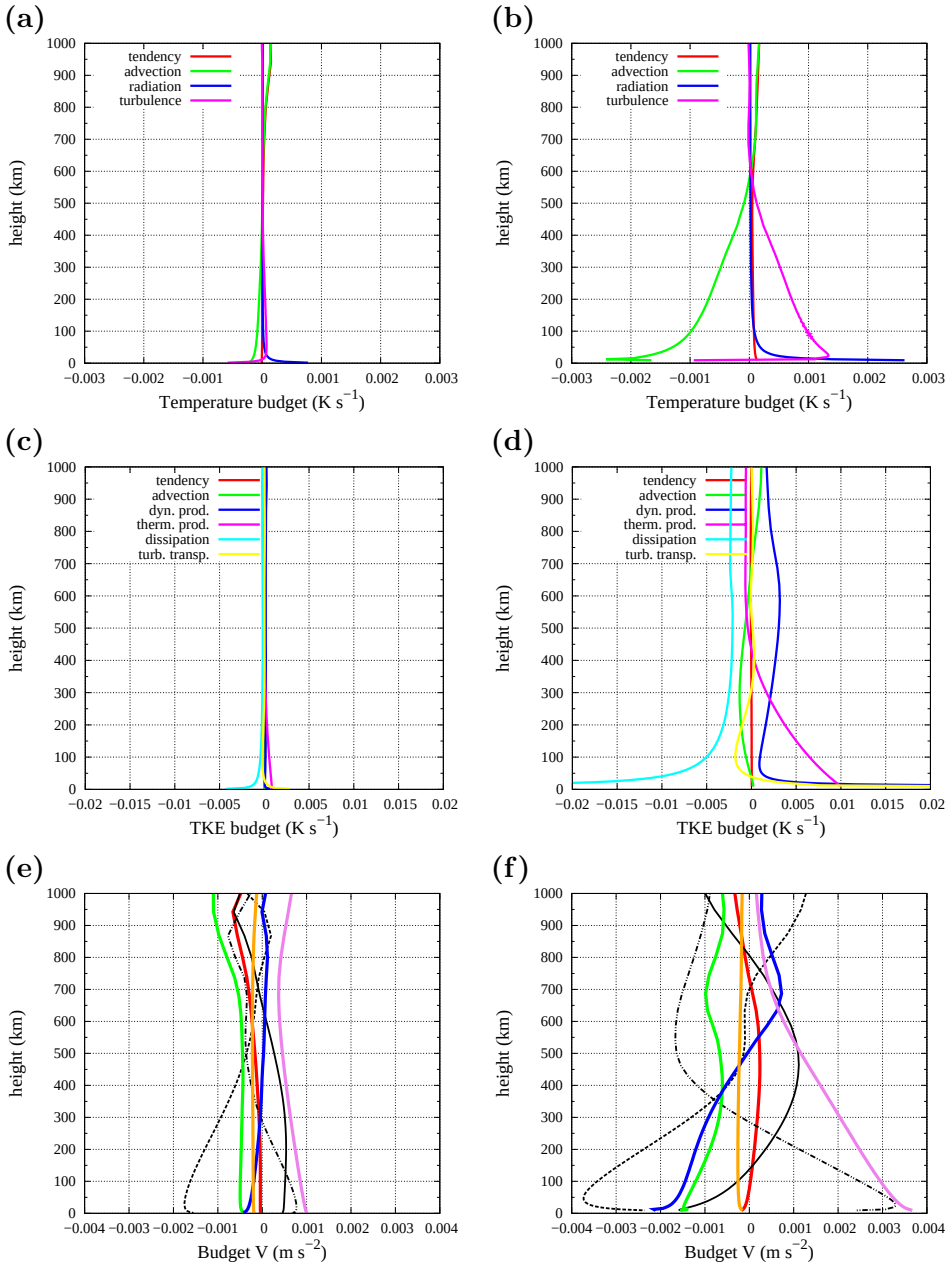

FIGURE 6.16: The same as Figure 6.14 but for the period 1000-1100 UTC.

It is noteworthy that the budgets during the LB are qualitatively inverted in respect those of the development phase, where the main activity takes place over the land (Figure 6.16). At the development phase, the budgets show that radiative warming dominates the surface layer and turbulence. Turbulence distributes the warm air in a layer up to 20 m above the sea and 400 m above the land. This warming is compensated with de cold advection in both cases. The TKE has a similar shape.

The time evolution of the temperature budget shown in Figures 6.17a and 6.17b for the sea and the land points. After sunrise (0600 UTC) radiation and turbulence start warming the surface. Advection start 2 hours and a half later begins at 0830 UTC with

the consequent increase of the turbulent warming by mechanical and thermal mixing. Over the sea, there are turbulence at night-time and cold advection that lasts up to 2 hours after sunset.

The evolution of the TKE budget (Figures 6.17c and 6.17d) shows that over the sea all the terms remain constant at all times, over the land, thermal production origin starts shortly 1 hour after sunrise. This means that almost 1 h are necessary to erode the previous nocturnal surface inversion and form the SB flow.

The V-component budget (Figures 6.17e and 6.17f) indicates that the main contribution of the tendency (once the SB is initiated) is the advection when the temperature gradient between land and sea is established. During nighttime these terms are much slower overland and sea.

6.5 Sensitivity of the minimum value of TKE in the turbulence scheme

It is a well known feature of the numerical models that are run with a TKE turbulence scheme, such as Meso-NH [Cuxart et al., 2000, Lafore et al., 1998], that they have one adjustable parameter, which is the minimum value allowed for the TKE (TKEMIN) in case of no turbulence present. In the model, the cold surface may decouple from the warmer air above, leading to unrealistic near-the-surface temperature values (the *runaway cooling* problem, as introduced by Viterbo et al. [1999]). Some models take a minimum value of the order of 0.1 $m^2\ s^{-2}$, large compared to the average values of a calm night [Cuxart and Jiménez, 2012]. This way they ensure mixing, even if there is in reality no turbulence performing it and other processes are acting. Comparing the observed and modelled temperature profiles (Figure 6.11) it is found that in the surface layer the model produced large turbulent mixing and the observed strong surface inversion in Ses Covetes is not captured by the model.

In our study above we have used a TKEMIN of $10^{-5}\ m^2\ s^{-2}$ (our standard run), which is well below the minimum observed values in stably stratified conditions. We have made another simulation with the default value in Meso-NH ($10^{-2}\ m^2\ s^{-2}$), to see what is the sensitivity of the model to this change, but without altering excessively the physical mechanisms as it would happen imposing an even larger minimal value.

Figure 6.18 summarizes some of the changes that take place in this exercise. The upper frames show that in the sites of Ses Covetes and Porreres the values at 10 m of TKE do not change significantly, but there are some evident differences in the vertically integrated values, especially in Ses Covetes where a cold pool is formed and turbulence

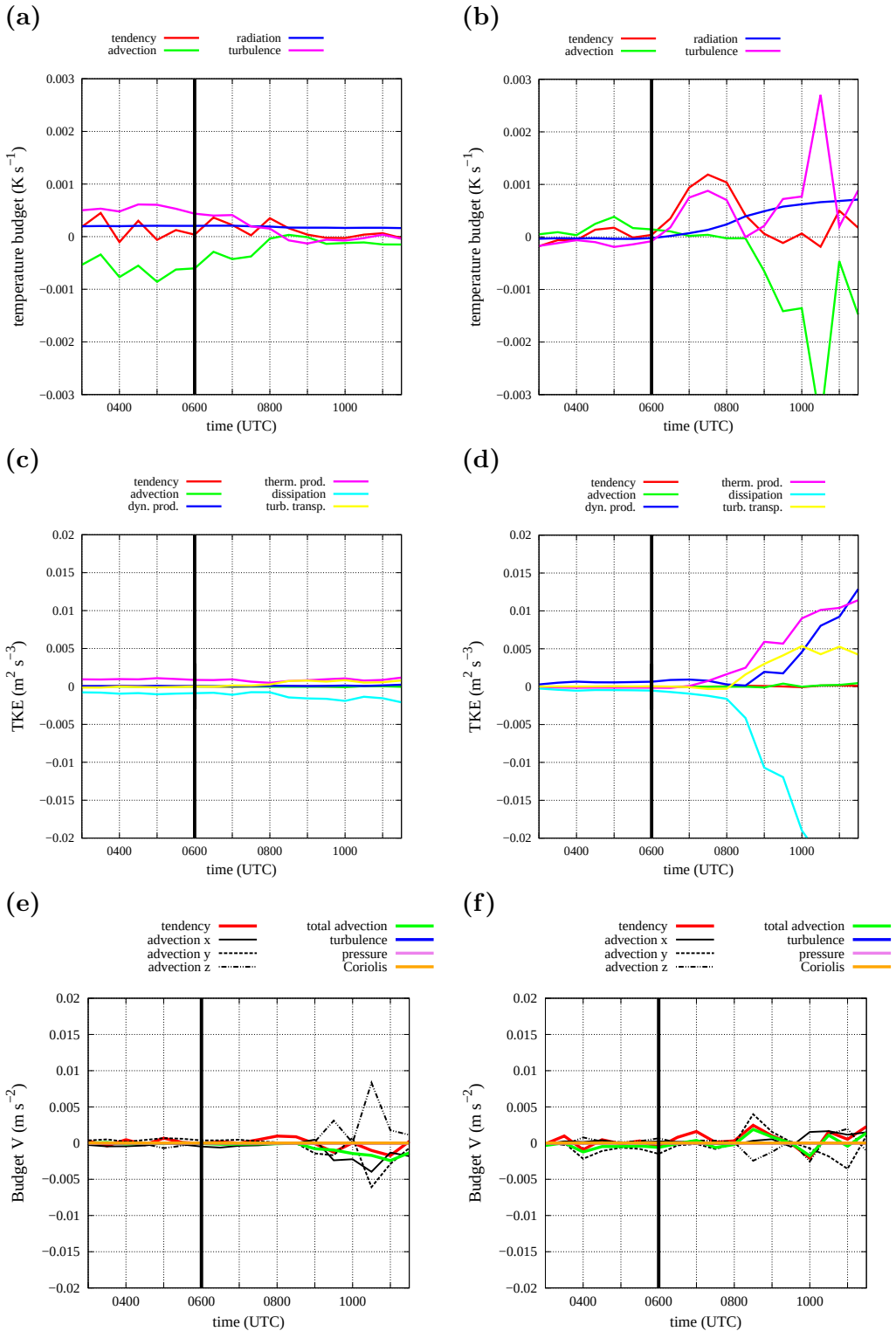

FIGURE 6.17: Time series of the Temperature budget at 10 m agl for a point **(a)** 6.5 km offshore and **(b)** 3.5 km inland. The same in **(c)** and **(d)** for the TKE budget and in **(e)** and **(f)** for the V-budget.

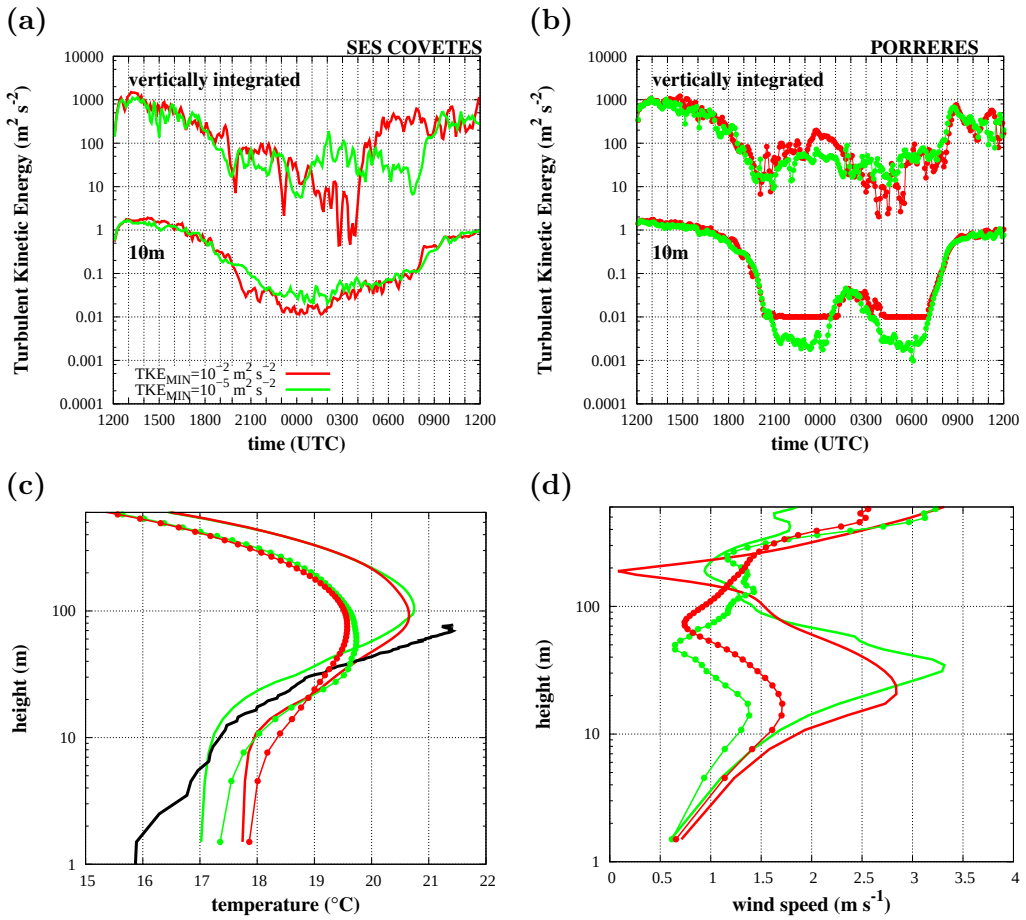

FIGURE 6.18: Temporal evolution of the 10 m (agl) TKE and the vertically integrated TKE over the first 1 km for **(a)** Ses Salines and **(b)** Porreres (see locations in Figure 6.1). In red the run with default TKE_{min} and in green the one with reduced TKE_{min}. In **(c)** and **(d)** there are the profiles of the temperature and wind speed at 0500 UTC for the same locations and runs (the same color and lines as in **(a)** and **(b)**). The multicopter observations at 0500 UTC are also shown with a black line.

is minimal. There, during the second part of the night and the early morning transition, when the lower TKEMIN manages to sustain a more turbulent regime than the artificially-increased one, and delays for some hours the establishment of a developed convective boundary layer over the site.

Looking at the profiles we see that the change of TKEMIN does not change much the direction or the wind speed of the lower layers of the LB, but has an appreciable effect on the layer above the jet. Our standard run has a softer transition between the jet and the slower air above, which allows the TKE to have significant values in that layer. The effects of this change in the integrated TKE value, which is larger for the default TKEMIN (10^{-2} m^2 s^{-2}) is that it allows for a more efficient transport upwards of the cold air at the surface and the resulting surface layer is colder and better mixed than the case with larger TKEMIN. Besides, the observed temperature profile in Figure 6.18c

indicates that once the TKEMIN is reduced, the modelled surface layer is closer to the observations, specially in Ses Covetes.

Similar results (Figures 6.18c and 6.18d) are found for the previous phase but for the rest of the MT phase, there are not significant differences in the profiles between the default and reduced TKEMIN.

6.6 Concluding remarks

This study has analysed a morning transition (MT) case between the Land-Breeze (LB) and the Sea-Breeze (SB) regimes taking advantage of the data gathered during an experimental campaign near the seashore, that has been used to check the performance of the numerical simulation of the case. The transition between LB and SB is seen to happen in four distinct steps, according to the observed temporal evolution of the wind and temperature in the lower atmosphere.

It is found that for all the different phases during the MT the model is able to capture the organization of the flow at lower levels. Nevertheless, the cold pool formed at the center of the basin during the LB seen by the model is about 1-2 K warmer than the observed one probably due to a too strong turbulent mixing in the model. The model is not able to capture adequately the temporal evolution of the thermal profile, showing that the morning transition, when the model energy budget usually differs a lot from the observed one, is a difficult regime for the physics of the model. This might be related to a wrong representation of the surface layer processes and an unrealistic surface properties (soil moisture or surface cover). Nevertheless, at the end of this phase the model agrees with the observations, showing that the general energetics of the MT are well captured. A sensitivity test on the imposed minimum value of the TKE in the turbulence scheme of the model shows that the most realistic model results are the ones with the reduced value.

The representation of the MT by the model is, in general, satisfactory, although an improvement of the morning heating of the surface would be needed and this issue must be further investigated, for instance comparing the modelled and measured surface energy budgets. There is a sustained lack of observational information over the sea that limits the capacity of interpretation of the coastal processes since verification is scarce in that area. The availability of vertical profiles of temperature and humidity has allowed to analyse in depth the evolution of the MT and it should be supplemented with wind profiles at both sides of the coast line. It has also been shown that the models results

are sensitive to relatively minor changes in their choices and that extreme caution must be taken when defining the simulation setup.

In this Chapter the attention is focused in studying the thermal heterogeneities at kilometric scale. Large-scale heterogeneities, such as land and sea, generate circulations like the land and the sea breezes during night and day, respectively. A case of a transition between LB and SB is taken to analyse (from observations and high-resolution mesoscale simulation) how the surface thermal heterogeneities are established close to sunrise and afterwards the atmosphere reacts to them.

Chapter 7

Relation between LST and the terms of the Energy Balance Equation in field studies

In the previous chapters, different experimental field campaigns and observations are used to characterize the land-surface temperature heterogeneities at different scales (hectometer and kilometer). In this Chapter, the evolution of the terms of the surface energy budget is explored for the experimental field campaigns that I have participated. All of them are conducted in complex terrain regions (surface cover and topography among others) and under different large-scale conditions (weak/strong winds, cloud/clear sky). The impact of these features in the diurnal evolution of these terms is explored to further understand the evolution of the land-surface temperature.

To proceed, a total of seven diurnal cycles are selected at different sites and days of the year. The first two cases of study correspond to a cloudy day (14-15/07/2016) and a clear day (21-22/07/2016) of the Subpixel Campaign that took place in the UIB, a heterogeneous area on a hectometric scale, during summer 2016. These two cases have been analysed in detail in Chapter 5. The other three cases are located in a complex terrain (topographically heterogeneous), the Cerdanya Valley, that is well vegetated all yearlong, for an autumn day (CCP15), and on two winter days (CCP17), one without snow and the other with snow, in order to see the differences in the same site, but with different conditions. The remaining two cases correspond to a flat and homogeneous terrain, the Pannonian Plain, in the cold season (PABLS13) and in summer (PABLS15).

These data have been collected in field campaigns made throughout the duration of this thesis, and they will be explained below in more detail.

7.1 Description of the field studies

A brief description of these field campaigns is detailed below. The selected cases were chosen so that each one was representative of the meteorological conditions that took place in the different campaigns. Besides, the campaigns with very close cases, only one of them is further analysed here.

7.1.1 Field studies in the UIB

In the warm season of 2016, the Subpixel Campaign took place on the UIB Campus, described in more detail in Chapter 5. The UIB Campus has an area of approximately 1 km^2, it is locally flat and it is considered heterogeneous since it is formed by large tiles of different types of surface as we have seen in Chapter 5.

For this study we have chosen 2 specific days of this campaign, 14-15/07/2016 corresponding to a cloudy day and the 21-22/07/2016 corresponding to a typical hot day of summer in this area.

7.1.2 Field studies in the Cerdanya Valley

The Cerdanya Cold Pool Experiments (CCP15 and CCP17) consisted in two field campaigns that took place in the Cerdanya valley, eastern Pyrenees (Figure 7.1). This valley, about 35 km long and 15 km wide, has a distinct ENE-WSW orientation that stands out among the rest of the Pyrenean valleys, generally oriented in the N-S direction. Its topographical configuration, with a valley floor at 1000 m above sea level (asl) and surrounded by mountain ranges rising above 2900 m asl to the North and up to 2700 m asl to the South, is prone for the development of intense cold-air pooling at its bottom part, even under the presence of significant synoptic pressure gradients [Conangla et al., 2018]. Furthermore, this topographic distribution plays a crucial role in the generation of slope and along-valley winds.

7.1.2.1 Cerdanya Cold Pool 2015 (CCP15)

The IOP 3 (10-11/10/2015) is further analysed in this section because that IOP is representative of an event with cold-air pool formation and the development of local winds due to the presence of a weak general wind channelled along the main valley axis. Besides, cloud cover increased as time advanced during that IOP. The most frequent case consisted in moderate valley winds before and after sunset of mesoscale origin, which

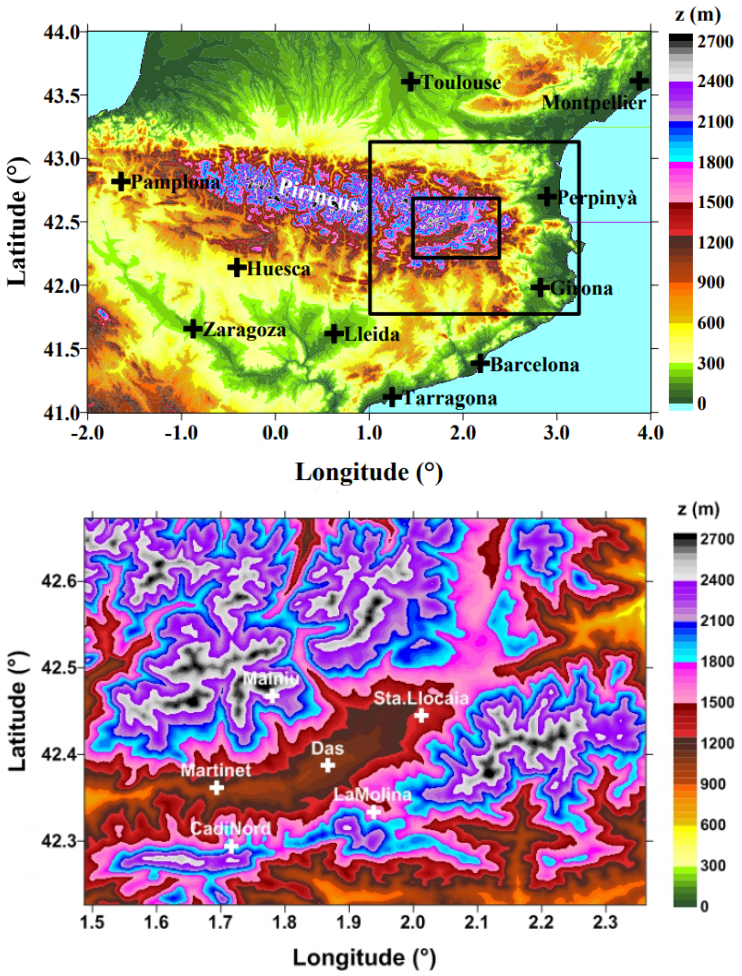

FIGURE 7.1: Topographic map of the Pyrenees mountain range of North-Eastern Spain and South of France, where the Cerdanya Valley is located. Source: Conangla et al. 2018

calmed down between 1 and 3 hours after dawn, leading to the late development of the cold pool. The second type of CP was in absence of the mesoscale winds, which allowed an evening transition with almost calm winds at sunset and establishment of down-slope and down-valley winds along the night, and the CP development starting around dawn.

IOP3 is of the second type of CP, without mesoscale NE winds and clear skies. Down-valley winds started at 1900-2000 UTC, having speeds up to 4 m s^{-1} between 100 and 300 m agl. At 2130 UTC there was an inversion at 150 m of 3 °C. After that, there was a very thin high cloud that made the stars less bright than the night before. The wind below 100 m was from 135 ° -outflow from La Molina valley, probably- and above it was downvalley weak wind (90-110 °). During the final part of the night an oscillatory behaviour in the 2 m temperature was observed, perhaps related to top-bottom mixing by the LLJ. The morning transition was under ideal conditions.

7.1.2.2 Cerdanya Cold Pool 2017 (CCP17)

Fifteen months later, in January 2017 the second part of this campaign began, CCP17, which ended at the end of February. The aims were to understand the mechanisms of CP formation, thermal surface inversions, the surface energy budget and the corresponding evolution in winter conditions, expanding the research currently in progress coming from the analysis of the previous CCP15 campaign.

In this campaign temperatures were very low and half of the campaign the soil was covered with snow, which began to fall on January 17th. Two cases of this campaign have been selected, one without snow in the ground (09-10/01/2017) and the other one with snow (24-25/01/2017).

The first case, had a northern wind with clouds snow precipitation at the mountain hills, but there was not raining in the measurement place at the center of the valley. During this case, there was a low temperature gradient. The first days of the campaign, in which it had not yet snowed, were under similar conditions, and we chose this day as representative of them.

During the second case, the whole valley was covered by melting snow from the previous week (8 cm layer depth). During the afternoon transition the wind was strong. The wind died down at 1900 UTC. Thin clouds covered the sky, but they disappeared at 0300 UTC, keeping a clear sky, and allowing a large surface cooling, attaining a minimum temperature of -12.0 °C at 0714 UTC.

7.1.3 Field studies in the Pannonian Plain

The measurements are made at the airfield of Szeged, Hungary (Figure 7.2). Szeged is in the center of the Pannonian plain at more than one hundred kilometers of the surrounding mountains. This plain is situated in the South-Eastern part of Central Europe. It forms a topographically distinct unit set surrounded by imposing geographic borders, the Carpathian Mountains, the Alps, the Dinarides and the Balkan mountains. The local topography is mainly flat and the heterogeneity of the terrain is low.

In the Pannonian Plain, 2 plurinational campaigns were made: one in the cold season at late fall of November 2013 (PABLS13) and the other in summer 2015 (PABLS15), in order to study the characteristics in the diurnal cycle of the atmospheric boundary layer and its interaction with the underlying surface. The intensive period of measurement of the winter campaign was between 25^{th} of November until 28^{th} of December 2013, when Szeged was at the edge of a high pressure system over central and Eastern Europe. The

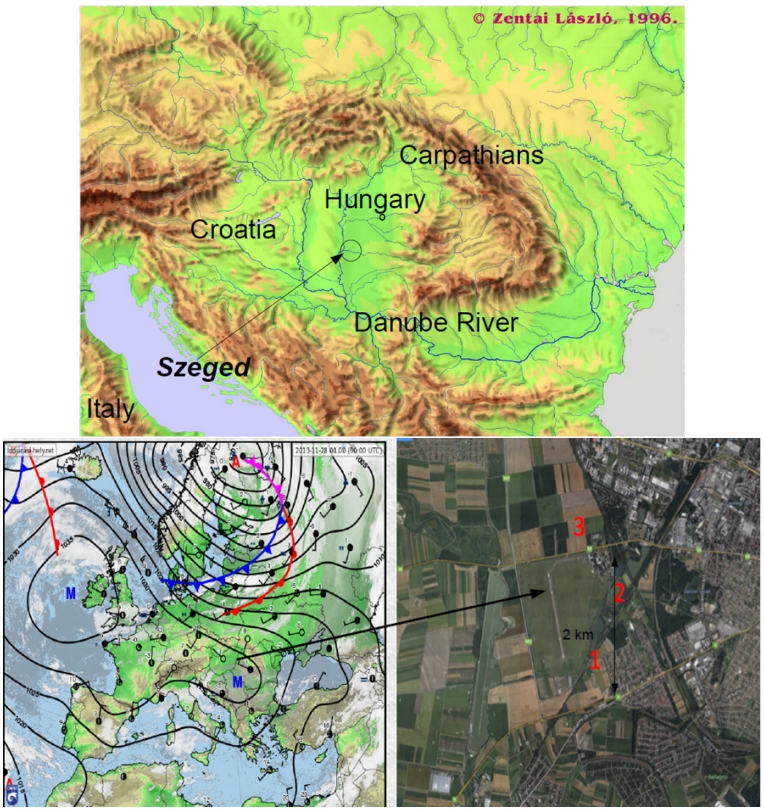

FIGURE 7.2: Locations of Szeged in the Pannonian Plain and the Airfield where the campaign took place.

summer campaign was between 26^{th} of June until 30^{th} of September 2015, with four IOPs (10^{th}, $14-15^{th}$, $15-16^{th}$ and $16-17^{th}$ of July), under high pressures and weak winds.

7.1.3.1 Pannonian Atmospheric Boundary Layer Study 2013

During the PABLS13 campaign, Szeged was at the edge of a high pressure system on Central Europe and a low over the Adriatic sea and the Southern Balkans (Figure 7.2b). The chosen study day, IOP1 (27-28 November 2013) was dominated at night by cold advection (cold air over warmer terrain) blowing from the mountains at the South, with middle clouds. This lead to a weakly unstable Nocturnal Boundary Layer some tens of meters deep. Close to dawn, wind stopped and skies cleared, with the fast formation of a strong and shallow surface inversion until the morning when solar radiation destroyed it by convection.

In IOP1, there was a high pressure system on Central Europe and low over the Adriatic sea and the Southern Balkans (Figure 7.2b), Szeged was located just at the interface between the two structures. The general wind was between East and South (Figure 7.2b), corresponding to the rotation of the low system, with clouds between 800 and

3000 meter agl during the first part of the night; 30 kilometers to the North the skies were clear. The skies were overcast until 2300 UTC, with occasional light snow fall, not staying over the surface, which was above 0°C.

After 2300 UTC, light precipitations stopped, and cloud monitoring through IR Meteosat scenes showed progressive thinning of the cloud depth over the area (not shown). In fact along the rest of the night, the cloud deck was thin enough to show the position of the moon (final last quarter) and occasionally holes in the deck through which stars could be seen. Clouds were at an estimated height of about 800 meters. From the rest of the night, the cloud stayed on place, until twilight (0511 UTC). Between twilight and sunrise (0558 UTC) the skies cleared, with no clouds at the sunrise.

7.1.3.2 Pannonian Atmospheric Boundary Layer Study 2015

More recently, in summer 2015, a similar display was repeated during the months of July and August, that included one week of intensive observations with soundings between July 10 and July 17. These particular days allowed measuring several canonical episodes of windy convective boundary layers, weakly stable nights, and evening and morning transitions, compiling a nice set of likely reference cases.

The chosen study day, IOP3 (night from 15 to 16 July 2015) was a good case study of moderate windy and clear skies case with a surface inversion increasing at night with a moderate strength (3 to 5 °C). There was an excellent calm morning transition. It was a day with weak westerly flow and clear skies with some broken occasional clouds at about 1000 m during the night. Regarding boundary layer evolution, there was a stable boundary layer, with an inversion of 3 to 5 °C from surface to more than 100 m, a depth that increased along the night to near 200 m.

7.2 Relation between LST and the Energy Balance Equation terms

In Chapter 1, the terms of the surface balance equation have been introduced: Rn, LE, H and G. In this Section, its relationship with the LST will be analysed for different cases.

7.2.1 Cloudy summer day in UIB 2016

The first case (Figures 7.3a and 7.3b) is a heterogeneous surface on a hectometric scale, the UIB Campus, on a cloudy summer day (14-15/07/2016). The ground was very hot and the soil temperature did not reached values below 25 °C. In this case, LST followed the same pattern as the R_n, except at night when R_n varied around -50 W m^{-2} and the LST continued to fall. It should be noted a peak in R_n around 0030 UTC that affected LST and ST that also increased, but not T2, which keeped going down (Figure 7.3b). G during the night oscillated around 35 W m^{-2}, and had a reverse behaviour to R_n, when one increased the other decreases. Turbulence during the night did not influence the LST at any time.

In the Figure 7.3b it is possible to see the behaviour of LST respect to ST and T2. After sunrise, it became cloudy and the daytime cycle of T2 was not intense. The soil showes higher temperatures than the air, therefore it was the source of heat to the surface. It was a hitched system, all response equally at the same time. The largest differences between T2 and LST are found during the day, while at night they were close to zero.

7.2.2 Sunny summer day in UIB 2016

In the same location, but a week later on a hot dry sunny summer day (21-22/07/2016) is the second case (Figure 7.3c and 7.3d). The soil was very dry, containing a small amount of water, so the upper soil was the one warming intensively. LST increased with R_n (but more slowly than the latter) until it reached the maximum, and continued to decrease 10 °C at night while R_n remained constant. R_n shows an ideal behaviour and it is practically compensated by G at night. Turbulence during the night had very little effect. The values of the fluxes and temperatures were high due to the strong turbulence within the convective boundary layer. In this case, also the greatest temperature differences between T2 and LST (Figure 7.3d) are found during the day, at night both temperatures had the same value, although there was a much warmer soil that did not allow the establishment of a temperature inversion. These results are consistent with those obtained in Chapter 4.

7.2.3 Autumn day in CCP15

The following cases took place in the Cerdanya Valley during CCP15 and CCP17, located in a complex terrain (topographically heterogeneous). The third one (Figures 7.4a and 7.4b) is from 10-11/10/2015, as it is a more humid area than the previous situations. LST did not respond so quickly to radiation, but experienced its same behaviour, except

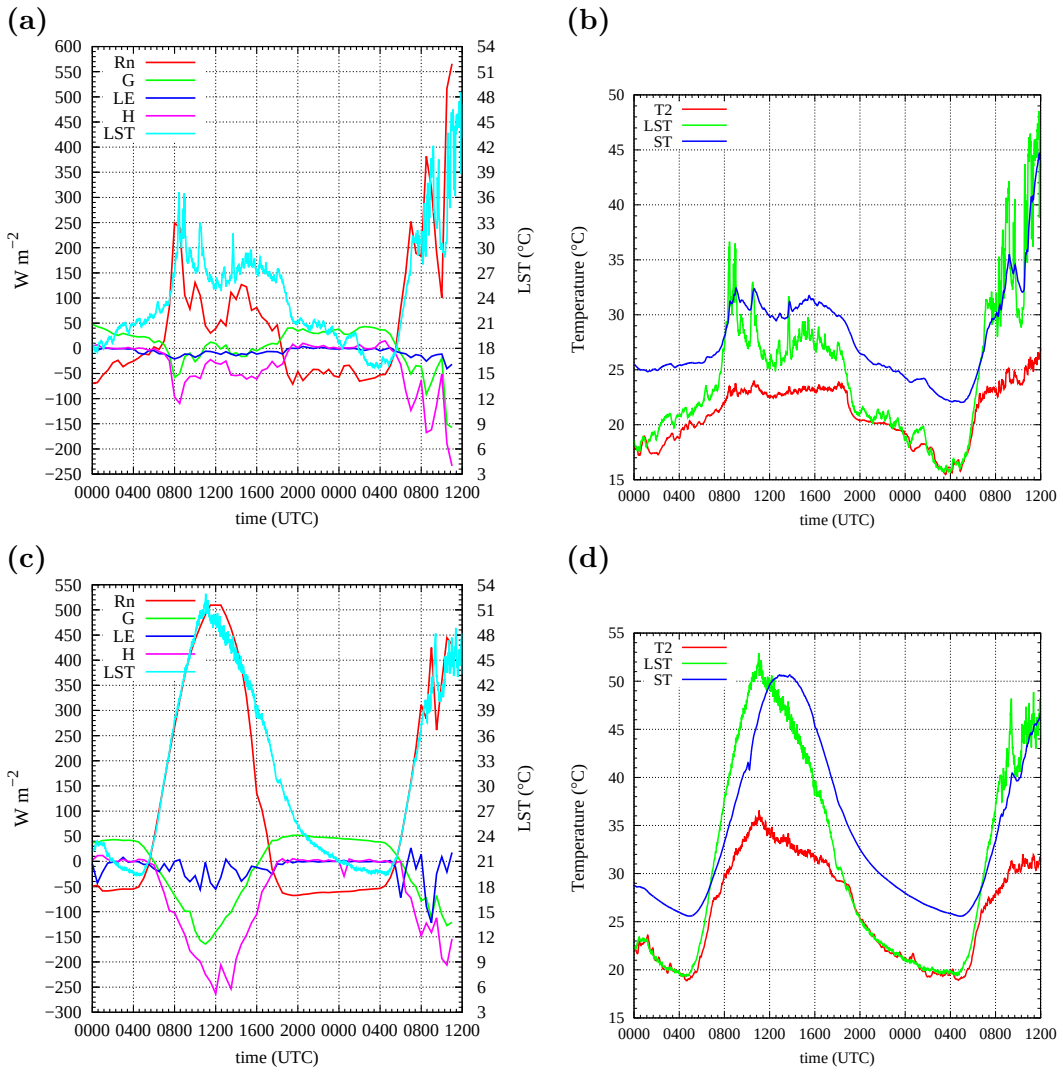

FIGURE 7.3: Subpixel Campaign July 2016 UIB: Relation between land surface temperature (LST) and terms of the energy balance equation: net radiation (R_n), ground heat flux (G), latent heat flux (LE) and sensible heat flux (H) for a heterogeneous terrain at hectometric scale, the UIB Campus during a **(a)** cloudy day (14-15/07/2016) and **(c)** sunny day (21-22/07/2016). The evolution of the air temperature (T2), the land surface temperature (LST) and the soil temperature at 2 centimeters depth (ST) is shown for the same days in **(b)** and **(d)** respectively. Vertical axes in each graph are different.

at night that R_n remained constant and tended to be compensated with G, but the LST decreased 9 °C. G increased at the end of the night, each time it was more stable and there was less mixing. The LST had peaks related to turbulent events. It should be noted that around 1900 UTC the LST increased 3 °C while the radiation experienced a downward peak, this was due to at the North wind inlet for about one hour (not shown) that caused an increase of LST of about 3 °C and T2 of about 1 °C, but the ST did not notice it (Figure 7.4b).

7.2.4 Winter day CCP17

The fourth case corresponds to a winter day (09-10/01/2017) in CCP17 (Figure 7.4c). The water in the soil was undergoing a phase change, it was freezing, and as it freezed it produced heat, which made the LST did not cool at night. At the beginning of the night, LST dropped more than 6 °C while R_n increased, this was due to the turbulence, which continued to cool the surface and the air, although ST remained constant (Figure 7.4d), which affected the fact that G also presented very small and constant values because there was no vertical temperature gradient. From 0800 UTC, LST increased with the R_n, but in the central hours of the day R_n experienced a drop that did not immediately affect the LST, but had an effect one hour later.

7.2.5 Winter day covered of snow CCP17

The fifth case is taken because the surface was covered by a layer of snow of about 8 cm depth (24-25/01/2017) in CCP17 (Figure 7.4e). The LST during the night decreased until after sunrise that R_n began to increase. It should be noted that in this case, G did not present any cycle, since it was isolated due to the layer of snow located on the surface, besides ST was also constant. Here, during the night although R_n remained more or less constant, the LST had peaks related to turbulent events, which were also seen in T2 although not as intense (Figure 7.4f). There was a stable stratification between LST and T2. The surface did not receive heat due to the snow, therefore, it cooled and there was an inversion of 4-5 °C in the first 2 m decoupled from the ground. The LST was positive during a few hours of the day, either the snow was melting and contained air or because there was a mistake in emissivity that has affected the calculation of LST.

7.2.6 Winter day in PABLS13

The sixth case is a winter day during PABLS13, on 27-28/11/2013 (Figure 7.5a and 7.5b), a homogeneous zone. In this case, at the first part of the night the sky was cloudy and LST increased approximately 1 °C. When the sky was uncovered (0230 UTC) no LST values were available, but T2 dropped 2-3 °C showing very slows surface inversion. LST values were available from 1200 UTC, this day showed a singular behaviour, while R_n remained constant and G had significant values. There were not loss by R_n and surface was heated by G. LST tended to heat up due to the contribution of heat from the ground to the surface. In addition, this behaviour was different from that of T2 and ST (Figure 7.5b), which in these cases decreases. T2 towards 2000 UTC presented a synoptic change, and arrived cooler wind from another direction (not shown).

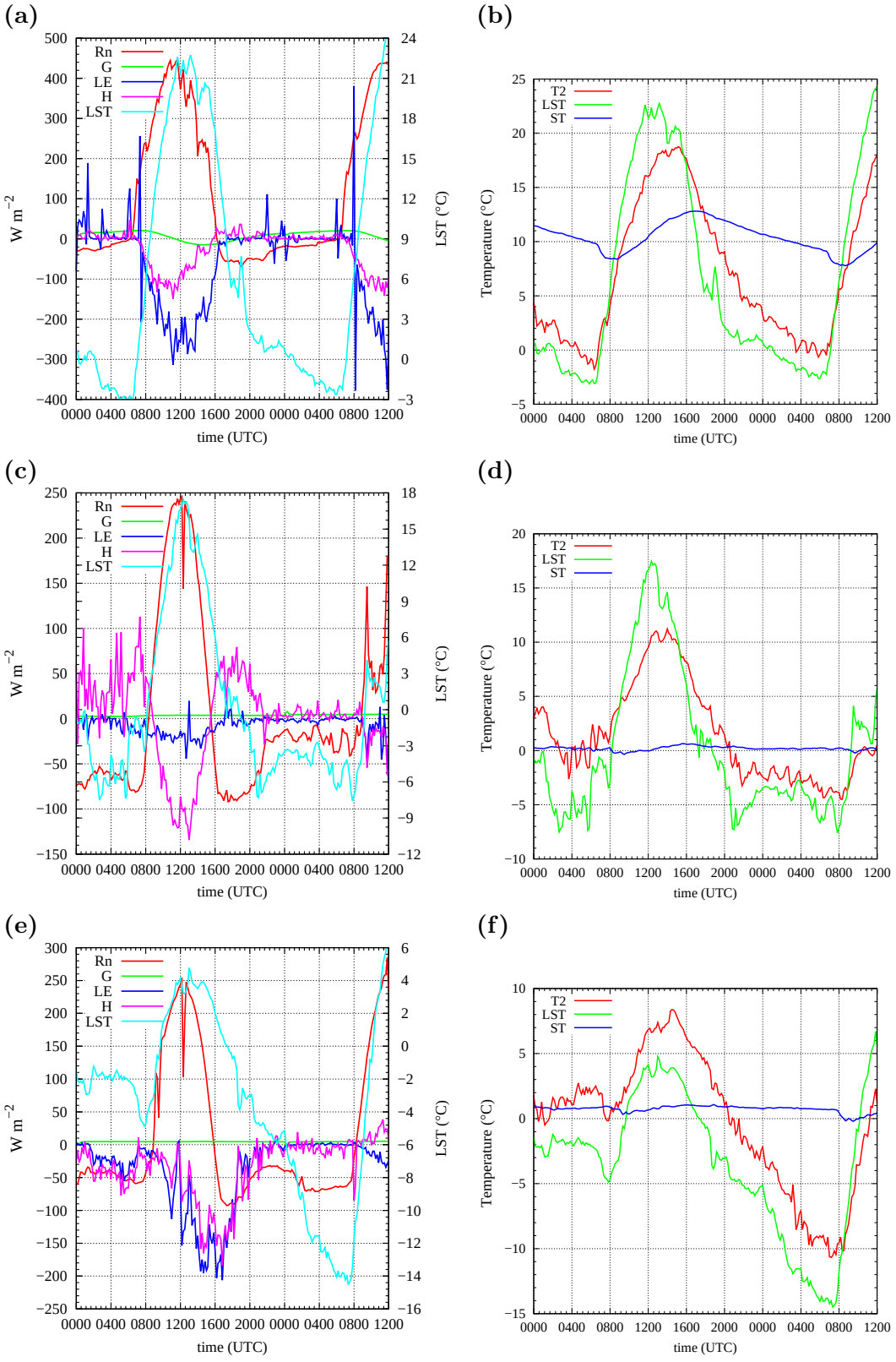

FIGURE 7.4: The same as Figure 7.3 but for the CCP campaigns: **(a)** and **(b)** CCP15 in autumn; **(c)** and **(d)** CCP17 in winter without snow and **(e)** and **(f)** with snow.

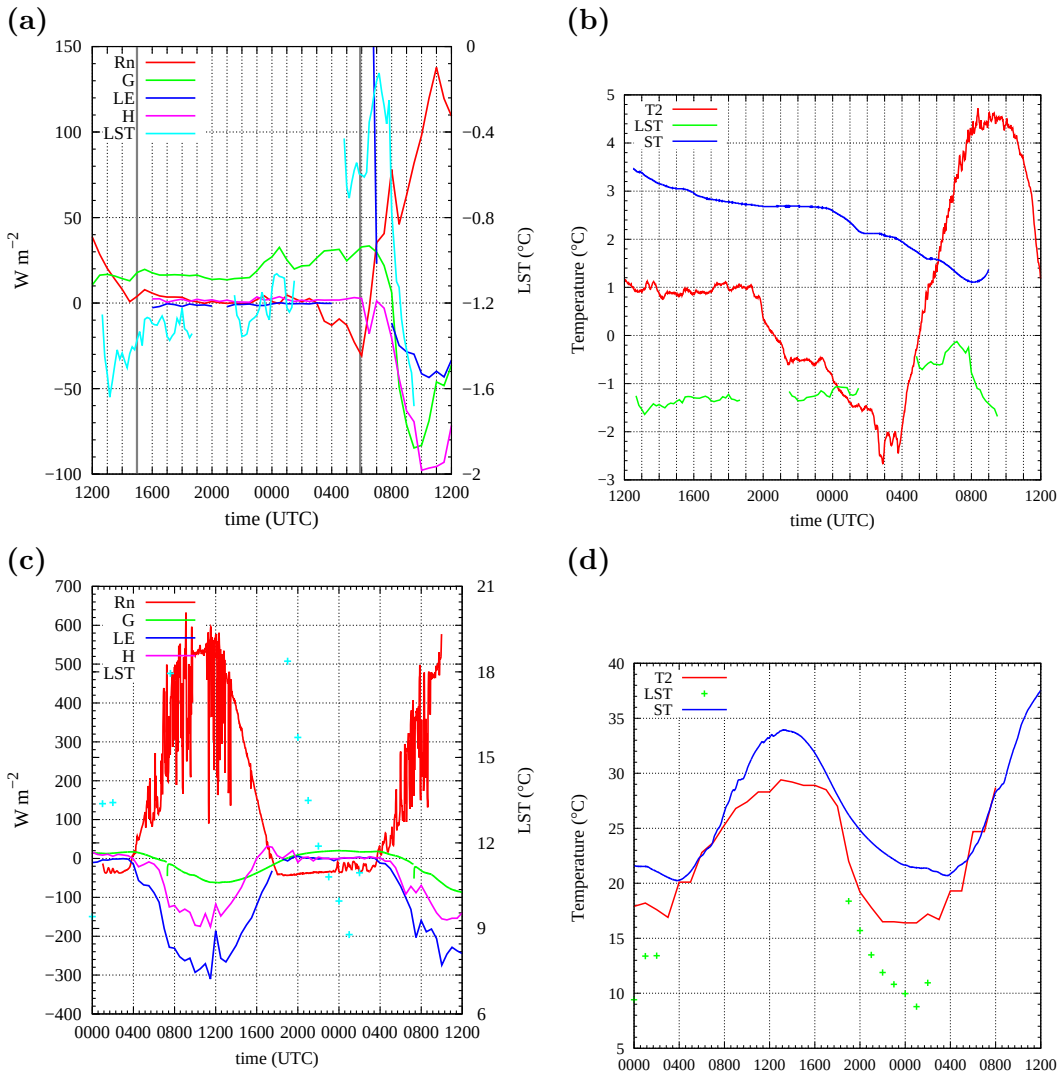

FIGURE 7.5: The same as Figure 7.3 but for the PABLS campaigns: **(a)** and **(b)** PABLS13 in cold season and **(c)** and **(d)** PABLS15 in summer.

7.2.7 Summer day in PABLS15

The seventh case (Figure 7.5c) is in the same location, but for a summer day in PABLS15 (15-16/07/2015). In this case, LST measurements were not available, so an approximation was made during the night from the net radiation, which was available with hour values. We have approximated L_{ms} (Equation 4.1) $\approx R_n$ (since there was no short wave radiation at night), L_{dn} has been obtained from the Equation 4.5. Replacing these terms in the Equation 4.2, we have obtained the estimated values for LST. If the values obtained from LST are compared with those from T2 and ST, it can be seen that the behaviour of LST is reasonable. It is possible to observe a decoupling between T2 and LST, thus showing a strong thermal inversion. In contrast, we observe some correlation between LST and ST.

7.3 Discussion

After analysing very distinct cases in several locations, and under different meteorological conditions: (i) heterogeneous surface at an hectometric scale on a cloudy summer day and a sunny day; (ii) the cases in complex terrain topographically heterogeneous that is homogeneously vegetated in autumn, in a winter day and a snowy day, respectively (iii) the cases in a homogeneous vegetated area in cold season and summer, it can be concluded that turbulence does not influence significantly the evolution of LST at night, whereas R_n and G play a very important role in all cases.

These cases can be grouped into two categories, those for T2 and LST decrease during the night, which are cloudy and cloudless cases in UIB Campus (Figure 7.3), CCP15 and CCP17 with snow (Figures 7.4a and 7.4e), and PABLS15 (Figure 7.5c) and the remaining two other cases that do not have this behaviour, CCP17 without snow in the soil (Figure 7.4c) and PABLS13 (Figure 7.5a). The cases of the first group (although have distinct characteristics and are under very different conditions) allow that during the night the surface temperature and the air temperature continue to decrease, since there is not a process strong enough interposing with it. One important factor that alters these processes, is the presence of snow since it behaves as an insulating layer that separates the soil from the air, so that, they are not affected by each other.

The second category corresponds to cases in which the LST does not decrease during the night. One of them is the case without snow in CCP17. In this case, temperatures are close to 0 °C, and the water that is located on the surface and in the first few centimeters of the ground, is undergoing phase changes. These phase changes give off heat to the surface and affect the surface temperature not letting it gets off. The other one in which the LST does not descend is the case of PABLS13, in which the first part of the night was cloudy, so the R_n is practically zero, as well as LE and H and there is only G that remains practically constant below the 20 W m^{-2} and does not allow the LST to go down. In this way it is possible to see, that if there is no mechanism to prevent the LST from decreasing during the night (such as phase changes or the presence of clouds), it continues to decrease until the sunrise.

7.4 Concluding remarks

The general conclusions that are obtained from this study are the following. One conclusion is that LST is a good indicator of energy balance behaviour, especially at night when R_n and G dominate. The second conclusion is that the processes of the soil and the surface (for example, snow) determine the behaviour of LST, especially if they are

capable of contributing energy to the surface as it loses it by irradiation. Furthermore, LST values and the terms of the surface energy balance equation can vary significantly from one point to another in a heterogeneous terrain, depending on the G behaviour. The last conclusion, although there is a great uncertainty on the LST variable (± 3 °C according to Chapter 4), the evolutions are very well-defined, and allow to evaluate the standard cases.

These results show that the behaviour of the LST at night depends on the state of the soil, so for heterogeneous terrain, the LST can have different behaviours in neighboring areas depending on the soil conditions of the site. These results indicate that the relationship between T2 and LST that we have studied in Chapter 4 is only valid for soils with the same conditions of our study since otherwise, the LST can vary in differently way and therefore its relationship with T2. In Chapter 5 we have seen that there are differences of LST during the night in heterogeneous terrain of 1 km^2, the data we have are scenes taken at specific moments (when the satellite passed or the drone was flying). The results obtained in this Chapter lead to think that the variation of LST may be different in each type of soil, and these differences obtained between the different zones are not constant during the night. These results indicate that there is a need for instruments measuring at high frequency to characterize the soil, the surface and the atmosphere.

Chapter 8

Conclusions

In this thesis, the effects of the surface thermal heterogeneities on the Atmospheric Boundary Layer at different scales have been studied. To proceed with, concepts of remote sensing and Atmospheric Boundary Layer have been used in order to understand the processes that take place in the soil-atmosphere interface in a heterogeneous terrain. For this purpose, I have tried to bring together the fields of remote sensing and Atmospheric Boundary Layer, interlacing information and knowledge between the two disciplines.

I have found that small-scale heterogeneities are able to create local circulations that can affect the atmosphere-soil system, as in the case of horizontal advection. These heterogeneities can contribute notably to the energy imbalance at the surface as seen in this thesis. Large-scale heterogeneities can also generate general circulations, such as in the case of the Land and Sea-Breeze or the case with valley winds. If the wind flow is significant, local circulations can be modified or even not present.

With the purpose of measuring the effects of small-scale heterogeneities, it is needed to sample at a rate at which small changes can be detected, even if it occurs in small-time intervals. Furthermore, it is needed enough of these sensors to cover the entire area of interest to accurately characterize the processes that are taking place on it. Regarding meteorological models, must be used spatial resolutions of hundreds of meters (the size of the heterogeneities) to properly reproduce them. The surface and soil features have to be given at these resolutions to include the topographical and surface variability in order to accurately reproduce the heterogeneities that they induce.

In order to study the heterogeneities with satellite data, high spatial resolution sensors are needed (higher than the size of heterogeneities) and with a temporal sampling frequencies the order of minutes. Thus, all the variations that occur at small-time intervals could be detected. However, current meteorological satellites do not cover both spatial

and temporal above mentioned requirements; if they have good spatial resolution, they do not have good temporal resolution and vice versa. If the heterogeneities are on a hecometric scale, satellites with spatial resolutions lower than 100 m can be used, as Landsat 7-ETM+, Landsat 8 or ASTER. Otherwise, if the heterogeneities are on a kilometric scale, satellites with spatial resolutions of the order of 1 km can be used, as MSG or MODIS. Finally, if the heterogeneities are at the scale of the few meters, the best option is to use UAVs flying at relatively low heights.

On the other hand, I have seen that the relation between air temperature and Land Surface Temperature does not follow any recurrent pattern. It does not depend solely on the surface or the atmosphere, but behaves like a system that has its own rules and its equilibrium. Moreover, when some variable gets out of this equilibrium, many elements of the system may change to move again towards the equilibrium. That is why it is very difficult to find a theory of similarity, like that of Monin-Obukhov, since there are many independent variables that often are mutually dependent and these relations are difficult to detect. As there is no other theory of similarity universally accepted, the models continue using Monin-Obukhov to link the surface and the atmosphere in some way, although it is not always the correct solution.

The main results of each chapter are the following:

In Chapter 3, the Land Surface Temperature (LST) differences in a heterogeneous terrain at hectometric scale, the Campus of the University of the Balearic Islands (UIB) were analysed. Data from Landsat-7 and observed data from the meteorological station located at one point of this study area have been used, and compared with MODIS data. From this study, a very large variability at scales under 1 km has been found, that MODIS, which has a spatial resolution of 1 km, is not capable of detecting. Landsat-7 instead, is useful to study the heterogeneities at hectometric scale because its spatial resolution is 30 meters. Other results obtained are that surface temperature differences are of the order of 5-10 K in winter and higher than 20 K in summer, with standard deviations of about 2 K. These results show us the variability of the surface temperature and the importance of choosing a location for a station in heterogeneous terrain, because if we put it in an area that gives us extreme values, when they are compared with data from satellite or from models, it gives us erroneous results. A possible solution would be to place the station in a location that gives us average values of the area if it exists.

In Chapter 4, different methods to obtain the LST and the errors that are made in using them were analysed, finding that there is a large experimental uncertainty due to the determination of the upward long-wave radiation that is of the order of 2-3 °C. The relation of the LST with the air temperature at two meters (T2) were analysed, getting differences between both temperatures during the day of the order of 3 °C in winter

and 10 °C in summer, with greater differences on dry and warm days. At night these differences are between 1-2 °C in winter and 0-1 °C in summer, were lower than the error of the LST measurement, but they indicate that there are no significant vertical gradients of temperature even if they are nights with stratified conditions. On the other hand, correlations between T2-LST with other variables were explored, obtaining that during the day it is well correlated with the flux, whereas the correlation becomes relatively low at night. This shows that, together with the fact that the difference between temperatures is less than 3 °C, the coupled system soil-atmosphere is able to respond quite well to the energy demand of the atmospheric surface layer as it cools during the night and does not allow the establishment of very strong stable gradients in the lowest two meters of the atmosphere for this location, specially in summer. To conclude, there are many processes that intervene at different temporal and spatial scales (from centimeter to meter), depending on the ambient and surface conditions. For this reason it is difficult to properly represent the SL in models.

In Chapter 5, the spatial variability at the hectometer scales of the temperature, humidity and wind were analysed in the Surface Layer and for the upper soil temperature and moisture, using nine instrumented Poles. During the day, the horizontal variability is very small, with differences of few degrees in temperature, 2 g kg^{-1} in the specific moisture or 1 m s^{-1} in the wind speed. Instead, the turbulent mixture causes a homogeneity in the atmospheric variables, but not in upper soil variables, which shows a relevant spatial inhomogeneity during the day. During nights, the upper soil variability behaves as in the day, but atmospheric variables show larger variability. This is due to the low mix of turbulence during clear nights with weak winds. The variability of vertical gradients is also explored, finding negative values during the day for temperature and specific humidity gradients (convective conditions). That shows that there are positive values of sensible and latent heat fluxes of different values from the Poles along the Campus. Instead at night, the temperature gradient may vary from small positive values to larger negative gradients, showing that depending on the Pole there will be unstable or stable stratification. The specific humidity gradient shows the same behaviour, which indicates that evaporation or condensation depending on each Pole. In addition to studying the variability, the horizontal advection has also been estimated and compared with the imbalance measured in the ECUIB. It is seen that the average values of horizontal advection are relatively small, specially in the daytime, but that individual values can become significant in nights with clear skies and very weak winds, when they may be larger than the turbulent heat fluxes.

In this thesis are also briefly inspected the results of several campaigns in which I participated. In Chapter 6 it has been studied a morning transition case between the Land-Breeze and the Sea-Breeze. The model detects well the organization of the flow

in lower layers, but does not detect properly the establishment of a Cold Pool that it is in the center of the basin. The model gives values between 1-2 °C warmer than the observed data and it is not able to capture adequately the temporal evolution of the thermal profile. This might be related to a wrong representation of the surface layer processes and an unrealistic surface properties. Nevertheless, at the end of this phase the model agrees with the observations, showing that the general energetics of the Morning Transition are well captured. To conclude, the models are capable of reproducing the heterogeneities at kilometric scales, such as the case of the Land and Sea-Breezes that result from the circulations generated by these heterogeneities.

Finally, in Chapter 7, it has been seen how variations in the terms of the energy balance equation directly influence the processes near the surface, reflected in the land surface temperature. Analysing different types of land in different conditions, it can be seen that the turbulence at night does not affect the LST significantly, however it is affected by R_n and G which in turn are directly influenced by the soil conditions, more precisely by its content in water and temperature. In this way, drier soils respond more abruptly to heat exchanges, while wet soils do not present these prominent changes due to the presence of water and how heat exchanges affect it. On the other hand, soils with temperatures close to the phase exchanges, present completely different behaviours, since the phase exchanges produce heat. The snowy soils are isolated from the air by the snow cover, so they are uncoupled.

To conclude, the surface thermal heterogeneities have a very important effect on the processes that take place in the surface layer. Although this thesis has allowed us to know the influence of these heterogeneities, many issues remain to be explored.

Outlook

Apart from the papers that are being written about the campaigns in which I have participated (MSB14, PABLS13, PABLS14, CCP15, CCP17, Subpixel Campaign), this thesis opens some ways to continue investigating these processes related to de surface heterogeneities.

a) Study the LST variability that we have seen in Chapter 3 but for many more years, in order to know if this variability remains constant over the years, or changes depending on the conditions of each year. In the Campus of the University of the Balearic Islands, the data is only available from 2015, it would be interesting to look for some other heterogeneous place that has a longer time series to be able to do this study.

b) Check if the results obtained in Chapter 4 that relate T2 and LST are valid for other zones and if they are not, understand why they differ.

c) Study in more detail the calculation of advections, a possible way would be through satellite scenes to have continuous data instead of having them in specific places as is the case of the Poles as Chapter 5.

d) With the data that we have of the Subpixel Campaign (Chapter 5), study the humidity advections, in order to know if they affect the imbalance or the LE calculation.

e) Another issue, may be to deepen the work of the last chapter, study more cases in the same places or in other places, and the dependence of LST in more detail. Furthermore, it is possible to study in more detail the lag between the increase of LST and the increase of net radiation in the morning and if it depends on the properties of the soil.

Appendix A

Time series for variables explored in Chapter 4

The time series of the variables explored in Chapter 4 have been represented in the next Figures of this appendix. It corresponds to the quantities measured in the meteorological research station located on the Campus of the University of the Balearic Islands (ECUIB) for the two studied years (from January 2015 to January 2017).

For all the Figures on the left side, there are the diurnal averages, calculated between 1000 and 1300 UTC with air temperatures higher than 20 °C in pink and lower than 20 °C in green. A similar plot is made for the nighttime averages (0000-0300 UTC) and they are placed on the right side of the figures.

Next figures show that the different magnitudes explored have a clear diurnal and annual cycle with distinct behaviour for the days/nights when the temperature is larger/lower than 20 °C.

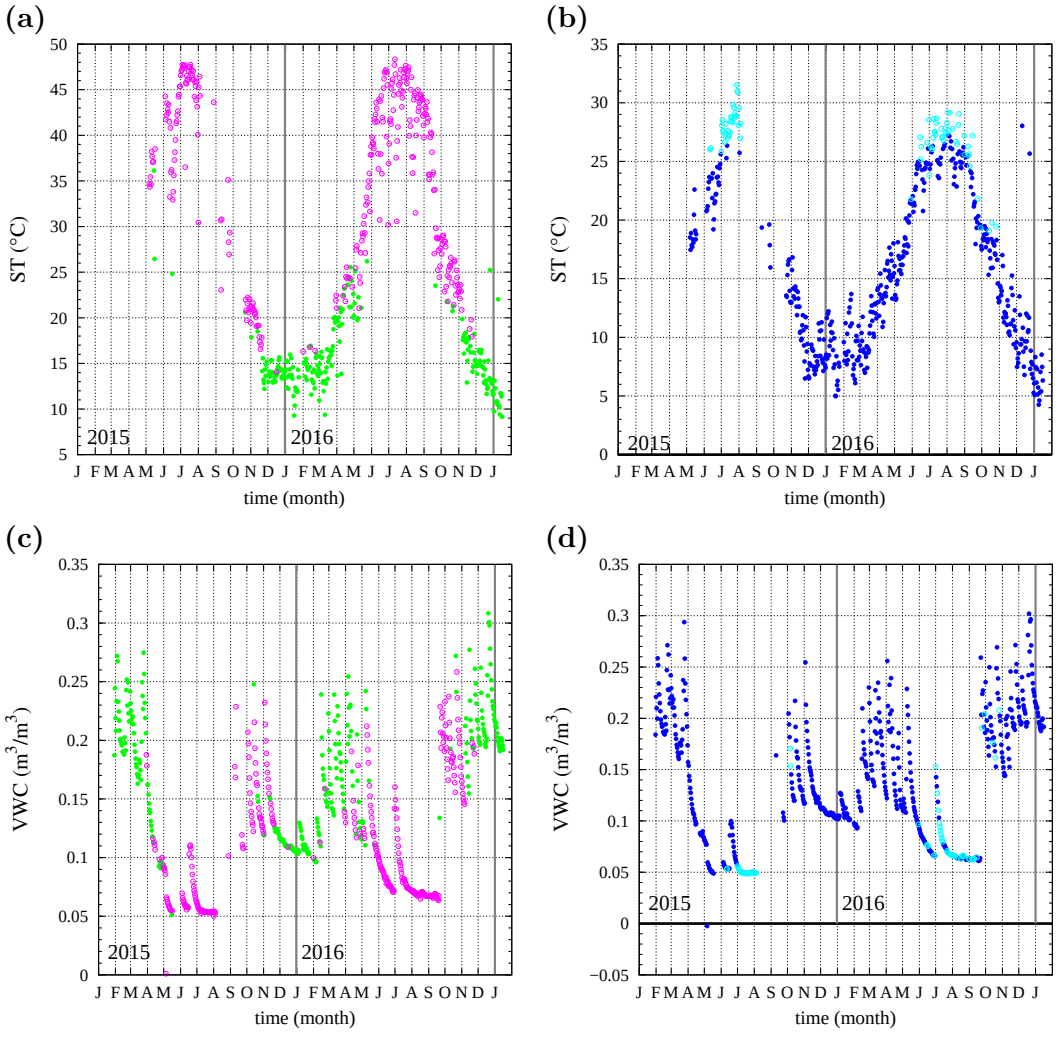

FIGURE A.1: Daily mean values of **(a)** and **(b)** soil temperature, **(c)** and **(d)** volumetric water content during the two years of study. These averages are made between 1000 and 1300 UTC for diurnal values (left) and between 0000 and 0300 UTC for nocturnal values (night).

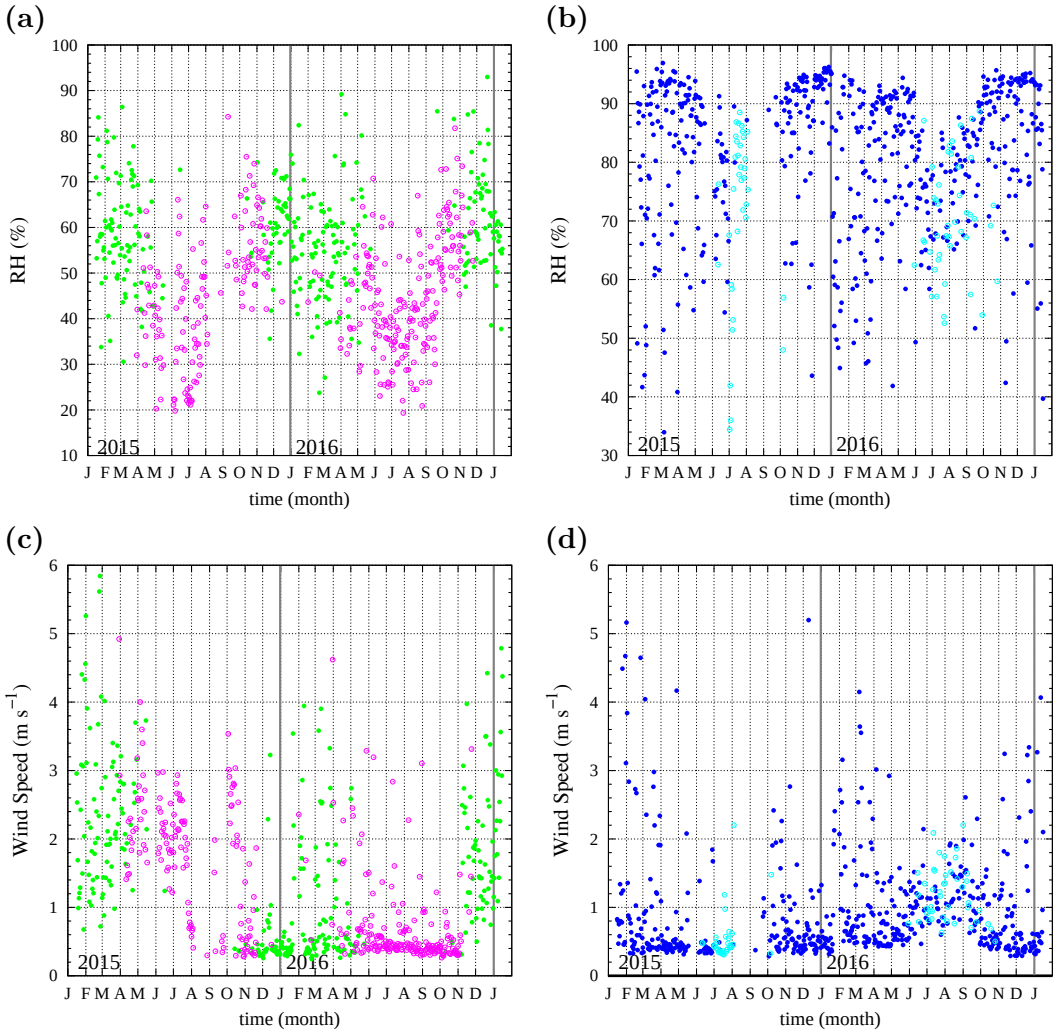

FIGURE A.2: Same than Figure A.1, but for **(a)** and **(b)** relative humidity, **(c)** and **(d)** wind speed.

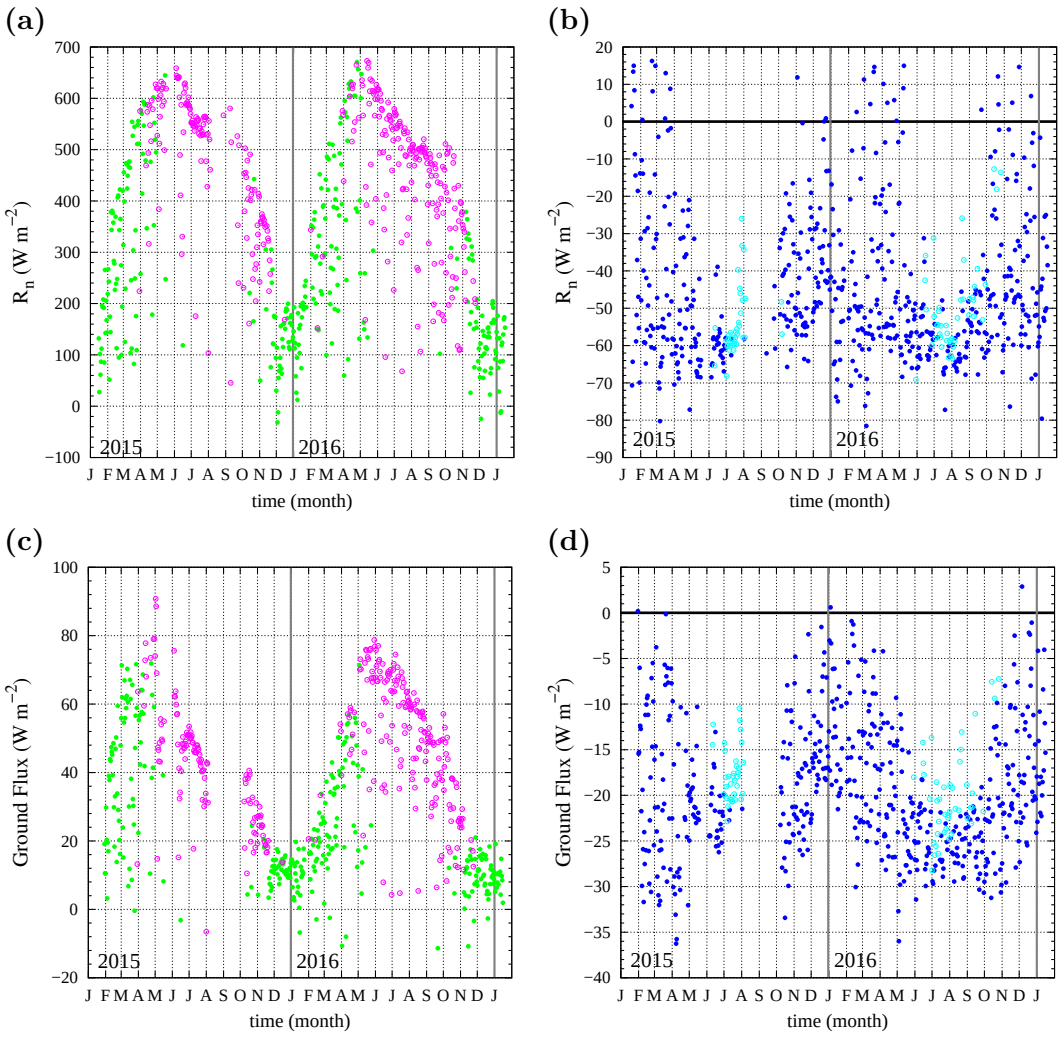

FIGURE A.3: Same than Figure A.1, but for **(a)** and **(b)** net radiation (R_n), **(c)** and **(d)** ground flux (G) at -8 cm.

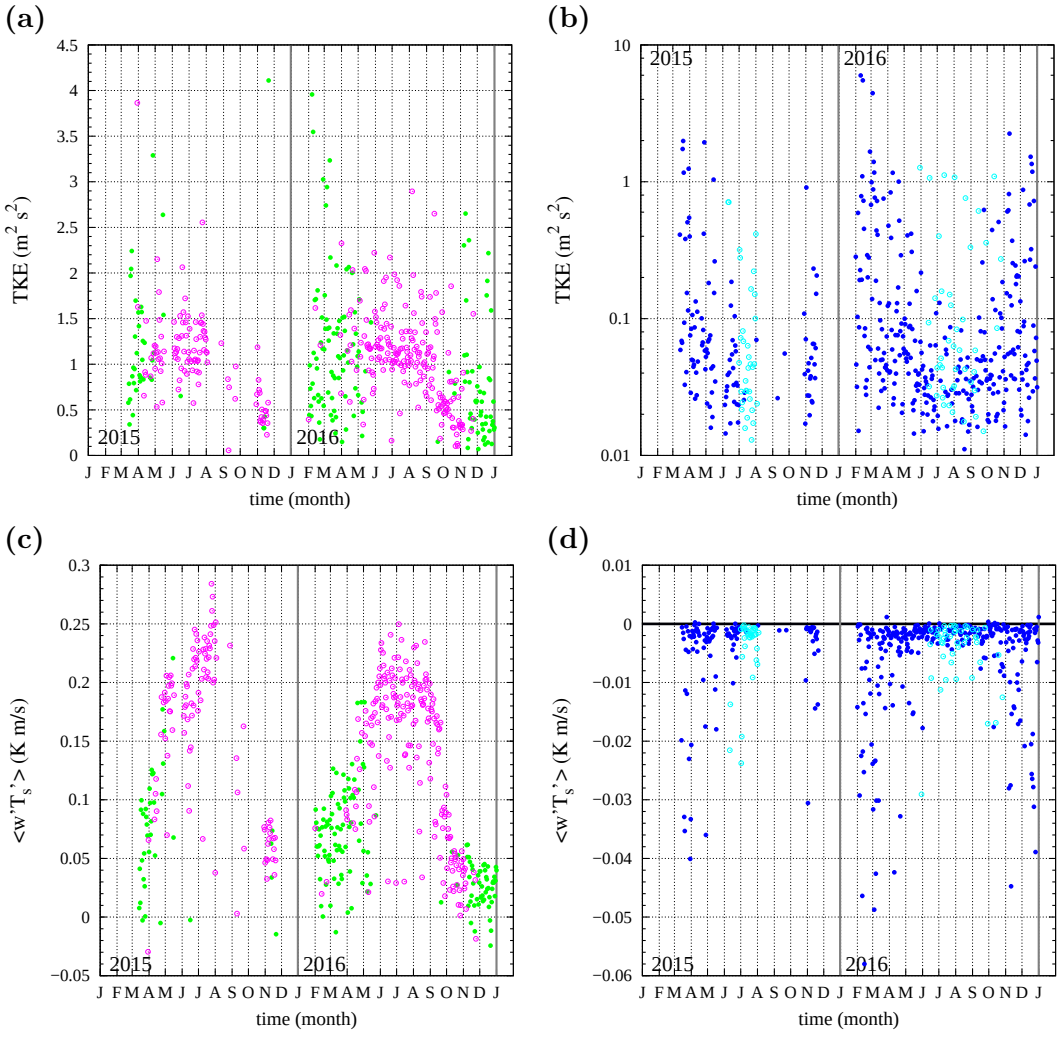

FIGURE A.4: Same than Figure A.1, but for **(a)** and **(b)** TKE, **(c)** and **(d)** <w'T_s'>.

Appendix B

Difference between cloudy and cloudless nights during the T2-LST study pointed in Chapter 4

In this Appendix the cloudy nights have been differentiated from the cloudless ones from the study of Chapter 4. The cloudy data were obtained from the METAR of the airport of Mallorca, Son Sant Joan, located 10 kilometers from the meteorological research station of the Campus of the University of the Balearic Islands (ECUIB) where the data have been measured.

Considering as cloudy nights those with a cloudiness greater than 6/8 and cloudless nights those with a cloudiness lower than 3/8.

Figure B.1 shows the nocturnal mean values (0000-0300 UTC) of temperature difference (T2-LST) during the two years of study. The relations of this temperature difference and other magnitudes are also included (LST, soil temperature, volumetric water content, relative humidity, wind speed, net radiation and ground flux).

Results from Figure B.1 show that there is no significant differences between the days with clouds or clear-skies and no separation is considered in the analysis of Chapter 4.

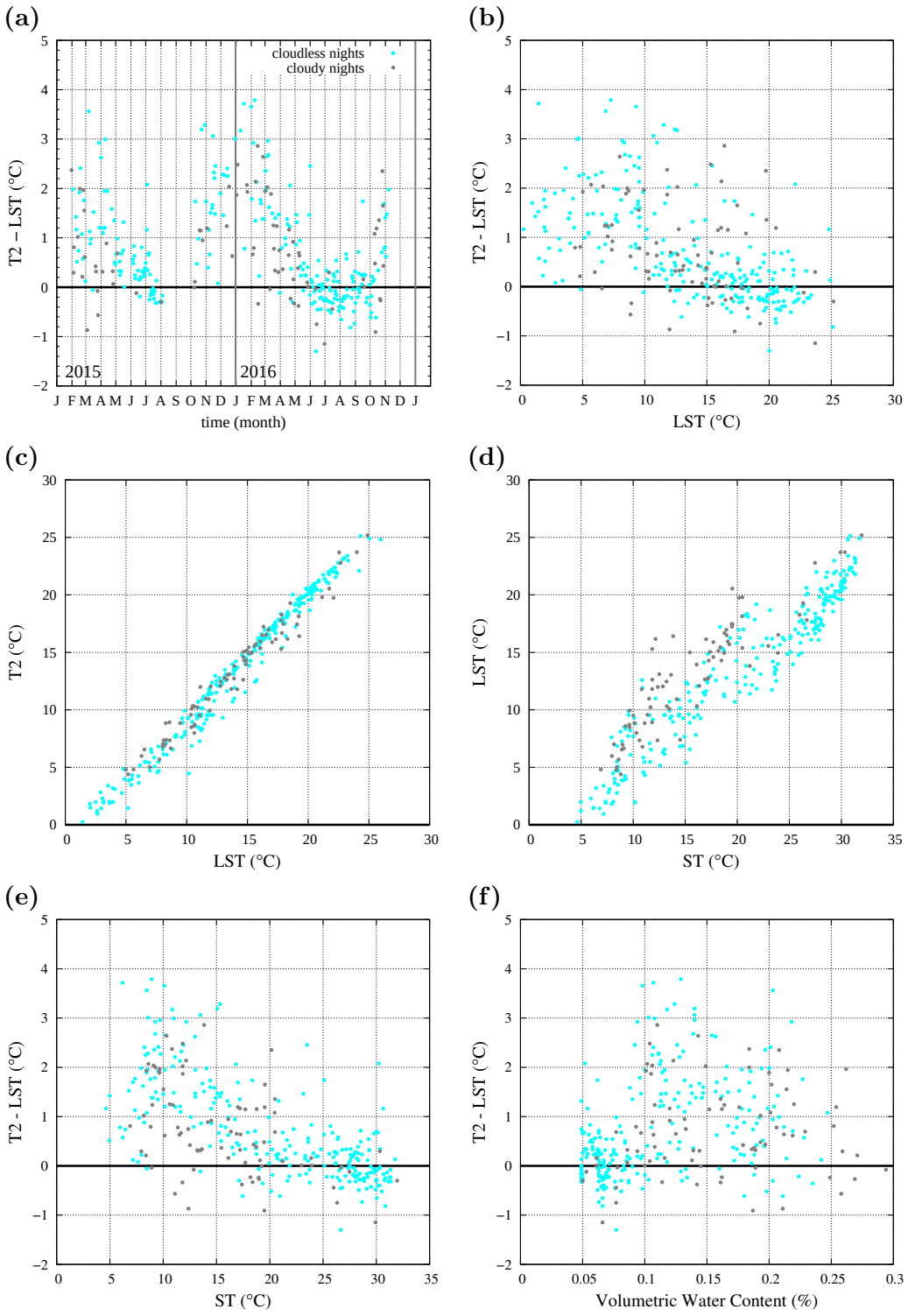
(a)
cloudless nights
cloudy nights
T2 – LST (°C)
2015
2016
J F M A M J J A S O N D J F M A M J J A S O N D J
time (month)
(b)
T2 - LST (°C)
LST (°C)
(c)
T2 (°C)
LST (°C)
(d)
LST (°C)
ST (°C)
(e)
T2 - LST (°C)
ST (°C)
(f)
T2 - LST (°C)
Volumetric Water Content (%)

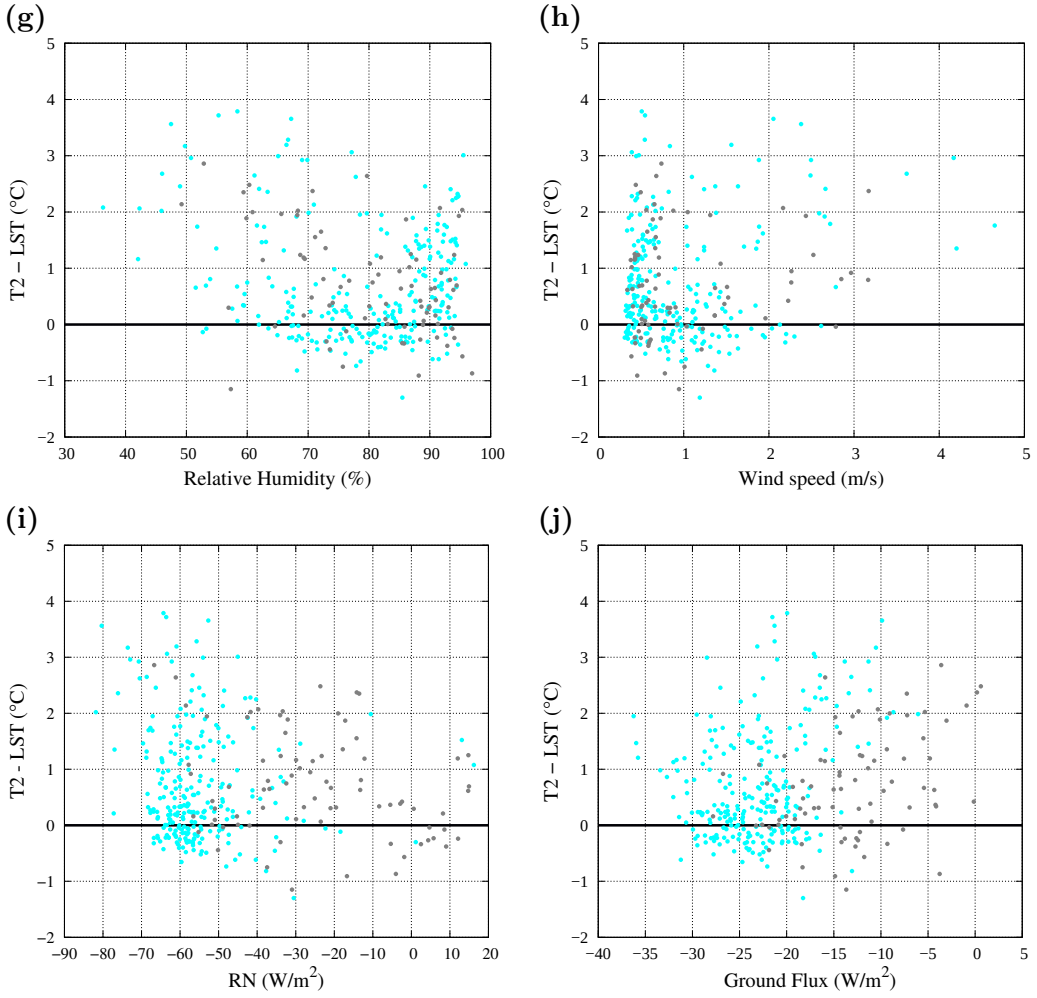

FIGURE B.1: Cloudy and cloudless nights during the T2-LST study (Chapter 4). **(a)** Daily mean values of temperature difference during the two years of study. These averages are made between 0000 and 0300 UTC. Relations of the temperature difference between T2 and LST respect **(b)** LST, **(e)** soil temperature (ST), **(f)** volumetric water content (VWC), **(g)** Relative Humidity, **(h)** wind speed, **(i)** Net radiation (RN) and **(j)** Ground Flux. In pannel **(c)** and **(d)** it is shown the relation between daily averages of T2 and LST, and LST and ST respectively.

Appendix C

Correlations between T2 and LST with the variables described in Chapter 4

In this Appendix are shown the correlations between T2 and LST with the variables described in Table 4.1 in Chapter 4. The coefficient of correlations is written in Table 4.3.

In Figure C.1 it can be seen the relation of the diurnal (1000 – 1300 UTC) and Figure C.2 for the nocturnal (0000 – 0300 UTC) temperature difference between T2 and LST respect to T2, LST, wind speed at 2 m height, net radiation (R_n), ground flux (G) and friction velocity.

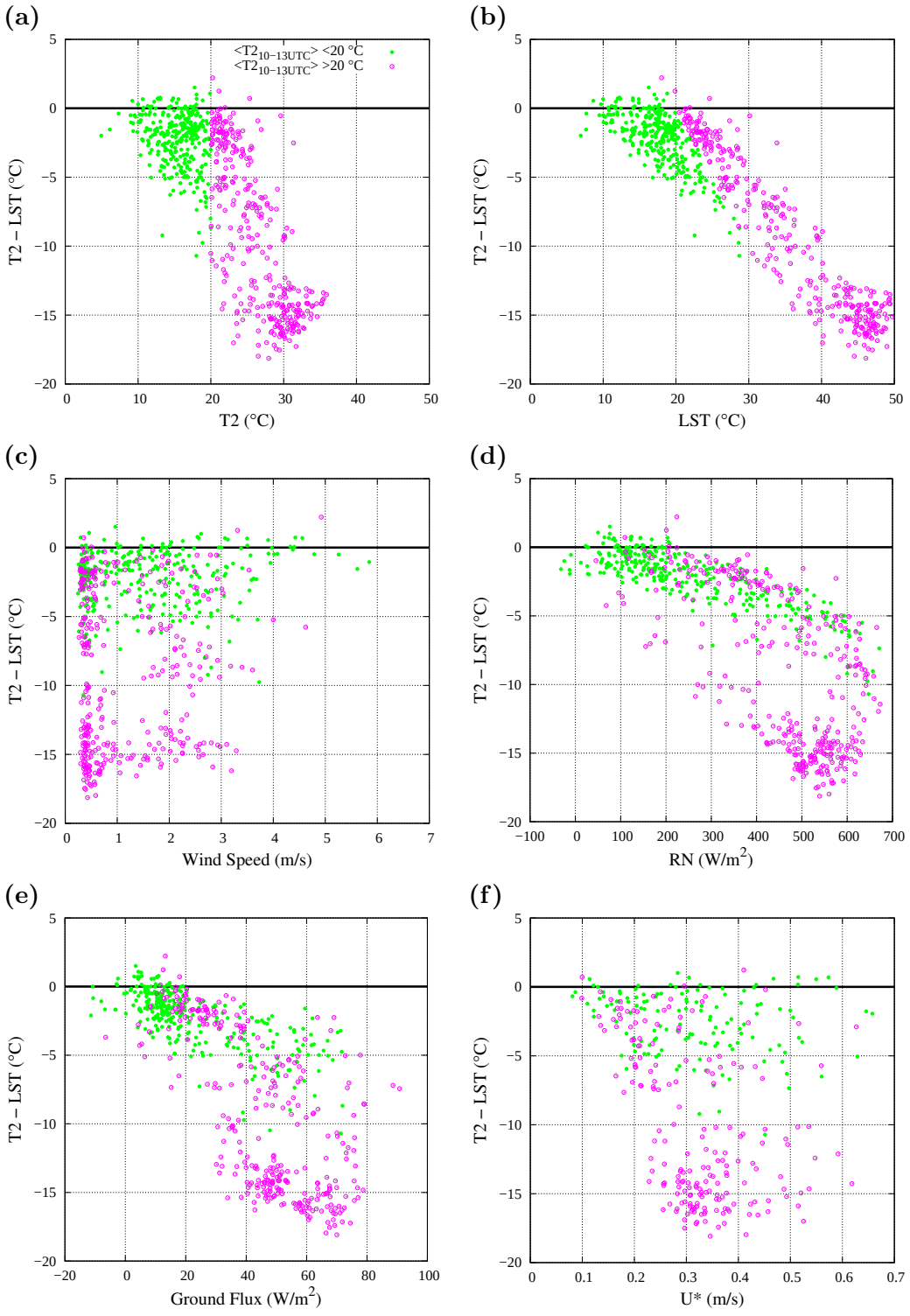

FIGURE C.1: Relation of the diurnal (1000 – 1300 UTC) temperature difference between surface (LST) and air at 2 m height ($T2$) respect to the **(a)** $T2$, **(b)** LST, **(c)** wind speed at 2 m height, **(d)** net radiation (RN), **(e)** ground flux and **(f)** friction velocity ($u*$).

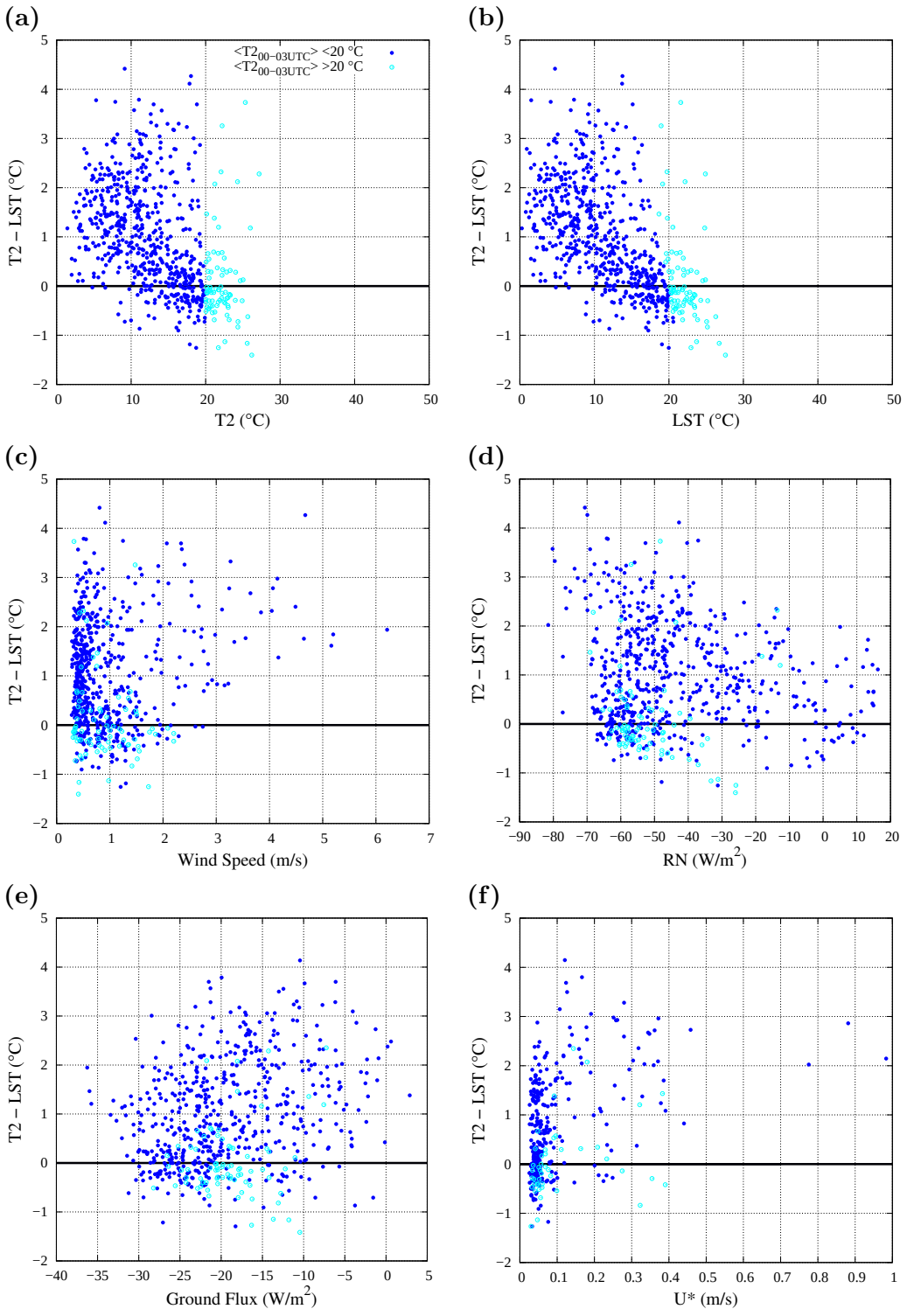

FIGURE C.2: The same as in Figure C.1 but for nocturnal values (0000 – 0300 UTC).

Appendix D

Time series of the diurnal and nocturnal daily averages of the temperature gradients discussed in Chapter 5

In Chapter 5, the vertical variability between 2 and 0.2 meters has been explored, but here the analysis is given for the vertical variability between 1 and 0.2 meters (Figure D.1) and between 2 and 1 meters (Figure D.2).

The following figures show that this temperature difference strongly depends on the levels where it is computed for all the Poles. This is due to the fact that during day/night there is a strong gradient in the surface layer (unstable/stable respectively). We have taken the level of 2 m as a level of reference (T from AWS are at this height).

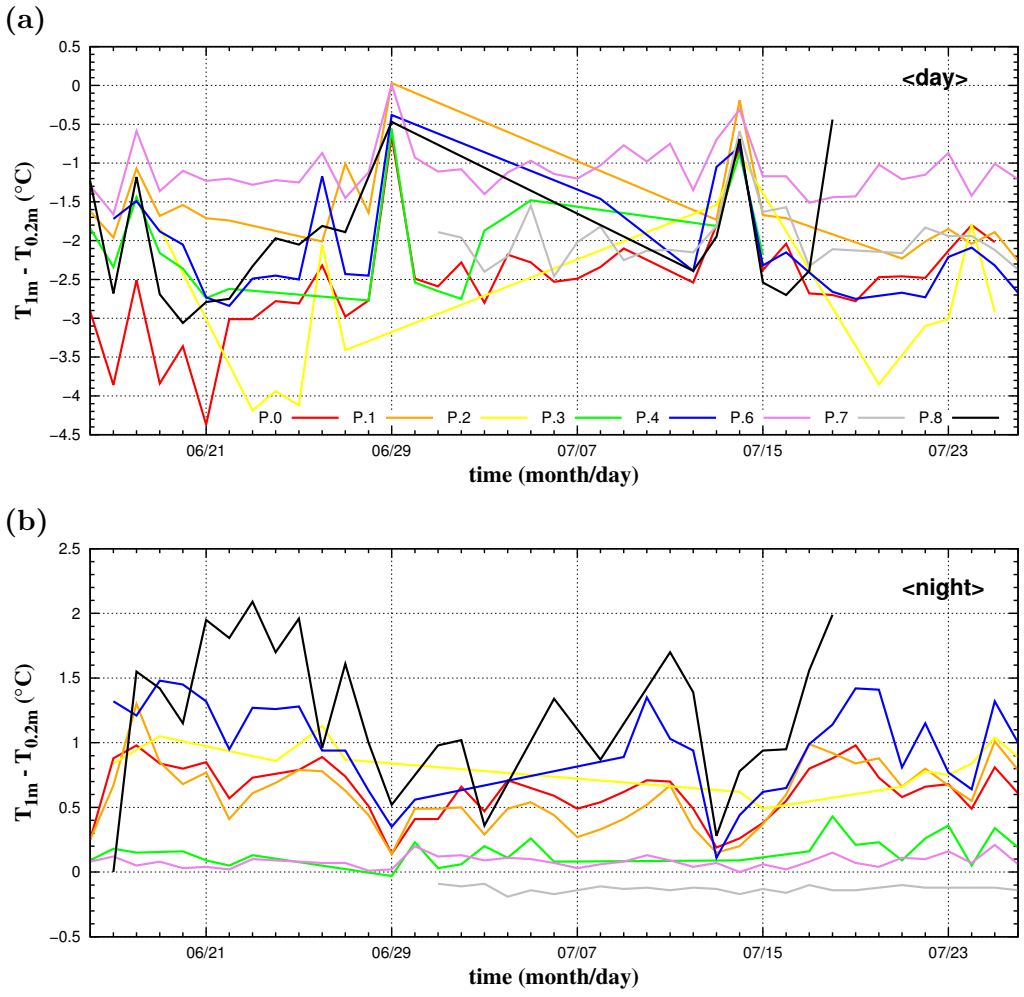

FIGURE D.1: Time serie of the vertical variability of temperature between 1 and 0.2 m for the averages of: **(a)** daytime (1000 – 1300 UTC) and **(b)** night-time.

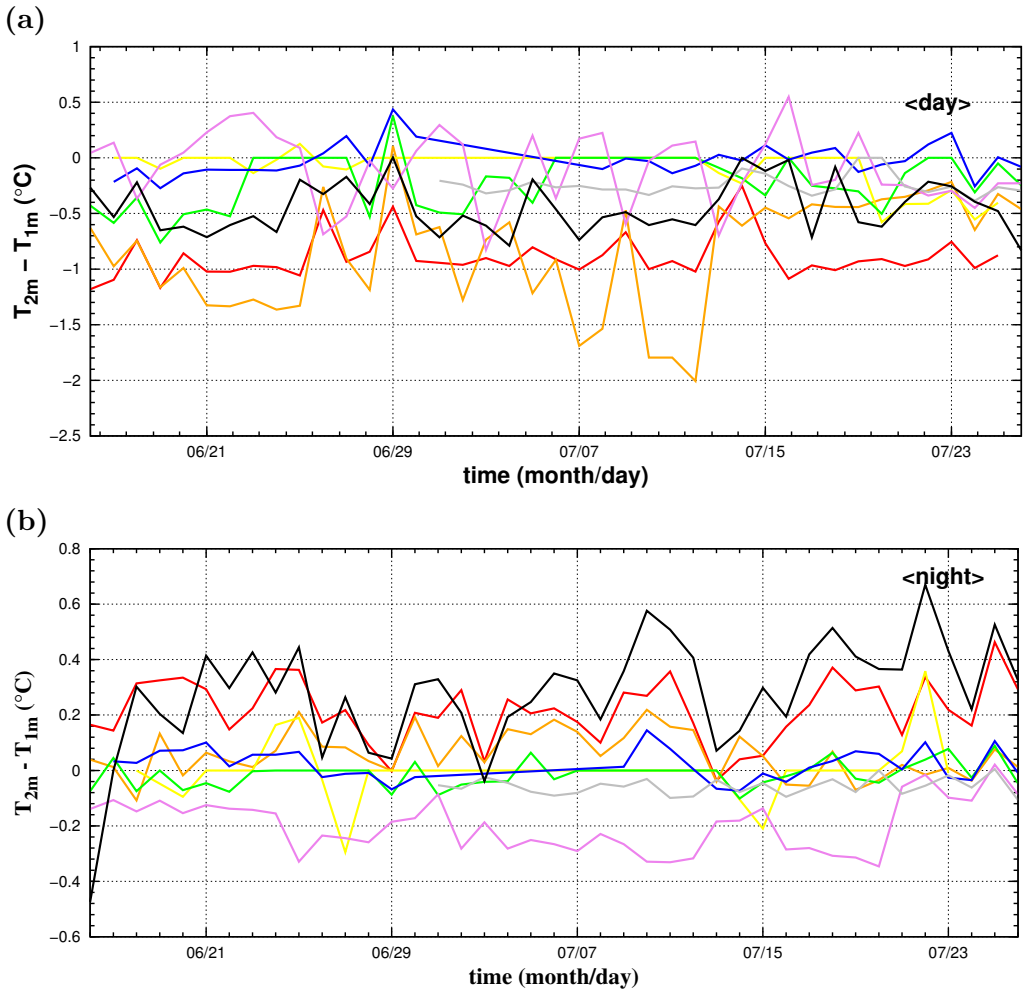

FIGURE D.2: Time serie of the vertical variability of temperature between 2 and 1 m for the averages of: **(a)** daytime (1000 – 1300 UTC) and **(b)** night-time.

Appendix E

Correlations between T2 and T0.2 with other variables explored in Chapter 5

In Chapter 4, the difference between the air temperature at 2 meters (T2) and land surface temperature (LST) has been explored. In this Appendix something similar has been done with the data of Chapter 5, in this case, since LST was not available in all the Poles, it has been done with differences of T2 and T0.2.

Results show that this difference (T2-T0.2) is well correlated with the wind speed and soil temperature during daytime. However, at night the correlations among the different magnitudes are not clear.

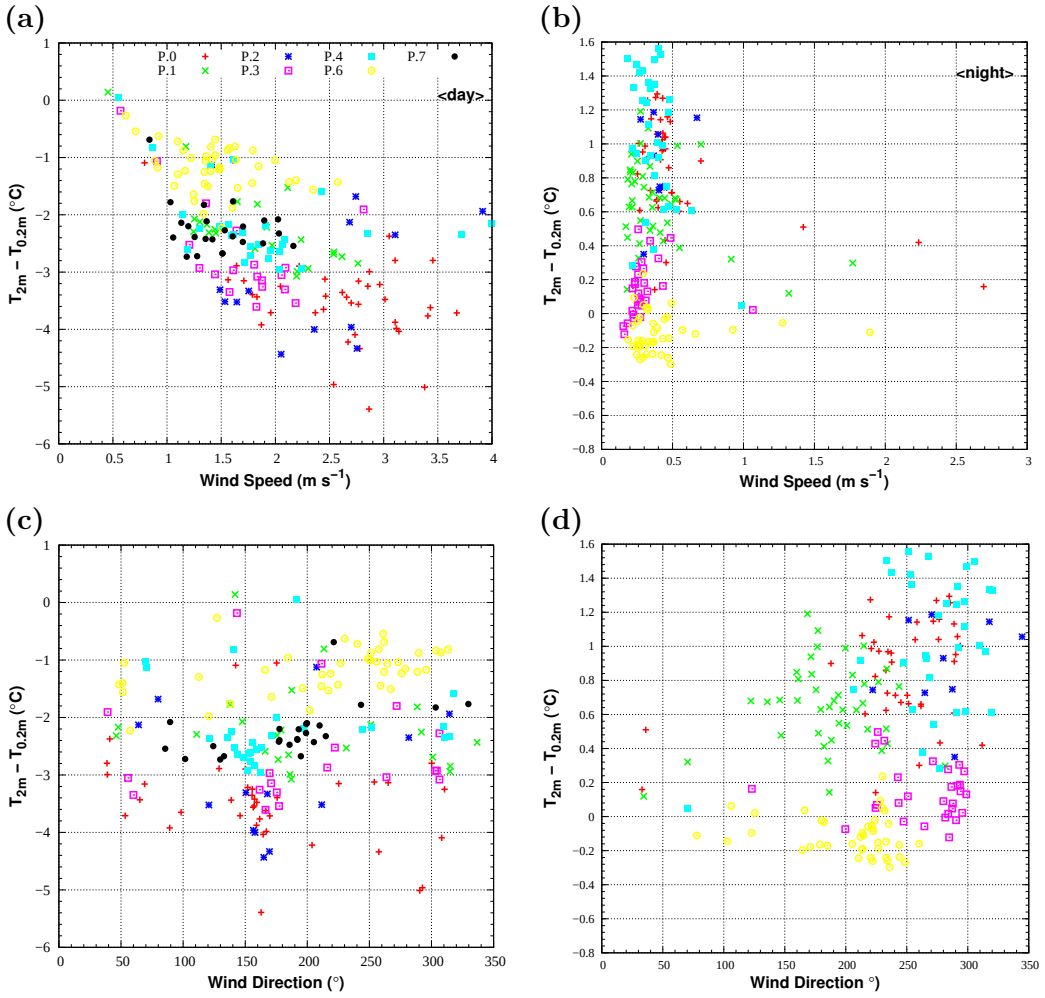

FIGURE E.1: Difference between air temperature at 2 meters and air temperature at 0.2 m with another variables for day averages (left) and night averages (right): **(a)** and **(b)** wind speed, **(c)** and **(d)** wind direction

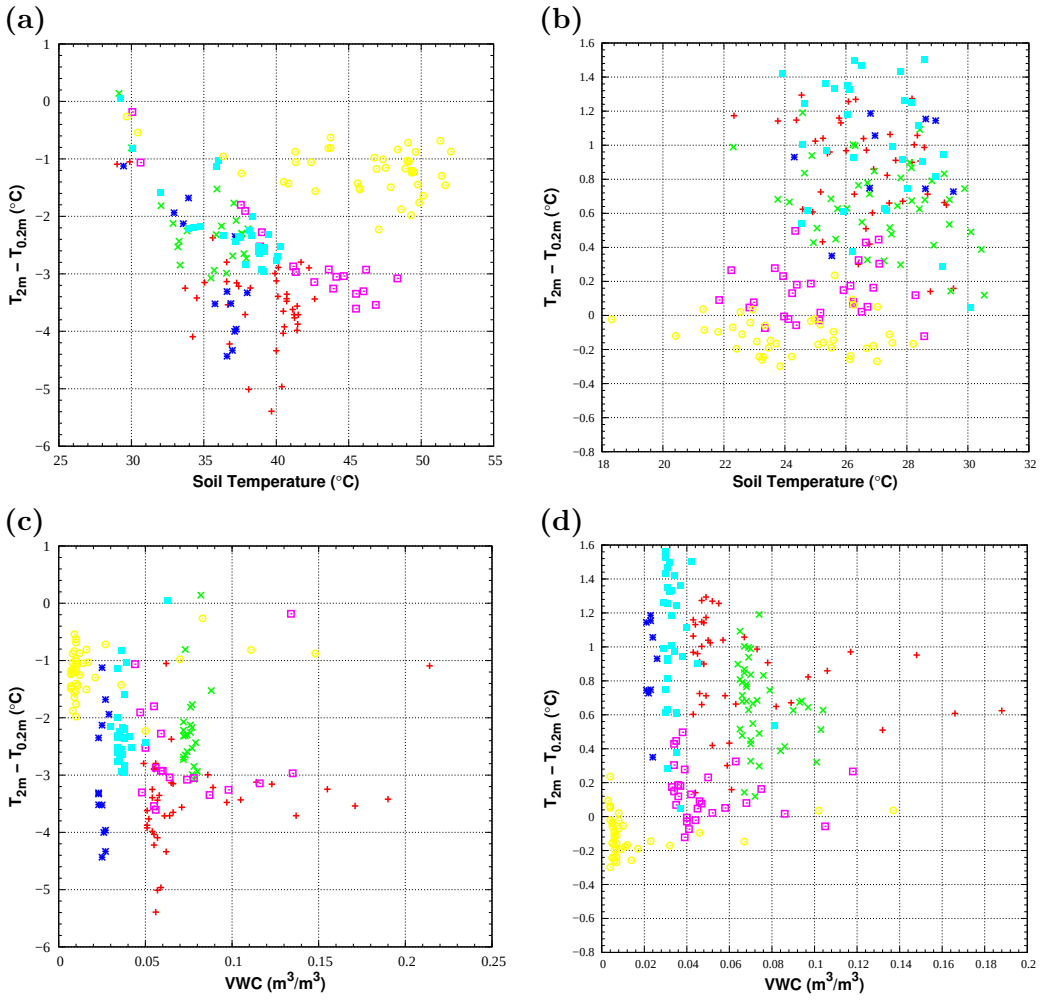

FIGURE E.2: Same than Figure E.1 but for **(a)** and **(b)** soil temperature, **(c)** and **(d)** volumetric water content.

Bibliography

Landsat 7 science data users handbook, http://landsathandbook.gsfc.nasa.gov. Technical report, U.S. Geological Survey, 1998. URL `http://landsathandbook.gsfc.nasa.gov/pdfs/Landsat7_Handbook.pdf`.

O. C. Acevedo and D. Fitzjarrald. The early evening surface-layer transition: Temporal and spatial variability. *Journal of the Atmospheric Sciences*, 58(17):2650–2667, 2001.

O. C. Acevedo and D. R. Fitzjarrald. In the core of the night-effects of intermittent mixing on a horizontally heterogeneous surface. *Boundary-Layer Meteorology*, 106(1): 1–33, 2003.

J. O. Adegoke and Andrew M. Pielke, R. C. Observational and modeling studies of the impacts of agriculture-related land use change on planetary boundary layer processes in the central US. *Agricultural and Forest Meteorology*, 142(2):203–215, 2007.

R. G. Allen, L. S. Pereira, D. Raes, and M. Smith. Crop evapotranspiration-guidelines for computing crop water requirements-fao irrigation and drainage paper 56. *FAO, Rome*, 300(9):D05109, 1998.

M. C. Anderson, R. G. Allen, A. Morse, and W. P. Kustas. Use of landsat thermal imagery in monitoring evapotranspiration and managing water resources. *Remote Sensing of Environment*, 122:50–65, 2012.

W. M. Angevine, H. K. Baltink, and F. C. Bosveld. Observations of the morning transition of the convective boundary layer. *Boundary-Layer Meteorology*, 101:209–227, 2001.

N. T. Atkins and R. M. Wakimoto. Influence of the synoptic-scale flow on sea breezes observed during cape. *Monthly Weather Review*, 125(9):2112–2130, 1997.

B. W. Atkinson. *Meso - scale Atmospheric Circulations*. Academic Press, 1981.

A. Aubinet, T. Vesala, and D. Papale, editors. *Eddy Covariance: A Practical Guide to Measurement and Data Analysis*. Springer Atmospheric Sciences. Springer Verlag, 2012.

V. Azeñas, J. Cuxart, R. Picos, H. Medrano, G. Simó, A. López-Grifol, and J. Gulías. Thermal regulation capacity of a green roof system in the mediterranean region: The effects of vegetation and irrigation level. *Energy and Buildings*, 2018.

C. Azorin-Molina and D. Chen. A climatological study of the influence of synoptic-scale flows on sea breeze evolution in the Bay of Alicante (Spain). *Theoretical and Applied Climatology*, 96:249–260, 2009.

C. Azorin-Molina, D. Chen, S. Tijm, and M. Baldi. A multi-year study of sea breezes in a Mediterranean coastal site: Alicante (Spain). *Int. J. Climatol.*, 31:468–486, 2011.

C. Azorin-Molina, S. Tijm, E. E. Ebert, S. M. Vicente-Serrano, and M. J. Estrela. Sea breeze thunderstorms in the eastern iberian peninsula. neighborhood verification of HIRLAM and HARMONIE precipitation forecasts. *Atmospheric Research*, 139:101–115, 2014.

D. Baldocchi, E. Falge, L. Gu, R. Olson, D. Hollinger, S. Running, P. Anthoni, C. Bernhofer, K. Davis, R. Evans, et al. Fluxnet: A new tool to study the temporal and spatial variability of ecosystem–scale carbon dioxide, water vapor, and energy flux densities. *Bulletin of the American Meteorological Society*, 82(11):2415–2434, 2001.

B. B. Balsley. The cires tethered lifting system: a survey of the system, past results and future capabilities. *Acta Geophysica*, 56(1):21–57, 2008.

J. G. Barr, J. D. Fuentes, M. S. DeLonge, T. L. O'Halloran, D. Barr, and J. C. Zieman. Influences of tidal energy advection on the surface energy balance in a mangrove forest. *Biogeosciences Discussions*, 9(8), 2012.

J. A. Barsi, J. R. Schott, F. D. Palluconi, and S. J. Hook. Validation of a web-based atmospheric correction tool for single thermal band instruments. In *Optics & Photonics 2005*, pages 58820E–58820E. International Society for Optics and Photonics, 2005.

W. Bastiaanssen, M. Menenti, R. A. Feddes, and A. Holtslag. A remote sensing surface energy balance algorithm for land (sebal). 1. formulation. *Journal of Hydrology*, 212: 198–212, 1998.

R. J. Beare, M. K. Macvean, A. Holtslag, J. Cuxart, I. Esau, J. Golaz, M. A. Jiménez, M. Khairoutdinov, B. Kosovic, D. Lewellen, et al. An intercomparison of large-eddy simulations of the stable boundary layer. *Boundary-Layer Meteorology*, 118(2):247–272, 2006.

P. Bechtold, J.-P. Pinty, and P. Mascart. A numerical investigation of the influence of large-scale winds on sea-breeze- and inland-breeze-type circulations. *Journal of Applied Meteorology*, 30:1268–1279, 1991.

A. Benedetti and M. Janisková. Assimilation of modis cloud optical depths in the ecmwf model. *Monthly Weather Review*, 136(5):1727–1746, 2008.

A. Berk, G. P. Anderson, P. K. Acharya, L. S. Bernstein, L. Muratov, J. Lee, M. Fox, S. M. Adler-Golden, J. H. ChetwyndJr, M. L. Hoke, R. B. Lockwood, J. A. Gardner, T. W. Cooley, C. C. Borel, P. E. Lewis, and E. P. Shettle. MODTRAN5: 2006 update. In *Defense and Security Symposium*, pages 62331F–62331F. International Society for Optics and Photonics, 2006.

A. K. Betts, J. H. Ball, A. C. M. Beljaars, M. J. Miller, and P. A. Viterbo. The land surface-atmosphere interaction: A review based on observational and global modeling perspectives. *Journal of Geophysical Research: Atmospheres*, 101(D3):7209–7225, 1996.

F. Beyrich and V. Kotroni. Estimation of surface stress over a forest from sodar measurements and its use to parameterize the stable boundary-layer height. *Boundary-Layer Meteorology*, 66(1-2):93–103, 1993.

F. Beyrich and H.T. Mengelkamp. Evaporation over a heterogeneous land surface: Eva_grips and the litfass-2003 experimentan overview. *Boundary-layer meteorology*, 121(1):5–32, 2006.

J. M. Blonquist, B. D. Tanner, and B. Bugbee. Evaluation of measurement accuracy and comparison of two new and three traditional net radiometers. *Agricultural and Forest Meteorology*, 149(10):1709–1721, 2009.

W. Blumen, R. Banta, S. P. Burns, D. C. Fritts, R. Newsom, G. S. Poulos, and J. Sun. Turbulence statistics of a kelvin–helmholtz billow event observed in the night-time boundary layer during the cooperative atmosphere–surface exchange study field program. *Dynamics of Atmospheres and Oceans*, 34(2-4):189–204, 2001.

H. J. Bolle, J. C. Andre, J. L. Arrue, H. K. Barth, P. Bessemoulin, A. Brasa, H. De Bruin, J. Cruces, G. Dugdale, E. T. Engman, et al. *EFEDA: European field experiment in a desertification-threatened area*, volume 11. Copernicus, 1993.

I. Braud, J. Noilhan, P. Bessemoulin, P. Mascart, R. Haverkamp, and M. Vauclin. Bare-ground surface heat and water exchanges under dry conditions: Observations and parameterization. *Boundary-Layer Meteorology*, 66(1):173–200, 1993.

M. Bravo, T. Mira, M. R. Soler, and J. Cuxart. Intercomparison and evaluation of MM5 and Meso-NH mesoscale models in the stable boundary layer. *Boundary-Layer Meteorology*, 128:77–101, 2008.

W. Brutsaert. On a derivable formula for long-wave radiation from clear skies. *Water Resources Research*, 11(5):742–744, 1975.

D. Cava, G. G. Katul, A. Molini, and C. Elefante. The role of surface characteristics on intermittency and zero-crossing properties of atmospheric turbulence. *Journal of Geophysical Research: Atmospheres*, 117(D1), 2012.

E. Chen, L. H. Allen, J. F. Bartholic, and J. F. Gerber. Comparison of winter-nocturnal geostationary satellite infrared-surface temperature with shelterheight temperature in Florida. *Remote sensing of environment*, 13(4):313–327, 1983.

J. Cheng, S. Liang, Y. Yao, and X. Zhang. Estimating the optimal broadband emissivity spectral range for calculating surface longwave net radiation. *IEEE Geoscience and Remote Sensing Letters*, 10(2):401–405, 2013.

A. A. Chernyshov, K. V. Karelsky, and A. S. Petrosyan. Validation of Large Eddy Simulation method for study of flatness and skewness of decaying compressible magnetohydrodynamic turbulence. *Theoretical and Computational Fluid Dynamics*, 23 (6):451, 2009.

R. H. Clarke. Sea-breezes and waves: the kalgoorlie sea-breeze and the goondiwindi breeze. *Aust. Met. Mag*, 37:99–107, 1989.

R. H. Clarke, A. J. Dyer, R. R. Brook, D. G. Reid, and A. J. Troup. Wangara experiment: boundary layer data. 1971.

C. Coll, V. Caselles, J. M. Galve, E. Valor, R. Niclós, J. M. Sánchez, and R. Rivas. Ground measurements for the validation of land surface temperatures derived from AATSR and MODIS data. *Remote Sensing of Environment*, 97(3):288–300, 2005.

C. Coll, V. Caselles, E. Valor, R. Niclòs, J. M. Sánchez, J. M. Galve, and M. Mira. Temperature and emissivity separation from aster data for low spectral contrast surfaces. *Remote sensing of environment*, 110(2):162–175, 2007.

C. Coll, Z. Wan, and Galve J. M. Temperature-based and radiance-based validations of the V5 MODIS land surface temperature product. *Journal of Geophysical Research*, 114(D20102):1–15, 2009.

C. Coll, J. M. Galve, J. M. Sánchez, and V. Caselles. Validation of Landsat-7/ETM+ thermal-band calibration and atmospheric correction with ground-based measurements. *Geoscience and Remote Sensing, IEEE Transactions on*, 48(1):547–555, 2010.

C. Coll, V. García-Santos, R. Niclòs, and V. Caselles. Test of the MODIS Land Surface Temperature and Emissivity Separation algorithm with ground measurements over

a rice paddy. *IEEE Transactions on Geoscience and Remote Sensing*, 54:3061–3069, 2016.

L. Conangla, J. Cuxart, M. A. Jiménez, D. Martínez-Villagrasa, J. R. Miró, D. Tabarelli, and Zardi D. Cold-air pool evolution in a wide pyrenean valley. *International Journal of Climatology*, 2018.

R. L. Coulter, M. S. Pekour, D. R. Cook, G. E. Klazura, T. J. Martin, and J. D. Lucas. Surface energy and carbon dioxide fluxes above different vegetation types within ABLE. *Agricultural and Forest Meteorology*, 136(3):147–158, 2006.

J. Cristóbal, M. Ninyerola, and X. Pons. Modeling air temperature through a combination of remote sensing and GIS data. *Journal of Geophysical Research: Atmospheres*, 113(D13), 2008.

E. T. Crosman and J. D. Horel. Sea and lake breezes: a review of numerical studies. *Boundary Layer Meteorology*, 137:1–29, 2010.

A. R. Cummings, A. McKee, K. Kulkarni, and N. Markandey. The rise of UAVs. *Photogrammetric Engineering & Remote Sensing*, 83(4):317–325, 2017.

J. Cuxart and M. A. Jiménez. Mixing processes in a nocturnal low-level jet: An les study. *J. Atmos. Sci.*, 64:1666–1679, 2007.

J. Cuxart and M. A. Jiménez. Deep radiation fog in a wide closed valley: study by numerical modeling and remote sensing. *Pure and Applied Geophysics*, 169:911–926, 2012.

J. Cuxart, P. Bougeault, and J.-L. Redelsperger. A turbulence scheme allowing for mesoscale and Large-Eddy Simulations. *Quarterly Journal of the Royal Meteorological Society*, 126:1–30, 2000.

J. Cuxart, A. A. M. Holtslag, R. J. Beare, E. Bazile, A. Beljaars, A. Cheng, L. Conangla, M. Ek, F. Freedman, R. Hamdi, A. Kerstein, H. Kitagawa, G. Lenderink, D. Lewellen, J. Mailhot, T. Mauritsen, V. Perov, G. Schayes, G.-J. Steeneveld, G. Svensson, P. Taylor, W. Weng, S. Wunsch, and K.-M. Xu. Single-column model intercomparison for a stably stratified atmospheric boundary layer. *Bound.-Layer Meteor.*, 118:273–303, 2006.

J. Cuxart, M. A. Jiménez, and D. Martínez. Nocturnal Meso-Beta basin and katabatic flows on a midlatitude island. *Monthly Weather Review*, 135:918–932, 2007.

J. Cuxart, J. Cunillera, M. A. Jiménez, D. Martínez, F. Molinos, and J. L. Palau. Study of mesobeta basin flows by remote sensing. *Boundary Layer Meteorology*, 143:143–158, 2012.

J. Cuxart, M. A. Jiménez, M. Telisman-Prtenjak, and B. Grisogono. Study of a sea-breeze case through momentum, temperature, and turbulence budgets. *Journal of Applied Meteorology and Climatology*, 53:2589–2609, 2014.

J. Cuxart, L. Conangla, and M. A. Jiménez. Evaluation of the surface energy budget equation with experimental data and the ECMWF model in the Ebro Valley. *Journal of Geophysics Research*, 120:1008–1022, 2016a.

J. Cuxart, B. Wrenger, D. Martínez-Villagrasa, J. Reuder, M. O. Jonassen, M. A. Jiménez, M. Lothon, F. Lohou, O. Hartogensis, J. Dünnermann, L. Conangla, and A. Garai. Estimation of the advection effects induced by surface heterogeneities in the surface energy budget. *Atmospheric Chemistry and Physics*, 16(14):9489, 2016b.

K. P. Czajkowski, S. N. Goward, S. J. Stadler, and A. Walz. Thermal remote sensing of near surface environmental variables: application over the oklahoma mesonet. *The Professional Geographer*, 52(2):345–357, 2000.

L. S. Darby, R. M. Banta, and R. A. Pielke. Comparison between mesoscale model terrain sensitivity studies and doppler lidar measurements of the sea breeze at Monterey Bay. *Monthly Weather Review*, 130:2813–2838, 2002.

C. Data. Guidelines on analysis of extremes in a changing climate in support of informed decisions for adaptation. *World Meteorological Organization*, 2009.

F. A. Davis and J. D. Tarpley. Estimation of shelter temperatures from operational satellite sounder data. *Journal of Climate and Applied Meteorology*, 22(3):369–376, 1983.

J. W. Deardorff. Parameterization of the Planetary Boundary Layer for use in General Circulation Models. *Monthly Weather Review*, 100(2):93–106, 1972.

S. H. Derbyshire. Stable boundary layers: Observations, models and variability. Part I: Modelling and measurements. *Boundary-Layer Meteorology*, 74(1):19–54, 1995a.

S. H. Derbyshire. Stable boundary layers: Observations, models and variability. Part II: data analysis and averaging effects. *Boundary-Layer Meteorology*, 75(1):1–24, 1995b.

F. Eder, A. Serafimovich, and T. Foken. Coherent structures at a forest edge: properties, coupling and impact of secondary circulations. *Boundary-layer meteorology*, 148(2): 285–308, 2013.

J. Ehinger. *Instruments and Observing Methods, Report No. 55, WMO/TD-No. 589 (Siting and exposure of meteorological instruments)*. World Meteorological Organisation, Geneva, 1993.

S. L. Ermida, I. F. Trigo, C. C. DaCamara, F. M. Göttsche, F. S. Olesen, and G. Hulley. Validation of remotely sensed surface temperature over an oak woodland landscape. the problem of viewing and illumination geometries. *Remote Sensing of Environment*, 148:16–27, 2014.

C. Fesquet, P. Drobinski, C. Barthlott, and T. Dubos. Impact of terrain heterogeneity on near-surface turbulence structure. *Atmospheric Research*, 94(2):254–269, 2009.

J. J. Finnigan and S. E. Belcher. Flow over a hill covered with a plant canopy. *Quarterly Journal of the Royal Meteorological Society*, 130(596):1–29, 2004.

M. L. Fischer, M. S. Torn, D. P. Billesbach, G. Doyle, B. Northup, and S. C. Biraud. Carbon, water, and heat flux responses to experimental burning and drought in a tallgrass prairie. *Agricultural and Forest Meteorology*, 166:169–174, 2012.

T. Foken. The energy balance closure problem: an overview. *Ecological Applications*, 18(6):1351–1367, 2008a.

T. Foken. *Micrometeorology, 308 pp.* Springer, Heidelberg, 2008b.

T. Foken, M. Mauder, C. Liebethal, F. Wimmer, F. Beyrich, J. P. Leps, S. Raasch, H. A. DeBruin, W. M. Meijninger, and J. Bange. Energy balance closure for the LITFASS-2003 experiment. *Theoretical and Applied Climatology*, 101(1-2):149–160, 2010.

T. Foken, R. Leuning, S. R. Oncley, M. Mauder, and M. Aubinet. *Corrections and data quality control*. Springer, 2012.

H. Fréville, E. Brun, G. Picard, N. Tatarinova, L. Arnaud, C. Lanconelli, C. Reijmer, and M. Van den Broeke. Using MODIS Land Surface Temperatures and the Crocus snow model to understand the warm bias of ERA-Interim reanalyses at the surface in Antarctica. *The Cryosphere*, 8(4):1361–1373, 2014.

D. C. Fritts, C. Nappo, D. M. Riggin, B. B. Balsley, W. E. Eichinger, and R. K. Newsom. Analysis of ducted motions in the stable nocturnal boundary layer during CASES-99. *Journal of the Atmospheric Sciences*, 60(20):2450–2472, 2003.

M. Furberg, D. G. Steyn, and M. Baldi. The climatology of sea breezes on Sardinia. *International Journal of Climatology*, 22(8):917–932, 2002.

V. García-Santos, J. Cuxart, M. A. Jiménez, D. Martínez-Villagrasa, G. Simó, R. Picos, and V. Caselles. Study of temperature heterogeneities at subkilometric scales and impact on surface atmosphere energy interacions. *Transactions on Geoscience and Remote Sensing*, Under Review, 2018.

J. R. Garratt. The inland boundary layer at low latitudes. *Boundary-Layer Meteorology*, 32(4):307–327, 1985.

J. R. Garratt. *The Atmospheric Boundary Layer*. Cambridge University Press, 1992.

R. Geiger, R. H. Aron, and P. Todhunter. *The climate near the ground*. Rowman & Littlefield, 2009.

T. W. Giambelluca, R. E. Martin, G. P. Asner, M. Huang, R. G. Mudd, M. A. Nullet, J. K. DeLay, and D. Foote. Evapotranspiration and energy balance of native wet montane cloud forest in Hawaii. *Agricultural and Forest Meteorology*, 149(2):230–243, 2009.

M. Gibson and B. Launder. Ground effects on pressure fluctuations in the atmospheric boundary layer. *Journal of Fluid Mechanics*, 86(3):491–511, 1978.

A. Gillespie, S. Rokugawa, T. Matsunaga, C. J. Cothern, S. Hook, and A. B. Kahle. A temperature and emissivity separation algorithm for Advanced Spaceborne Thermal Emission and Reflection Radiometer (ASTER) images. *IEEE Transactions on Geoscience and Remote Sensing*, 36(4):1113–1126, 1998.

R. C. Gilliam, S. Raman, and D. S. Niyogi. Observational and numerical study on the influence of large-scale flow direction and coastline shape on sea-breeze evolution. *Boundary-Layer Meteorology*, 111(2):275–300, 2004.

T. S. Glickman. Glossary of Meteorology. American Meteorological Society. *MA, USA*, 2000.

M. P. González-Dugo, X. Chen, A. Andreu, E. Carpintero, P. Gómez-Giráldez, and Z. Su. Evolution of evapotranspiration and water stress of oak savanna vegetation in the Iberian Peninsula (2001-2015). *Revista de Teledetección*, 50:27–36, 2017.

F. M. Göttsche, F. S. Olesen, and A. Bork-Unkelbach. Validation of Land Surface Temperature derived from MSG/SEVIRI with in situ measurements at Gobabeb, Namibia. *International Lournal of Remote Sensing*, 34(9-10):3069–3083, 2013.

R. M. Green and S. I. Hay. The potential of Pathfinder AVHRR data for providing surrogate climatic variables across Africa and Europe for epidemiological applications. *Remote Sensing of Environment*, 79(2):166–175, 2002.

V. Guenard, P. Drobinski, J. L. Caccia, B. Campistron, and B. Bench. An observational study of the mesoscale mistral dynamics. *Boundary Layer Meteorology*, 115(2):263–288, 2005.

W. Gutiérrez, M. García, V. O Magaña, and J. A. Escalante. Diseno y construcción de un globo meteorológico cautivo instrumentado. *Ingeniería y Ciencia*, 3(5), 2007.

J. R. Holton and G. J. Hakim. *An introduction to dynamic meteorology*, volume 88. Academic press, 2012.

S. J. Hook, A. R. Gabell, A. A. Green, and P. S. Kealy. A comparison of techniques for extracting emissivity information from thermal infrared data for geologic studies. *Remote Sensing of Environment*, 42(2):123–135, 1992.

S. J. Hook, R. G. Vaughan, and H. Tonooka. Absolute radiometric in-flight validation of mid infrared and thermal infrared data from ASTER and MODIS on the Terra spacecraft using the Lake Tahoe. CA/NV, USA, automated validation site. *IEEE Transactions on Geoscience and Remote Sensing*, 45:1798–1807, 2007.

G. Hulley, S. Hook, and C. Hughes. MODIS MOD21 Land Surface Temperature and emissivity algorithm theoretical basis document. *Jet Propulsion Lab. publications*, pages 12–17, 2012.

G. C. Hulley and S. J. Hook. Intercomparison of versions 4, 4.1 and 5 of the MODIS land surface temperature and emissivity products and validation with laboratory measurements of sand samples from the Namib Desert, Namibia. *Remote Sensing of Environment*, 113:1313–1318, 2009.

G. C. Hulley, S. J. Hook, E. Abbott, N. Malakar, T. Islam, and M. Abrams. The ASTER Global Emissivity Dataset (ASTER GED): Mapping Earth's emissivity at 100 meter spatial scale. *Geophysical Research Letters*, 42(19):7966–7976, 2015.

Editors IJRS. Unmanned Aerial Vehicles for environmental applications. *International Journal of Remote Sensing*, 38(8-10):2029–2036, 2017.

J. Imberger. The diurnal mixed layer. *Limnology and Oceanography*, 30(4):737–770, 1985.

A. F. Jacobs, B. G. Heusinkveld, and A. A. Holtslag. Seasonal and interannual variability of carbon dioxide and water balances of a grassland. *Climatic Change*, 82(1):163–177, 2007.

J. M. Jansà and E. Jaume. The sea breeze regime in the Mallorca island (in Spanish). *Revista de Geofísica*, 19:304–328, 1946.

M. A. Jiménez and J. Cuxart. Large-eddy simulations of the stable boundary layer using the standard Kolmogorov theory: range of applicability. *Boundary-Layer Meteorology*, 115:241–261, 2005.

M. A. Jiménez and J. Cuxart. Study of the probability density functions from a Large-Eddy Simulation for a stably stratified boundary layer. *Boundary-Layer Meteorology*, 118:401–420, 2006.

M. A. Jiménez and J. Cuxart. A study of the nocturnal flows generated in the north side of the Pyrenees. *Atmospheric Research*, 145–146:244–254, 2014.

M. A. Jiménez, A. Mira, J. Cuxart, A. Luque, S. Alonso, and J. A. Guijarro. Verification of a clear-sky mesoscale simulation using satellite - derived surface temperatures. *Monthly Weather Review*, 136:5148–5161, 2008.

M. A. Jiménez, A. Ruiz, and J. Cuxart. Estimation of cold pool areas and chilling hours through satellite - derived surface temperatures. *Agricultural and Forest Meteorology*, 207:58–68, 2015.

M. A. Jiménez, G. Simó, B. Wrenger, M. Telisman-Prtenjak, J. A. Guijarro, and J. Cuxart. Morning transition case between the land and the sea breeze regimes. *Atmospheric Research*, 172:95–108, 2016.

M. Jin and R. E. Dickinson. Land surface skin temperature climatology: benefitting from the strengths of satellite observations. *Environmental Research Letters*, 5:044004, 2010.

M. Jin, R. E. Dickinson, and A. M. Vogelmann. A comparison of CCM2-BATS Skin Temperature and Surface-Air Temperature with satellite and surface observations. *Journal of Climate*, 10(7):1505–1524, 1997.

A. Johnson and J. J. O'Brien. A study of an Oregon sea breeze event. *Journal of Applied Meteorology*, 12:1267–1283, 1973.

J. C. Kaimal and J. J. Finnigan. *Atmospheric boundary layer flows: their structure and measurement*. Oxford university press, 1994.

J. C. Kaimal, J. C. Wyngaard, D. A. Haugen, O. R. Coté, Y. Izumi, S. J. Caughey, and C. J. Readings. Turbulence structure in the convective boundary layer. *Journal of the Atmospheric Sciences*, 33(11):2152–2169, 1976.

J. Kala, T. J. Lyons, D. J. Abbs, and U. S. Nair. Numerical simulations of the impacts of land-cover change on a southern sea breeze in south-west western Australia. *Boundary-Layer Meteorology*, 135:485–503, 2010.

J. D. Kalma, T. R. McVicar, and M. F. McCabe. Estimating land surface evaporation: A review of methods using remotely sensed surface temperature data. *Surveys in Geophysics*, 29(4-5):421–469, 2008.

S. Kang, D. Lenschow, and P. Sullivan. Effects of mesoscale surface thermal heterogeneity on low-level horizontal wind speeds. *Boundary-Layer Meteorology*, 143(3):409–432, 2012.

S. L. Kang, K. J. Davis, and M. LeMone. Observations of the abl structures over a heterogeneous land surface during ihop_2002. *Journal of Hydrometeorology*, 8(2): 221–244, 2007.

L. H. Kantha and C. A. Clayson. *Small scale processes in geophysical fluid flows*, volume 67. Elsevier, 2000.

M. Kilinc, J. Beringer, L. B. Hutley, V. Haverd, and N. Tapper. An analysis of the surface energy budget above the world's tallest angiosperm forest. *Agricultural and Forest Meteorology*, 166:23–31, 2012.

J. Kondo, T. Kuwagata, and S. Haginoya. Heat budget analysis of nocturnal cooling and daytime heating in a basin. *Journal of the Atmospheric Sciences*, 46(19):2917–2933, 1989.

K. Y. Kondratyev. Radiation in the Atmosphere Academic. *New York*, page 915, 1969.

P. Krishnan, J. Kochendorfer, E. J. Dumas, P. C. Guillevic, C. B. Baker, T. P. Meyers, and B. Martos. Comparison of in-situ, aircraft, and satellite land surface temperature measurements over a NOAA Climate Reference Network site. *Remote Sensing of Environment*, 165:249–264, 2015.

L. Kroon and H. De Bruin. The Crau field experiment: turbulent exchange in the surface layer under conditions of strong local advection. *Journal of Hydrology*, 166 (3-4):327–351, 1995.

W. P. Kustas and J. M. Norman. Use of remote sensing for evapotranspiration monitoring over land surfaces. *Hydrological Sciences Journal*, 41(4):495–516, 1996.

W. P. Kustas, J. M. Norman, C. R. Hain, J. R. Mecikalski, L. Schultz, M. P. González-Dugo, C. Cammalleri, G. d'Urso, A. Pimstein, F. Gao, et al. Mapping daily evapotranspiration at field to continental scales using geostationary and polar orbiting satellite imagery. *Hydrology and Earth System Sciences*, 15(1):223, 2011.

J. P. Lafore, J. Stein, N. Asencio, P. Bougeault, V. Ducrocq, J. Duron, C. Fisher, P. Héreil, P. Mascart, J.-P. Pinty, J.-L. Redelsperger, E. Richard, and J. Vilà-Guerau de Arellano. The Meso-NH atmospheric simulation system. Part I: Adiabatic formulation and control simulation. *Annales Geophysicae*, 16:90–109, 1998.

A. Lapworth. Factors determining the decrease in surface wind speed following the evening transition. *Quarterly Journal of the Royal Meteorological Society*, 129:1945–1968, 2003.

A. Lapworth. The morning transition of the nocturnal boundary layer. *Boundary-Layer Meteorology*, 119:501–526, 2006.

M. A. LeMone, R. L. Grossman, F. Chen, K. Ikeda, and D. Yates. Choosing the averaging interval for comparison of observed and modeled fluxes along aircraft transects over a heterogeneous surface. *Journal of Hydrometeorology*, 4(2):179–195, 2003a.

M. A. LeMone, K. Ikeda, R. L. Grossman, and M. W. Rotach. Horizontal variability of 2-m temperature at night during CASES-97. *Journal of the atmospheric sciences*, 60 (20):2431–2449, 2003b.

M. A. LeMone, F. Chen, J. G. Alfieri, R. H. Cuenca, Y. Hagimoto, P. Blanken, D. Niyogi, S. Kang, K. Davis, and R. L. Grossman. NCAR/CU surface, soil, and vegetation observations during the international H2O project 2002 field campaign. *Bulletin of the American Meteorological Society*, 88(1):65–81, 2007a.

M. A. LeMone, F. Chen, J. G. Alfieri, M. Tewari, B. Geerts, Q. Miao, R. L. Grossman, and R. L. Coulter. Influence of land cover and soil moisture on the horizontal distribution of sensible and latent heat fluxes in Southeast Kansas during IHOP_2002 and CASES-97. *Journal of Hydrometeorology*, 8(1):68–87, 2007b.

D. H. Lenschow, B. B. Stankov, and L. Mahrt. The rapid morning boundary-layer transition. *Journal of Atmospheric Sciences*, 36:2108–2124, 1979.

R. Leuning, E. Van Gorsel, W. J. Massman, and P. R. Isaac. Reflections on the surface energy imbalance problem. *Agricultural and Forest Meteorology*, 156:65–74, 2012.

F. Li, T. J. Jackson, W. P. Kustas, T. J. Schmugge, A. N. French, M. H. Cosh, and R. Bindlish. Deriving land surface temperature from Landsat 5 and 7 during SMEX02/SMACEX. *Remote sensing of environment*, 92(4):521–534, 2004.

Z. L. Li and F. Becker. Feasibility of land surface temperature and emissivity determination from AVHRR data. *Remote Sensing of Environment*, 43(1):67–85, 1993.

Z.-L. Li, B.-H. Tang, H. Wu, H. Ren, G. Yan, Z. Wan, I. F. Trigo, and J. A. Sobrino. Satellite-derived land surface temperature: Current status and perspectives. *Remote Sensing of Environment*, 131:14–37, 2013.

C. Liebethal, B. Huwe, and T. Foken. Sensitivity analysis for two ground heat flux calculation approaches. *Agricultural and Forest Meteorology*, 132(3-4):253–262, 2005.

T. Lillesand, R. W. Kiefer, and J. Chipman. *Remote sensing and image interpretation*. John Wiley & Sons, 2014.

K. N. Liou. *An introduction to atmospheric radiation*, volume 84. Academic press, 2002.

M. Lothon, F. Lohou, D. Pino, F. Couvreux, E. R. Pardyjak, J. Reuder, J. Vilà-Guerau de Arellano, P. Durand, O. Hartogensis, D. Legain, et al. The BLLAST field experiment: Boundary-Layer Late Afternoon and Sunset Turbulence. *Atmospheric Chemistry and Physics*, 14:10931–10960, 2014.

L. Mahrt. Stratified atmospheric boundary layers. *Boundary-Layer Meteorology*, 90(3): 375–396, 1999.

L. Mahrt. Surface heterogeneity and vertical structure of the boundary layer. *Boundary-Layer Meteorology*, 96(1):33–62, 2000.

L. Mahrt. Computing turbulent fluxes near the surface: Needed improvements. *Agricultural and Forest Meteorology*, 150(4):501–509, 2010.

N. K. Malakar and G. C. Hulley. A water vapor scaling model for improved land surface temperature and emissivity separation of MODIS thermal infrared data. *Remote Sensing of Environment*, 182:252–264, 2016.

E. Malek, T. Davis, R. S. Martin, and P. J. Silva. Meteorological and environmental aspects of one of the worst national air pollution episodes (January, 2004) in Logan, Cache Valley, Utah, USA. *Atmospheric Research*, 79(2):108–122, 2006.

J. Mallick, Y. Kant, and B. D. Bharath. Estimation of land surface temperature over Delhi using Landsat-7 ETM+. *Journal of Indian Geophysical Union*, 12(3):131–140, 2008.

H. Mannstein. *Surface energy budget, surface temperature and thermal inertia*. Springer, 1987.

B. Martí, D. Martínez-Villagrasa, and J. Cuxart. Nocturnal fine structure of the temperature column between 2 and -0.1 m. In *EMS Annual Meeting Abstracts*, volume 13, Trieste, Italy, 12-16 September 2016.

D. Martínez, M. A. Jiménez, J. Cuxart, and L. Mahrt. Heterogeneous nocturnal cooling in a large basin under very stable conditions. *Boundary-Layer Meteorology*, 137:97–113, 2010.

P. M. Mather and M. Koch. *Computer processing of remotely-sensed images: an introduction*. John Wiley & Sons, 2011.

M. Mauder, C. Liebethal, M. Göckede, J. P. Leps, F. Beyrich, and T. Foken. Processing and quality control of flux data during litfass-2003. *Boundary-Layer Meteorology*, 121 (1):67–88, 2006.

M. Mauder, S. P. Oncley, R. Vogt, T. Weidinger, L. Ribeiro, C. Bernhofer, T. Foken, W. Kohsiek, H. A. De Bruin, and H. Liu. The energy balance experiment EBEX-2000. Part II: Intercomparison of eddy-covariance sensors and post-field data processing methods. *Boundary-Layer Meteorology*, 123(1):29–54, 2007.

W. D. McComb. The physics of fluid turbulence. *Chemical Physics*, 1990.

R. D. McPherson. A numerical study of the effect of a coastal irregularity on the sea breeze. *Journal of Applied Meteorology*, 9:767–777, 1970.

W. Meijninger, F. Beyrich, A. Lüdi, W. Kohsiek, and H. Bruin. Scintillometer-based turbulent fluxes of sensible and latent heat over a heterogeneous land surface–a contribution to litfass-2003. *Boundary-layer meteorology*, 121(1):89–110, 2006.

J. F. Miao, L. J. M. Kroon, J. Vilà-Guerau de Arellano, and A. A. M. Holtslag. Impacts of topography and land degradation on the sea breeze over eastern Spain. *Meteorology and Atmospheric Physics*, 84:157–170, 2003.

D. J. Mildrexler, M. Zhao, and S. W. Running. A global comparison between station air temperatures and modis land surface temperatures reveals the cooling role of forests. *Journal of Geophysical Research: Biogeosciences*, 116(G3), 2011.

S. T. K. Miller, B. D. Keim, R. W. Talbot, and H. Mao. Sea breeze: structure, forecasting and impacts. *Reviews of Geophysics*, 41:1011, 2003.

Y. Mintz and G.K. Walker. Global fields of soil moisture and land surface evapotranspiration derived from observed precipitation and surface air temperature. *Journal of Applied Meteorology*, 32(8):1305–1334, 1993.

U. Moderow, M. Aubinet, C. Feigenwinter, O. Kolle, A. Lindroth, M. Mölder, L. Montagnani, C. Rebmann, and C. Bernhofer. Available energy and energy balance closure at four coniferous forest sites across Europe. *Theoretical and Applied Climatology*, 98 (3):397–412, 2009.

U. Moderow, C. Feigenwinter, and C. Bernhofer. Non-turbulent fluxes of carbon dioxide and sensible heat. A comparison of three forested sites. *Agricultural and Forest Meteorology*, 151(6):692–708, 2011.

A. S. Monin and A. Obukhov. Basic laws of turbulent mixing in the surface layer of the atmosphere. *Contributions of the Geophysical Institute of the Slovak Academy of Sciences*, 151(163):e187, 1954.

H. Montenegro, D. Malagón C, and L. Guerrero. Propiedades físicas de los suelos. Technical report, 1990.

S. Mukherjee, P. K. Joshi, and R. D. Garg. Evaluation of LST downscaling algorithms on seasonal thermal data in humid subtropical regions of India. *International Journal of Remote Sensing*, 36(10):2503–2523, 2015.

D. F. Nadeau, E. R. Pardyjak, C. W. Higgins, H. J. S. Fernando, and M. B. Parlange. A simple model for the afternoon and early evening decay of convective turbulence over different land surfaces. *Boundary-Layer Meteorology*, 141:301–324, 2011.

D. F. Nadeau, E. R. Pardyjak, C. W. Higgins, H. Huwald, and M. B. Parlange. Flow during the evening transition over steep alpine slopes. *Quarterly Journal of the Royal Meteorological Society*, 139(672):607–624, 2013.

A. Nelci, M. M. Miglietta, U. Rizza, O. C. Acevedo, and G. A. Degrazia. Investigation of sea-breeze convergence in Salento Peninsula (southeastern Italy). *Atmospheric Research*, 160:68–79, 2015.

R. K. Newsom and R. M. Banta. Shear-flow instability in the stable nocturnal boundary layer as observed by Doppler lidar during CASES-99. *Journal of the Atmospheric Sciences*, 60(1):16–33, 2003.

R. Niclòs, M. J. Estrela, J. A. Valiente, and M. J. Barberà. Análisis de correlaciones entre la temperatura del aire y la temperatura de las superficies vegetadas medida con radiometría térmica (regression analysis between air temperature and vegetated-surface temperature measured by thermal radiometry). *Revista de Teledetección*, 34: 36–43, 2010.

R. Niclos, J. A. Valiente, M. J. Barbera, and V. Caselles. Land surface air temperature retrieval from EOS-MODIS images. *IEEE Geoscience and Remote Sensing Letters*, 11(8):1380–1384, 2014.

R. Niclòs, J. A. Valiente, M. J. Barberà, and C. Coll. An autonomous system to take angular thermal - Infrared measurements for validating satellite products. *Remote Sensing*, 7(11):15269–15294, 2015.

E. Nilsson, M. Lothon, F. Lohou, E. Pardyjak, O. Hartogensis, and C. Darbieu. Turbulence kinetic energy budget during the afternoon transition–Part 2: A simple TKE model. *Atmospheric Chemistry and Physics*, 16(14):8873–8898, 2016.

J. Noilhan and S. Planton. A simple parameterization of land surface processes for meteorological models. *Monthly Weather Review*, 117:536–549, 1989.

T. R. OKE. Boundary layer climates. *London, Methuen and Co., Ltd.; New York, Halsted Press, 1978. 390 p*, 1978.

R. C. Olsen. *Remote sensing from air and space*, volume 229. SPIE Press, 2007.

S. P. Oncley, T. Foken, R. Vogt, W. Kohsiek, H. A. DeBruin, C. Bernhofer, A. Christen, E. van Gorsel, D. Grantz, C. Feigenwinter, et al. The energy balance experiment EBEX-2000. Part I: overview and energy balance. *Boundary-Layer Meteorology*, 123 (1):1–28, 2007.

M. Orlić, B. Penzar, and I. Penzar. Adriatic sea and land breezes: Clockwise versus anticlockwise rotation. *Journal of Applied Meteorology*, 27(5):675–679, 1988.

J. A. Otkin and T. J. Greenwald. Comparison of wrf model-simulated and modis-derived cloud data. *Monthly Weather Review*, 136(6):1957–1970, 2008.

N. S. Panchal. Onset characteristics of land/sea breeze circulation and its effect on meterological parameters at a coastal site. *Atmósfera*, 6:155–162, 1993.

G. N. Panin, G. Tetzlaff, and A. Raabe. Inhomogeneity of the land surface and problems in theparameterization of surface fluxes in natural conditions. *Theoretical and Applied Climatology*, 60(1):163–178, 1998.

D. K. Papanastasiou, D. Melas, and I. Lissaridis. Study of wind field under sea breeze conditions; an application of WRF model. *Atmospheric Research*, 98:102–117, 2010.

R. Pape and J. Löffler. Modelling spatio-temporal near-surface temperature variation in high mountain landscapes. *Ecological Modelling*, 178(3):483–501, 2004.

E. G. Patton, P. P. Sullivan, and C. H. Moeng. The influence of idealized heterogeneity on wet and dry planetary boundary layers coupled to the land surface. *Journal of the Atmospheric Sciences*, 62(7):2078–2097, 2005.

C. A. Paulson. The mathematical representation of wind speed and temperature profiles in the unstable atmospheric surface layer. *Journal of Applied Meteorology*, 9(6):857–861, 1970.

R. P. Pearce. The calculation of a sea-breeze circulation in terms of the differential heating across the coastline. *Quarterly Journal of the Royal Meteorological Society*, 81(349):351–381, 1955.

L. F. Peres and C. C. DaCamara. Land surface temperature and emissivity estimation based on the two-temperature method: Sensitivity analysis using simulated MSG/-SEVIRI data. *Remote Sensing of Environment*, 91(3):377–389, 2004.

Ll. Pérez-Planells, V. García-Santos, and V. Caselles. Comparing different profiles to characterize the atmosphere for three MODIS TIR bands. *Atmospheric Research*, 161-162:108–115, 2015.

W. L. Physick. Numerical experiments on the inland penetration of the sea breeze. *Quarterly Journal of the Royal Meteorological Society*, 106(450):735–746, 1980.

M. Pidwirny. Global heat balance: Introduction to heat fluxes. *Fundamentals of Physical Geography*, pages 1999–2008, 2006.

H. Pietersen, J. Vilà-Guerau de Arellano, P. Augustin, A. van de Boer, O. de Coster, H. Delbarre, P. Durand, M. Fourmentin, B. Gioli, O. Hartogensis, et al. Study of a prototypical convective boundary layer observed during bllast: contributions by large-scale forcings. *Atmospheric Chemistry and Physics*, 15(8):4241–4257, 2015.

Y. Plokhenko and W. P. Menzel. The effects of surface reflection on estimating the vertical temperature–humidity distribution from spectral infrared measurements. *Journal of Applied Meteorology*, 39(1):3–14, 2000.

G. Poljak, M. T. Prtenjak, M. Kvakić, N. Strelec Mahović, and K. Babić. Wind patterns associated with the development of daytime thunderstorms over Istria. *Annales Geophysicae*, 32:401–420, 2014.

C. O. Popiel, J. Wojtkowiak, and B. Biernacka. Measurements of temperature distribution in ground. *Experimental Thermal and Fluid Science*, 25:301–309, 2001.

J. Porta, M. López-Acevedo, and C. Roquero. Edafología: para la agricultura y el medio ambiente. *Ed. Mundi-Prensa, Madrid*, page 807, 2003.

M. C. Potter, D. C. Wiggert, and B. H. Ramadan. *Mechanics of fluids*. Nelson Education, 2016.

Gregory S Poulos, William Blumen, David C Fritts, Julie K Lundquist, Jielun Sun, Sean P Burns, Carmen Nappo, Robert Banta, Rob Newsom, Joan Cuxart, et al. Cases-99: A comprehensive investigation of the stable nocturnal boundary layer. *Bulletin of the American Meteorological Society*, 83(4):555–581, 2002.

J. G. Powers. Numerical prediction of an antarctic severe wind event with the Weather Research and Forecasting (WRF) model. *Monthly Weather Review*, 135(9):3134–3157, 2007.

L. Prihodko and S. N. Goward. Estimation of air temperature from remotely sensed surface observations. *Remote Sensing of Environment*, 60(3):335–346, 1997.

S. Raasch and G. Harbusch. An analysis of secondary circulations and their effects caused by small-scale surface inhomogeneities using large-eddy simulation. *Boundary-Layer Meteorology*, 101(1):31–59, 2001.

P. Ramamurthy and E. R. Pardyjak. Toward understanding the behavior of carbon dioxide and surface energy fluxes in the urbanized semi-arid Salt Lake Valley, Utah, USA. *Atmospheric Environment*, 45(1):73–84, 2011.

C. Ramis and S. Alonso. Sea-breeze convergence line in Majorca: a satellite observation. *Weather*, 43:288–293, 1998.

C. Ramis and R. Romero. A first numerical simulation of the development and structure of the sea breeze on the island of Mallorca. *Annales Geophysicae*, 13:981–994, 1995.

C. Recondo and C. S. Pérez-Morandeira. Obtención de la temperatura del aire de asturias a partir de la temperatura de superficie calculada con imágenes noaa-avhrr. *Revista de Teledetección*, 17:5–12, 2002.

A. Rojas, O. Zúñiga, M. de Prager, J. Pérez, and J. M. Gascó. Conductividad térmica del suelo, materia orgánica, actividad y biomasa microbianas en sistemas de cultivo de maracuyá en toro, valle del cauca. *Acta Agronómica*, 56(1):17–22, 2007.

C. Román-Cascón, C. Yagüe, L. Mahrt, M. Sastre, G.J. Steeneveld, E. Pardyjak, A. Boer, and O. Hartogensis. Interactions among drainage flows, gravity waves and turbulence: a bllast case study. *Atmospheric Chemistry and Physics*, 15(15):9031–9047, 2015.

R. Romero and C. Ramis. A numerical study of the transport and diffusion of coastal pollutants during the breeze cycle in the island of Mallorca. *Ann. Geophys.*, 14:351–363, 1996.

J. M. Sánchez, W. P. Kustas, V. Caselles, and M. C. Anderson. Modelling surface energy fluxes over maize using a two-source patch model and radiometric soil and canopy temperature observations. *Remote Sensing of Environment*, 112(3):1130–1143, 2008.

T. Saravanapavan and D. G. Dye. Satellite estimation of environmental variables by the contextual analysis method: validation in a seasonal tropical environment. *Global Engineering Laboratory Institute of Industrial Science University of Tukyo*, 1995.

M. Sastre, C. Yagüe, C. Román-Cascón, and G. Maqueda. Atmospheric boundary-layer evening transitions: a comparison between two different experimental sites. *Boundary-Layer Meteorology*, 157(3):375–399, 2015.

T. J. Schmugge and F. Becker. *Remote sensing observations for the monitoring of land-surface fluxes and water budgets*. Springer, 1991.

P. Schotanus, F. Nieuwstadt, and H. De Bruin. Temperature measurement with a sonic anemometer and its application to heat and moisture fluxes. *Boundary-Layer Meteorology*, 26(1):81–93, 1983.

P. J. Sellers, F. G. Hall, G. Asrar, D. E. Strebel, and R. E. Murphy. The first ISLSCP field experiment (FIFE). *Bulletin of the American Meteorological Society*, 69(1):22–27, 1988.

P. J. Sellers, R. E. Dickinson, D. A. Randall, A. K. Betts, F. G. Hall, J. A. Berry, G. J. Collatz, A. S. Denning, H. A. Mooney, C. A. Nobre, N. Sato, C. B. Field, and A. Henderson-Sellers. Modeling the exchanges of energy, water, and carbon between continents and the atmosphere. *Science*, 275(5299):502–509, 1997.

E. Shamir and K. P. Georgakakos. MODIS Land Surface Temperature as an index of surface air temperature for operational snowpack estimation. *Remote Sensing of Environment*, 152:83–98, 2014.

G. D. Silcox, K. E. Kelly, E. T. Crosman, C. D. Whiteman, and B. L. Allen. Wintertime PM2. 5 concentrations during persistent, multi-day cold-air pools in a mountain valley. *Atmospheric Environment*, 46:17–24, 2012.

G. Simó, V. García-Santos, M. A. Jiménez, D. Martínez-Villagrasa, R. Picos, V. Caselles, and J. Cuxart. Landsat and local land surface temperatures in a heterogeneous terrain compared to modis values. *Remote Sensing*, 8(10):849, 2016.

G. Simó, D. Martínez-Villagrasa, M. A. Jiménez, V. Caselles, and J. Cuxart. Impact of the surface-atmosphere variables on the relation between air and land surface temperatures. *Pure and Applied Geophysics*, Under Review, 2018.

J. E. Simpson. *Sea breeze and local winds*. Cambridge University Press, 1994.

B. Smith and L. Mahrt. A study of boundary-layer pressure adjustments. *Journal of Atmospheric Sciences*, 38(2):334–346, 1981.

R. L. Snyder and J. P. Melo-Abreu. Frost protection: fundamentals, practice and economics. Volume 1. *Frost protection: fundamentals, practice and economics*, 1:1–240, 2005.

W. C. Snyder, Z. Wan, Y. Zhang, and Y.-Z. Feng. Classification-based emissivity for land surface temperature measurement from space. *Journal of Remote Sensing*, 19 (14):2753–2774, 1998.

H. Soegaard, N. O. Jensen, E. Boegh, C. B. Hasager, K. Schelde, and A. Thomsen. Carbon dioxide exchange over agricultural landscape using eddy correlation and footprint modelling. *Agricultural and Forest Meteorology*, 114(3):153–173, 2003.

M. A. Strunin and T. Hiyama. Spectral structure of small-scale turbulent and mesoscale fluxes in the atmospheric boundary layer over a thermally inhomogeneous land surface. *Boundary-Layer -Meteorology*, 117(3):479–510, 2005.

R. B. Stull. *An Introduction to Boundary Layer Meteorology*. Springer Netherlands, 1988.

J. Sun, S. P. Burns, D. H. Lenschow, R. Banta, R. Newsom, Ri. Coulter, S. Frasier, T. Ince, C. Nappo, J. Cuxart, W. BlumenXuhui, and L.Z. Hu. Intermittent turbulence associated with a density current passage in the stable boundary layer. *Boundary-Layer Meteorology*, 105(2):199–219, 2002.

J. Sun, D. H. Lenschow, S. P. Burns, R. M. Banta, R. K. Newsom, R. Coulter, S. Frasier, T. Ince, C. Nappo, and B. B. Balsley. Atmospheric disturbances that generate intermittent turbulence in nocturnal boundary layers. *Boundary-Layer Meteorology*, 110 (2):255–279, 2004.

J. Sun, L. Mahrt, R. M. Banta, and Y. L. Pichugina. Turbulence regimes and turbulence intermittency in the Stable Boundary Layer during CASES-99. *Journal of Atmospheric Sciences*, 69:338–351, 2012.

Y. J. Sun, J. F. Wang, R. H. Zhang, R. R. Gillies, Y. Xue, and Y. C. Bo. Air temperature retrieval from remote sensing data based on thermodynamics. *Theoretical and Applied Climatology*, 80(1):37–48, 2005.

C. Talbot, P. Augustin, C. Leroy, V. Willart, H. Delbarre, and G. Khomenko. Impact of a sea breeze on the boundary-layer dynamics and the atmospheric stratification in a coastal area of the North Sea. *Boundary-Layer Meteorology*, 125:133–154, 2007.

M. Telisman-Prtenjak, M. Viher, and J. Jurkovic. Sea-land breeze development during a summer bora event along the north-eastern Adriatic coast. *Quarterly Journal of the Royal Meteorological Society*, 136:1554–1571, 2010.

H. Tennekes and J. L. Lumley. *A first course in turbulence*. MIT Press, 1972.

J. E. Tierney, J. M. Russell, Y. Huang, J. S. S. Damsté, E. C. Hopmans, and A. S. Cohen. Northern hemisphere controls on tropical southeast african climate during the past 60,000 years. *Science*, 322(5899):252–255, 2008.

H. Tonooka. Accurate atmospheric correction of ASTER thermal infrared imagery using the WVS method. *IEEE Transactions on Geoscience and Remote Sensing*, 43:2778–2792, 2005.

T. E. Twine, W. P. Kustas, J. M. Norman, D. R. Cook, P. Houser, T. P. Meyers, J. H. Prueger, P. J. Starks, and M. L. Wesely. Correcting eddy-covariance flux underestimates over a grassland. *Agricultural and Forest Meteorology*, 103(3):279–300, 2000.

M. Urban, J. Eberle, C. Hüttich, C. Schmullius, and M. Herold. Comparison of satellite-derived land surface temperature and air temperature from meteorological stations on the pan-Arctic Scale. *Remote Sensing*, 5(5):2348–2367, 2013.

C. Vancutsem, P. Ceccato, T. Dinku, and S. J. Connor. Evaluation of MODIS land surface temperature data to estimate air temperature in different ecosystems over Africa. *Remote Sensing of Environment*, 114(2):449–465, 2010.

M. Vich, M. A. Jiménez, and J. Cuxart. A study of three well-defined temporal intervals in a stably stratified night. *Tethys*, 4:33–43, 2007.

P. Viterbo and A. Beljaars. An improved land surface parameterization scheme in the ECMWF model and its validation. *Journal of Climate*, 8(11):2716–2748, 1995.

P. Viterbo, A. C. M. Beljaars, J. F. Mahfouf, and J. Teixeira. The representation of soil moisture freezing and its impact on the stable boundary layer. *Quarterly Journal of the Royal Meteorology Society*, 125:2401–2426, 1999.

L. Vlassova, F. Perez-Cabello, H. Nieto, P. Martín, D. Riano, and J. de la Riva. Assessment of methods for land surface temperature retrieval from Landsat-5 TM images applicable to multiscale tree-grass ecosystem modeling. *Remote Sensing*, 6(5):4345–4368, 2014.

J. V. Vogt, A. A. Viau, and F. Paquet. Mapping regional air temperature fields using satellite-derived surface skin temperatures. *International Journal of Climatology*, 17 (14):1559–1579, 1997.

R. M. Wakimoto and N. T. Atkins. Observations of the sea-breeze front during CaPE. Part I: Single-Doppler, satellite, and cloud photogrammetry analysis. *Monthly Weather Review*, 122(6):1092–1114, 1994.

J. P Walawender, M. Szymanowski, M. J. Hajto, and A. Bokwa. Land surface temperature patterns in the urban agglomeration of Krakow (Poland) derived from Landsat-7/ETM+ data. *Pure and Applied Geophysics*, 171(6):913–940, 2014.

Z. Wan. New refinements and validation of the modis land-surface temperature/emissivity products. *Remote Sensing of Environment*, 112:59–74, 2008.

Z. Wan and J. Dozier. A generalised split-window algorithm for retrieving land-surface temperature from space. *IEEE Transactions on Geoscience and Remote Sensing*, 34: 892–905, 1996.

Z. Wan and Z.-L. Li. A physics-based algorithm for retrieving land-surface emissivity and temperature from EOS/MODIS data. *IEEE Transactions on Geoscience and Remote Sensing*, 35(4):980–996, 1997.

Z. Wan, Y. Zhang, Y. Q. Zhang, and Z.-L. Li. Validation of the land surface temperature products retrieved from Moderate Resolution Imaging Spectroradiometer data. *Remote Sensing of Environment*, 83:163–180, 2002.

Z. Wan, P. Wang, and X. Li. Using MODIS land surface temperature and normalized difference vegetation index products for monitoring drought in the southern Great Plains, USA. *International Journal of Remote Sensing*, 25(1):61–72, 2004.

Q. Wang, M. Watanabe, and Z. Ouyang. Simulation of water and carbon fluxes using BIOME-BGC model over crops in China. *Agricultural and Forest Meteorology*, 131 (3):209–224, 2005.

T. T. Warner. *Desert meteorology.* Cambridge University Press, 2009.

Q. Weng, D. Lu, and J. Schubring. Estimation of land surface temperature–vegetation abundance relationship for urban heat island studies. *Remote sensing of Environment*, 89(4):467–483, 2004.

Q. Weng, P. Fu, and F. Gao. Generating daily land surface temperature at Landsat resolution by fusing Landsat and MODIS data. *Remote Sensing of Environment*, 145: 55–67, 2014.

C. D. Whiteman. *Mountain meteorology. Fundamentals and applications.* Oxford University Press, 2000.

C. D. Whiteman, S. Zhong, W. J. Shaw, J. M. Hubbe, X. Bian, and J. Mittelstadt. Cold Pools in the Columbia Basin. *Weather and Forecasting*, 16:432–447, 2001.

C. D. Whiteman, S. W. Hoch, M. Hahnenberger, A. Muschinski, V. Hohreiter, M. Behn, Y. Cheon, S. Zhong, W. Yao, and D. Fritts. METCRAX 2006: Meteorological experiments in Arizona's Meteor Crater. *Bulletin of the American Meteorological Society*, 89(11):1665–1680, 2008.

N. Wildmann, G. A. Rau, and J. Bange. Observations of the early morning boundary-layer transition with small remotely-piloted aircraft. *Boundary-Layer Meteorology*, 157(3):345–373, 2015.

S. N. Williamson, D. S. Hik, J. A. Gamon, J. L. Kavanaugh, and G. E. Flowers. Estimating temperature fields from MODIS land surface temperature and air temperature observations in a Sub-Arctic Alpine environment. *Remote Sensing*, 6(2):946–963, 2014.

WMO. *Guide to Meteorological Instruments and Methods of Observation: (CIMO guide)*. World Meteorological Organisation, 2014.

B. Wrenger and J. Cuxart. Evening transition by a river sampled using a remotely-piloted multicopter. *Boundary-Layer Meteorology*, 165(3):535–543, 2017.

P. Wu, H. Shen, L. Zhang, and F.-M. Göttsche. Integrated fusion of multi-scale polar-orbiting and geostationary satellite observations for the mapping of high spatial and temporal resolution land surface temperature. *Remote Sensing of Environment*, 156: 169–181, 2015.

T. Yamada and G. Mellor. A simulation of the wangara atmospheric boundary layer data. *Journal of the Atmospheric sciences*, 32(12):2309–2329, 1975.

Y. Yamaguchi, A. B. Kahle, H. Tsu, T. Kawakami, and M. Pniel. Overview of advanced spaceborne thermal emission and reflection radiometer (ASTER). *IEEE Transactions on Geoscience and Remote Sensing*, 36(4):1062–1071, 1998.

W. Yu and M. Ma. Scale mismatch between in situ and remote sensing observations of land surface temperature: Implications for the validation of remote sensing lst products. *Geoscience and Remote Sensing Letters, IEEE*, 12(3):497–501, 2015.

P. Zhang, L. Bounoua, M. L. Imhoff, R. E. Wolfe, and K. Thome. Comparison of modis land surface temperature and air temperature over the continental usa meteorological stations. *Canadian Journal of Remote Sensing*, 40(2):110–122, 2014.

Y. C. Zhang, W. B. Rossow, and A. A. Lacis. Calculation of surface and top of atmosphere radiative fluxes from physical quantities based on ISCCP data sets: Part 1. Method and sensitivity to input data uncertainties. *Journal of Geophysical Research: Atmospheres*, 100(D1):1149–1165, 1995.

S. Zhong and E. S. Takle. The effects of large-scale winds on the sea–land-breeze circulations in an area of complex coastal heating. *Journal of Applied Meteorology*, 32(7): 1181–1195, 1993.

J. Zhou, X. Zhang, W. Zhan, and H. Zhang. Land surface temperature retrieval from MODIS data by integrating regression models and the genetic algorithm in an arid region. *Remote Sensing*, 6(6):5344–5367, 2014.